Final Report

Design of a Scaled Demonstrator Flight Test Model+

Fall DSE 2025/2026 - Group 2

Delft University of Technology

TU Delft

This page was intentionally left blank.

Design of a Scaled Demonstrator Flight Test Model+

by

Group 2

Student Name	Student Number	Task
Arend Winkel	5543177	Propellers, Project management, Sustainability
Daniel Jacobs	5484332	Electronics, Chairman, LaTeX management, Git organization, Organization & Planning
Hubert Blijie	5508835	Stability & control, Performance, Operations
Jakub Wysocki	5689996	Stability & control, Performance, System engineering
Jasmijn Burgers	5520991	Structures, Sustainability
Jasper Jansen	5508258	CAD Management, Modularity, Structures
Jules van Loon	5522099	Structures, Modularity, Production, Meeting minutes
Lennart Oosterholt	5299594	Aerodynamics, Market analysis, Cost breakdown
Ned Pigott-Rowles	4785541	Aerodynamics, Risk assessment
Philippe Beaumont	5575265	Stability & control, Performance, Editorial tasks

Tutor:	Prof.dr.ir. L.L.M. Veldhuis
Coaches:	A. Caon, Q. van Hilten
Project Duration:	November, 2025 - January, 2026
Faculty:	Faculty of Aerospace Engineering, Delft

Cover: Elysian E9X Render - Elysian Press Distribution

TU Delft

Executive Summary

The demand for scaled down versions of innovative aircraft has been steadily increasing over the last few years. These so-called scaled flight demonstrators (SFDs in short) can be used to perform flight testing for a fraction of the price, and with considerably more flexibility, with respect to full-scale testing. They also provide more certainty in result quality than can be done solely using computer simulations. One project that could benefit from such an SFD is Elysian. With their E9X battery-electric aircraft, Elysian hopes to conquer the short-range passenger aircraft market and provide a more sustainable future for aviation.
Therefore, the goal of this project is to develop an SFD based on the Elysian E9X, incorporating modular components, to provide Elysian and other potential customers with a possibility to adjust the configuration, and perform a multitude of research activity.

Functional analysis

A functional analysis was performed to identify the goal product's functionality. Starting with that aids in obtaining the optimal designs rather than an optimal way to implement a design. The systems of the airplane were broken down. Then, a Functional Breakdown Structure was performed. This helped in identifying the Functional Flow Diagram.

Requirements

The design is led by requirements set by stakeholders. These include performance requirements, stating the objective of the model, operational and safety requirements, sustainability requirements, and financial requirements. These can be summarised in the following statement: The model shall perform flight tests to determine the flight mechanical behaviour of various configurations, based on the conceptual Elysian E9X electric aircraft, within specified geometrical, operational, and sustainable limits for at least 20 20-minute missions with a development budget of €1M.
From these main requirements, system and subsystem requirements followed, defining the constraints of all components of the model, its production, and operation.

Aerodynamics

Maintaining similitude in flight mechanical behaviour between the full-scale ELysian E9X and the sub-scale SFD is a key objective of this project. The airframe of the SFD was obtained by geometrically scaling the E9X by a factor of approximately 10 % to maintain the Froude number between the two aircraft. From this, it was determined that at this scale the SFD would have to have a mass between 142 and 150 kg to best replicate the E9X at the altitude range of the test area at NLR Marknesse. Furthermore, 43. 8 m/s was determined to be the velocity that the SFD would be required to fly at based on the scale factor and cruise velocity of the E9X. Another factor that had to be scale to maintain similitude is the mass moments of inertia. For this scale factor it was calculated that the ratio of the SFD moments of inertia to E9X moments of inertia would have to be between 1.62 and $1.71 \cdot 10^{-5}$.

The aerodynamics of the airframe of both the E9X and SFD was analysed using Flow5. The E9X was an analysed in the flow conditions for it's cruise altitude and speed, namely 7000 m and 140,5 m/s. The SFD meanwhile was analysed for the flow conditions at 750 m and 43.8 m/s. The lift curve of both aircraft matched well for the linear range. The drag polar of the aircraft are significantly different, with the C_D of the SFD larger for a given C_L than the E9X. This is expected as the SFD will be at approximately 5% of the Reynolds number and 30% of the Mach number of the E9X. Therefore, effects due to compressibility and the local flow around the wing is not preserved at scale. The flow transition point on the airfoil can be forced to try and better replicate the local flow conditions using grit on the foil surface. This was investigated in Flow5 and a transition point X_{tr} of 1 was determined to be optimal. The optimal N-factor, which is a measure of free-flow turbulence, was also investigated. This cannot be changed for free flight testing but can be applied to wind tunnel testing.

A design feature of the E9X, and therefore the SFD, is that it employs a distributed propulsion system. This will significantly effect the lift and drag of the aircraft due to interactions between the system and the wing. It is also relevant to the objectives that the SFD should be a testbed to investigate distributed electric propulsion system. Therefore, the effect of this system was calculated using a simplified Aero-Propulsive Interaction Model. The additional lift and drag generate induced from this had minimal effect on the similitude.

With the additional lift induced by the distributed propulsion system the SFD was able to meet the $C_{L_{max}}$ required for take-off. However, during landing this effect will be minimised therefore high lift devices were sized to meet the $C_{L_{max}}$ requirement for landing. A plain flap system with with a chord of 20 % of the wing and taking up 31.72 % of the span was sufficient to meet this requirement at a deflection of 40°

Structures

The structural design of the SFD is composed of several, modular parts. Starting with the wing assembly, this complete Carbon Fibre Reinforced Polymer (CFRP) structure is capable of carrying the loads generated by the wing and transferring them to the fuselage. At the same time, it holds the engines and main landing gear, making the total wing assembly 33.65 kg. The thicknesses for both the wing skin and wingbox were constrained by to buckling, giving them thickness ranges between 1.5 mm and 2 mm. The wingbox design, consists of two spars with two webs and a circular leading-edge section which allows for easy engine integration.

The fuselage section is composed of five elements, the nose cone, top fairing, load bearing bottom half and tail section are all made of CFRP, the payload mounting plate, located inside the bottom half of the fuselage made of the aluminium alloy 7075-T7451. The CFRP fuselage structures all have a 1.75 mm thickness, both for buckling limitations and consistency throughout the structure. The full structural fuselage totals a weight of 12.33 kg, excluding the payload within the fuselage.

The structures within the SFD were analysed on multiple levels and failure modes. It was found here that buckling was the limiting factor for all load-bearing structures within the SFD. Load paths were also analysed and found stress concentrations up to a third of what the structure can handle, which thereby also eliminates failure modes such as fracture. Vibrations such as flutter were also analysed and found to not play a crucial role in the SFD.

Two ballast weights, 23.17 kg each, are placed in the main wing to ensure scaled matching mass moments of inertia to the Elysian-E9X aeroplane. These weights can also be removed, and different weights can be attached to this wing section as well as other locations. Other modular components are the detachable wings, nose cone, tail section, empennage, and engines. Giving the SFD a near infinite of different design configurations.

With the model designed to be modular, the assembly and detachment of principal components should be quick and convenient. The wing-to-fuselage connection is inspired by those of sailplanes. Which consists of a single spar on one side and a forked spar on the other. The spars of both wings slide into each other and are secured by two longitudinal pins near each wing's root. The assembly sits in a rectangular structure in the fuselage. The engines are bolted directly onto the wing's leading edge surface, at locations with an underlying rib. Lastly, the nose and tailcone feature extrusions sliding into similarly shaped holes on the fuselage tube. A total of 4 bolts, evenly distributed along the circumference, secures the connection.

Powertrain

The propeller is one of the most important parts of the SFD since it is essential for the propulsion of the demonstrator. The analysis starts of by selection of the amount of blades and a propeller diameter. The TUD-XPROP is used as reference since this is a propeller already that already exists and has been tested. Consequently, a thorough analysis of the advance ratio and methods to optimise efficiency are given. The pitch setting is essential for an optimal efficiency; the propeller is designed to be most efficient during cruise conditions, as this is the largest mission phase. A pitch setting of 36.5 [°] was determined using $javaProp$, whereafter, it is confirmed this pitch setting is also appropriate for take-off. The thrust over velocity curve for full power is given for this pitch setting, in the same diagram also the efficiency

over velocity is displayed. Finally, the blade design made by $javaProp$ is shown.

The electronics system was designed to efficiently provide enough power and energy to perform a flight with 20 minutes of cruise. It makes use of a set of five 14S LiPo batteries, made by Tattu, together storing over 5.6 kWh of energy. The system is also supplied with backup power from a backup battery that is made to provide power to all avionics & control systems for at least five minutes after possible battery failure. Using the recommended charging infrastructure, the system can be fully recharged in an hour, making for a quick turn-around time.

The system was inspired by the robustified infrastructure of the DEP-SFD project, where fire safety measures were implemented after an accident occured with an earlier test model. Through use of redundant fusing, and fully isolatable batteries, the safety of the system is guaranteed in case of a battery failure.

The system is controlled by the Embention Veronte flight computer, that uses a set of custom C++ software scripts to give the operator full control over the aircraft, as well as possibility to gather data on in-flight behaviour of the aircraft. This software also consists of a number of systems that can check the state of the aircraft to make sure all components are in fully healthy conditions, and with possibility to warn the operator. This should help prevent accidents from happening, as the operator can take action before critical values are reached.

Finally, the full design of the powertrain is put together into a Hardware Diagram that displays all connections (see Figure 1). Here, power lines, as well as the communication network are laid out onto the layout of the aircraft, also showing the rough location of the individual components.

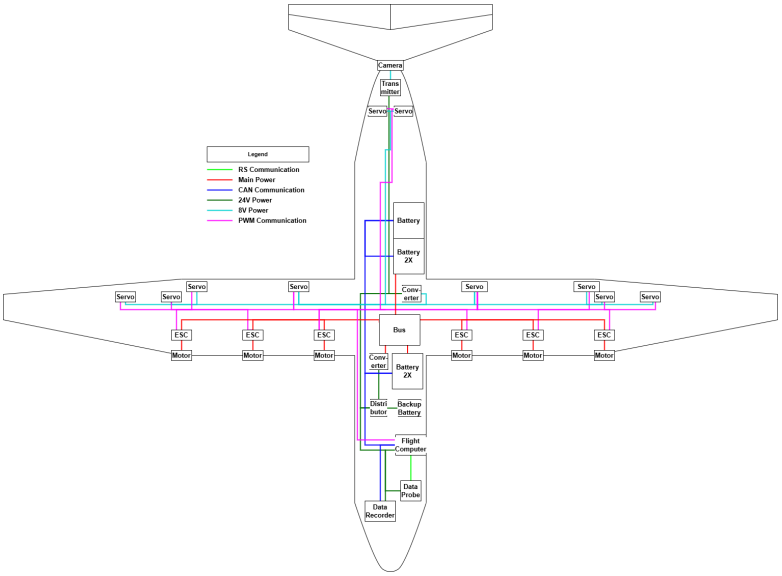

Figure 1: Hardware Diagram showing physical connections between electronic components in their location

Stability & Control

This chapter provides a comprehensive design and analysis framework for the stability and control characteristics of the SFD in relation to the Elysian E9X conceptual design. The primary objective of this work is to ensure that the SFD reassembles the flight-mechanical behaviour, enabling the validation of DEP effects on aircraft handling qualities.

To achieve dynamic similitude, the mass moments of inertia (I_{xx}, I_{yy}, I_{zz}) for the E9X were approximated using Roskam's empirical methods, accounting for the unique mass distribution of wing-mounted batteries and motors. Using Froude scaling, target inertia values were established (for example an average I_{yy} of 43.08 kg $\cdot$ m^2 for a 146 kg model). This ensures that the rotational accelerations and time-constants of the SFD are kinematically representative of the full-scale aircraft.

A rigorous longitudinal stability analysis was performed by integrating aerodynamic data from Flow5 with a propulsion normal-force model based on USAF DATCOM (LR-761).

- **Longitudinal:** The analysis identified a powered stick-fixed neutral point at 1.74 m from the nose. By maintaining a minimum static margin of 5% MAC, the aft CG limit was defined to ensure safety during all flight phases.
- **Lateral-Directional:** Stability derivatives (C_{y_β}, C_{n_β}, C_{l_β}) were derived for both scales. While side-force scaling remains exact due to geometric similarity, minor deviations in dihedral effect (9.81%) and directional stability (3.29%) were identified and found to be within acceptable tolerances for conceptual validation.

Control surfaces were sized to satisfy quality requirements and safety margins:

- **Ailerons:** Sized for Class III "Level 1" criteria for reassembling the Elysian E9X. The design allows for full control authority in 6 m/s crosswinds with a 10.6% safety margin before stall.
- **Elevator:** Designed for a $15°/s^2$ rotation rate at take-off. With an elevator-to-tail chord ratio of 0.26, the aircraft can be trimmed across the entire flight envelope without risking horizontal tail stall.
- **Rudder:** Governed by the critical One Engine Inoperative (OEI) condition. The rudder provides sufficient yawing moment to counteract asymmetric thrust with a required deflection of 22.32°, well within the 25° physical limit.

Eigenvalue analysis of the state-space equations confirms that the longitudinal modes (Short Period and Phugoid) are naturally stable and scale according to Froude laws. However, the analysis revealed a naturally unstable Dutch Roll mode for both scales. This finding necessitates the implementation of a Stability Augmentation System within the flight control laws to artificially increase damping. Sensitivity analysis showed potential improvement of longitudinal stability, which cannot be said about the Dutch roll.

The design successfully meets the defined stability and control requirements. The SFD is confirmed to be a representative platform for investigating the flight mechanics of the Elysian E9X, provided that active damping is employed to manage lateral-directional oscillations.

Performance

The SFD, as any other aircraft, has certain performance metrics that must be quantified, subject to requirements depending on the mission. The mission of this SFD is to replicate and examine the flight mechanical behaviour of the Elysian E9X. This is done through testing, both in a wind tunnel and in flight at Marknesse Drone-Centre.

The SFD requires a take-off distance of 227.18 m, adhering to FAR-25 regulations. Once take-off has occured, the SFD has a steady rate of climb of 5.75 m/s. Once at cruise flight level, the expected flight speed is 43.8 m/s. Including a 20% energy buffer, the SFD has a minimum range of 20km and an endurance of 35 minutes. It has a glide path angle of -3.55 ° and a rate of descent of 2.58 m/s. Finally, starting from a screen height of 15 m, it has a landing distance of 146.75 m, thus also adhering to FAR-25 regulations.

Production

To produce the SFD, three different material types of components must be produced. The first type, the majority of components are CFRP parts, which make up most of the SFD structure. These components will be produced using vacuum-bag-only (VBO) procedure using out-of-autclave (OaA) prepreg materials. This process uses moulds in which the carbon fibres are layered after which they are enclosed in resin, vacuumed and heated to obtain the manufactured part. The aluminium mounting plate for the payloads will be manufactured using conventional cutting and welding techniques. Finally, to ensure all avionic and electronic parts are removable for maintenance, some non-boltable parts will receive a 3D-printed polyamide support bracket.

Most of the integration of the components, such as fuselage compartments and the wing, will be done

using the modular attachment points on the SFD. However, to join smaller sections together, such as the full wing assembly, the Araldite 2031 adhesive will be used to bond sections together.

Operations & Logistics

In the operations and logistics chapter is discussed what operational environments and facilities are being used during the test campaign. First, there is a central integration and support facility, where maintenance takes place, integration and storage. This location is undecided, as it depends on the available options of the customer. Instead, there are requirements set for the central facility: it must provide controlled storage for batteries and sensitive avionics, and include a dedicated charging area sized for the campaign's electrical load and equipped with appropriate fire-safety provisions. The second environment is the DNW-LLF wind-tunnel in Marknesse, which perfectly fits the needs for the SFD test campaign. The third environment is the NLR Drone Centre, where the EHR66 opens the possibility of making BVLOS test flights possible. Due to the controlled operational volume and safety taken in to account in our design (such as a flight termination system) this SFD passes through all required BVLOS regulations. Transport between all locations is made easy with wheeled racks for the disassembled components of the SFD, a support kit and standardised cases containing all the ground systems.

Maintenance is divided into two levels. Line maintenance is on-site and can be done by field tools and spares. Depot maintenance is done atthe central facility. If the repair affects safety-critical behaviour, it will always be chosen for depot maintenance.

It is chosen for staged verification, which means that when a critical failure occurs, it is easy to identify which stage was the defined safe state before. After integration, stationary powertrain validation will be done first, then wind tunnel test, and after the stationary powertrain tests and taxi tests, outside the flight testing at Marknesse starts. During tests, the team is divided into authority and responsibility roles. At the beginning of the flight test day, the chief of operations decides if the missions can go through based on go/no-go requirements. If the day goes through, the chief of operations will brief the entire team

In order to make sure no failures would violate safety, safe states are defined in which the system will be transferred to if a failure occurs, to get the SFD safely on the ground. If the SFD is uncontrolable there is a flight termination system to make sure the SFD stays in the controlled operational volume.

Finances & Market analysis

The financial feasibility and market viability is almost always one of the most driving factors in the design of a product. In order to get a good indication of the status of those factors, one can perform a cost breakdown and a market analysis. The combination of these analyses will find whether the potential revenue of a product is enough to compensate the cost. The SFD project consists of 3 main cost categories: R&D cost, manufacturing cost and operational cost. the course of all the design phases, a total of 4500 hours are spent on the SFD. This equates to a total R&D stage cost of €675,000. The component and manufacturing cost turn out to be €121,770 and the operational costs equate to €40,505. Combining these costs and adding a 20% margin on the second and third category, results in a final cost of €869,730. This value falls within the stakeholder requirements and thus complies.

The market analysis performed gives an insight into the market landscape, how big the addressable market is and what consumers to focus on. A number of potential market players was identified, from commercial aircraft manufacturers and OEM's, to innovative aviation startups and research institutions. All of these parties could use the model for a number of research purposes. A potential interest was also determined to come from defence contractors and government agencies. These parties would mainly be interested in having access to modular SFD concepts, to be able to test a wide range of layout varieties. With this information a stakeholder analysis was performed to find out which parties hold the most influence and interest in the envisioned design, showing that especially OEM's, aviation start-ups and research institutes would be influential high-interest stakeholders.

After performing a SWOT analysis, showing mainly that opportunities lie in accommodating for sustainable aviation. Since there is significant sustainability-driven funds going into the flight demonstrator

market, and there is an increasing number of start-ups, it can be derived that designing for a low-cost, standardised (modular) design is the most viable design for market entry.

RAMS Characteristics

To get a good overview of the cost- an operational effectiveness of the aircraft, a RAMS analysis was performed. Here, it was found that the testing environment is a big advantage: it adds reliability, due to the fact that checks can be performed in between each 20 minute flight, and the same goes for the maintainability. The design choices also strongly add on to this reliability by using a design for maintainability approach which, in turn, allows for better ability of inspections. The use of only commercially available components also allows for quicker replacements.

There are also a few downsides to the model. Due to the fact only one is produced (or at least a small amount), the backup options available

Technical Risk Assessment

An full assessment of the all the technical risks identified for the project is given. These risks were used to help develop some of the requirements of the design. For each risk, a risk rate is evaluated based on their likelihood of occurrence and consequence if they were to occur. For the most severe risks, a mitigation plan is developed and the risk rate reassessed. The effect of mitigation was displayed in the risk maps and showed a reduction of the risk rate of the most severe to acceptable level after the implementation the the mitigation plans. A contingency plan for the most severe risks is also presented.

Sustainability

A Life Cycle Analysis (LCA) is performed in the SFD with the system boundary Cradle-to-Grave. This LCA focused mainly on the batteries used and the CFRP as these two components have the greatest impact. From this, the main contributing steps of the life-cycle of the two components were identified, and strategies were set up to improve their sustainability. Additionally, a complementary analysis was performed of the social and economic impacts of the design, and an analysis was performed on the sustainability impacts of adopting a modular approach to the SFD.

Development plan

As the Design Synthesis Exercise is finished, the team plans to establish a cooperation with NLR and visit their research facilities in Marknesse. With their help, industry specialists feedback from the incoming symposium and based on conclusions drawn from this report, a final design is planned to be achieved, which is to be proceeded by production, assembly and testing. It is planned to obtain the final, tested product by May 2027. The plan together with a timeline is presented on a Gantt chart.

Conclusion and Recommendations

The goal of this project was to design an SFD inspired by the Elysian E9X, with modularity options. The main performance conclusions can be summarised as: the SFD is capable of demonstrating the flight mechanical behaviour of the E9X, the SFD is able to fit an FCMS (Flight Control and Measurement System), the subtotal mass is equal to 107.58 [kg], a scale of 10% is used, and the wingspan is 5.044 [m]. The structure of the SFD is designed in such a way that it can sustain sufficient structural integrity for at least 20 flights, and the powertrain allows for a minimum cruise phase of 20 minutes per flight. The BVLOS regulations have been checked and it was decided to fly the SFD at drone-port Marknesse for safety reasons. The demonstrator is equipped with 6 engines and 5 LiPo batteries allowing for distributed electric propulsion, the design allows for many modularity options, and the equipment and propulsion system consists of COTS (Commercial Off-The Shelf) components except for the propeller blades. The cost limitation of 1 million euro is met easily as the total ready-to-fly manufacturing cost comes down to 821,124 euros. In conclusion, an SFD has been created that is fitting to the needs of Elysian and also hosts modular features, is safe and can perform 20 missions of 20 minutes, is fully battery-electric, and managed to stay within budget.

The report establishes an overall design for the SFD, though further details need to be developed, and

some design choices could be reconsidered. The design process prioritised replicating the Elysian E9X first, with modularity incorporated afterwards. For future studies that focus more on modularity, it is recommended to consider modularity at an earlier stage, ensuring that all potential modular options are possible to be integrated in the design. In addition, closer collaboration with Elysian is recommended to obtain more precise data, as current methods used, such as pixel counting, could provide inaccuracies. Finally, a significant amount of estimations were done by the tool Flow5, though this is an acceptable method at this design phase, when working out further details, it is advised to utilise different methods such as Computational Fluid Dynamics (CFD) simulation tools or calculations.

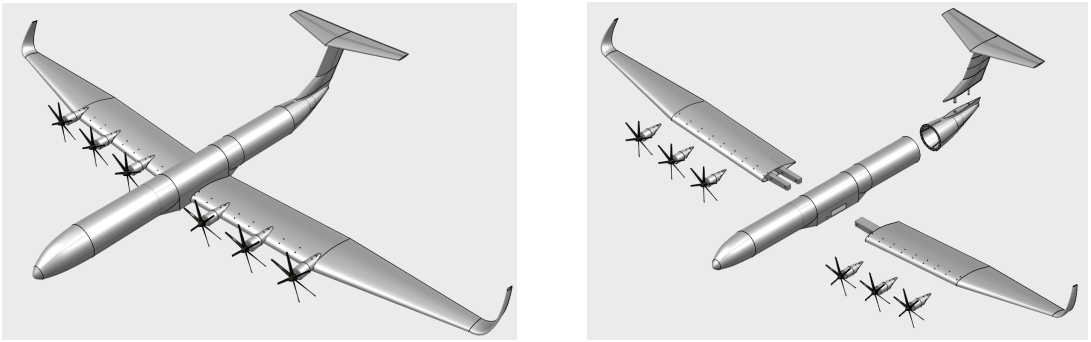

(a) SKRIBBL 3D model

(b) SKRIBBL exploded view of modular components

Figure 2: 3D CAD representation of the SKRIBBL and its modular components

Table 1: SKRIBBL dimensions, weight, and layout

Parameter	**Unit**	
Length	[m]	3.4
Wingspan	[m]	5.044
Height from ground	[m]	1.208
Fuselage diameter	[m]	0.3
Wingarea	[m^2]	2.02
Motor count	[-]	6
Propeller blade diameter	[m]	0.4064
Propeller blade count	[-]	6
Battery capacity	[kWh]	5.6
Flight endurance	[min]	35
Production cost	[€]	121,770
Weight	[kg]	150

Contents

Nomenclature

Abbreviations

AC	Alternating Current
BMS	Battery Management System
$BVLOS$	Beyond Visual Line Of Sight
CAN	Controller Area Network
$CFRP$	Carbon Fibre Reinforced Polymers
CPU	Central Processing Unit
DC	Direct Current
DEP	Distributed Electric Propulsion
DOT	Design Option Tree
DP	Distributed Propulsion
EDF	Electric Ducted Fan
EMS	Energy Management System
ESC	Electronic Speed Controller
$FCMS$	Flight Control & Management System
FPV	First Person View
FRP	Fibre Reinforced Polymer
$GFRP$	Glass Fibre Reinforced Polymers
$GNSS$	Global Navigation Satellite System
GPS	Global Positioning System
HV	High-Voltage
$KFRP$	Kevlar Fibre Reinforced Polymers
LV	Low-Voltage
OEI	One Engine Inoperative
POV	Point of View
PWM	Pulse Width Modulation
RF	Radio Frequency
RS	Recommended Standard
SFD	Scaled Flight Demonstrator
SoC	State of Charge
$SoCe$	State of Charge Estimator
SoH	State of Health
VMC	Visual Meteorological Conditions

Subscripts

0	Initial condition
$0L$	Zero lift
α	Angle of attack
β	Sideslip angle
∞	Free-Stream
A	Full scale aircraft
a	Of aileron
$aileron$	Of aileron
ax	Axial
B	Blades
$c/2$	Half chord
$c/4$	Quarter chord
c	Coefficient
$climb$	Climb phase
cr	Cruise
$Crit$	Critical
$cruise$	Cruise phase
D	Drag
d	Section drag
des	Design
f	Flap
$hortail$	Of horizontal tail
i	induced
$L, airframe$	Airframe lift
L	Landing
L	Lift
l	Rolling force moment
l	Section lift
LOF	Lift-Off
M	Subscale Model
m	Moment
m	Pitching force moment
Max	Maximum
Min	Minimum
$motor$	Motor
n	Yawing force moment
P	Power
p	Propeller
p	Rolling rate
$prop$	Propeller
q	Pitching rate
r	Yawing rate
ref	Reference
rot	Rotational
T	Thrust
TO	Take-Off
$total$	Total
TR	Transition
$trim$	trim
$vertail$	Of vertical tail
w	Wing
X	Force in the X axis

X	Of X axis	
xx	Around X axis	
Y	Force in the Y axis	
Y	Of Y axis	
yy	Around Y axis	
Z	Force in the Z axis	
Z	Of Z axis	
zz	Around Z axis	

Symbols

α	Angle of Attack	$\circ$
β	Pitch Angle	$\circ$
β	Slipstream correction factor	–
$\Delta()$	Change in aerodynamic coefficient	–
Δq	Shear flow increment	m/s
ΔY	Span fraction occupied by distributed-propulsion system	–
Δy	Lateral clearance between propellers as a fraction of propeller diameter	–
δ	Deflection	rad
ϵ	Horizontal tail downwash angle	rad
η	Efficiency	%
γ	Buckling knockdown factor	m/s
Λ	Sweep angle	$\circ$
π	Mathematical Constant	–
ρ	Density	kg/m^3
σ	Air density ratio	–
σ	Solidity	–
σ	Stress	m/s
τ	Change of pitch angle	rad
τ	Change of roll angle	rad
τ	Control surface effectiveness	–
τ	Shear Stress	Pa
υ	Poisson's ratio	–
A	Aspect ratio	–
a	Axial induction factor	–
b	Safety factor	–
b	Wingspan	m
C	Coefficient	–
c	Chord	m
C_f	Skin-friction coefficient	–
c_f	Sectional skin-friction coefficient	–
C_{a_b}	Derivative of a over b	–
D	Drag	N
D	Propeller Diameter	m
E	Energy	J
E	Young's Modulus	Pa
e	Oswald efficiency factor	–
h	Altitude	m
I	Mass moment of inertia	$kg \cdot m^2$
J	Advance Ratio	–
K'	Correction factor for plain flaps	–
K	Ratio of incremental section lift coefficient to max incremental section lift coefficient due to flaps	–
k	Buckling coefficient	–
K_i	Coefficient row vector for slipstream factor surrogate model	–
K_Λ	Correction factor sweep angle	–
L	Length of the fuselage	m
L	Moment force in roll axis	$N \cdot m$
M	Mach Number	–
M	Moment	$N \cdot m$
m	Mass	kg
N	Number	–
N	Turbulence N factor	–
n	Geometric scale factor	–
n	Rotational Speed of the Propeller	RPS
P	Power	W
p	Rolling rate	rad/s
q	Pitching rate	rad/s
R	Radius	m
r	Yawing rate	rad/s
Re	Reynolds Number	–
ROC	Rate of Climb	m/s
RPM	Revolutions Per Minute	$1/min$
S	Reference Area	m^2
S	Wing surface area	m^2
s_{FL}	Field length distance	ft
T	Thrust	N
t	Time	s
TOP_{25}	FAR 25 take-off parameter	lbs/ft^2
u	Change of speed in the X direction	m/s
V	Velocity	m/s
v	Change of speed in the Y direction	m/s
W	Weight	N
w	Change of speed in the Z direction	m/s
X	Column vector for slipstream factor surrogate model	–
x	Axial position	m

Introduction

In 2023, commercial aircraft operators burned 348.75 billion litres of jet fuel, presenting 8% of the total worldwide liquid fuel usage. In turn, the global aviation idustry accounted for more than 2 percent of all human-induced CO_2 emissions[1]. Although Sustainable Aviation Fuels are on their way to create a sustainable alternative, this effect is only marginal: By 2030, the goal is that Aviation fuel should be 5% less carbon intensive, compared to today's fossil fuels. Therefore, the aviation industry is looking into more efficient alternative energy sources.

One of these options is to use battery-electric aircraft. In the coming years, Elysian plans to create a 90-seater battery-electric propeller aircraft with an design range of 1000 km. Initial research already suggests a reduction of CO_2 emissions of around 90% compared to an Airbus A320 (based on g/pax-km metrics)[71].

While this is a very promising outlook, there is still an obstacle to overcome: Before any new aircraft model can take flight, it needs to be fully certified. For new aircraft types, this process can take up to almost 10 years from the moment the final design is done[2]. This would mean that the earliest moment the Elysian E9X would take flight is in 2036. And this does not even take into account the use of a fully experimental powertrain. Therefore, it is necessary to find a way of speeding up this process. Although simulations can go a long way in performing initial estimations of the aircrafts behaviour, they are very theoretical, and thus far from perfect.

Another way of testing new designs is through the use of scaled down models of the aircraft. These so-called Scaled Flight Demonstrators (SFD's) can be designed in such a way, that they mimic the flight mechanical behaviour of the full scale aircraft. However, because of the smaller scale, they can become airworthy much faster than their full-scale counterparts. This means these SFD's are a very viable alternative to full-scale flight testing, and they can significantly speed up the design and certification process.

The S.K.R.I.B.B.L. project is centred on this concept. In ten weeks, a group of ten student engineers, spend their time on coming up with a design for an SFD with the Elysian E9X as a use case. Its design is made to model the behaviour of the full-scale model as well as possible, while built on a 10% scale. This model will be used to perform flight dynamics tests, as well as performance analyses, with the main goal to collect in-flight data on these subjects. It should use commercially available components where possible and comply to all regulations with regards to Beyond-Visual-Line-Of-Sight flight (BVLOS in short).

Another aspect that is of importance for this design is that it should embody the possibility to exchange different aircraft layouts with the goal to allow operators to have more control over what designs they want to test. This will, in turn, enlarge the marketing feasibility of the model once produced, possibly attracting customers outside of the initial client Elysian (e.g. research institutes like the TU Delft or Dutch Aerospace Centre NLR).

This report is the final report in a series of four, explaining the final design of the project, its technical performance, and the specific design features. The report following structure: chapter starts out with giving a more elaborate introduction into the project and its objectives. Afterwards chapter 1.2 shows the functional analysis performed. Here the functions of the design are explained in the form of multiple diagrams. This is then followed up by a list of the stakeholder and system requirements in chapter 2.3.

The technical part of the report is kicked off in chapter 2.3. Here, a summary is given of all the design work that has been done up until the start of this report. Then, the technical analyses of the final design start with Aerodynamics in chapter 4.5. The details of the scaling methods, as well as an aerodynamic analysis of the model. Afterwards chapter 5.6 handles the structural design of the aircraft. Here, the first technical analysis of the modularity aspects is also given.

[1] https://atag.org/facts-figures , accessed on 21/01/2026

[2] https://www.faa.gov/aircraft/air_cert/airworthiness_certification, accessed on 21/01/2026

In chapter 6.7, a detailed analysis is performed for the design and performance of the propeller. Then, the internal hardware and software of the demonstrator is explained, using a set of diagrams. chapter 7.6 displays an analysis of the stability characteristics, going into an approximation of the mass moment of inertia, as well as the control surfaces. This is supplemented in chapter 8.5.2 with a full analysis of the performance of the aircraft. After this is done, the analyses are followed up by a summary of the complete design, including modularity aspects in chapter 9.4.

chapter 10.3 explains both the production of the components, as well as a plan for assembling them together to form the model. The operational concept is described in chapter 11.2.0.0.3. This chapter consists of an overview of the logistics involved with the usage of the designed aircraft, as well as an explanation of all the limits set on testing by national and international regulations with regard to unmanned BVLOS flight. Afterwards, chapter 12.8.1 delves deeper into the commercial use of the aircraft, through a market analysis. It also supplies a cost breakdown, containing the ready-to-fly price of the final design.

chapter 13.4 serves as an introduction into the risks associated with the demonstrator. A RAMS analysis is performed, that gives insight into the operational- and cost efficiency. This flows into the technical risk assessment, which is performed in chapter 14.4. Through use of a mitigation plan, the risks are assessed, and brought down to acceptable probability levels. When this is done, chapter 15.3 provides an outlook in the sustainability aspects that have been kept in mind throughout the different stages of the design process, and gives a life cycle assessment for the final product. Lastly chapter 16.4 shows an outlook into the future. Here, the next steps of the project are discussed, supported by a Gantt chart to determine a planning for the followup of this report. The report is concluded with conclusions and recommendations in chapter 16.4.

1
Project Motivation and Background

1.1. Project Motivation

In the Introduction of this report, it has already been stated that the usage of a Scaled Flight Demonstrator (SFD) can be valuable as it can speed up the design and certification process of an aircraft. This is due to the fact that it is significantly easier to get an SFD up to the requirements and certifications needed to fly than a full-scale model. But why is this design relevant?

Today, an ever increasing stream of technological developments is ongoing, having the need to be tested, validated, and verified. Especially in the aviation sector, where the demand and search for efficiency, alternative energy sources, and sustainability is higher than ever. Many new developments and extraordinary concepts are to be tested on scaled models before being implemented on real aircraft. This ensures a safe development without risking, in case of failure, huge financial consequences, human safety, and project time. Concluding, by the use of scaled demonstrators, new technologies can be tested and proven in a safe, efficient, relatively low-cost, and yet reliable manner.

For this report, the Elysian E9X was used as a case study. However, the concept is intended to be applicable to a range of different interested parties. This particular scaled flight demonstrator has multiple purposes. The primary objective is to test, validate, and verify flight characteristics of a full-scale aircraft. Furthermore, it can be used to explore the behaviour of unconventional aircraft configurations using distributed electric propulsion. The SKRIBBL is specifically scaled, designed, and set up to determine stability and controllability characteristics. Results from these tests could verify computer simulations, avoiding the necessity to perform this early stage verification with a full-scale aircraft. It cannot replace any of the tests required to certify the real full-scale aircraft, but major flaws or unexpected behaviour of the concept can be determined and resolved at an early design stage, avoiding expensive modifications.

The SKRIBBL has certain limitations to its testing capabilities. Different flight characteristics, such as flutter, performance, stability and control, or speed regimes, require different scaling methods. The main objective of the model is to determine the stability and control characteristics. Therefore, the control surfaces, centre of gravity, and mass moment of inertia are scaled as such to provide the most accurate resemblance to the full-scale system. An overview of the SKRIBBL's testing capabilities are given in table 1.1 below.

Table 1.1: Full-scale characteristics accurately represented by SKRIBBL

Realistic	Not suitable for
✓ Longitudinal stability	✗ Flutter behaviour
✓ Lateral stability	✗ Drag estimations
✓ Control characteristics	✗ Take-off and Landing performance
✓ Cruise performance	✗ High and Low speed performance
✓ Distributed propulsion influence	✗ Aeroelastic effects
✓ Assymetric thrust behaviour	✗ Flap characteristics

Furthermore, a scaled representation of a conceptual aircraft will contribute greatly to a company's marketing strategy. It provides an actual physical model, which makes a better impression than on screen. It can be brought and displayed at various conventions or air shows, attracting attention from investors, clients, and the public. At last but not least, it proves that the concept can be taken from the page and actually be flown.

In addition, the SKRIBBL was designed to make its sector more sustainable. This was achieved through a number of ways, but modularity and reusability play the biggest roles.

As previously mentioned, if customers suddenly make major changes in their design, or they wish to test different alternative layouts, the SKRIBBL does not need to be completely rebuilt. Instead, only specific parts need to be replaced. Furthermore, the internal layout was designed to ensure accessibility and easy component replacement. As a result, batteries and other key components can be reused across multiple customer projects.

The modular and reusable design approach directly reduces material consumption, waste, and unnecessary man-hours made for alternative designs. This contributes not only to the SFD's environmental sustainability but also to its social and economic sustainability. The modular and reusable design reduces costs, thereby making the use of the KRIBBL accessible to smaller players in the aircraft manufacturing and testing sector.

1.2. Project Background

Before proceeding with the report, some general background is needed to ensure a full understanding of the subjects and concepts that will be discussed.

Elysian E9X

The objective of this project was to develop a concept of modular SFD that is applicable to different types of customers. In collaboration with Elysian Aircraft, their conceptual E9X was used as a case study. Therefore, to proceed with this report, the following background information on this aircraft is required.

The Elysian E9X is a conceptual design of a 90-seater battery electric propelled aircraft. The E9X is planned to have a battery-only range of 750 [km] and a maximum take-off mass of 82.5 [t] [71]. The E9X uses Distributed Electric Propulsion (DEP); every wing hosts three electric propeller engines responsible for generating thrust, also one of the similarities that explains why the E9X was chosen as a reference case. Elysian's goal is to decarbonise the aviation sector, starting with creating a regional jet capable of competing with conventional kerosene fuelled regional jets. Our SFD should enable Elysian to replicate the full-scale E9X flight mechanical behaviour.

Modularity

Although the Elysian E9X is taken as the main reference case, the design of the SFD has many modular aspects that enable it to easily be transformed into alternative layouts. The demonstrator will therefore also be attractive for other manufacturers seeking an instrumented testbed to replicate their full-scale model flight mechanical behaviour. The main modularity aspects focused on are: interchangeable tail and nose, interchangeable wings, and adjustable motor position and layout.

Scaled Flight Demonstrator

The use of scaled flight demonstrators has always represented a viable option for aircraft manufacturers. The ability to realistically mimic the flight behaviour of full scale models for a relatively low price makes them popular for validating conceptual aircraft designs. The SFD has taken inspiration from the DEP-SFD2, also an SFD with DEP that was produced by NLR and OrangeAerospace [17]. The design was based upon the A320 and could also host various engine configurations, twin-engine conventional turbojet or six-engine distributed electrically propelled.

2 Functional analysis

The determination of the product's functions is the basis of each project. It helps in a better understanding of the customer's needs. Starting with the system breakdown in section 2.1, the aircraft's systems are introduced. Proceeding to Functional Flow Diagram in section 2.3, the demonstrator's life cycle is discovered, and all required functions are found. That is followed by a functional breakdown in section 2.2. It provides a more detailed description of the super-system's functions.

2.1. System breakdown

For systems engineering purposes and enabling better design organization, a system breakdown was introduced. As the project is still in its initial phase, its structure might change later. It is presented in figure 2.1.

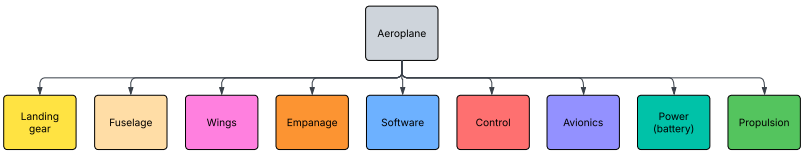

Figure 2.1: System breakdown

2.2. Functional Breakdown Structure

The Functional Breakdown Structure (FBS), presented figure 2.2, illustrates the hierarchical decomposition of the Scaled Flight Demonstrator's (SFD) operational goals. The analysis begins with the top-level functions representing the entire life-cycle of the product.

The primary functions are systematically broken down into sub-functions, such as "Perform a take-off", and further decomposed into elementary functions. This top-down approach ensures granularity and completeness. As shown in the diagram legend, the colour coding differentiates between hierarchical levels.

This decomposition remains solution-free where possible; for example, the function "Increase lift" is identified before assigning it to a specific "Wing" structure and a design option. This ensures that the subsequent physical allocation is logical and traceable, even though some design options are enforced by the requirement of using the Elysian E9X aeroplane as a base for the modular demonstrator.

2.3. Functional Flow Diagram

While the FBS defines what functions exist, it does not describe when they occur. To address the flow aspect of the mission, a Functional Flow analysis was conducted, as shown in figures 2.3 and 2.4 (part 1 and part 2).

This diagram organizes the identified functions across the system's complete lifecycle, categorizing them into distinct phases, By mapping functions to the lifecycle, the analysis highlights critical dependencies and interfaces between systems. For instance, the "Monitor Battery Health" function is critical across multiple phases, whereas "Retract Landing Gear" is isolated to the transition between take-off and cruise. For better readability, the functional flow diagram does not include the lowest level functions.

Figure 2.2: Functional Breakdown Structure (FBS)

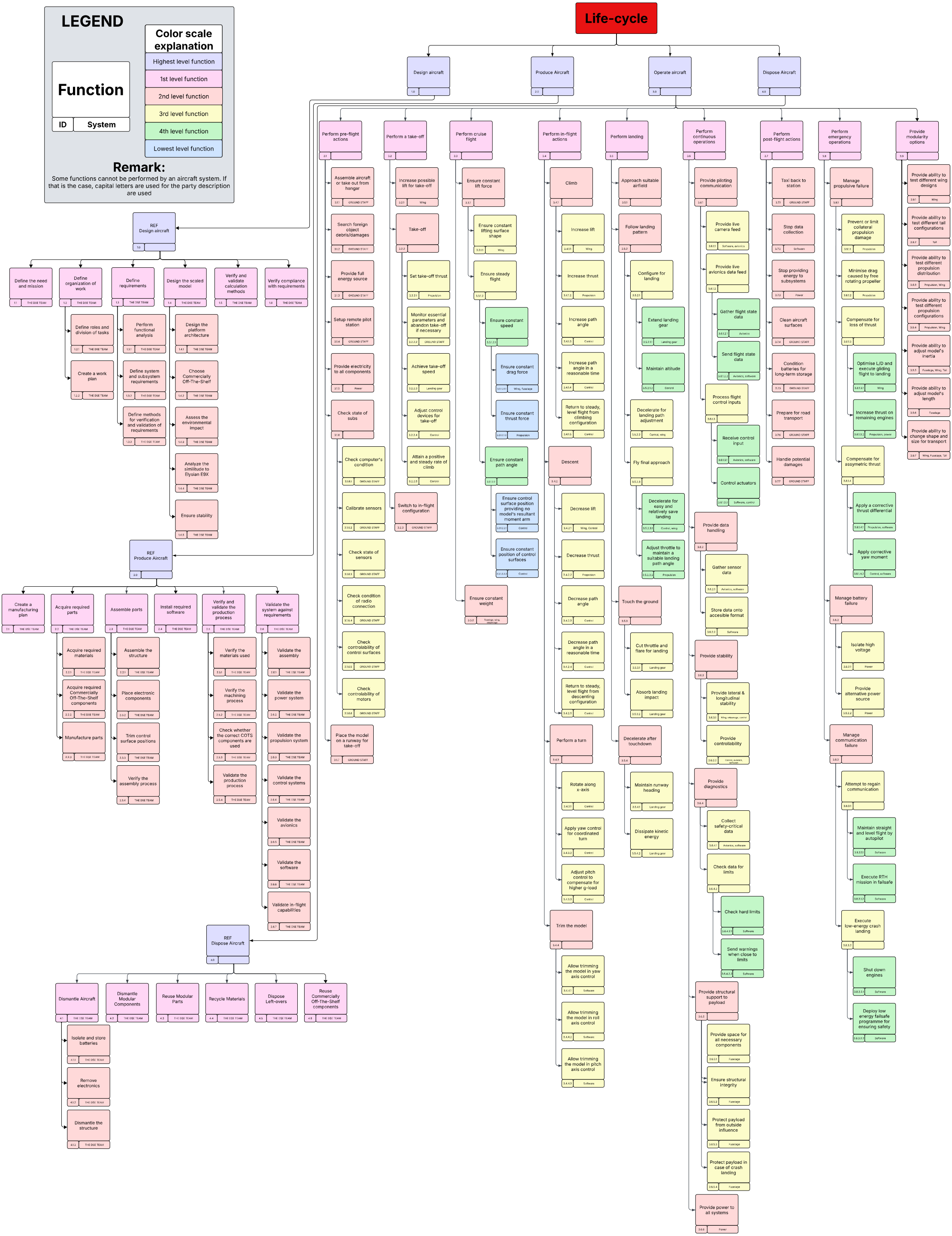

Figure 2.3: Functional Flow Diagram (FFD) (part 1)

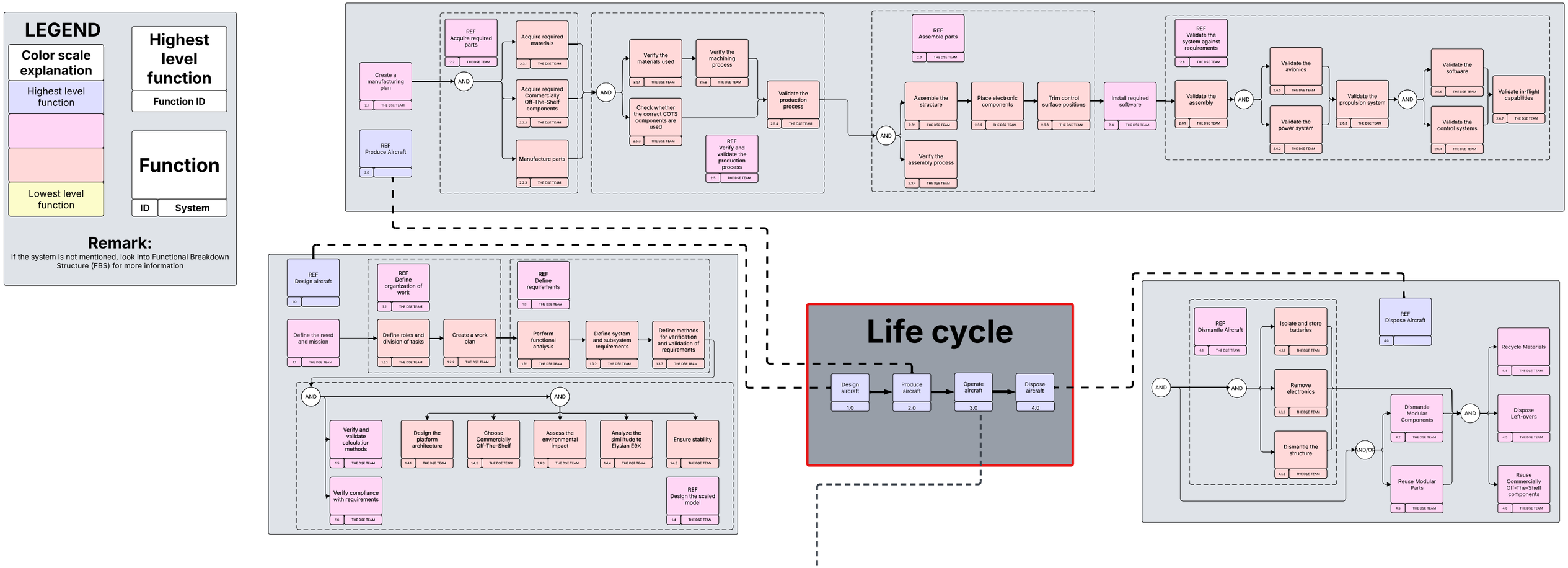

Figure 2.4: Functional Flow Diagram (FFD) (part 2)

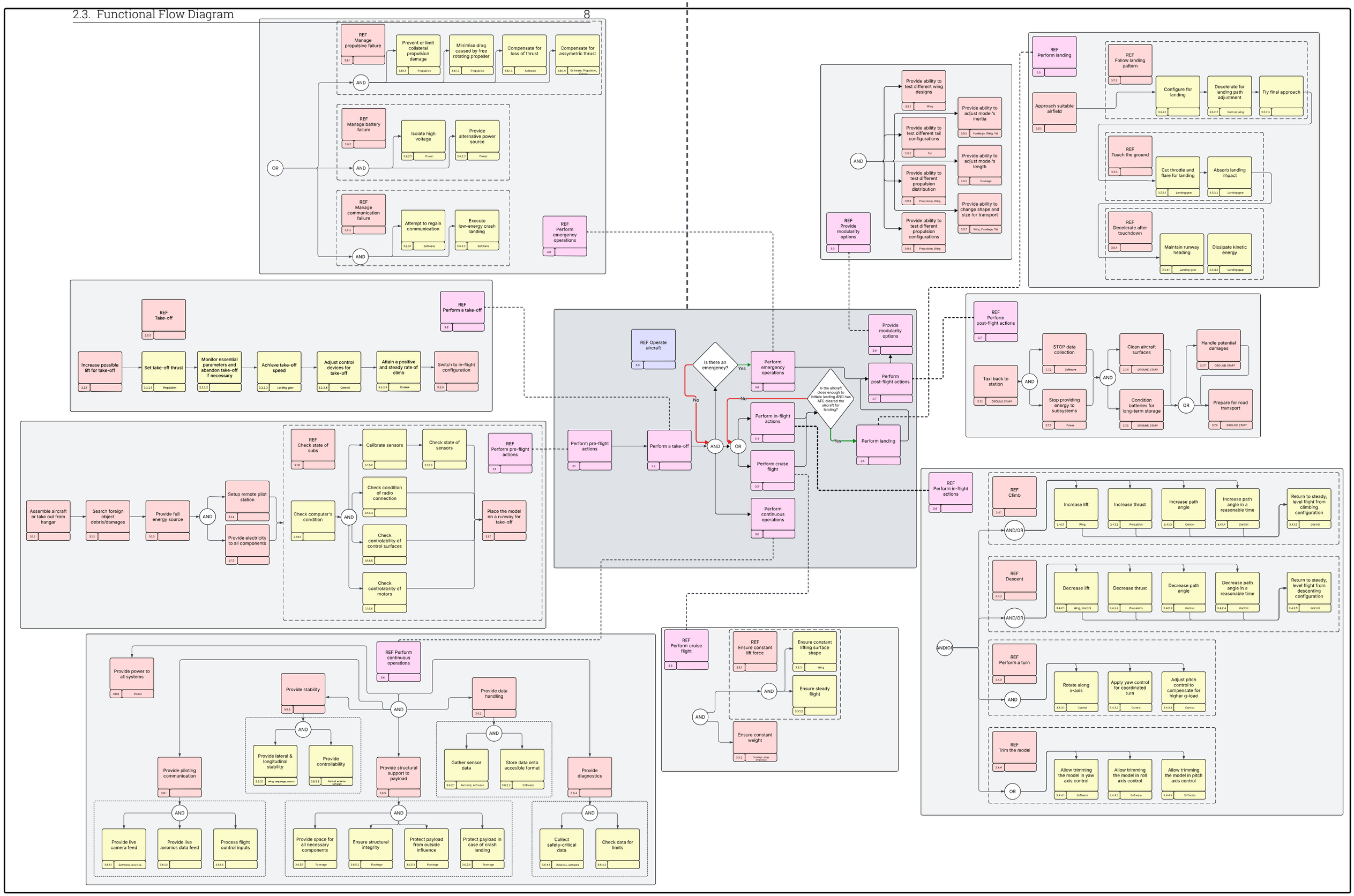

3
Requirements

This chapter presents the technical and operational boundaries for the Scaled Flight Demonstrator (SFD) project. As the Following systems engineering principles, the requirements were written in a hierarchical structure. This ensures that every technical decision can be traced back to a specific user need.

Stakeholder requirements represent the top-level 'Voice of the Customer', defining the mission objectives, safety constraints, and operational needs of the OEM and regulatory bodies. With the usage of these requirements and the Requirements Discovery Tree [19], lower-level requirements were found. Starting with System Requirements, these translate the stakeholder needs into quantifiable technical specifications for the aircraft as a whole (such as range, weight, stability). The subsystem requirements however translate the system requirements into quantifiable specifications for specific systems. The stakeholder requirements are broken down in appropriate technical chapters. After the stakeholder requirements are introduced, a verification and validation plan of the model against stakeholder requirements is presented in table 3.1

Verification is applied to the integration of the system. Whether elements are designed in-house or selected from existing suppliers, they must be verified to ensure they theoretically comply with the system's constraints. This includes verifying that mass, geometry, and performance estimates fit within the defined mission profile and that the capacity of the chosen solution matches the estimated load, be it structural, aerodynamic, or electrical. To ensure objectivity, these checks are frequently reviewed by team members other than the original designer.

Once physical components or prototypes are realized, a thorough experimental validation campaign is required. These practical tests allow for the determination of actual performance metrics versus the rated or predicted values. This stage validates whether the efficiency, output, and operational limits of the physical system meet the requirements necessary to fulfill the mission. If the physical validation reveals lower efficiency or performance gaps compared to the design phase, the impact on the overall mission requirements is assessed to ensure the feasibility of the final product.

Table 3.1: SFD Verification and Validation Requirements

Area	ID	Requirement	Verification	Validation
Performance	SFD-STK-PER-01	The flight vehicle shall be able to perform tests on flight mechanical behaviour to support OEM validity checks.	**Analysis:** Research on scaling laws and flight similarity requirements.	**Test:** Flight testing specific maneuvers to correlate with OEM models.
	SFD-STK-PER-02	Size/mass shall allow carrying an FCMS for powered, partly powered, and unpowered analysis.	**Analysis:** Mass and volume budget analysis for payload accommodation.	**Demonstration:** Physical integration of the FCMS hardware into the airframe.

Continued on next page

Table 3.1 – continued from previous page

Area	ID	Requirement	Verification	Validation
	SFD-STK-PER-03	The model shall meet initial specifications of maximum 150 kg mass.	**Analysis:** Complex estimate of mass tracked through the design process.	**Test:** Measurement of final assembly weight using calibrated scales.
	SFD-STK-PER-04	Trade-off study on scale factors 5%, 8%, and 10% to determine optimal choice.	**Analysis:** Review of trade-off study report for evaluation factors.	**Inspection:** Stakeholder acceptance of scale factor justification.
	SFD-STK-PER-05	The model shall meet initial specifications of maximum 7.5 m wingspan.	**Inspection:** Check whether the wingspan resultant from STK-PER-04 meets the requirement.	**Test:** Physical measurement of the manufactured wingspan.
Safety & Ops	SFD-STK-SOP-01	Satisfy all Dutch/International regulations regarding BVLOS flight.	**Analysis:** Assessment against SORA and regulatory compliance matrix.	**Demonstration:** Receipt of permit-to-fly from civil aviation authority.
	SFD-STK-SOP-02	The system shall be able to finish a minimum of 20 flight missions.	**Analysis:** Reliability/-fatigue analysis to ensure life-cycle > 20 missions.	**Test:** Review of flight logs after 20th successful mission.
	SFD-STK-SOP-03	System shall finish a minimum time-permission of 20 minutes.	**Analysis:** Energy budget based on battery, propulsion, and mission profile.	**Test:** Flight test measuring endurance from take-off to landing.
Sustainability	SFD-STK-SUS-01	Complete proof-of-concept flight-testing using battery-electric motors.	**Analysis:** Review of propulsion architecture for motor specs.	**Demonstration:** Successful mission flight powered solely by electric propulsion.
	SFD-STK-SUS-02	System set up to allow key parts to be used in multiple configurations.	**Analysis:** Reviewing the modularity design.	**Demonstration:** Assembly/disassembly into two distinct configurations.
	SFD-STK-SUS-03	Only use Commercially Off-The-Shelf (COTS) available components.	**Inspection:** Verification of components used during design process.	**Inspection:** Audit of documentation and physical hardware.
Costs	SFD-STK-COS-01	The system shall have a total research and design cost not exceeding 800,000 euros	**Analysis:** Continuous tracking of engineering hours and material quotes.	**Analysis:** Audit of final financial reports post-manufacturing.

Continued on next page

Table 3.1 – continued from previous page

Area	ID	Requirement	Verification	Validation
	SFD-STK-COS-02	Total ready-to-fly manufacturing cost not exceeding 1 million euros.	**Analysis:** Budget breakdown of assembly, integration, and testing.	**Analysis:** Stakeholder acceptance of final project cost report.

4
Design Foundation and Motivation

As this is not the first study into the SKRIBBL SFD, a substantial body of work precedes this report. The aim of this chapter is to summarise the relevant previous research to provide the reader with a clear understanding of the foundation and motivation on which the work of this report is built. In the earlier report, trade-offs were established and performed for major design choices. To conclude this chapter, the modular aspects of the SFD will be introduced, which drive many design choices in this report.

4.1. Aerodynamics

The design of the SKRIBBL SFD is based on the Elysian E9X. Consequently, the first step in the design process was to analyze the E9X and to scale it down. Three scaling methods were considered: Froude, Mach, and Reynolds number scaling. Froude number scaling was ultimately selected as the most suitable approach for the SFD, in preference to Mach and Reynolds number scaling. This decision was motivated by the lower operating speeds required for the SFD, since the SFD can be tested at higher Mach numbers during wind tunnel testing.

To achieve comparable airfoil performance and to retain sufficient internal volume to house equipment in the wing, several airfoils were proposed, analysed and finally discussed with Elysian. The NASA/Langley MS(1)-0317 airfoil was selected for the full-scale configuration. This airfoil was subsequently modified to obtain similar lift and moment characteristics across the relevant Reynolds number regimes. The final SFD airfoil retains the same foil, with a thickness to cord ratio of 20% and a camber of 3%.

Finally, the initial SFD wing planform was sized using a 10% scaling factor. From this planform, preliminary performance metrics, such as take-off distance were derived. It was found that the available runway length at the Marknesse site provided sufficient margin for take-off without high-lift devices. Nevertheless, the inclusion of such devices was ultimately considered beneficial, as they would enhance the overall usefulness of the SFD for testing purposes.

4.2. Structures

To determine the initial structural sizing of the SFD, the flight envelope and associated loads were analysed. It was found that the design load factors for the SFD are 3.75 and -1.5. In addition, load distribution along the wingspan was evaluated for several mission phases, such as taxiing, cruise, and maximum climb.

Three wingbox concepts were proposed to carry and transfer the wing loads to the fuselage: a two-spar design, a three-spar design, and a second two-spar design with a circular leading-edge section. The latter was selected as the most suitable due to its superior structural performance and its favourable integration with other components that must be mounted in or on the wing. The remaining aircraft structures, such as the fuselage and tail, were also analysed, resulting in initial sizing estimates.

Based on this preliminary structural analysis, several potential materials were identified for the application within the SFD. These include Carbon, Glass, and Kevlar Fibre Reinforced Polymers (xFRP), as well as the aluminium alloy 7075-T7451. Of these, CFRP and aluminium were found to be the most suitable. CFRP for its exceptionally high strength-to-weight ratio in both tension and compression, while the aluminium alloy had a favourable shear strength-to-weight ratio, which is particularly relevant given the high shear loads in the SFD.

Finally, using the initial structural sizing together with preliminary selections for avionics and propulsion components, an estimate of the centre of gravity location along the longitudinal axis of the SFD was obtained. This value was then compared to the required centre of gravity range determined by the Stability & Control department, which confirmed the feasibility of the current design philosophy.

4.3. Powertrain

The first step in defining the SFD powertrain was the selection of a suitable energy source. Four battery chemistries, Na-ion, NMC, LFP and LiPo were evaluated, as well as the potential use of supercapacitors. Although Na-ion batteries achieved a higher trade-off score, LiPo batteries were selected due to their proven track record in scaled flight demonstrators and high efficiency.

The propulsion system will employ a brushless DC electric motor. This motor type is widely used in scaled aircraft and can also be found in general aviation applications. Moreover, such motors are readily available as COTS components, supporting this requirement. The propeller selected for the SFD is the TUD-XPROP, a six-bladed propeller designed by the TU Delft and previously used on the DEP-SFD-D08. Publicly available experimental data of this propeller further support its suitability for the present design.

The final decision within the powertrain domain concerns communication between the SFD and the ground. Starlink, 5G and SHF were all considered viable options. However, each was found to have the potential for communication disruptions. This risk was deemed unacceptable, and therefore, a combined Starlink and 5G communication architecture was selected.

4.4. Stability & Control

Several avionics systems are required to ensure stable and controlled flight. Multiple trade-off studies were conducted to select the following components. The Simtec AG ADP-55, combined with the Hensoldt SferiRec LCR 100, was chosen as the flight management system due to its high reliability and the absence of a requirement for additional hardware. For the flight controller, the Embention Veronte Autopilot was selected because of its ease of integration within the SFD controls.

Using the initial empennage sizing and flight performance estimates, preliminary centre of gravity limits were established. For the 10% scaled SFD, the centre of gravity must lie between 1.58 [m] and 1.62 [m] from the nose. As noted previously, this range was verified by the Structures department and found to be feasible.

Finally, the initial performance of the SFD was analysed using the derived aerodynamic characteristics. This formed the basis for assessments of aerodynamic, longitudinal, and dynamic stability. The early design phase predicted a climb performance of 6.3 [m/s], which satisfies the imposed requirement of 4 [m/s].

4.5. Modularity

As the design of the Elysian-E9X has not yet been finalised and is expected to evolve through further research, the SFD is based on the most recent available configuration. Nevertheless, future design changes may require corresponding adaptations to the demonstrator. The model is therefore intended not only to test and validate the current configuration, but also to explore the feasibility of alternative concepts. To enable this, the SFD must be designed with a high degree of modularity.

In addition, the market for scaled flight demonstrators extends well beyond the Elysian programme. The aviation industry is currently experiencing a rapid technological development, driven by the need for improved efficiency and more sustainable energy solutions. Many of these innovations must be tested, verified and validated using scaled models before full-scale implementation. To both support the Elysian E9X programme and appeal to this broader market, the modularity of the SFD is approached from two perspectives.

First, the design addresses the requirements and expectations of Elysian, as obtained through direct collaboration. This includes the ability to vary motor positions and to implement different empennage configurations. While the primary dimensions and general configuration are not expected to deviate

much from the current design.

Second, to ensure suitability for external research applications, the SFD is designed such that nearly all major sections can be removed and replaced. In essence, the fuselage functions as a testbed onto which a wide range of aerodynamic and propulsive devices can be integrated and flown.

On this testbed, the following modular attachments can be implemented:

- **Screw in weights:** By having multiple locations on the model where additional weight can be added, different mass moments of inertia can be achieved to achieve similitude to certain full-scale aircraft.
- **Detachable wing:** This allows for a large number of wing planforms to be used. Since the E9X has a very high aspect ratio, this wing planform might not be desirable for demonstrators that do not require distributed electric propulsion.
- **Detachable tail:** By making the aft section and empennage detachable, a large multitude of tail sections can be tested. This is likely required when a different wing planform is used, but can also be used for exploring concepts like tail-propulsion.
- **Detachable nose cone:** Since the structural de- and attachment mechanism for the tail section will be developed, a detachable nose cone does not require additional development and could pose the possibility of extending the fuselage.
- **Detachable engines:** In the default configuration of the SFD, the engines should be de- and attachable at a large multitude of locations, which allows for different engine sizes and configurations to be placed on the wing.
- **Adjustable payload:** Not every scaled demonstrator requires the same payload. Some demonstrators might require other avionics or more batteries. The fuselage should be able to accommodate these changes.

5
Aerodynamics

In this chapter, the aerodynamics regarding the full-scale Elysian E9X and the SFD will be discussed. It will continue upon the work done on the aerodynamics in the midterm report [20] and apply 3D analyses to the existing 2D analysis. First, the scaling will be discussed. Here, the method of scaling and its effect on the fight parameters will become apparent. Then, the use of these values in Flow5 and the results of the simulation will be discussed. Here, the flow parameters are chosen and the final similitude between the E9X and the SFD will be analysed. After, additional effects of transition point, turbulence, and distributed propulsion will be investigated. Then, a high lift device sizing will be performed. Finally, the use of the earlier mentioned will be validated.

5.1. Scaling

As was presented in the midterm report, it was decided to geometrically scale the E9X airframe by a factor that preserves Froude number at the expense of Mach number and Reynolds number. This maintains the kinematic properties between the model and the full scale aircraft at the expense similitude of compressibility and the local flow conditions [20]. The initial design analysed in the midterm report was based upon the the Elysian E9X Froude scaled with scaling factor of 10 % with a mass of 150 kg. This scaling was done with an assumed MTOW for the E9X of 76000 kg [70]. However, after discussing with Elysian directly, it was determined that a MTOW of 82500 kg would be more appropriate [71].

A comparison geometrically scaling the E9X by 5%, 8%, 9%, 9.7% and 10% are given in Table 5.1. The mass range is the model mass required to achieve the same relative density factor between the aircraft at 7000 m and the model flying at the altitude range allowed at the EHR66 test area which is between 400 and 1000 m. This was calculated using Equation 5.1, with the values of the E9X taken from de Vries [71]. Similarly the cruise velocity is based on the cruise velocity of the E9X scaled to maintain Froude

similitude with Equation 5.2. The ratio between the Mach numbers and Reynolds numbers of the model and aircraft are also given. As the scale factor is decreased the required mass range falls much faster than velocity and the scale factor itself. Consequently, with decreasing scale factor it is increasing difficult to achieve the require mass range and velocity with off the shelf components and available materials. A higher scale factor will increase the cost of the scaled demonstrator but will improve the Mach number and Reynolds number similitude. Furthermore it would be more feasible to achieve the required mass range and velocity. At 10% scale the mass range is greater than 150 kg which is the maximum allowed take off mass at NLR Marknesse [42]. Therefore, a final scale factor of 9.7% was selected for the SFD and will be used for further analysis in this report. However, in practise the difference between 9.7% and 10% scale is within the margin of error and therefore for ease of manufacturing 10% will likely be used for many components.

Finally, the relative mass moment of inertia must be kept the same between the model and the aircraft. The ratio of the model to aircraft mass moment of inertia is given by Equation 5.3 which for a scale factor of 9.7% must be in the range of $1.62 - 1.71 \cdot 10^{-5}$ according to the required mass range[72].

$$\frac{m_M}{m_A} = \left(\frac{\rho_M}{\rho_A}\right) n^3 \tag{5.1}$$

$$\frac{V_M}{V_A} = \sqrt{n} \tag{5.2}$$

$$\frac{I_M}{I_A} = \left(\frac{m_M}{m_A}\right) n^2 \tag{5.3}$$

Scale [%]	5	8	9	9.7	10
Mass Range [kg]	19.4-20.5	80-84	113-119	142-150	150-164
Cruise Velocity [m/s]	31.4	39.7	42.2	43.8	44.4
$(\frac{M_{ss}}{M_{fs}})$ [%] $\approx$	20	26	28	29	29
$(\frac{Re_{ss}}{Re_{fs}})$ [%] $\approx$	2	4	4.6	5	5

Table 5.1: Comparison of the required mass and cruise velocity based on different scale factors

5.2. Aerodynamic Analysis

5.2.1. Flow5 simulation

In the preliminary design of the SFD as seen in the mid-term report[20], an aerofoil was selected through a trade-off and its optimal parameters were investigated with the use of XFLR5. This resulted in the commonly used narrow-body aircraft aerofoil NASA/LANGLEY MS(1)0317. The optimal parameters were found by trading-off between performance and required thickness to account for potential batteries needed to be placed in the wingbox. This resulted in the following parameters:

Aerofoil	**Thickness [%]**	**Camber [%]**
NASA/LANGLEY MS(1)-0317	18	3

However, after the preliminary design, the client has opted for a slightly different configuration as they found that a minimum of 20% thickness ratio is required. Therefore, 20% is used to have the minimum required thickness but still the most optimal performance, since the thickness and performance were found to be inversely related from 18% onwards. [20].

This slight redesign leads to the aerofoil shown on the right in figure 5.1. With this new aerofoil, new XFLR5 polars can be computed. Due to licensing limitations, in the preliminary design only XFLR5 was used which is not able to model lift and drag contributions of a fuselage and empennage. This meant that, in order to find the full SFD lift and drag values, empirical estimation methods were needed. Due to newly acquired Flow5 access, the full aircraft can be readily simulated.

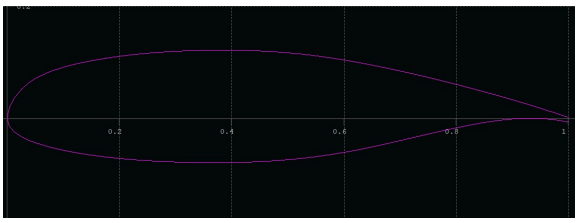

Figure 5.1: Aerofoil redesign in XFLR5

Flow5 is a program affiliated to XFLR5 which builds upon the 2D analysis made through XFLR5 in order to give a full 3D aerodynamic analysis which includes the effects of fuselages and empennages. The validity and accuracy of the program has been investigated and can be found at the end of the chapter in section 5.4. Flow5 computes aerodynamic values at various points on the wing and aircraft through a Uniform Density Panel Method [21]. Additionally, even though the panel method is used for incompressible and inviscid flow, Flow5 is able to add viscous forces and skin-friction drag due to the fuselage through the Schlichting method [56]. With this method, the skin friction coefficient can be estimated for wings, fuselage and tail through the following relation:

$$C_f = \frac{0.455}{(log_{10}Re)^{2.58}} \tag{5.4}$$

Since the SFD flies at a low altitude, the changes in Reynolds number over the wing and fuselages are relatively large, as well as the flow velocity. In order for Flow5 to be able to simulate a flow around every point on the wing and aircraft, polars with a wide range of Reynolds numbers and mach numbers need to be imported from XFLR5. For this, polars ranging from 50,000 up until 7,000,000 for the SFD, and 30,000,0000 up until 72,000,000 for the E9X are simulated as seen in figure 5.2, with the Mach number ranging from 0 to 0.5.

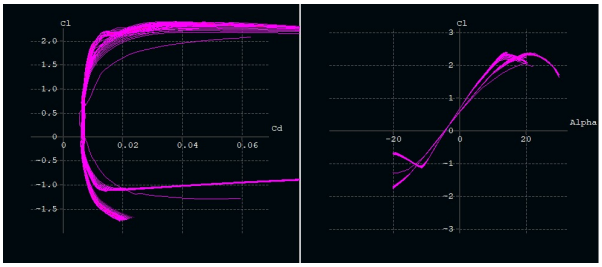

Figure 5.2: Lift and drag polars over wide range of Reynolds numbers

Then, in Flow5 a model of the full-scale aircraft as seen in [71] was created. This model contains the most essential components contributing to the lift, drag and moment coefficients such as the fuselage, vertical and horizontal tail and the winglets. A render of the model used for the 3D simulations can be seen in figure 5.3

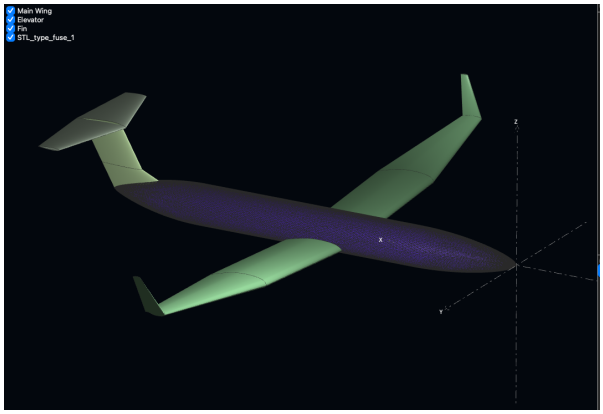

Figure 5.3: Flow5 model of the E9X

Then, using the model, the first aerodynamic analysis of the full-scale E9X could be performed. It is important to note the flow parameters applied to the simulation as they greatly impact the polars and should be picked carefully for both the full-scale E9X and the SFD in order to get a realistic comparison.

5.2.1.1. E9X simulation

The full-scale E9X analysis is performed at a fixed height of 7000 meters. In order to properly simulate flight at this level, it is of importance to use the correct flow properties as given by ISA. The values use can be found in table 5.2.

Altitude $[m]$	**Density** $[kg/m^3]$	**Viscosity** $[m^2/s]$	**Free-stream velocity** $[m/s]$	**Friction coefficient**
7000	0.59	2.646e-05	140.5	0.0026

Table 5.2: Parameters of E9X simulation

The value for the free-stream velocity, V_∞, has been deduced in earlier research [20]. The friction coefficient follows from the Schlichting relation as shown in 5.4.

5.2.1.2. SFD simulation parameters

As explained in section 5.1 is the height the SFD flies at determined by the allowed range at the EHR66 test area. This stipulates that the SFD must be flown at an altitude between 500 and 1000 meters. For this reason, an altitude of 750 meters is used for the simulation. The free-stream velocity used is a direct result of the froude scaling done in section 5.1. Finally, similar to the full-scale E9X, the friction coefficient is deduced from the Schlichting relation in equation 5.4. This yield the following values as shown in table 5.3.

Altitude $[m]$	**Density** $[kg/m^3]$	**Viscosity** $[m^2/s]$	**Free-stream velocity** $[m/s]$	**Friction coefficient**
750	1.15	1.505e-05	43.8	0.0095

Table 5.3: Parameters of SFD simulation

5.2.1.3. Similitude comparison

Building on the initial comparison between the SFD and the E9X in the mid-term report [20], it's now possible to visualize to what extent Froude scaling is able to maintain the scaled E9X's aerodynamic performance. Focussing on the $C_L - \alpha$ curve on the lift, a few things become apparent.

First of all, as Flow5 is not able to properly simulate stall behaviour, only the linear part of the lift curve is of interest. This also means that when the simulation cannot converge to a single value anymore, that is where the aircraft stalls. As both aircraft are analysed over a range of -20 to 20 degrees angle of attack, it can be seen that the SFD stalls rather early. This behaviour follows logically from boundary layer theory [56], where at lower Reynolds numbers the flow is not able to keep the flow attached long enough

and the separation bubble, and thus stall, happens prematurely. In practice, this might be overcome by introducing inefficiency's on the wing and increasing Reynolds number. An attempt to simulate this behaviour is made in section 5.2.2.

Furthermore, the linear part itself can be seen to be almost identical. This logically follows from the aerofoil and its parameters being kept the same for the E9X and the SFD, as Elysian requested the SFD to have a thickness of 20% as well. The rest of the aircraft has also been scaled proportionally, as seen in section 5.1. This means the aspect ratio, which also impacts the lift coefficient, also remains constant. Something which is not included in this analysis, however, is the effect of the propellers. This effect is investigated in section 5.2.4.

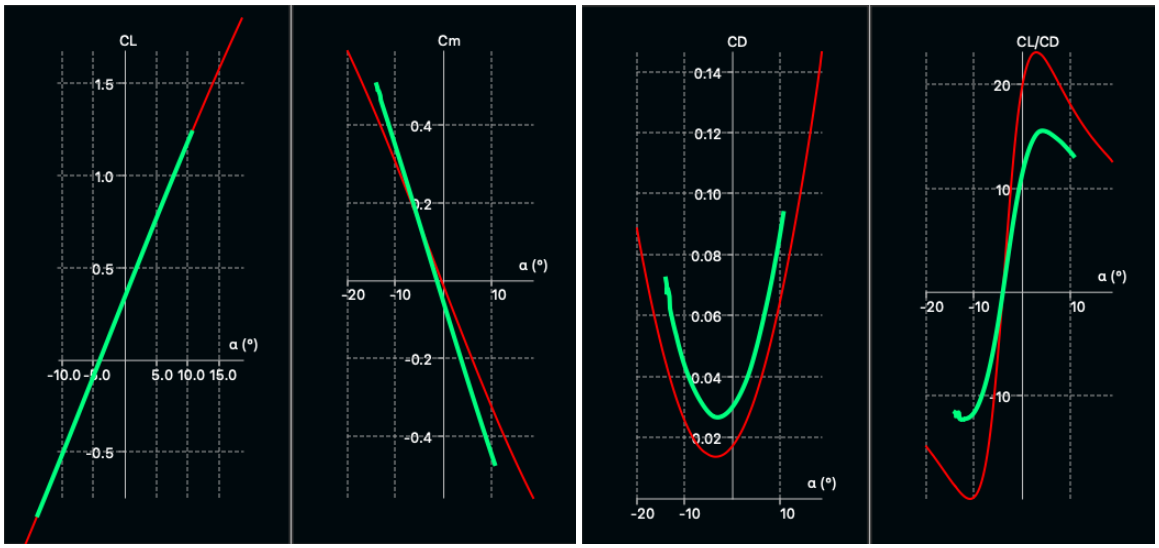

(a) Lift & moment curves - Green = SFD & Red = Full-scale E9X

(b) Drag & C_L/C_D curve - Green = SFD & Red = Full-scale E9X

Figure 5.4

Now, analysing the drag polar as seen in figure 5.5, there are some things to be noted. At first glance, it can be seen that the SFD drag polar does compare quite well to the full E9X. The green graph is seen to be shifted to the right and is slightly less steep. The shift to the right, also seen as C_{D_0}, logically follows from the definition of parasite drag. It consists predominantly of skin friction and form (pressure) drag [3]. As explained before, the SFD has a much higher skin friction coefficient, resulting in this shift. Additionally, the SFD would experience an even higher C_{D_0} due to the excrescence drag. The testing equipment and latches would cause this increase, however they are not accounted for in this Flow5 model.

Furthermore, it can be seen that the SFD graph is less steep, meaning for every increase in C_L, there is a greater increase in C_D then compared to the full E9X. This is caused by the laminar separation bubble, which forms sooner at lower Reynolds numbers. This effect will be elaborated upon in section 5.2.2.
As the mentioned lift and drag curves, as well as the additional curves in figure 5.4 show, they are rather similar. It can be seen that even though the 2 simulations are done at significantly different heights and Reynolds numbers, the scaling of the aircraft combined with the velocity has impacted similitude greatly.

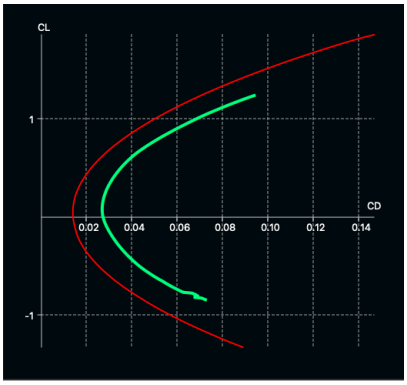

Figure 5.5: Drag polar for both simulation - Green = SFD & Red = Full-scale E9X

5.2.2. Influence of transition point

The transition point of the boundary layer is a significant element in the lift and drag generated by an aerofoil or wing. As flow generally starts of laminar at the leading edge of an aerofoil, it is less energetic and has very little friction drag. This lack of energy leads to the flow not being able to stay attached to the aerofoil and the formation of laminar separation bubbles (LSBs) begin. These bubbles induce a significant amount of pressure drag and a reduction in (maximum) lift. Turbulent flow on the other hand, is very energetic which leads to it having significantly more friction drag. However, this increased energy also means the flow is able to stay attached to the aerofoil for longer, leading to smaller separation bubbles. [56]

Due to the positive effects of turbulent flow, since the pressure drag is often less wanted than friction drag, a commonly used method is forcing transitions on aerofoils. By adding irregularities on the wings surface, the flow is pre-emptively transitioned into turbulent flow, leading to a (re)attachment on the wing's surface.

In order for the SFD lift (C_L), and efficiency (C_L/C_D) to potentially be more similar to the full-scale aeroplane, the transition point along the chord can be altered. As explained, an early transition leads to a significant increase in friction drag, but delays separation. Transitioning too early however, might cause unnecessary friction drag if separation was too happen much more aft. Therefore it is detrimental to find the optimal transition point, which minimizes both friction drag, as well as pressure drag. As currently the sub-scale aerofoil is designed to reach flight mechanical similitude with the full-scale aeroplane, iterations of various transitions will be performed to match the aerodynamics of the SFD to the full-scale Elysian. This is the digital equivalent of forcing the transition through putting irregularities on a wing. The result of these iterations can be found in 5.6 below.

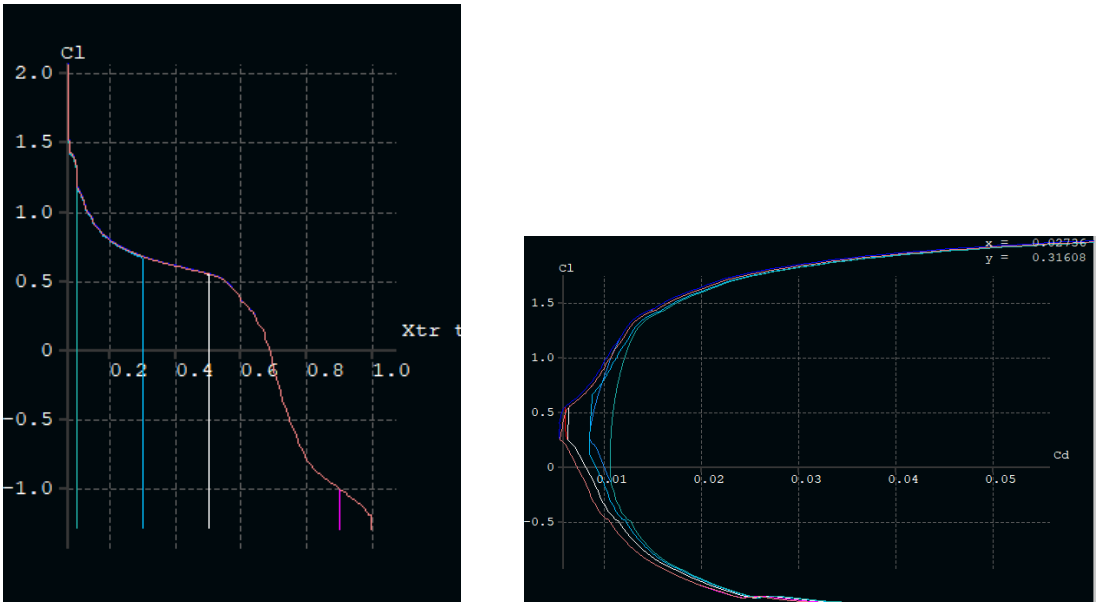

(a) Boundary layer transition points

(b) $C_l - C_d$ with changing transition points

Figure 5.6: Influence of boundary layer transition on $C_l - C_d$ curve

From this figure it can be deduced that the initial transition point at $X_{tr} = 1$ was already optimal. Every increment shifting the transition point forward induces more drag. This can be seen in the figure on the left: the drag polar shifts to the right. This means that the energy gained from inducing turbulent flow earlier and potentially preventing separation does not outweigh the significant increase in skin friction drag. Additionally, the effect of altering the bottom boundary transition point was negligible. Therefore, changing the transition point does not lead to any performance increase and it will remain unchanged.

5.2.3. Turbulence level effect

The turbulence level is an aerodynamic flow parameter which has an influence on the aerodynamic performance of a wing or aircraft. The N-factor is a measure of free-flow turbulence, the disturbance of the flow. Then, the e^n method by van Ingen[32] predicts the transition point by predicting the growth of the disturbance. The e^n method actually computes how much so called instability waves grow, determined by an N-factor inherent to the flow. In flow5, this translates to the use of N_{crit}, the critical N-factor. As it is supposed to simulate real world behaviour, the N_{crit} stipulates the point up until the flow disturbance can grow until it transitions. In this case, one is able to choose a certain N-factor which one expects to encounter in flight. This usually ranges from 4 until 14, where 4-8 is rather turbulent and 9-14 are rather clean and laminar conditions. Increasing the N_{crit} value in flow5 basically means allowing the disturbances to grow until calling the flow turbulent.

As universally, the N_{crit} is defined to be 9, this is also the value used for the similitude comparison and most likely representative for the flow the SFD will encounter at an altitude of 750 meters. However, for the purpose of modifying the SFD in order to achieve flight mechanical similitude, a brief investigation is done into the effect on the SFD.

In order to investigate the effect of the changing turbulence on the SFD, 11 iterations are done at a fixed Reynolds number of 3,000,000 with N_{crit} ranging from 4 until 14. The result of this can be seen in figure 5.7.

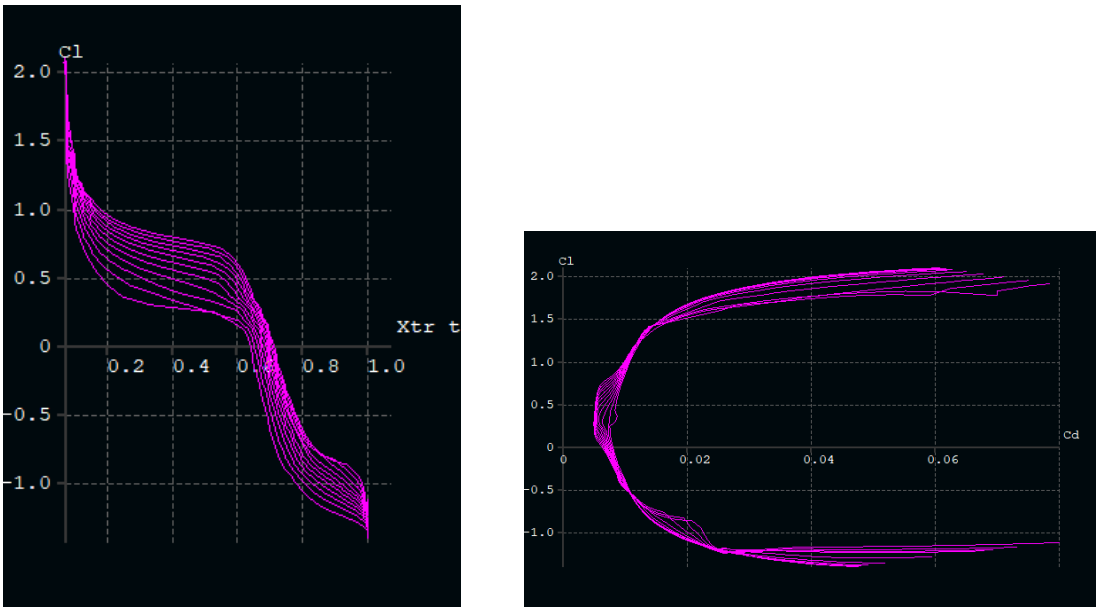

(a) XFLR5 boundary layer transition change with changing Ncrit

(b) XFLR5 CL-CD change with changing Ncrit

Figure 5.7: Turbulence level effect on boundary layer and drag polar

A few things can be deduced from figure 5.7. First of all, it should be noted that in the transition point plot, the bottom graph corresponds to $N_{crit} = 4$ and it moves upward with increasing N_{crit}. This corresponds to the boundary layer theory, as the flow stays laminar for longer, thus shifting the right (later transition point). Now, relating it to the graph on the right, in that figure the graph moves to the left with increasing N_{crit}. However, every shift to the left makes the slope less steep, thus creating more drag per lift increase. This follows from the skin friction drag reducing significantly due to the laminar flow, therefore shifting the C_{D_0}, and the graph, to the left. However the later transition point also means more time for laminar separation bubbles to form, therefore increasing drag at higher C_L.

A conclusion which can be derived from this, is that forcing a transition in the flow conditions as shown in section 5.2.2 might not be beneficial. However, flying the SFD in different flow conditions, which naturally moves the transition point more forward, will also shift the drag polar more to the left. As seen in section 5.2.1 this increases similitude. From this the conclusion can be derived that flying the

SFD in a windtunnel where flow conditions are subject to change by manual input, one might be able to create more flight mechanical similitude.

5.2.4. Distributed Propulsive System Effects

As explained in chapter one of the objectives of the scaled flight demonstrator is to be a test bed for distributed electric propulsion research. Distributed propulsion offer serval advantages including increasing C_L due to the interaction between the propeller slipstream and the wing especially during take off.

The effect of the distributed propulsion system is analysed using the Aero-Propulsive Interaction Model outlined by Reynard de Vries [69].

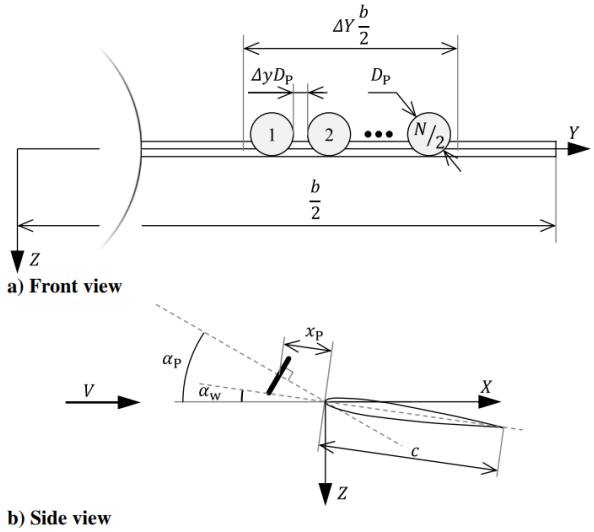

Figure 5.8: Simplified DP-system representation, indicating the main geometrical parameters [69]

c [m]	D_P [m]	α_p [deg]	x_p [m]	$\Delta y D_p$ [m]	$\Delta Y(b/2)$ [m]
0.486	0.4064	0	0.04	0.04	1.27

Table 5.4: SFD distributed propulsion system geometric properties

First, from actuator disk theory, the axial induction factor at the propeller must be calculated using Equation 5.5. A typical value for the thrust coefficient T_c at cruise is 0.1 [22], which gives a a_p of 0.06.

$$a_p = \frac{1}{2}\left(\sqrt{1+\frac{8}{\pi}T_c}-1\right) \tag{5.5}$$

Using this induction factor, the axial distance of the propeller from the leading edge of the wing x_p, and the propeller radius R_p the contraction ratio of the slipstream at the wing leading edge can be calculated using Equation 5.6 [67]. For the SFD DP geometry and a T_c of .1, the contraction ratio is equal to 0.9779.

$$\frac{R_w}{R_p} = \sqrt{\frac{1+a_p}{1+a_p\left(1+\frac{x_p/R_p}{(x_p/R_p)^2+1}\right)}} \tag{5.6}$$

The axial induction factor at the wing a_w is calculated from Equation 5.7 which is derived from conservation of mass in incompressible flow. Using the values above it is equal to 0.1085

$$a_w = \frac{a_p + 1}{(R_w/R_p)^2} - 1 \tag{5.7}$$

The angle of attack of the wing is estimated using Equation 5.8. The Aero-Propulsive Interaction Model assumes zero sweep angle $\Delta_{c/2}$. The values of lift coefficient of the airframe $C_{L_{airframe}}$ are generated from Flow5 as explained in subsection 5.2.1.

$$\alpha_W \approx \frac{C_{L_{airframe}}}{2\pi A}\left[2 + \sqrt{A^2(1-M^2)(1+\frac{\tan^2\Lambda_{c/2}}{1-M^2}) + 4}\right] \tag{5.8}$$

The slipstream correction factor β corrects for the fact that the slipstream is not infinite and is estimated using the Surrogate Model presented by Patterson [47]. β is calculated using Equation 5.11 with the values of the K_i matrices given in Equation 5.9 and X is defined by Equation 5.10. For the SFD DP geometry and a T_c of 0.1, this was found to be 1.3847.

$$\begin{aligned}
K_0 &= \begin{bmatrix}0.378269 & 0.748135 & -0.179986 & -0.056464 & -0.146746 & -0.015255\end{bmatrix} \\
K_1 &= \begin{bmatrix}3.071020 & -1.769885 & 0.436595 & 0.148643 & -0.989332 & 0.197940\end{bmatrix} \\
K_2 &= \begin{bmatrix}-2.827730 & 2.054064 & -0.467410 & -0.277325 & 0.698981 & -0.008226\end{bmatrix} \\
K_3 &= \begin{bmatrix}0.997936 & -0.916118 & 0.199829 & 0.157810 & -0.143368 & -0.057385\end{bmatrix} \\
K_4 &= \begin{bmatrix}-0.127645 & 0.135543 & -0.028919 & -0.026546 & 0.010470 & 0.012221\end{bmatrix}
\end{aligned} \tag{5.9}$$

$$X = \begin{bmatrix}1 & x_p/c & (x_p)^2 & (x_p)\cdot a_p & a_p & a_p^2\end{bmatrix}^T \tag{5.10}$$

$$\beta = \sum_{i=0}^{4} K_i X \left(\frac{R_p}{c}\right)^i \tag{5.11}$$

From these values the sectional lift coefficient increase Δc_l for a $C_{L_{airframe}}$ is calculated using Equation 5.12

$$\Delta c_l = 2\pi\left[(\sin\alpha_w - a_w\beta\sin(\alpha_p - \alpha_w))\sqrt{(a_w\beta)^2 + 2a_w\beta\cos\alpha_p + 1} - \sin\alpha_w\right] \tag{5.12}$$

The new C_L which takes into account the effect of the distributed propulsion system is finally calculated from Equation 5.13.

$$C_L = C_{L,airframe} + \Delta C_L = C_{L,airframe} + \Delta c_l \cdot \Delta Y \tag{5.13}$$

The distributed propulsion system will also cause an increase in both the zero lift drag and the induced drag. The new C_D taking these into account is calculated from Equation 5.14. A sectional skin friction coefficient c_f of 0.009 was used as it is a typical value [6].

$$C_D = C_{D,airframe} + \Delta C_{D_0} + \Delta C_{D_i} = C_{D,airframe} + \Delta Y a_w^2 c_f + \frac{\Delta C_L^2 + 2C_{L,airframe}\Delta C_L}{\pi A e} \tag{5.14}$$

Figure 5.9 shows the effect of the distributed propulsion on the C_L and C_D on the model at a cruise T_c of 0.1.

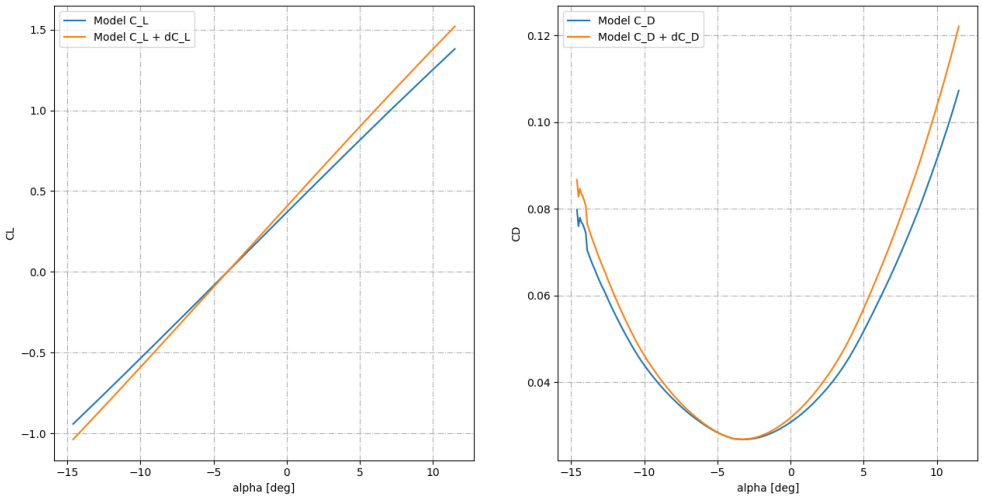

Figure 5.9: Change in C_L and C_D induced by aero propulsive interaction effect for $T_c = 0.1$

Figure 5.10 compares the lift curve and drag polar of the aircraft and model at a T_c of 0.1. The implementation of the effect of the propeller on the lift curve and drag polar does not significantly effect their similitude as compare with Figure 5.6b.

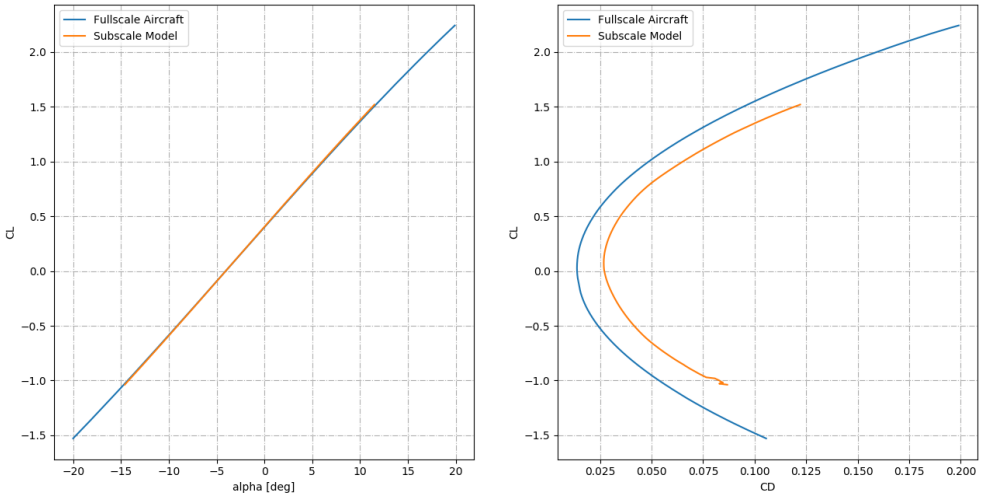

Figure 5.10: Model and Aircraft Lift Curve and Drag polar including aero propulsive interactions ($T_c = 0.1$)

5.3. High Lift Devices

5.3.1. Required Lift Coefficient

In order to size the high lift devices the values of the required maximum lift coefficient at take off and cruise must be determined. These are the values for SFD-SYS-PER-14 and SFD-SYS-PER-15 requirements that still needed to be determined. SFD-SYS-PER-06 requires the SFD to pass a screen height of 10 m at no greater than 325 m. This is equivalent to a FAR 25 requirement which requires a passing a screen height of 35 ft at the distance of the field length s_{FL}. The air density ratio σ is equal to 1 for NLR Marknesse. [42]

Equations 5.15, 5.16, and 5.17 are all taken from Roskam however are all in imperial units [50]. Therefore, for all values were converted to imperial for calculations and the results converted back to metric.

From the field length of 325 m, using Equation 5.15, the TOP_{25} parameter was equal to 28.4. The maximum wing loading W/S is based on the MTOW of 150 kg as discussed in section 5.1 and is equal to 762.9 N/m^2. The maximum thrust at take-off was estimated to be 390 N as explain in subsubsection 7.1.3.2, giving a T/W of 0.265. Therefore, from Equation 5.16, $C_{Lmax_{TO}}$ must be at least 2.11.

$$TOP_{25} = \frac{s_{FL}}{37.5} \tag{5.15}$$

$$C_{Lmax_{TO}} = \frac{(W/S)}{\sigma(T/W)TOP_{25}} \tag{5.16}$$

Similarly, using Equation 5.17, C_{Lmax_L} must be at least 1.94.

$$C_{Lmax_L} = 1.014\frac{(W/S)}{s_{FL}\rho_0} \tag{5.17}$$

5.3.2. Stall Performance Estimation

In subsection 5.2.1, a VLM method implemented in Flow5 was used to model the aircraft performance. This method is unable to accurately model stall behaviour. Therefore, the semi-empirical DATCOM method was used to get a preliminary estimation of the maximum lift coefficient and the stall angle of attack at clean configuration.

The maximum C_L is calculated from Equation 5.18 with $\Delta C_{L_{max}}$ equal to zero, as the model Mach number is less than 0.2, so compressibility can be neglected. Given the aerofoil leading edge sharpness Δy is equal to 3.5 % and leading edge sweep Δ_{LE} is approximately zero, the $\left[\frac{C_{L_{max}}}{C_{l_{max}}}\right]$ was taken from Figure 5.11a [49][14]. The stall angle of attack is calculated using Equation 5.19 with α_{0L} equal to -5.25 and C_{L_α} equal to 0.089 [20]. From Figure 5.11b the $\Delta\alpha_{CL_{max}}$ is derived.

$$C_{L_{max}} = \left[\frac{C_{L_{max}}}{C_{l_{max}}}\right]C_{l_{max}} + \Delta C_{L_{max}} \tag{5.18}$$

$$\alpha_s = \frac{C_{L_{max}}}{C_{L_\alpha}} + \alpha_{0L} + \Delta\alpha_{CL_{max}} \tag{5.19}$$

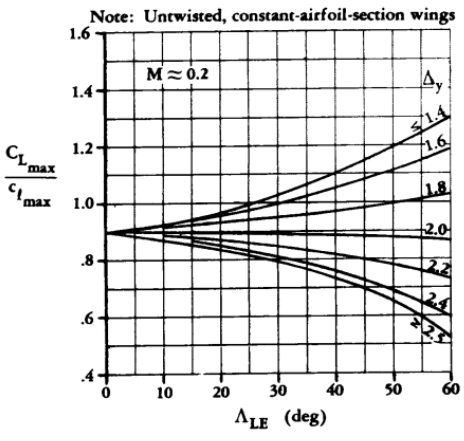

(a) Subsonic maximum lift of high-aspect-ratio wings

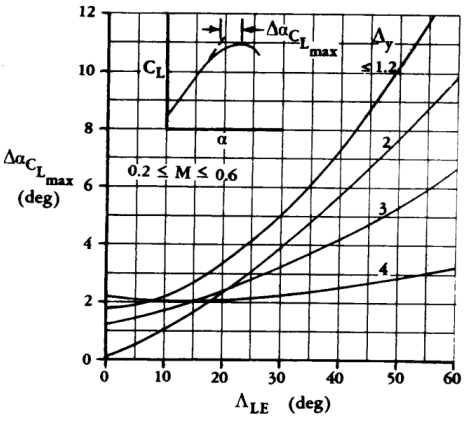

(b) Angle-of-attack increment for subsonic maximum lift of high-aspect ratio wings.

Figure 5.11: Aspect ratio relations from Raymer [49]

Equation 5.20 was used to estimate the cruise lift coefficient [14]. From this and Figure 5.10, the trim angle of attack was estimated and is given in Table 5.5.

$$C_{L_{des}} = 1.1\frac{2}{\rho V^2}\frac{W}{S} \tag{5.20}$$

$C_{L_{max}}$ [-]	α_{stall} [deg]	C_{L_α} [deg^{-1}]	$C_{L_{cr}}$ [-]	α_{trim} [deg]
1.86	16.7	0.098	2.04	3.6

Table 5.5: SFD DATCOM estimated stall and cruise performance

5.3.3. Sizing

The maximum clean C_L, not including the effect of the propllers, estimated in subsection 5.3.2 is less than the requirement for take-off and landing calculated in subsection 5.3.1.

The lift curve estimated in subsection 5.3.2 did not take into account the effect of the distributed propulsion system. This will have a negligible effect for landing as the engine will be at low power or idling therefore the thrust coefficient T_c will is assumed to be zero. However, a typical value for T_c at take off is 1.0 which gives a large increase in lift for aircraft that employs a distributed propulsion system [22]. A T_c of 1.0 is also consistent with the values found from Javaprop in section 7.1.

Using the estimated value of $C_{L_{max}}$ from subsection 5.3.2 and the dC_L Aero Propulsive model with a $T_c = 1.0$ in subsection 5.2.4 gives a take off $C_{L_{max}}$ of 3.32. This meet the take-off C_L requirement without the need for high lift devices.

High lift devices are needed to meet the landing requirement, plain flaps were chosen as they are the least complex and lightest. The percentage of chord to be taken up by the flap system cf/c is chosen to be 20 %, which results in a K factor value of 0.82 and $C_{l_{\delta_f}}$ of 3.7 using the relations given in Roskam. At a flap deflection δ_f of 40 degrees K' is equal to 0.58. From Equation 5.21 $\Delta c_{l_{max}}$ at this deflection angle is equal to 0.437. The quarter chord deflection angle $\Lambda_{c/4}$ is 3.2 degrees which using Equation 5.22 gives a K_Λ of 0.92. The flapped wing area chosen is given in Figure 5.12, the flap area does not extend all the way to the fuselage to allow for the placement of the landing gear faring. This gives a flap area ratio $\frac{S_{wf}}{S}$ of 0.387. Finally, from Equation 5.23 the increase in $C_{L_{max}}$ for this flap configuration of 0.437 and therefore a final $C_{L_{max_L}}$ of 2.29. This more than meets the requirement for landing calculated in subsection 5.3.1.

[51]

$$\Delta c_{l_{max}} = KK'\delta_f c_{l_{\delta_f}} \tag{5.21}$$

$$K_\Lambda = (1 - 0.08\cos^2\Lambda_{c/4})\cos^{3/4}\Lambda_{c/4} \tag{5.22}$$

$$\Delta C_{L_{max}} = K_\Lambda \Delta c_{l_{max}}\frac{S_{wf}}{S} \tag{5.23}$$

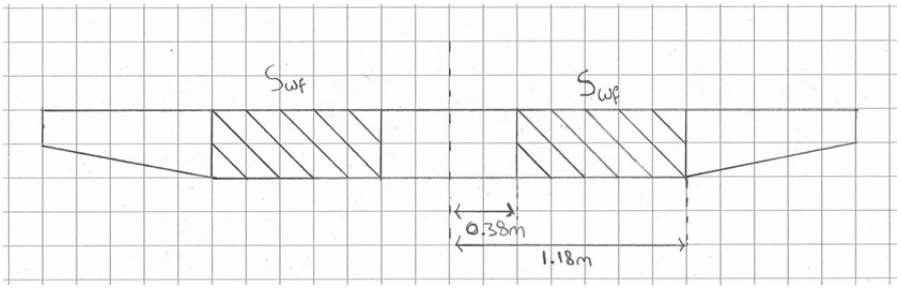

Figure 5.12: Flap wing area S_{wf} of the SFD

Configuration	Thrust coefficient T_c	Flap Deflection δ_f [deg]	$C_{L_{max}}$	C_{L_α} [deg^{-1}]
Take-off	1.0	0	3.32	0.16
Landing	0	40	2.29	0.089

Table 5.6: Summary of take-off and landing configurations of the SFD

A summary of the take-off and landing configurations are given in Table 5.6. From these configurations the the clean lift curve estimated using the DATCOM method is modified with the impact of the high lift devices and propeller effects. These lift curves are presented in Figure 5.13.

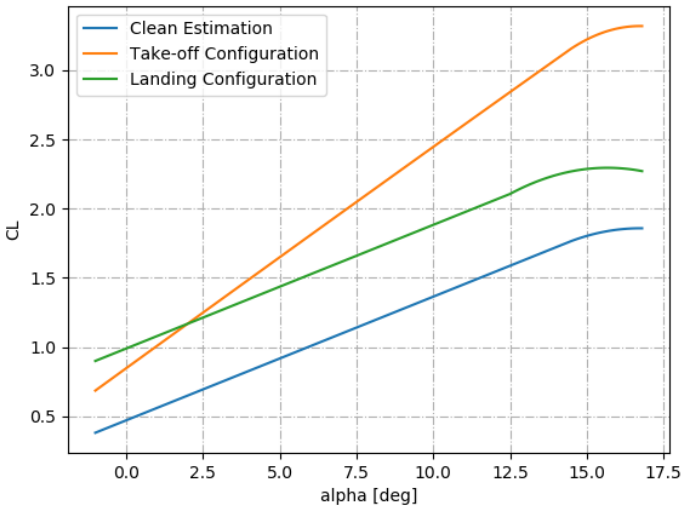

Figure 5.13: Lift curves for Take-off and landing configurations and DATCOM estimated clean lift curve

5.4. Verification and Validation

5.4.1. Verification

In order to implement the analytic methods presented in this chapter serval tools were developed to implement calculations and respond to design changes quickly. These tools were verified using the framework of the verification plan presented in the midterm report [20].

Python tools were developed to implement the methods presented in section 5.1, subsection 5.3.2 and subsection 5.2.4. Unit testing was performed before a full module test on each of the python code. The scaling tool was tested using the example data provided by Wolowicz [72]. The tool for implementing the DATCOM method and the propeller effects were compared with results calculated manually.

The sizing process for the high lift devices presented in subsection 5.3.3 was implemented in excel. These results were check against hand calculations and the examples given in Roskam [50] [51].

5.4.2. Flow5 Validation

The use of programs such as XFLR5 (which is based on XFoil) for aerodynamic analysis has been widely accepted and validated throughout the years through multiple papers [63]. However, the use of its newer, 3D, affiliated program Flow5 is less common. As the aerodynamic properties of the SFD and the full-scale Elysian are compared through flow5, and as its used for the stability and control analysis, a validation of the program of some sort seems appropriate. Therefore, a simple validation of the lift curve and drag polar in Flow5 will be performed by calculating these values for the wing through lifting line theory and estimating the fuselage contribution. This is a rigorous estimation method, used to verify whether Flow5 is in the correct range, neglecting some minor details such as the drag contribution of the empennage.

5.4.2.1. Lifting line theory for main wing

As explained, in order to validate Flow5, the lifting line theory as seen in Anderson [3] will be used. From 2D airfoil lift relations, the following relation can be deduced for an airfoil:

$$C_l = a_0(\alpha_{eff} - \alpha_{0L}) \tag{5.24}$$

Where a_0 is the 2D lift-curve slope (2π from subsonic, thin airfoil theory), α_{eff} is the effective angle of attack and α_{0L} is the angle of attack at zero-lift.

Now, introducing finite wing theory, the 2D relation can be converted to a 3D finite wing relation. By introducing the induced angle of attack cost by wing-tip vortices, the effective angle of attack changes, which affects the wing lift coefficient as follows:

$$\alpha_{eff} = \alpha - \alpha_i \tag{5.25}$$

Substituting in equation 5.24 above:

$$C_{L_w} = a_0(\alpha - \alpha_i - \alpha_{0L}) \tag{5.26}$$

Where:

$$\alpha_i = \frac{C_{L_W}}{\pi e AR} \tag{5.27}$$

This gives:

$$C_{L_w} = a_0(\alpha - \frac{C_{L_W}}{\pi e AR} - \alpha_{0L}) \tag{5.28}$$

$$C_{L_w} + \frac{a_0}{\pi e AR} C_{L_w} = a_0(\alpha - \alpha_{0L}) \tag{5.29}$$

$$C_{L_w} = \frac{a_0}{1 + \frac{a_0}{\pi e AR}}(\alpha - \alpha_{0L}) \tag{5.30}$$

With this equation, the C_L component of the wing can be calculated. As per the lifting line theory $a_0 = 2\pi$. All the necessary values can be found in Table 5.7.

a_0 [rad]	e [-]	AR [-]	α_{L0} [deg]
2π	0.68	13	-4.5

Table 5.7: Aerodynamic properties of the SFD wing

From these values, the C_L is estimated from an angle of attack ranging from -20 to 20 degrees. The C_L curves can be seen in figure 5.14. Here, the left graph is the SFD's lift coefficient plot, and the right is the plot derived from the above calculations. As stall behaviour is not taken into account in flow5 and thus not of importance, the range actually plotted is adjusted from -10 to 10 degrees. It can be seen that the lifting line theory slightly underestimates the lift coefficient compared to the flow5 simulation. This minor deviation (2-3%) can most likely be attributed to the fuselage contribution to the lift which is accounted for in the flow5 curve.

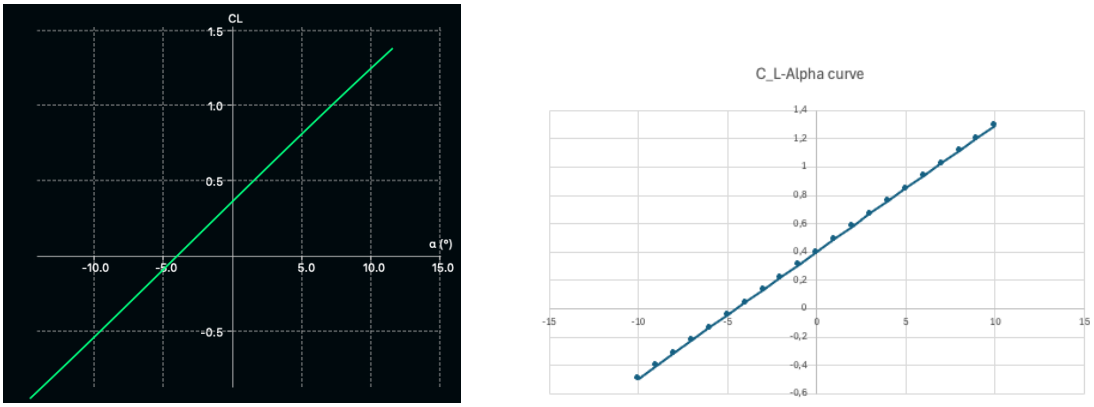

(a) Flow5 $C_l - \alpha$ curve

(b) Lifting line theory curve

Figure 5.14: C_L-α curve comparison

5.4.2.2. Drag polar

The drag was done in a similar fashion, estimating it using a method as presented in Anderson. For this, the following equation is used:

$$C_D = C_{D_0} + \frac{C_L^2}{\pi e AR} \tag{5.31}$$

Where the Oswald efficiency factor and aspect ratio remain unchanged and $C_{D_0} = 0,05$. With these values, the drag polar can be computed and compared to the one computed by flow5. This can be seen in figure 5.15.

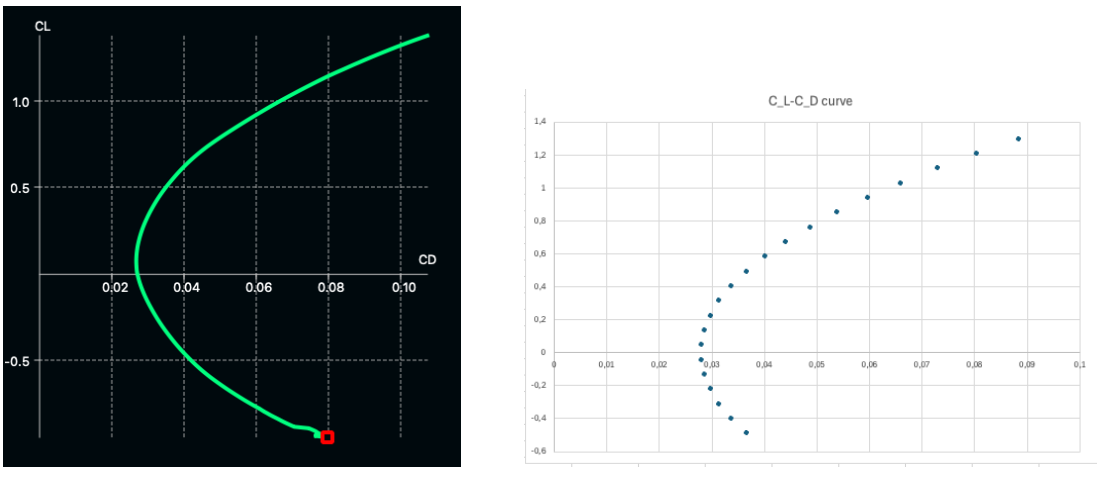

(a) Flow5 drag polar

(b) Lifting line theory drag polar

Figure 5.15: Drag polar comparison

Comparing these curves, it can be observed that the computed drag through Anderson slightly underestimated the drag compared to flow5, on average 4%. This can again be attributed to the

simple nature of the estimation method. Although most of the contribution of the fuselage to drag is incorporated through C_{D_0}, the empennage is not included.

From the above two comparisons we see that flow5 is able to calculate 3D lift components sufficiently well. Additionally, the slight deviation can be attributed to logical simplifications and assumptions. What must be noted is that although Flow5 in this case rather accurately simulates the drag, in the Aerospace design community it is notorious for under-estimating drag contributions and therefore its drag values cannot be used with the same confidence as its lift values. However, as the values are in this case validated, for the scope of this research the values can be used for further analysis.

5.4.3. Aero-Propulsive Interaction Model

The Aero-Propulsive Interaction Model used in subsection 5.2.4 utilizes a number of simplifications and assumptions. These simplifications and assumptions are listed below [69].

- Assumes that the wing has a rectangular planform of span b and chord c.
- Assumes the propellers are not located near the wing root or tip.
- The propeller is modelled as an actuator disk in uniform axial flow and upstream effect are neglected.
- The effect of each propeller on the adjacent ones is neglected.
- The wing is assumed to have a symmetric airfoil.
- The flow is attached, and the wing is fully immersed in the slipstream; that is, half of the slipstream flows under the wing and half over the wing
- The effect of the propellers on the wing is limited to the spanwise interval occupied by the disks ΔY. Within this interval the effect on the wing is uniform in spanwise direction
- $\Delta y \ll 1$
- Oswald efficiency factor is assumed to be unchanged by the aeropropulsive interaction

For the model Δy is equal to 0.0985 so that assumption holds. The part of the wing planform that the propellers are located is rectangular with a constant chord. However, the outmost propeller slightly overlap the tapered section of the wing therefore the model will slightly overestimate the ΔCL generated by the SFD. The propellers are far from the tip of the wing but the innermost propeller is close to the fuselage which might cause significant interaction between the fuselage and this propeller.

The airfoil used in the SFD is not symmetric. A value of α_p could be found to adjust the model to more accurately account for the effect of the non symmetric air foil. However, experimental or numerical data is required to establish the exact value required for α_p to model this effect.

As the change in Oswald efficiency factor induced by the propulsion system is ignored the model will slightly underestimate the increase in induce drag caused by the system. Estimating the change in Oswald efficiency factor and applying it to the model would increase its accuracy.

Results from the Aero-Propulsive Interaction Model and CFD simulation of the NASA X-57 are given in Figure 5.16. The model ΔC_L and CFD ΔC_L are very similar at lower $C_{L_{airframe}}$ values but start to diverge above a $C_{L_{airframe}}$ of 2.4. Therefore, the model should not be used for these high values of $C_{L_{airframe}}$. The model slightly underestimates the ΔC_D as compared with the CFD results. This is due to the discounting of the change in Oswald efficiency factor.

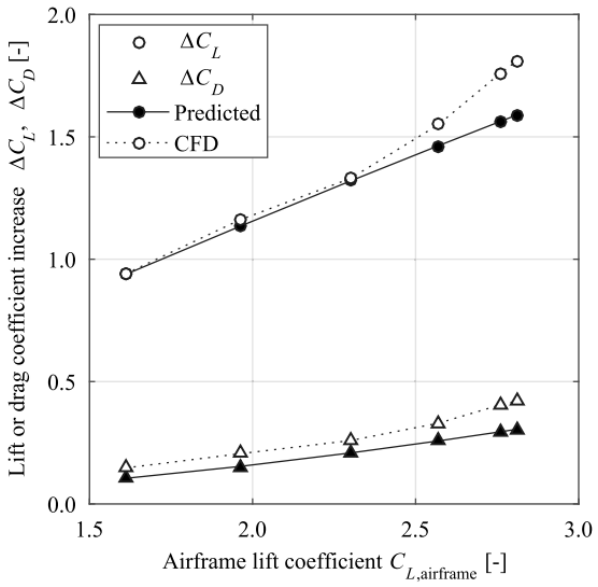

Figure 5.16: NASA X-57 predicted and CFD ($T_c = 0.6111$, $\alpha_p = 0$) [69]

From this we can determine that for this stage of the design process the model is sufficient in predicting ΔC_L and ΔC_D. However, in the future this model should be augmented to take into account the unsymmetrical airfoil and change using α_p in Oswald efficiency factor.

5.5. Sensitivity Analysis

The sensitivity of the model mass, wing loading, mass moment of inertia and cruise velocity to changes in geometric scale factor was investigated and the results are shown in Figure 5.17. These were calculated using the scaling relations to maintain similitude between the model and the aircraft given in section 5.1. The baseline values are for a geometric scale factor of 0.097 also given in section 5.1.

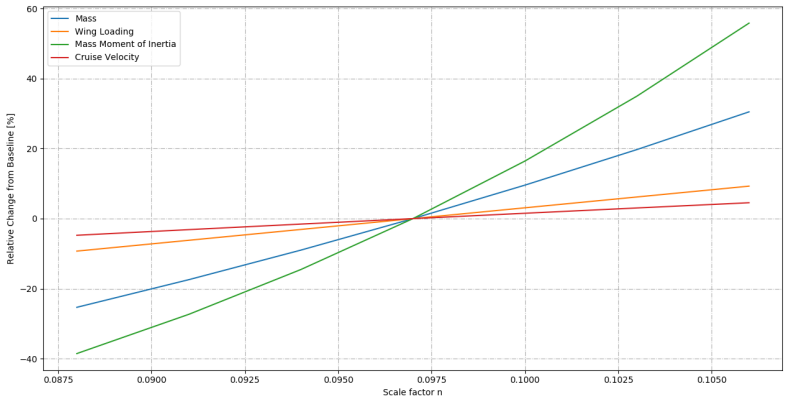

Figure 5.17: Sensitivity of the design to a change in scale factor n

As can be seen from Figure 5.17 wing loading and cruise velocity are less sensitive to changes in scale factor. On the other hand, a small change in scale factor causes a large relative change in mass and especially mass moment of inertia. This sensitivity can be mitigated somewhat by the modular weights included in our design that can change the mass and moment of inertia as elaborated upon chapter 9.4.

5.6. Requirement Compliance

With the finalization of the wing planfrom and the completion of the aerodynamic analysis reverent requirements can be checked for compliances. Requirement SFD-SYS-PER-12 was for a maximum wing loading that was still to be determined. However, it was not driven by any stakeholder or regulation and as such is not relevant for the design process. Therefore, SFD-SYS-PER-12 was removed as a requirement. The maximuum lift coefficient for SFD-SYS-PER-13 was determined based on the cruise velocity required for Froude scaling at 9.7%.

Table 5.8: Requirement compliance aerodynamic requirements

ID	Requirement Description	Verification Method	Compliance Level
~~**SFD-SYS-PER-12**~~	~~The aircraft shall have a wing loading (W/S) of at most **<TBD>** N/m^2.~~		Requirement eliminated as it is not relevant to the design meeting the mission objective
SFD-SYS-PER-13	The aircraft shall generate a maximum lift coefficient in clean configuration ($C_{L_{max}}$) of at least 0.69.	Anlaysis	From calculations the $C_{L_{max,L}}$ is estimate to be 2.04
SFD-SYS-PER-14	The aircraft shall generate a maximum lift coefficient in take-off configuration ($C_{L_{max,TO}}$) of at least 2.11	Analysis	From calculations the $C_{L_{max,TO}}$ is estimate to be 3.32
SFD-SYS-PER-15	The aircraft shall generate a maximum lift coefficient in landing configuration ($C_{L_{max,L}}$) of at least 1.94.	Analysis	From calculations the $C_{L_{max,L}}$ is estimate to be 2.29

6
Structures

This chapter details the complete structural design of the SKRIBBL SFD, this structure carries all the major loads acting on, and generated by the SFD. Additionally, it carries the payload and is the segment of the SFD on which the modularity aspect has the most impact. Therefore, a detailed and sound design of the structural aspect of the SFD is of utmost importance. In section 6.1 the major design choices and general aspects of the SFD will be discussed. Secondly, in section 6.2, the different structures of the SFD will be sized and analysed followed by a detailed analysis of the entire structure in section 6.3. This is followed by the modular assembly of the structural subsystems in section 6.4. After this, the structures subsystem is verified and validated in section 6.5 followed by a sensitivity analysis is performed in section 6.6. Finally, to close the chapter, the SFD structure is compared in section 6.7 to the requirements set.

6.1. General Design and Dimensions

In this section, the general structural design of the SFD will be described. This will be done by going over the different design choices made during the design process. The load cases the structure will have to withstand, and finally, the mass breakdown and moments of inertia will be given for the complete SFD.

6.1.1. Design Choices

To create a proper structure for the SFD several design choices must be made, some having a larger impact than others. Most of the major design choices such as material choice and wingbox design have been made in the previous report and are already stated in chapter 2.3. However, the major choices will be elaborated on a bit more. After this the new design choices will be discussed in more detail.

6.1.1.1. Wingbox Design

Due to the greater performance in nearly all structural performance criteria, as well as its superior integration with other subsystems, the third design for the wingbox was chosen as seen in Figure 6.1. Its somewhat higher weight was in the initial analysis, deemed to cancel out by the fact that a more structurally sound wingbox could be made out of a thinner material.

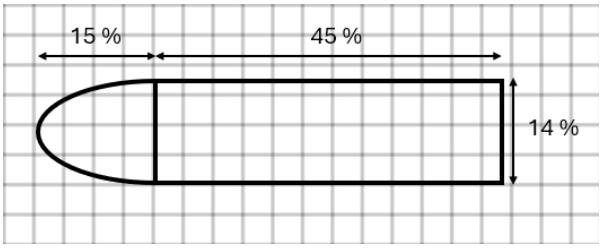

Figure 6.1: Chosen wingbox layout expressed as a percentage of the wing cord.

6.1.1.2. Fuselage Design

In the initial design stages, the proposed plan for the fuselage was to create a complete round hull as the load bearing structure. In turn this fuselage would have access hatches to ensure maintenance, repairs and replacement could be made on vital components. However, after the initial design stage it was found that the fuselage does not require extensive structural support to carry the loads induced on it. Therefore, it was deemed more logical to approach the access to vital components in a different way. The current load bearing part of the fuselage will consist of the bottom half-circle, allowing the top half to snap on or off using simple clamps. This not only provides more and easier access to components but

also prevents multiple cutouts in a load bearing structure. The more detailed analysis of this design choice is described in subsection 6.2.4.

6.1.1.3. Material Choice

Based on the trade-off study, both carbon fibre reinforced polymer (CFRP) and the aluminium alloy 7075-T7451 were identified as viable material options for the structures within the SFD. CFRP showed clear advantages in the specific tensile and compressive strength criteria, making it particularly attractive for load-bearing components dominated by axial stresses. While aluminium 7075-T7451 showed great specific shear strength as well as a more balanced performance across multiple secondary criteria including manufacturability, sustainability and cost.

Given these material characteristics, it was concluded that a definitive material choice for the SFD could not be made. Instead, a component-level material selection approach was chosen, whereby each structural element is analysed to determine the most suitable material. This approach ensures that each component is optimised for its purpose and keeps the weight to an absolute minimum. Some important data for both materials is shown in Table 6.1

Table 6.1: Important Material Properties of CFRP and Al 7075-T7451

Ultimate Strenght	Tensile[MPa]	Compressive [MPa]	In-Plane Shear[MPa]	Density [kg/m^3]
CFRP	600	570	90	1600
7075-T7451	524	524	303	2830

6.1.2. Mass Breakdown and Moment of Inertia

The mass breakdown serves as a definitive accounting of all components of the scaled flight demonstrator as it is intended to be built and flown. This overview clearly identifies the weight of the entire system, its subsystems and the components within each subsystem. This mass breakdown also lays the foundation for the calculation of the moments of inertia calculated in subsection 6.1.2, as well as the manufacturing plan described in chapter 10.3. It also gives a good insight into the impact of swapping components, this is not only relevant for minor upgrades but also shows the consequences regarding modular changes. The total mass breakdown of the SFD can be seen in Table 6.3 where the x-location is from the front of the SFD, the y-location is from the centre of the SFD, and the z-location is from the ground. When adding these weights together, the cg locations depicted in Table 6.2 are found.

The data found in Table 6.3 were used to find the mass moment of inertia on the x-, y-and z-axes located on the cg of the SFD. All components were assumed to act as a point mass except for the fuselage, nose, tail, horizontal stabiliser, vertical stabiliser, and the wing. They were assumed to act as a hollow cylinder, hollow ellipsoid, hollow cone, a hollow cuboid, a hollow cuboid, and a hollow cuboid and trapezium, respectively. This together, resulted in the mass moment of inertia depicted in Table 6.2.

Table 6.2: The mass moment of inertia and centre of gravity of the SFD without correction weights.

	X-axis	Y-axis	Z-axis
Centre of gravity [m]	1.66	0	0.11
Mass moment of inertia without correction weights [$kg \cdot m^2$]	54.99	42.75	84.309
Mass moment of inertia with correction weights [$kg \cdot m^2$]	140.46	43.5894	168.748

To get the desired mass moment of inertia for similitude described in section 8.1 (I_{xx} = 146.77, I_{yy} = 46.08, and I_{zz} = 167.40), and the desired cg for longitudinal stability talked about in subsection 8.2.1 (x_{cg} = 1.67m, y_{cg} = 0m, and z_{cg} = 0.08m), correction weights are added in the SFD.

Table 6.3: Total Mass Breakdown of the SFD

Subsystem	Component	Mass [kg]	X-loc [m]	Y-loc [m]	Z-loc [m]
Structures		54.29			
	Load-bearing Fuselage	2.99	1.53	0	0.16
	Fuselage Top Fairing	2.99	1.53	0	0.22
	Fuselage Component Floor	2.51	1.53	0	0.15
	Nose cone	1.83	0.39	0	0.20
	Tail	2.01	2.67	0	0.20
	Empennage	5.31	3.38	0	0.70
	Wingbox	10.24	1.61	0	0.03
	Wing Skin	14.06	1.61	0	0.03
	Wing tip 1	0.06	1.61	2.52	0.09
	Wing tip 2	0.06	1.61	-2.52	0.09
	Front Landing Gear	3.00	0.42	0	0
	Right Landing Gear	4.00	1.77	0.44	0
	Left Landing Gear	4.00	1.77	0.44	0
	Landing Gear Fairing	1.23	1.77	0.44	0
Avionics		3.031			
	Camera	0.0416	3.30	0	0.15
	Camera Transmitter	0.0154	3.17	0	0.15
	Flight Computer	0.198	0.75	0	0.10
	Flight Data Recorder	1	0.32	0	0.10
	5G Transmitter	0.376	1.61	0	0
	Data Collection System	0.900	0.47	0	0
	RF Antenna	0.05	1.61	0	0
	GNSS Antenna	0.25	1.61	0	0
	Buck Converter 1	0.2	1.81	0	0.10
	Buck Converter 2	0.2	1.36	0	0.10
Powertrain		43.73			
	Engine 1 + fairing + propeller + ESC	1.16	1.61	0.44	0.06
	Engine 2 + fairing + propeller + ESC	1.16	1.61	0.89	0.06
	Engine 3 + fairing + propeller + ESC	1.16	1.61	1.33	0.06
	Engine 4 + fairing + propeller + ESC	1.16	1.61	-0.44	0.06
	Engine 5 + fairing + propeller + ESC	1.16	1.61	-0.89	0.06
	Engine 6 + fairing + propeller + ESC	1.16	1.61	-1.33	0.06
	Battery 1	7.35	1.26	0	0.12
	Battery 2	7.35	1.26	0	0.27
	Battery 3	7.35	1.85	0	0.12
	Battery 4	7.35	1.85	0	0.27
	Battery 5	7.35	2.09	0	0.12
	Backup Battery	0.018	1.08	0	0.10
Stability and Control		2.60			
	R-High Lift Actuator 1	0.186	1.61	0.75	0.03
	R-High LIft Actuator 2	0.186	1.61	1.52	0.05
	L-High Lift Actuator 1	0.186	1.61	-0.75	0.03
	L-High LIft Actuator 2	0.186	1.61	-1.52	0.05
	R-Aileron Actuator 1	0.186	1.61	1.75	0.09
	R-Aileron Actuator 2	0.186	1.61	2.43	0.09
	L-Aileron Actuator 1	0.186	1.61	-1.75	0.09
	L-Aileron Actuator 2	0.186	1.61	-2.43	0.09
	Elevator Actuator	0.186	3.0	0	0.15
	Rudder Servo	0.186	3.0	0	0.15
SFD Subtotal		**103.65**			
Correction weights		42.24			
	Correction weight 1	23.17	1.61	1.41	0.05
	Correction weight 2	23.17	1.61	-1.41	0.05
SFD Total Weight		**150**			

6.2. Detailed Design

In this section, the detailed design of each component within the structures subsystem will be conducted in a systematic manner. For each component, the design process starts with a clear definition of its functional role within the airframe. Based on this, the relevant load cases are identified, including both normal operating conditions and ultimate load cases. Following the load identification, each component is analysed to determine the internal stresses, deformations, and failure modes. These, together with the minimisation of the component's weight, drive the decision-making process on both the material choice and the dimensions of the component. This iterative process ensures that each structural component meets its functional and performance requirements while contributing effectively to the integrity and efficiency of the structures subsystem, and thereby the SFD as a whole.

6.2.1. Wing Skin

The first structural component to be analysed is the outer skin of the wing, hereafter often referred to as the skin. The detailed design of the wingbox, which is the primary load-bearing element of the wing, is treated separately in subsection 6.2.3. Although the wing skin itself is not considered a primary load-bearing structure, it plays a vital aerodynamic role since its surface generates all the lift. The aerodynamic forces acting on the skin must therefore be transferred efficiently and reliably to the wingbox to ensure structural integrity.

Despite its secondary structural role, the skin is still subjected to significant loading due to the bending moment induced by the generated lift. This bending moment induces both compressive and tensile stresses in the skin, particularly in regions between the ribs, making it susceptible to instabilities such as buckling. As a result, buckling resistance becomes the primary design driver for the thickness of the skin and the placement of supporting elements. The detailed design must therefore find a balance between sufficient stability margins and a low structural mass while maintaining the shape of the airfoil.

In addition to the local structural behaviour of the skin, the structure by which the aerodynamic loads are transferred to the wingbox is a major aspect of the analysis. This load transfer is facilitated by multiple ribs distributed along the wingspan. These ribs ensure that the skin can maintain the airfoil shape under load, while also transferring this same load to the wingbox. The following sections, therefore, address the detailed design of the wing skin in combination with the structural role of the ribs.

6.2.1.1. Buckling

During flight, the wing endures high bending stresses due to the lift it produces. As a result, the upper surfaces of the outer wing and the wingbox risk buckling. Therefore, both surfaces were analysed under the most extreme loading case, a lift of 5518 Newton. For this analysis, some assumptions would have to be made. Firstly, the surface between the first and last spar was taken as most critical to buckling, and assumed to be a flat surface where both unloaded edges were assumed to be simply supported. The maximum allowable stress σ_{max} was determined from the stress at which a thin plate elastically buckles as every form of buckling is not desired. The formula for this is depicted in Equation 6.1 where, E is the Young's modulus, v is the Poisson's ratio, and t is the thickness [39]. Finally, k is the buckling coefficient taken from Figure 6.3 where a is the length of the unloaded edges and b is the width of the analysed plate [39].

$$\sigma_{max} = \frac{k \cdot \pi^2 \cdot E}{12(1 - v^2)} \cdot (\frac{t}{b})^2 \tag{6.1}$$

The experienced stress is estimated with Equation 6.2 where, M equals the moment around the X-axis, z is the horizontal distance from the x-axis, and I_x is the moment of inertia of the combined wingfoil and wingbox. The moment about the Y-axis was neglected since it is over an order of magnitude lower than the X-axis moment in this loading case.

$$\sigma = \frac{M \cdot z}{I_x} \tag{6.2}$$

For the entire span of the SFD, both the stress at which the upper section of the airfoil will buckle, and the stress experienced at that section were calculated. From these calculations, it was deduced that

adding more ribs did not influence the outcome by a significant amount and that, therefore, the skin thickness of the outer wing must be $2mm$ to not experience buckling. The final results are visualised in Figure 6.2. The kink visible in the graph of the stress experienced is because for the first part of the span, the moment applied to the skin was the maximum moment calculated at the root to ensure safety.

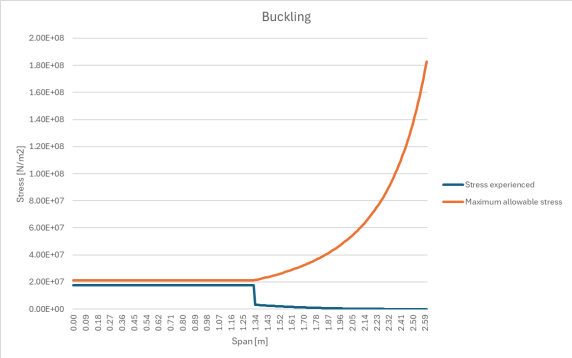

Figure 6.2: Graph of the difference between the stress at which the airfoil will buckle versus the stress it experiences at a loading factor of 3.75.

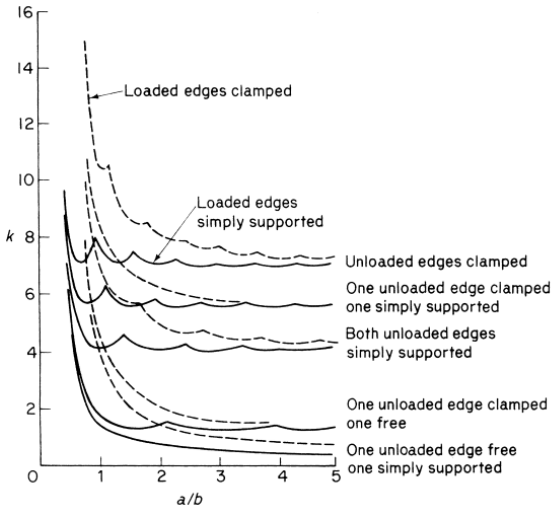

Figure 6.3: Buckling Coefficients for Flat Plates in Compression [39].

6.2.2. Ribs

In the previous section is was found that increasing the number of ribs has a negligible influence on the buckling behaviour of the skin; consequently, the spacing and amount of ribs is not governed by buckling considerations. Instead the number and placement is primarily driven by the load transfer requirements and by the need to control the relative deformation of the wing with respect to the wingbox. Although just a single rib with a thickness of 1 mm would, in principle, be sufficient to carry the lift from the skin to the wingbox, such a configuration is not structurally viable. A single rib configuration would allow excessive torsional deformation, leading to a loss of alignment between the two wing components and thereby compromising the structural integrity and aerolastic behaviour.

For this reason, a more logical approach was adopted to determine the number and spanwise locations of the ribs. The the default configuration of the SFD-2, there are three engines located on each half-wing, requireing the thrust loads generated by the engines to be transferred effectively into the wingbox. Placing ribs at the same spanwise locations of the engines facilitates this load transfer while simultaneously providing strong structural interfaces for engine attachment and routing of associated cabling. In addition to the ribs located at the engine stations, ribs are placed at the wing root, wing tip and at an intermediate location between the outermost engine and the wing tip. This baseline configuration would result in a total of 12 ribs for the complete wing.

However, there is also a modularity option to consider for the ribs, specifically, the detachable engine configuration which requires the wing structure to accommodate multiple engine mounting locations. This modularity requirement, which is described in more detail in Figure 6.4, requires the inclusion of additional ribs beyond those used in the default configuration. Consequently, five extra ribs are distributed along the straight half-span of each wing to enable alternative engine layouts. This results in the total number of ribs rising to 22 for the full wing. Due to the thickness of just 1 mm for these ribs, each one is just 12.8 grams, with the smaller ribs in the tapered section and wing-tip 8.6 and 4.4 grams respectively. Making the total contribution of the ribs just 256 grams.

6.2.3. Wingbox

As stated in subsection 6.1.1, the third wingbox configuration was selected for further analysis and detailed design. The wingbox must be designed to withstand two primary failure modes: material failure due to the applied loads and structural instability due to buckling. Both of these failure mechanisms are

analysed in the following sections, which will provide contstraints on the required thickness of each individual wingbox element. The overall geometry and relative dimensions of the wingbox cross-section are illustrated in Figure 6.4. All dimensions are expressed as a percentage of the cord length, as the wingbox maintains a geometrically similar cross-section throughout the tapered portion of the wing.

6.2.3.1. Wingbox Loading

To evaluate the structural performance of the wingbox under the applied loads, a number of assumptions are introduced to simplify the analysis while maintaining adequate safety margins. First, it is assumed that the wingbox carries the entire load from aerodynamic, gravitational, and propulsive forces, with no contribution from the wing skin. Second, the wingbox cross-section is modelled using a boom idealisation. And finally, the most critical loading condition is assumed to act trough a single wingbox cross-section. The adopted ign conventions and boom representation of the wingbox are shown in Figure 6.4.

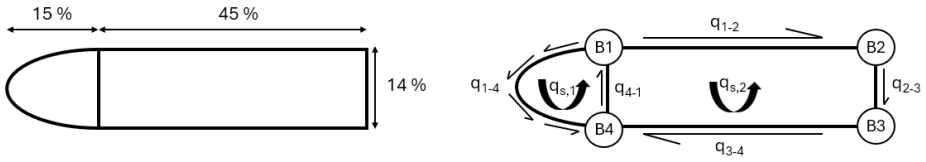

Figure 6.4: Wingbox Dimensions [L] and Boom Representation Including Shear Flows [R]

To calculate the effective boom areas using Equation 6.3, the normal stresses at the boom locations have to be determined first. These stresses are computed by considering bending moments about both the x- and z-axes. Since for all considered load cases there is no contributing force in the y-direction, it does not effect the normal stress distribution. As shown in Equation 6.4, the normal stress depends on both the x- and z-coordinates of a given point on the wingbox cross-section. Five locations were identified as potential extremes: Points 1 through 4, as indicated in Figure 6.4, and an additional point located at the tip of the rounded section between points 1 and 4. The resulting normal stresses at these locations are listed below, together with the calculated boom areas and the corresponding shear flow increments. Using these values, the unknown shear flows within the multi-cell wingbox can be determined.

$$B_1 = \frac{t_{skin} b}{6}\left(2 + \frac{\sigma_2}{\sigma_1}\right) \qquad B_2 = \frac{t_{skin} b}{6}\left(2 + \frac{\sigma_1}{\sigma_2}\right) \tag{6.3}$$

$$\sigma_y = \frac{(M_x I_{zz} - M_z I_{xz})y + M_z I_{xx} - M_x * I_{xz})x}{I_{xx} Izz - Ixz^2} \tag{6.4}$$

- σ_1: 33.5 MPa
- σ_2: 31.3 MPa
- σ_3: -34.3 MPa
- σ_4: -32.1 MPa
- σ_5: 1.41 MPa

- Boom Area 1: 421 mm^2
- Boom Area 2: 437 mm^2
- Boom Area 3: 218 mm^2
- Boom Area 4: 242 mm^2

- Δq_1: -22.1 N/mm
- Δq_2: 15.7 N/mm
- Δq_3: 13.2 N/mm
- Δq_4: -6.8 N/mm

Using these results there are still unknown shear flows within the multi-cell wingbox. To solve for these unknowns a cut was made in the vertical section 1-4 followed by a moment summation and the torsional equivalency of both wingbox cells. This yields the following shear flows and final shear stresses.

1. Rounded 1-4: 18.4 N/mm
2. Section 1-2: -37.0 N/mm
3. Section 2-3: -14.3 N/mm
4. Section 3-4: -4.1 N/mm
5. Section 4-1: 2.3 N/mm

1. Rounded 1-4: 9.2 MPa
2. Section 1-2: 18.5 MPa
3. Section 2-3: 14.3 MPa

4. Section 3-4: 4.1 MPa
5. Section 4-1: 2.3 MPa

From the resulting shear stress levels and the material properties listed in Table 6.1, it is evident that the wingbox does not fail due to material strength limitations, with a significant margin still left. This is because during the iterative design process it was evident that buckling would become the limiting factor in the thickness of the wingbox elements. From this load analysis aluminium shows the best potential as the material for the wingbox, for when buckling is neglected, and the design is iterated to its bare minimum thickness, the aluminium wingbox is nearly half the weight of the CFRP wingbox. However, at the same time, the thicknesses of these elements would drop below 0.5mm, at which point buckling can absolutely not be neglected.

6.2.3.2. Buckling

The buckling analysis of the wingbox follows a methodology similar to that used for the wing skin. This similarity arises because the effective panel width of the wing skin is defined by the spacing between the wingbox spars. This results in identical panel widths and modelling assumptions. The primary difference between the wingbox and the wing skin analysis lies in the vertical distance from the x-axis, which affects the local stress magnitude. However, this difference is sufficiently small that is has a negligible influence on the final buckling results.

Using Equation 6.1 to determine the critical buckling stress and Equation 6.2 to evaluate the applied stress under the most severe load case, corresponding to a load factor of 3.75, the minimum required thickness for each element was determined. Since the Young's modulus for CFRP and Aluminium is very similar, 70 GPa and 71.7 GPa respectively, the thicknesses required for each element in the wingbox is nearly identical. Section 1-2 requires the highest thickness of 2 mm, the rest of the elements has received either the same or a slightly lower thickness if the stresses allowed it and can be seen in the list below.

1. Rounded 1-4: 2 mm
2. Section 1-2: 2 mm
3. Section 2-3: 1.5 mm
4. Section 3-4: 2 mm
5. Section 4-1: 1.5 mm

Since these required thicknesses are for both CFRP and aluminium, a wingbox of either material would have the same geometry. But due to aluminium's density which is nearly twice as high as CFRP, an aluminium wingbox was ruled out and CFRP was chosen as the desired material for the wingbox. The total weight for the CFRP wingbox is 9.99 kg.

6.2.4. Fuselage

The fuselage of the SFD consists of several distinct structural sections, each fulfilling a specific functional role. These sections include the nose cone, the load-bearing middle fuselage, the upper middle fairing, and the aft section. The nose cone is a non-load-bearing structure and serves purely as an aerodynamic shell. The load-bearing middle fuselage forms the primary structural core of the aircraft and is configured as a lower half-cylindrical shell. This section transfers all loads which originate in the wing into the rest of the airframe while simultaneously housing critical onboard systems of the SFD.

The upper half of the middle fuselage forms a removable fairing that can be detached with ease from the lower shell to provide direct access to internal components. Although this upper structure does not contribute to the global load transfer, it is still subjected to compressive stresses induced by the fuselage bending, and is therefore still susceptible to buckling. For this reason, as further justified in subsection 6.2.6, the upper fairing is designed with the same skin thickness as the load-bearing lower fuselage. The aft, or tail section of the fuselage is responsible for transferring aerodynamic and inertial loads from the empennage into the load-bearing middle fuselage, thereby completing the primary load path of the aircraft.

6.2.5. Fuselage Loading

The most critical loading condition for the fuselage was identified to occur during wind-tunnel testing. In this configuration, the SFD is mounted at the aft end of the load-bearing middle fuselage structure. When the aircraft generates its maximum lift at the design load factor of 3.75, the wind-tunnel mounting interface applies a reaction force that effectively pulls the SFD back down. This opposite force of over 5kN is the largest concentrated load on the structure. In addition to this vertical force, the bending moment induced by lift and the axial force due to aerodynamic drag represent the dominant loads transmitted through the wind-tunnel attachment.

As with the wingbox, the fuselage loading analysis does not ultimately govern the structural sizing, but still has to be performed to arrive at this conclusion. Instead, buckling considerations, as will be discussed in subsection 6.2.6, are the primary design drivers. Nevertheless, using the final fuselage geometry, the resulting stress states within the load-bearing fuselage section was evaluated. The maximum and minimum normal stresses, as well as the associated shear stress were found to be as follows:

- σ_{max}: 17.3 MPa
- σ_{min}: -17.5 MPa
- τ: 3.3 MPa

These stress levels remain well below the material strength limits, as can be viewed in Table 6.1, and therefore do not impose additional constraints on the fuselage design.

6.2.6. Fuselage Buckling

As previously stated, buckling is the governing failure mode for determining the skin thickness of the fuselage. Unlike the wing skin and wingbox elements, the fuselage has a cylindrical geometry, resulting in a completely different buckling behaviour. The critical axial buckling stress for a cylindrical shell is given by Equation 6.5, where γ is a knockdown factor, E the Young's modulus, υ the Poisson ratio, t the shell thickness, and r is the radius of the fuselage. [28]

To ensure a conservative and robust design, the load-bearing fuselage was assumed to be entirely unsupported and treated as an isolated structure. Under this assumption, a conservative knockdown factor of $\gamma = 0.05$ was selected. Using this value, in combination with the material properties listed in Table 6.1, the minimum required skin thickness for the load-bearing fuselage was determined to be 1.75 mm, since a thinner skin would result in the axial stresses exceeding the critical buckling stress.

$$\sigma_c = \frac{\gamma E}{\sqrt{3(1-\upsilon^2)}} \frac{t}{r} \tag{6.5}$$

Although the upper fuselage fairing is not primarily a load-bearing structure, but rather a protective and aerodynamic shell, it still experiences compressive stresses due to global fuselage bending and must therefore also be designed to resist buckling. Consequently, it cannot be realised as an extremely thin shell. The design choice was therefore made to assign the exact same skin thickness to both the upper and lower fuselage portions. This approach allows both halves to be manufactured using a single mould, reducing production complexity, cost and environmental impact, while also simplifying assembly. Additionally, identical thicknesses facilitate the integration of a reliable clamping mechanism to secure the upper fairing to the bottom structure.

For the same reasons that motivated the material selection of the wing skin and box, CFRP was chosen over 7075-T7451 for the fuselage structure. While the use of aluminium could marginally reduce the required skin thickness, it would result in an overall mass increase factor exceeding 1.5. The combined mass of the upper and lower fuselage halves is 5.97 kg, with each half contributing equally to the total. Finally, to attach all vital components to the fuselage, an aluminium sheet of thickness 1.5 mm was places within the fuselage so all components could be screwed in pre-drilled holes within this sheet, contributing 2.5 kg to the overall SFD weight.

6.2.6.1. Nose Cone

Since the nose cone serves exclusively as an aerodynamic fairing and does not contribute to the primary load-carrying structure of the aircraft, no significant structural loads act on this component. Its primary function is to provide a smooth aerodynamic shape while housing a limited number of low-mass systems that must be positioned in this foremost section of the aircraft, such as the forward facing camera required to support BVLOS operations.

Given the absence of major mechanical loads, the structural design of the nose cone is not governed by strength considerations. Instead, the design emphasis is placed on manufacturability and structural compatibility with adjacent fuselage sections, and ease of integration. For these reasons, the decision was made to use the same skin thickness as the load-bearing fuselage section of 1.75 mm. Due to the absence of major loads in this fairing, there is no benefit to using aluminium. Therefore, using CFRP, the total weight of the nose cone becomes 1.83 kg.

6.2.6.2. Tail Section

The tail, or aft section, of the SFD fulfils a primarly structural function by transferring the aerodynamic loads generated by the empennage into the main fuselage. These loads are nearly an order of magnitude smaller than the forces acing on the main wing, resulting in substantially lower structural requirement for this section of the SFD. Consequently, the baseline structural concept, derived from the cross-section of the main fuselage is expected to provide plenty of strenght and stiffness to ensure reliable load transfer.

At the maximum control surface deflection, the control surfaces generate an additional -48 N, 685 N, and 337 N in the x-, y-, and z- directions, respectively. These forces in addition to a baseline estimate for the drag were used as input for a structural analysis similar to the one performed for the fuselage in subsection 6.2.4, with the key difference that the aft section is modelled as a fully closed cylindrical shell. Due to the reduced loading, structurally efficient cylindrical geometry and the use of a higher knockdown factor γ the required skin thickness was found to be well below 1 mm.

In addition, the structural demands decrease progressively along the lenght of the tail section. Moving aft, both the fuselage radius and the bending moments acting acting on the structure decrease, further reducing stresses experienced by the structure and consequently the required thickness. However, the design choice was made to adopt the same skin thickness for the tail section as for the main fuselage and nose cone. This decision was driven by considerations of manufacturing efficiency and ease of integration. Additionally, since the SFD will receive additional ballast weights to achieve similitude to the Elysian-E9X, mass minimisation is of less importance. As a result, with a skin thickness of 1.75 mm, the mass contribution of the tail section to the SFD is 2.29 kg.

6.2.7. Landing Gear

The landing gear subsystem cis a critical element of the aircraft configuration and therefore requires detailed sizing and definition. Its primary function is to ensure safe ground operations, including take-off, landing and taxiing, while providing adequate clearance for both the propellers and the tail. In addition, the landing gear fairing must fully enclose the retracted rear landing gear during flight and minimize its aerodynamic impact on the overall performance of the SFD. The sizing of the landing gear and the associated design considerations are discussed in the following sections.

6.2.7.1. Landing Gear Sizing

In the baseline configuration of the SFD, the propellers have a radius of 0.2032 m. While propeller clearance is an important consideration, the most restrictive geometric constraint is the prevention of a tail strike during take-off. At the nominal take-off condition, the SFD operates at an agle of attack of 16.2°. This results in a minimum required landing gear height of 37 cm to avoid contact between the tail and the ground. However, to account for uncertainties and to provide a modest safety margin, an additional 2° was applied to the take-off angle, leading to a required landing gear height of 44cm.

The nose landing gear does not impose a strict clearance requirement. However, excessive nose-down pitch during take-off is undesirable, as the engines in the standard configuration already have a slight downward inclination. Increasing this configuration further would reduce propulsive during one of the most critical phases of flight. At the same time, a higher nose gear would result in an imbalance in the

SFD which is therefore also undesirable. Consequently, the nose landing gear height is constrained to a minimum of 40cm and cannot exceed the main landing gear's height. This ensures a balanced aircraft attitude during all ground operations.

A comprehensive market survay revealed that no commercially available landing gear system meets the above requirements, primarily due to the relatively large scale of the SFD compared to typical remotely piloted aircraft. As a result, the landing gear subsystem will be outsourced to an external supplier to be selected at a later design stage. To facilitate this process, a set of clear design constraints has been defined adn will be provided to the supplier.

Main landing gear:

- The rear landing gear must provide at least 44 cm of ground clearance.
- The rear landing gear must not be taller than 50 cm.
- The rear landing gear must be able to sustain a landing impact of 2 g.
- The rear landing gear must be able to retract.
- The stored rear landing gear must fit within the landing gear fairing.
- Each rear landing gear must not be heavier than 4 kg.
- The rear landing gear must provide sufficient braking during landing.

Nose landing gear:

- The nose landing gear must sustain the weight of the aircraft acting on it.
- The nose landing gear must provide at least 44 cm of ground clearance.
- The nose landing gear must not exceed the height of the rear landing gear.
- The nose landing gear wheel must be able to rotate around the z-axis freely.

6.2.7.2. Design Landing Gear Fairing

The fairing of the landing gear will house the landing gear during flight. This fairing will be attached below the wing and extend further behind the wing. The front fuselage which will be attached to the wing from 26% of the cord until the aft edge, will follow Equation 6.6.

$$\frac{x^2}{0.1225} + \frac{y^2}{0.0256} + \frac{z^2}{0.01} = 1 \tag{6.6}$$

The aft part which will extend past the wing cord will follow the shape as seen in Equation 6.7.

$$\frac{x^2}{0.09} + \frac{y^2}{0.0064} + \frac{z^2}{0.01} = 1 \tag{6.7}$$

The thickness of the fairing will stay consistent with the rest of the wing skin at a thickness of 2 mm. To account for moving parts that will be required within this fairing, a design factor of 1.5 is added to the calculated weight. Giving each of the two landing gear fairings a weight of 1.23 kg.

6.3. Detailed Analysis

The detailed structural analysis covered in this section involves the response and consequences of the structure to extreme operating conditions and fracture analysis due to hatch cutouts. The goal of the analysis is to find the structural limitations and, if required, iterate the design accordingly or set operational limits.

6.3.1. Vibrations

Vibrations occur in any moving object at some scale. If not designed appropriately or if limits are exceeded, resonating oscillations may cause catastrophic failure to the structural integrity of the model. The most critical form of structural vibrations for the model is due to aerodynamic flutter. At a certain flight speed, wing surfaces may enter an unstable oscillation due to aeroelastic effects. Amplitudes growing to infinity can do significant structural damage and eventually break the wing apart.

Flutter can be described as the behaviour of a wing when two of its natural modes, bending and torsion, enter an unstable coupled oscillation, amplifying each other. The dynamics can be modelled as drawn in diagram 6.5, where an aerofoil, representing a section of the 3D wing, is mounted on a 2-degree-of-freedom system. The aerofoil can translate along the z-direction, representing wing bending

and deflection. Secondly, it can rotate around its center of gravity, modelling wing torsion. In reality, both modes are damped due to material stiffness and resistance during dynamic movements[43].

The modes and active forces during several phases of a single period are drawn in figure 6.6 in a simplified manner. Such a movement may be initiated by a change of angle of attack during flight, as shown in the situation at phase 1. The aerodynamic lift bends the wing upwards, and if both modes oscillate at the same frequency, there will only be an elastic force resisting wing bending, pulling the wing back towards the neutral axis. During the downwards motion, the local angle of attack becomes negative due to the torsional oscillation, creating a downwards aerodynamic force aligned with the elastic force. Back at the neutral axis, the oscillation enters its second half-period, which behaves the same as phases 1 to 3 but in opposite vertical directions[59].

When the aerodynamic forces are relatively light, as is the case during slow-speed flight, the damping by the material of the wing creates a stable and decaying oscillation. However, at some higher flight speeds, the aerodynamic forces overcome the damping, resulting in a dynamically stable, and for even higher speeds, unstable oscillation.

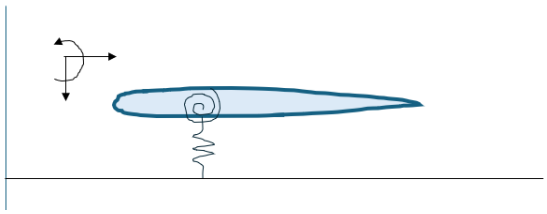

Figure 6.5: 2-DoF vibrational model of an aircraft wing

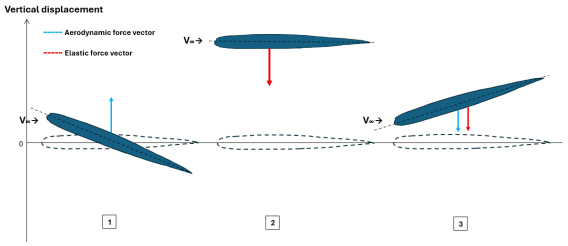

Figure 6.6: Aeroelastic flutter motion

Determining the speed at which the oscillation becomes unstable, the flutter speed, is a very complicated field of study. The most important parameters are the ones defining the wing's stiffness and geometry. Large span, flexible wings tend to flutter earlier. Increasing the resistance and speed are the parameters defining torsional stiffness, GJ, where the aerofoil's t/c ratio is of has a huge influence. Due to the complexity of this phenomena, there is no single expression to determine the flutter speed.

Empirical data show that for similar aircraft geometry and structures, the flutter speeds lie around $150[m/s]$. Given the fact that the model has a relatively high thickness over chord ratio, greatly increasing the critical speed, the actual value might be a lot higher[25]. Without delving too deeply into estimating this complex subject, the speeds flown during normal operations are far below the estimated flutterspeed and therefore, this phenomenon will not impose a risk to the model. Consequently, no structural adaptations resisting flutter are considered for the design.

Other vibrations occurring during operations, such as propeller imbalance, turbulence, or due to an uneven surface during ground roll, are deemed to have a negligible influence on the structural integrity of the model.

6.3.2. Thermal loads

Thermal stresses are induced by temperature differences in the space or time domain. Thermal differences cause expansion or shrinkage of a material, which induces internal stresses and influences its connections to adjacent components. The largest temperature differential in both the space and time domains during normal operations of the model will be due to the electronic speed controllers, which generally are the hottest components of electric aircraft systems. Other components that undergo an increase in temperature during operation are the batteries, motors, and flight computer.

The temperature increase of both the batteries and the flight computer is insignificant to influence the structure supporting these elements. Without adequate cooling, the motors and ESCs could reach higher temperatures. However, the normal operating temperatures stay well below the limits of significance for the materials used in the construction of the model. Therefore, no additional measures are taken. Radio-controlled modelling experience shows, however, that the temperature rise of these components should be moderated to prevent the components themselves from catching fire. The motors will be

mounted in nacelles without any insulation, sitting in free stream outside air, which allows for sufficient heat extraction. The ESCs are mounted inside the wingbox, posing a higher thermal threat. To moderate their temperature, cooling fans are installed on or near the components. Often, cooling systems are included with off-the-shelf ESCs.

Thermal outbursts due to component failure, such as a battery or ESC fire, are not considered in the design.

6.3.3. Crack initiation and propagation

Another relevant aspect in structural design is fracture analysis. Cracks are initiated by cyclic loadings, evolving from microcracks, often referred to as fatigue, in the material. The microcracks weaken the material and may eventually propagate to the point of fracture. Cracks may also be formed due to impact damage, which could remain unnoticed initially, meanwhile weakening the structure and propagating to a more severe extent.

Cracks are more prone to form in stress-concentrated areas, such as sharp corners or around holes and cutouts. The first countermeasure to be taken to limit the formation of cracks is the rounding of sharp components and reinforcing frames around cutouts. Further analysis in a later design stage should determine and assess the necessity of such reinforcements. However, the expectations are that it will be of low relevance, as the structural loads are relatively low and the current design is already multiple factors stronger than required for normal operations. For this reason, it is safe to assume that the loads that are carried around a cut-out, adding up to the normal loads of that section, will still not exceed the stress limits of the material. However, this is valid under the condition that stress-concentrated regions do not have sharp, crack-inducing geometry.

Another factor inducing cracks is fatigue, occurring due to local stresses lower than the ultimate stress being applied cyclically. Being loaded periodically, materials weaken over time, lowering their fracture resistance. This behaviour can be described with the $S-N$ curve. Contrary to civil aircraft, the model will not perform as many missions during its lifespan, making the crack formation due to fatigue less likely. Yet, to determine the full capabilities and limitations of the model, it is valuable to assess the fatigue characteristics of the material.

The $S-N$ curve plots the relative failure stress after a certain number of loading cycles. The rate at which it decreases also depends heavily on the loading magnitude of each cycle. The degradation rate can be described with Basquin's law:

$$S_a^m \cdot N = C \tag{6.8}$$

Here, S_a is the loading magnitude, N the number of cycles to failure, and C and m are material properties.

The model will be constructed mainly from carbon fibre reinforced polymers, or CFRP. Only the fuselage floor, carrying the electronics and payload will be constructed from aluminium. This component, however, is not subject to cyclic loading. The fatigue life of composites are more complicated to analyse and estimate than uniform metals having isentropic material properties. Composite material properties heavily depend on the composition and orientation of the layers. Therefore, composites do not have a universal $S-N$ curve. For this research, published data of tested composite configurations are used. The values for CFRP relevant for the model design are given in table 6.4 below. Important to note is that these values are based on a rewritten form of the Basquin Law: $S = K \cdot N^m$.

Table 6.4: S-N curve properties of Carbon Fibre Reinforced Polymers [2]

Material	Stress ratio	Fatigue Model Parameter K [MPa]	Fatigue Model Parameter m
CFRP	0.80	1048	-0.019
	0.5	1026.8	-0.025
	0.10	1033.8	-0.040

This results in the $S-N$ curve as shown in figure 6.7 to the right. Evident from this curve is that after a thousand cycles, the composites are still able to withstand over 25 MPa. As determined in section 6.2.3, the peak stresses acting on the wingbox components under extreme loading conditions are 33.5$[MPa]$. From the graph can be seen that the material after a million maximum stress load cycles can still withstand over 800$[MPA]$.

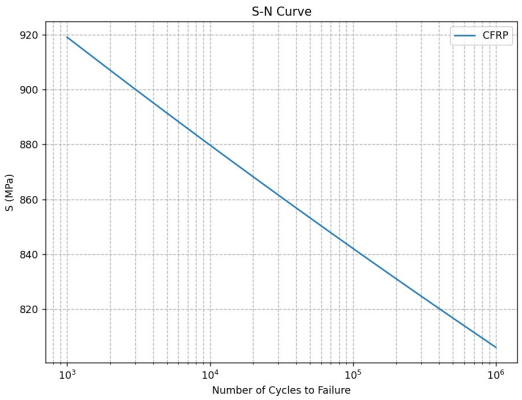

Figure 6.7: S-N curve of CFRP based on values from table 6.4 using stress ratio 0.8

Concluding, fatigue should not impose a risk for the models structural integrity.

If due to impact damage, a crack is formed, its propagation until observation can be determined with the following equations. Here, a crack is estimated to grow from its initial length a_s with N cycles to length a_f. The function $f(R, \Delta K)$ depicts the crack growth rate and is defined in equation 6.10, where R is the ratio of minimum and maximum applied loading $\frac{S_{min}}{S_{max}}$, and ΔK the stress intensity factor. $C, n,$ and α are material and non-dimensional coefficients.

$$N = \int_{a_s}^{a_f} \frac{1}{f(R, \Delta K)} da \tag{6.9}$$

$$\frac{da}{dN} = C \cdot (\Delta K)^n = C \cdot ((S_{max} - S_{min}) \cdot \sqrt{\pi \cdot a} \cdot \alpha)^n \tag{6.10}$$

Combining these equations yields the following expression:

$$N = \frac{1}{C \cdot ((S_{max} - S_{min} \cdot \sqrt{\pi} \cdot \alpha)^n} \cdot \left[\frac{a^{1-\frac{n}{2}}}{1-\frac{n}{2}} \right]_{a_s}^{a_f} \tag{6.11}$$

This relation can be used to assess the number of cycles after which any unnoticed damage becomes a threat to the structural integrity of the model.

6.4. Modular Assembly

Designing the model to be modular introduces several structural challenges. Principal components of the model must be removable without major construction effort or significantly modifying other components. Together with the quick-assembly methodology, the connections must be strong enough to transfer the loads for all loadcases and maintain structural integrity. Designing a sufficiently strong and non-permanent assembly usually comes with the cost of being more expensive and less weight-efficient. This drawback, however, is prioritized lower than the model's modular capabilities.

The assembly points must also be overdesigned with respect to the pure Elysian E9X resemblance. For modular testing, heavier and bigger components may be attached, introducing higher loads to the structure and connections. Therefore, the main design can not be fully optimized for minimum weight. Although modular items do not necessarily require a stronger construction, the wings could also be smaller and lighter than the default. However, to remain suitable for the largest possible selection of modular components, increasing the model's research potential, heavier and higher structural-demanding attachments are considered.
As discussed in section 16.3, the model will be compatible with the following modularity options:

- Interchangeable tail and nose

- Interchangeable wings
- Adjustable motor position and layout
- Screw-in weights

The structural adaptations and assembly designs to accommodate the modularity are discussed in the following sections.

Interchangeable tail and nose
Having a conveniently removable nose or tail offers the opportunity to test different aerodynamic shapes, weights changing the mass moment of intertia, and tail configurations.

The sections are to be connected via 4 extrusions, neatly sliding into slots in the other section. The assembly will be secured with a total of 8 screws, distributed over the 4 connection points. A schematic of the assembly is shown in figure 6.8 below.

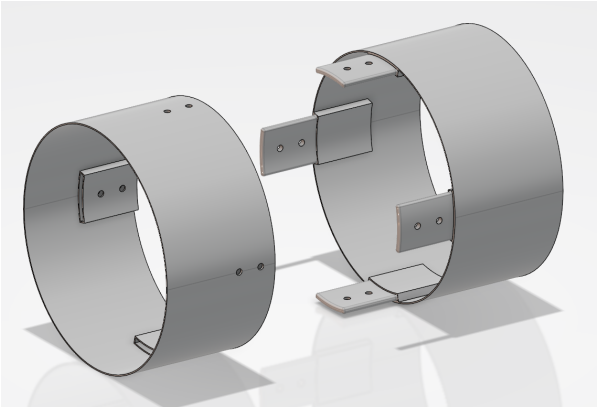

Figure 6.8: Fuselage joint mechanism

The primary loads present in the fuselage are due to bending by its own weight. The peak loads are near the wingbox, loading the bottom half of the fuselage in compression and the top half in tension. The tensional stresses are carried around the roof of the fuselage, which is removable to access the electronics. Furthermore, the model shall be suitable for wind tunnel testing, with the model mounted on the testing rig through the rear of the fuselage.
With the above-mentioned load cases, the front section split only has to carry any additional nose weight. The rear split has to carry and transfer the loads of the entire model when mounted in a wind tunnel. However, in wind tunnel testing, the batteries can be removed to reduce the weight and thereby lower structural loads.
Following the fuselage structural design from section 6.2.4, the fuselage is capable of resisting loads multiple factors higher than those imposed in flight in the default configuration. Therefore, the design can be assumed sufficiently resistant to bear any increased loading due to heavier nose or tail cone. Consequently, no additional structural reinforcements are required to accommodate the modular aspects.

Wing assembly
Arguably, for flight mechanical research purposes, the most relevant adaptation of modularity to the model is the changeability of the wings. Many aspects can be subject of interest, such as a different aerofoil, planform, material, high-lift devices, span, distributed propulsion layout, and many more. For research purposes, the fuselage acts like a hub to fit and test different wings and their respective aerodynamic properties. Consequently, the wing-fuselage joint shall be able to fit different shapes and support the different loads the wing is subjected to.
The fuselage-wing connection is a complex structural piece. It is subjected to the highest loads of the entire aircraft and must support a quick and convenient attachment and detachment method of the wing structure. Due to its complexity, the fuselage structure is designed to remain constant for any wing variant. The design is inspired by those of modern sailplanes. Here, a single spar of one wing slides in

between a split spar of the other wing, fixed in place by two longitudinal titanium pins near both wings' roots. These pins carry the wings' bending moment. This construction slides into a similar-shaped box within the fuselage, introducing only vertical loads into the fuselage construction, which supports only the weight of the fuselage in flight. This design also allows for quick assembly and removal of the wings of the sailplane, as well as variable wingspans or geometry with attachable wing sections further along the span. An example of such a construction is shown in figure 6.9.

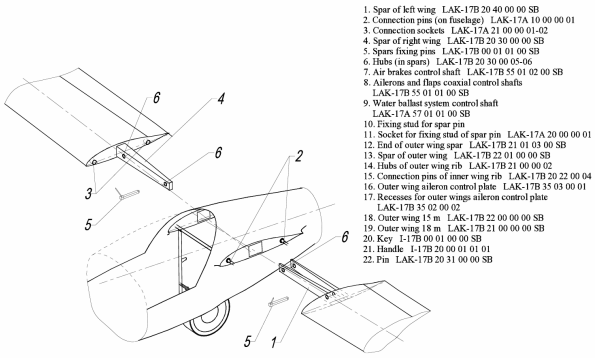

Figure 6.9: Wing-fuselage connection of LAK17 sailplane [34]

Based on this design, the model has a single spar sliding into the split spar of the other wing, fixed with two longitudinal pins situated left and right. A 3D model of the construction and its connection with the fuselage is shown in figures 6.10 and 6.11. The fuselage floor, which will carry the batteries and electronics, will feature a hatch to access and insert the main pins.

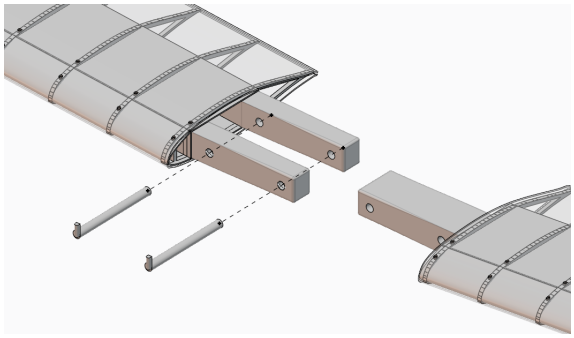

Figure 6.10: Left and right wing connection with main pins

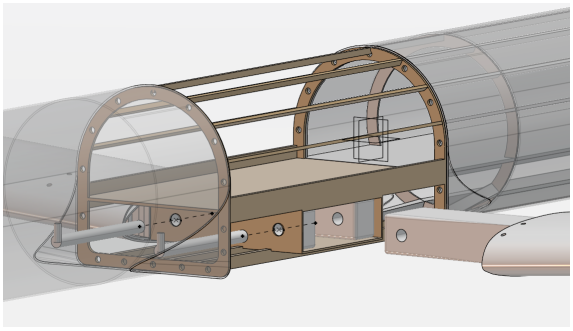

Figure 6.11: Wing to fuselage connection, viewed from left-front

The modularity options of the wings of the model are mainly constrained by the fuselage connectivity. Similar to the sailplanes design, the spars which slide into the fuselage will be considered as default and cannot be changed without severe modifications to the fuselage. Therefore, any modular wings shall incorporate a method to connect these spars to their wingbox. Although having some limitations, the current dimensions allow for a high degree of modular design freedom within similar aircraft scaling factors. Furthermore, to account for possible higher structural loads with different wing aerodynamics and weights, the wing-fuselage structure shall be over-designed with respect to the pure Elysian E9X resemblance. This increases the compatibility with a larger set of modular options.

Engine mounts

One of the main objectives of the project is to investigate the properties and flight mechanical behaviour due to distributed electric propulsion. Therefore, the motors of the model shall be designed so that they can be placed at arbitrary positions. Furthermore, the system must allow for different motor sizes and amounts.

The default design is based on the Elysian E9X, having the propellers situated in front of the leading edge of the wing along the straight, non-tapered section. A 3-view schematic of the nacelle is shown in

figure 6.12. The electric motor is fitted inside the cylindrical section of the nacelle. The aft part follows the curvature of the aerofoil to have a neat fit onto the leading edge of the wing. The length of the nacelle can be individually redesigned if required for adequate propeller spacing, if larger propellers were to be used. The nacelles are mounted to the wing with two vertical bolts.
To provide sufficient structural support for transferring the thrust loads to the wing and the rest of the model, only the ribs are to be used as motor mounting positions. Per rib, two screw holes are present, aligned with those on the motor nacelle. With this construction method, motors can conveniently be attached and removed from the wing with 2 screws. However, the power provision to the electric motors has several complications, limiting the full flexibility of motor positioning. Based on the Elysian E9X, the model has a total of 3 engines per wing. For each electric motor operation an electronic speed controller, ESC, is required. This component will be situated in the wingbox around the same spanwise location as the motor it is operating. The ESC's forward and manipulate the power delivery from the batteries in the fuselage to the motors. This results in 3 sets of cables running from the fuselage through the wingbox to each ESC. From each ESC a set of 3 cables, one for each phase, must be connected to the motor. The wingbox and wingsurface are not designed to incorporate hatches or openings along the entire span of the wing. Therefore, due to limited accessibility after production, the default model will only operate with 3 ESC's with the option to position the motors over 3 positions per ESC. At each motor attachment point, the electric power is fed through a connector mounted in the wingsurface between the screwholes. The current design features 8 attachment points per wing, of which counting from the root attachment point 1 and 2 are powered by ESC 1, 3 to 5 by ESC 2, and 6 to 8 by ESC 3. This philosophy offers some flexibility in motor positioning and number. However, the main limitation is that only one motor can be connected per ESC. Yielding a maximum of three per wing, and no more than one per set of adjacent attachment points. Important to note is that rib number one is not considered as an attachment point, as it is too close to the fuselage. There is no adequate spacing for any geometry to be mounted on the first rib. In conclusion, the current design based on the Elysian E9X supports a maximum of 3 motors per wing, which can be positioned at 3 different span-wise positions each. Modularity-wise, to incorporate more motors and at more unusual positions, for example along the tapered wing section or wingtip, the layout of the wingbox and the electronics within must be restructured. Due to the internal space and accessibility limitations, this will most likely require a new design and construction of the complete wing, which can be assembled to the fuselage as explained in section 6.4.
The possibility of mounting the engines at locations other than the wing, like the fuselage or tail-mounted, is not considered in this design. Such a construction would require a redesign of the fuselage, substantially changing stability properties and the electronic layout. This concept is therefore deemed outside the scope of the current project objective.

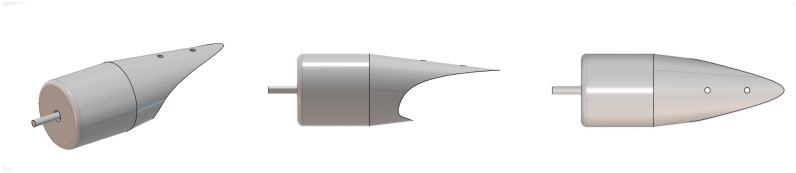

Figure 6.12: Isometric, side, and top view of motor nacelle

The engine nacelles are mounted as illustrated in figure 6.13 below. This configuration resembles the default Elysian E9X layout. Counted from root to tip, motor 1 is connected to rib 3, motor 2 to rib 6, and motor 3 to rib 9. Note that the connectors to feed the electric motors, situated between the screw holes, are not drawn in this figure. Furthermore, as explained before, the attachment point and rib numbering do not fully align.

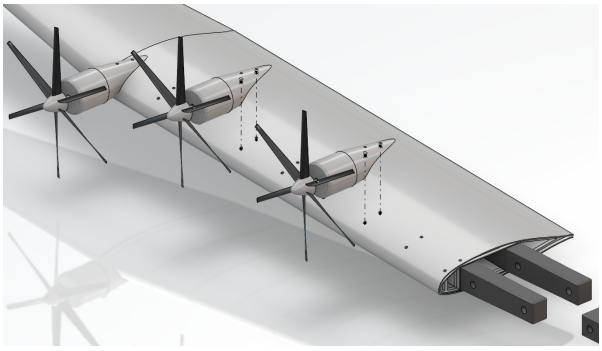

Figure 6.13: Nacelle to wing integration and assembly method

6.4.0.1. Tail assembly

The entire tailcone of the model is designed to be interchangeable, offering opportunities to test different tail configurations and sizes. The default configuration, based on the Elysian E9X, is a standard T-Tail layout. The entire tailcone can be attached and removed as described in section 6.4. Additionally, the empennage itself can be separated from the tailcone, as shown in figure 6.14. The vertical fin root and profile are embedded in the tailcone structure. Therefore, the flexibility to interchange the fin is limited. Modularity-wise, the focus is on switching out the entire tailcone instead.

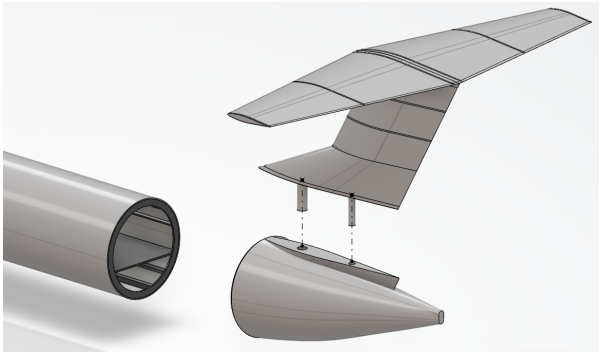

Figure 6.14: Tailcone and empennage assembly, viewed from left-aft

6.5. Verification & Validation

All calculations made regarding the structural aspects have been made in Microsoft Excel using formula's both from TU Delft courses as well as formulas found in published reports. The verification and validation of this process will follow the outlines given in the previous report [20].

6.5.1. Verification

The verification of the structural calculations is performed using three independent procedures: Unit control, independent recalculation, and sensitivity checks. Each verification method addresses a different potential source of error in the calculation process. When all three procedures yield consistent and plausible results, the calculations are considered verified. One of the advantages of using spreadsheet-based tools, in this case Excel, is that the software itself provides warnings for certain consistency and computational errors, which further supports the verification process.

6.5.1.0.1 Unit Control The first step in unit control is the verification of the dimensional consistency of all calculations. This involves checking whether the units resulting from each calculation are consistent with the physical quantity being evaluated. This verification is performed manually by checking the units after each equation. Closely related to this step is ensuring that all inputs and intermediate values are expressed in consistent magnitudes, for example the difference between m and mm or MPa and GPa.

Another critical aspect of unit control is the consistent application of the set sign convention, which is a common pitfall in such calculations. The coordinate system and sign conventions used are clearly defined in Figure 6.4, and the spreadsheet was systematically reviewed to confirm that these conventions were consistent across all calculations.

6.5.1.0.2 Recalculation After the iterative sizing process of the structural components, such as the wingbox and fuselage, within the spreadsheet, the same calculations were redone independently by hand using the same analytical formulation. The consistency between the manually obtained results and the spreadsheet output confirms that the spreadsheet formulas were implemented correctly without any computational errors.

6.5.1.0.3 Sensitivity Checks The final verification step consists of sensitivity checks aimed at identifying numerical or logical inconsistencies within the spreadsheet. These checks involve applying limiting input values to the calculations and assessing whether the resulting outputs remain meaningful. For example, setting the applied loads to zero correctly results in zero stress. In addition, the spreadsheet was examined for the occurrence of impossible intermediate values, such as negative thickness or negative stiffness values. No such inconsistencies were observed, providing confidence in the robustness of the calculations.

6.5.2. Validation

The validation of the structural calculations is, similarly to the verification, performed trough multiple steps. Which, when combined provide confidence in that the applied methods and resulting conclusions are realistic results for the structural properties of the SFD. The validation consists of assessing the validity of the formulas used, followed by an evaluation of the results against physical reasoning and expected behaviour.

6.5.2.0.1 Formula Validation The majority of the formulas used in the structural calculations come from multiple courses at the Aerospace Faculty of TU Delft. In addition, several well-established sources were used to complete the calculations and cross-check used formulas. Some of the sources used include the textbook *Aircraft Structures for Engineering Students* by T.H.G. Megson [39] and the publication *Buckling of Thin-Walled Cylinders* by M.W. Hilburger et al. [28].

While each of these sources provide specific stand-alone formulas, most of the equations used in the analysis performed can be found in multiple independent references. This redundancy provides confidence in the validity of the formulas used in the structural sizing process.

6.5.2.0.2 Realism Comparison To further validate the results of the calculations, the obtained stress distributions, shear flows, and load paths were evaluated against engineering intuition developed trough the years at the Aerospace Faculty. The directions and relative magnitudes of the stresses and shear flows were found to be consistent with the expected structural behaviour.

Additionally, small changes were applied to each input parameter, after which the resulting changes in both temporary values and final values were analysed. These changes showed logical outputs, such as increase structural thickness leading to reduced stresses and higher moments of inertia. And when the loads were slightly reduced, the stresses lowered as well. This form of validation was conducted for all major input categories, including loads, geometric dimensions and material properties.

The final outcome of the structural analysis shows that, in its current configuration, the structural parts of the SFD are most likely to fail due to buckling when its envelope is pushed over its limits. As described in sources used, this is the likely failure mode of such thin walled structures [39] [28]. The observation therefore supports and validates the conclusions draw in in section 6.2.

To validate the calculation within the wingbox and the produced shear flows and stresses their directions are compared by the intuitive engineering knowledge the team has gained over the years of studying aerospace engineering, and was deemed logical. Secondly, small changes to the separate inputs were made and the results were analysed. This showed logical behaviour, such as, increase in thickness to

lower stress and higher moments of inertia, lower loads to lower stresses. This validation method was performed for all input variables: Loads, dimensions and material properties.

The final outcome of the structural analysis is that all of the structures will likely, in its current design, fail due to buckling when the SFD is pushed over its edge. As described in Aircraft Structures for Engineering Students, for thin skin structures, this is indeed what is supposed to happen. Thereby validating the conclusions drawn in section 6.2.

6.6. Sensitivity Study

Changes in the design parameters may have a significant impact on the overall structural behaviour of the SFD, and in the most extreme cases, could drive the design beyond the boundaries set by the system requirements. It is therefore essential to perform a sensitivity study on the structural design to assess the robustness of the SFD and to bring the influence of potential variations in scope. This section discusses the sensitivity of the structural design with respect to several dominant parameters that were identified during the design phase of the SFD.

6.6.0.0.1 Load Cases Variations in the applied loads have a direct effect on the structural requirements of the SFD. The current design is based on a maximum operational load factor of 2.5, increased by a safety factor of 1.5, resulting in a design load factor of 3.75. In the event that the aerodynamic loads on the aircraft were to increase, the required structural thicknesses would also have to increase accordingly. For example, a load increase of 30% would drive the required skin thickness up by slightly less than $\sqrt{1.3}$, it being slightly lower than that due an increase in mass moment of inertia which lowers the required skin thickness.

As long as the loads do not increase by more than 50%, the resulting stresses in the wing and fuselage remain within the available safety margins. Conversely, a reduction in the applied loads would result in an over-engineered structure. In the case of the SFD, this has a very limited impact on overall performance since the SFD requires ballast masses to achieve similitude to the Elysian-E9X.

6.6.0.0.2 Material Variations The structural design of the SFD is directly affected by the performance of the materials used. If, for instance, the Youngs Modulus of a material were be lower than the value used in calculations, buckling failure of sections would show earlier. In the design, the only load-carrying material is CFRP, as the aluminium mounting sheet is not subject to structural performance requirements. The current design assumes CFRP laminates with fibres oriented bi-directionally, providing high stiffness and strength in both directions. However, the structural loading is not uniformly distributed across all axes.

As a result, the design has plenty of room for improved structural efficiency by layering the fibre orientations to better align with the dominant load paths. While such tailored layups would increase manufacturing complexity and production cost due to the higher precision required, they would allow the SFD to remain within the current structural and performance limits set by the requirements. Additionally, given that the material data used in this study is several years old, and advances in CFRP performance have already been made and will continue to do so, could further show potential to compensate for potential reductions in material strength.

A more extreme variation would be the complete exclusion from CFRP from the design, for instance due to manufacturing constraints or sustainability considerations. As discussed previously in subsubsection 6.2.3.2, the buckling behaviour of aluminium and CFRP sheets is comparable, but the aluminium alloy 7075-T7451 would increase each structural components weight by a factor of 1.77. This would raise the total mass of the structural elements to 69.6 kg, leaving roughly 10 kg available to achieve similitude. Although correction weights, each weighing 23.17 kg in the baseline configuration, would still be required to achieve similitude, their mass and exact spanwise location would be altered due to the heavier aluminium wings. Consequently, a switch to aluminium would not fundamentally compromise the baseline SFD design. However, for modular configurations where such correction weights are not required, the overall performance and flexibility of the SFD would drastically decrease.

6.6.0.0.3 Buckling Knockdown Factors The buckling analysis of the cylindrical structures within the SFD relies on the use of a knockdown factor, as shown in Equation 6.5. This factor has a direct influence on the predicted buckling stress, and consequently, on the required skin thicknesses of all circular components. The value adopted in this study is intentionally very conservative. However, it is still very depended on this value.

Should the actual applicable knockdown factor be lower than assumed, the required skin thickness would increase proportionally. For example a reduction of the knockdown factor by a factor of two would result in a doubling of the required skin thickness. This would have a substantial impact on the mass budget, reducing the available margin for ballast weights use to achieve similitude. This effect however, is less critical than for a change to an aluminium structure. This is because the buckling knockdown factor for flat panels contains a lot more certainty, therefore a change in the thickness of the fuselage is more likely to occur than in the wing structure. However, in extreme changes in both the flat plate and cylindrical knockdown factors, the required location for ballast weights could be in the tapered wing section. This would severely limit the modularity aspect of the design since weights in this section of the wing are impossible to remove.

6.6.0.0.4 Component Mass Variations in component masses have more or less been addressed in earlier sections of this sensitivity analysis. Due to the presence of correction weights and their, although limited, adjustability in both mass and position, changes in the mass of individual avionics components have only a minor influence on the structural behaviour of the SFD. As a result, variations in component mass is not considered a critical sensitivity driver for the design.

6.6.0.0.5 Modularity Changes Modularity constitutes one of the defining characteristics of the SFD and has therefore been a key consideration throughout the design process. Nevertheless, this modularity is also subject to certain structural limitations. The fuselage, which is one of the few constants in the modular design, is designed for a maximum load factor of 3.75. Therefore, a modular wing configuration producing more than twice the lift of the baseline wing would exceed this limit, leading to fuselage buckling. Although the detailed design of the modular attachments lies outside the scope of this report, this section highlights the necessity for all modular configurations to remain within the established design envelope.

6.7. Compliance To Requirements

In this section, the compliance of the structural requirements is shown in Table 6.5. An important note is that due to buckling being the primary failure mode, some requirements regarding maximum deflection have become irrelevant, although they are left in the compliance matrix for completeness.

Table 6.5: Requirement compliance matrix for the structural requirements

ID	Requirement Description	Verification Method	Compliance Level
SFD-SYS-STR-01	The total structural mass shall not exceed 75 kg.	Analysis	The total structural weight of the SFD is 54.29 kg.
SFD-SYS-STR-02	~~The aircraft centre of gravity shall be adjustable by +/-% MAC via battery placement.~~		The centre of gravity is adjustable by ballast weights.
SFD-SYS-STR-03	The structure shall withstand loads under ultimate loading conditions without failure.	Analysis	Calculations show the structure will not fail under a loading factor up to 3.75
SFD-SYS-STR-04	The structure shall be free from flutter up to an airspeed of 60 m/s ($1.2V_{dive}$).	Analysis	The flutter speed of the main wing is 120 m/s
SFD-SYS-STR-05	The structure shall withstand vibrational loads across the full operational flight envelope for all frequencies from 0 Hz up to 100 Hz.	Testing	Vibrational test shall be performed before flight.

SFD-SYS-STR-06	The structure shall sustain a landing impact of 2 g's without plastic deformation	Analysis	A loading factor of -2 is not enough to plastically deform the structure.
SFD-SYS-STR-07	The structure shall not fail due to fatigue, creep, or fracture during sustained operations for at least 20 missions of 20 minutes.	Analysis	Fatigue, creep and fracture were found to not be the cause of failure when pushed past the SFD's envelope.
SFD-SYS-STR-08	After completing 20 operational missions, the structure shall retain at least 99% of its original load-carrying capability.	Analysis	Fatigue in the structure only occurs after 10^5 cycles.
SFD-SYS-ENV-01	The structure shall operate without degradation in temperatures between 0° and 30°	Analysis	Thermal stresses are insignificant relative to loading stresses.
SFD-SYS-ENV-02	The structure shall maintain watertight and dust tight integrity up from an IP65 rating.	Testing	Water- and dust-tightness must be verified during pre-flight testing.
SFD-SYS-ENV-03	The structure shall withstand debris impact of 1 cm^3 10 g at 50m/s relative speed.	Testing	The impact resistance of the structures must be verified during pre-flight testing.
SFD-SYS-ENV-04	The structure shall house and provide access to the avionics, batteries, and additional payloads via hatches with minimal aerodynamic interference.	Demonstration	The removal of the top fairing indicates the possibility for access to these parts.
SFD-SYS-ENV-05	The electrical systems shall not be interrupted or degraded by Electromagnetic Interference generated by the motors or external sources.	Testing	Although electromagnetic interference is expected to be minimal, it will be tested pre-flight.
SFD-SYS-STR-LAN-XX	Landing gear requirements	Outsourced	All landing gear requirements will be pushed to an external company which will have to design and verify the landing gear
SFD-SYS-STR-FUS-01	The fuselage internal volume shall accommodate the FDCMS box dimensions defined in SYS-PER-01	Inspection	The fuselage can house this system.
SFD-SYS-STR-FUS-02	The fuselage skin shall incorporate access hatches for battery swapping and avionics maintenance	Demonstration	The fuselage has a top fairing, which can be seen as one large hatch.
SFD-SYS-STR-FUS-03	Under ultimate loading conditions, the fuselage shall not deflect more than TBD mm vertically or horizontally.	Analysis	Deflection due to stresses was found to not be the likely failure mode for the fuselage
hline **SFD-SYS-STR-FUS-04**	Under ultimate loading conditions, the fuselage shall not twist more than TBD degrees.	Analysis	Twisting due to stresses was found to not be the likely failure mode for the fuselage.
SFD-SYS-STR-FUS-05	The fuselage shall incorporate attachment points for modular wing and empennage configurations	Demonstration	Modular attachment points have been modelled.
SFD-SYS-STR-FUS-06	The fuselage shall house the avionics, additional payloads and the from landing gear	Inspection	The avionics, payload and landing gear fit within the fuselage.
SFD-SYS-STR-WNG-02	The wings shall be detachable from the fuselage to facilitate transport and storage	Demonstration	Wings are modular and detachable.

SFD-SYS-STR-WNG-03	Under ultimate loading conditions, the wing shall not deflect more than TBD mm vertically or horizontally.	Analysis	Deflection due to stresses was found to not be the likely failure mode for the wing
SFD-SYS-STR-WNG-04	Under ultimate loading conditions, the wing shall not twist more than TBD degrees	Analysis	Twisting due to stresses was found to not be the likely failure mode for the wing
SFD-SYS-STR-WNG-05	The wing structure shall contain attachment points for modular wing-tips.	Demonstration	The wing-tips can be removed.
SFD-SYS-STR-WNG-06	The wing structure shall contain attachment points for modular engines.	Demonstration	The engines can be placed at 8 locations per half-wing.
SFD-SYS-STR-WNG-07	~~The wing structure shall house the batteries and rear landing gear~~		The batteries and landing gear are housed in the fuselage and below-wing fairing respectively.
SFD-SYS-STR-WNG-08	The wing structure shall incorporate high-lift devices sized to achieve the $C_{L_{max,TO}}$ and $C_{L_{max,L}}$ targets defined in SYS-PER-14 and SYS-PER-15.	Demonstration	High lift devices can show functionality.
SFD-SYS-STR-EMP-02	The vertical stabilizer stiffness shall be sufficient to prevent flutter up to 60 m/s.	Analysis	Flutter is insignificant for such a short wing.
SFD-SYS-STR-EMP-03	Under ultimate loading conditions, the horizontal stabilizer shall not deflect more than TBD mm vertically and horizontally or twist more than TBD degrees.	Analysis	Bending and twisting due to stresses were found to not be the likely failure mode for the vertical stabilizer.
SFD-SYS-STR-EMP-04	Under ultimate loading conditions, the vertical stabilizer shall not deflect more than TBD mm vertically and horizontally or twist more than TBD degrees.	Analysis	Bending and twisting due to stresses were found to not be the likely failure mode for the vertical stabilizer.

7
Powertrain

To make sure the aircraft is capable of performing powered flight, it is important to properly design the system responsible for converting the electric energy into kinetic energy. This chapter therefore explains the design of the powertrain. It starts in section 7.1 with the design of the propeller and the calculations behind it. Then section 7.2 displays the design of the electronic systems inside the aircraft. From batteries, to the motors and avionics; the choice of components, as well as their implementation into the system is explained here. Supported in section 7.3 with a diagram showing the internal communication between these components, and an explanation of the software that will drive them in section 7.4. Lastly, the full design is summarized in section 7.5 with visual support of a Hardware Diagram. This final design is proven to be compliant with subsystem requirements in section 7.6.

7.1. Propeller

The propellers of the SFD form a critical part of the propulsion system; they are responsible for the thrust of the demonstrator. Essentially, the engine power is converted into thrust for the SFD. The design of the propeller starts by analysing the TUD-XPROP in subsection 7.1.1. Consequently, subsection 7.1.2 explains the advance ratio and evaluates the influence of the pitch setting on the efficiency of a propeller.

In subsection 7.1.3, the optimal pitch setting for cruise is determined, whereafter it is confirmed that this pitch setting is also suitable for take-off. Finally, subsection 7.1.4 showcases the design of a propeller blade with figures generated by *javaProp*.

7.1.1. Propeller Design

The main limitation of the SFD propellers is their diameter. The wing shall fit 3 on either side, following the latest developments of the Elysian E9X [71]. Furthermore, the aerodynamic properties of the propellers, such as advance ratio J, influence the aircraft aerodynamics and stability characteristics. Designing an optimal propeller for the SFD, which provides sufficient thrust and while also meeting the research and testing purposes, is outside the scope of this project. Therefore, as a preliminary design choice, the characteristics of the TUD-XPROP have been selected as the starting point for the design of the propeller. The propeller concerned is the TUD-XPROP, developed by TU Delft. Moreover, a lot of performance and testing data is publicly available, which is of great importance to evaluate the aerodynamic and stability influences on the aircraft. The TUD-XPROP is displayed on a test rig in Figure 7.1 below.

Figure 7.1: TUD-XPROP propeller that is used in the initial design [4]

7.1.2. Propeller Dynamics

The propeller has an advance ratio (J), which can be computed using Equation 7.1, where the rounds per second (RPS) is given by n, and the diameter of the propeller is given by D [58]. The TUD-XPROP is a 6-bladed propeller constructed from carbon fibre reinforced polymer, and has a diameter of 0.4064 [m] [4]. Since the diameter is set for the chosen propeller, the advance ratio (J) is dependent on the free-stream velocity (V_∞) and rounds per second (n). Consequently, the advance ratio (J) is proportional to the axial velocity (V_{ax}) divided by the rotational velocity (V_{rot}). By taking the inverse tangent of $\frac{V_{ax}}{V_{rot}}$ angle ϕ is obtained, as displayed in Figure 7.2. In conclusion, the angle of attack (α) is inversely proportional to the advance ratio (J), see Equation 7.2 [58].

$$J = \frac{V_\infty}{nD} \propto \frac{V_{ax}}{V_{rot}} \rightarrow \phi = tan^{-1}\left(\frac{V_{ax}}{V_{rot}}\right) \propto J \quad (7.1)$$

$$\alpha = \beta - \phi \propto -J \quad (7.2)$$

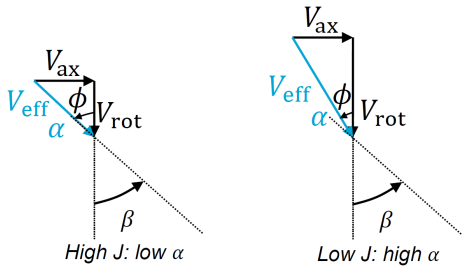

Figure 7.2: Relation between advance ratio (J) and angle of attack (α) [58]

The TUD-XPROP is a propeller whose pitch angle (β) can be adjusted, not in-flight but when stationary on the ground. The pitch setting can be adjusted in a way that optimises the propeller for efficiency. The propeller should be most efficient at cruise speed, as this is the speed at which the SFD will mainly fly. However, the demonstrator also needs to take-off properly, a mission phase that ideally would need a much smaller pitch setting than cruise. The pitch setting cannot be adjusted during flight, which means some middle ground should be found for which take-off works, and cruise is efficient as well. By increasing the pitch setting, the thrust coefficient over the advance ratio curve shifts upwards and to the right, as can be seen in Figure 7.3a. The efficiency of the propeller (η) can be calculated using Equation 7.3 [58]. Figure 7.3b can be explained by this equation; an increased thrust coefficient (C_T) and an increased advance ratio (J) result in a higher efficiency (η).

$$\eta = J\frac{C_T}{C_P} = f(J, \beta_{ref}, M_\infty, Re_D, \sigma, N_B),\ C_T = \frac{T}{\rho n^2 D^4},\ C_P = \frac{P}{\rho n^3 D^5} \tag{7.3}$$

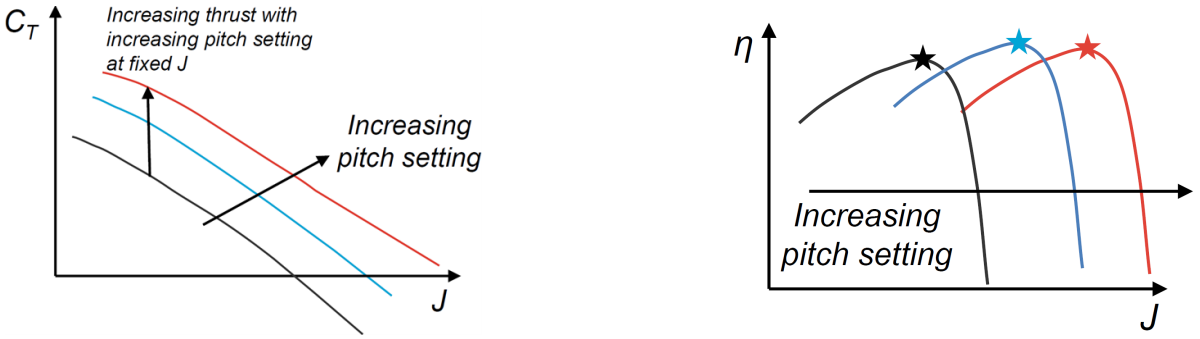

(a) Thrust Coefficient (C_T) against Advance Ratio (J)

(b) Efficiency (η) against Advance Ratio (J)

Figure 7.3: Effects of increasing pitch setting on Thrust Coefficient (C_T) and Efficiency (η) [58]

7.1.3. Propeller Pitch

7.1.3.1. Cruise Conditions

The SFD-2 will primarily fly in cruise conditions, which are listed in Table 7.1. The characteristics of the TUDELFT XPROP ($N_B = 6$, $D = 0.4064$ [m]) have been used to simulate the propeller in $javaProp$ together with the cruise conditions. From the propeller characteristics and cruise conditions, $javaProp$ designs a propeller with certain dimensions and a pitch setting (β). The results are in Figure 7.4 showing the propeller efficiency (η) and pitch setting (β) against RPM. The drag coefficient ($C_{D_{Flow5}} = 0.0428374$) is the value found for the cruise angle of attack; $\alpha = 2.81$ [°]. Although $Flow5$ has enabled us to model the essential aerodynamics for our demonstrator, the program has certain limitations. The drag estimations of $Flow5$ are usually lower than real-life simulations show [26]. To be conservative, it was decided to apply a safety factor of $b = 1.5$ to the drag coefficient $C_{D_{Flow5}}$; in doing so, the drag will be overestimated rather than underestimated.

Table 7.1: Cruise Conditions

Parameter	Value	Unit
V_c	43.8	m/s
h_c	800	m
S	1.997	m^2
α	2.81	°
b	1.5	-
$C_{D_{Flow5}}$	0.0428374	-
$b * C_{D_{Flow5}} = C_D$	0.0642561	-

Table 7.2: Results of analysis with javaPROP during cruise

Parameter	Value	Unit
T_c	139.73	N
T_{prop}	23.29	N
η_c	73.2	%
β	36.5	°
Q_{prop}	2.96	Nm
P_{prop}	1.39	kW

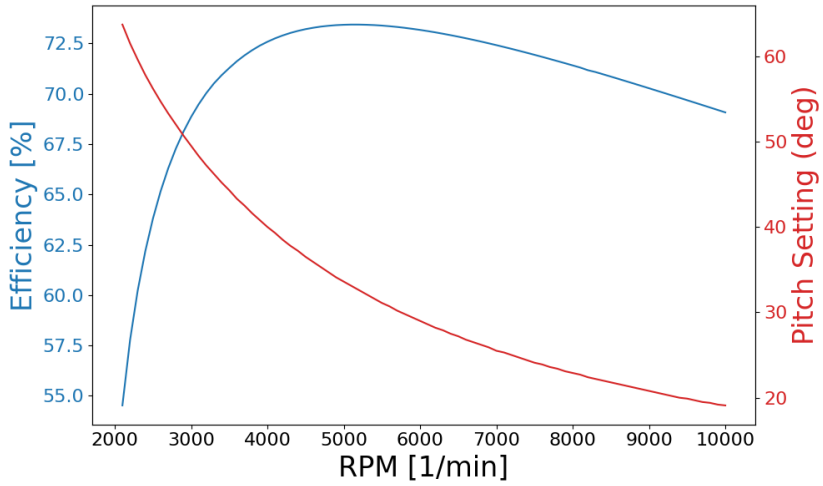

Figure 7.4: Efficiency (η) and Pitch Setting (β) of one propeller for Thrust (T_{prop}) against RPM during Cruise Conditions

The graph shows a maximum for $RPM = 5100$ [1/min], the efficiency of the propeller is then $\eta = 73.432$ [%]. The demonstrator will thus fly most efficiently at this RPM; however, the motor used only goes up to slightly over 6000 RPM. The cruise conditions require a much lower amount of thrust than during take-off. In order for the demonstrator to have a sufficient range of RPM left above the cruise RPM for take-off thrust, a lower RPM at cruise conditions is chosen where the efficiency is still adequate. For cruise a $RPM = 4500$ [1/min] is chosen where the efficiency is $\eta_c = 73.2$ [%] and the pitch setting is $\beta = 36.5$ [°], as can be seen in Figure 7.4. The pitch setting is taken at $r/R = 0.75$; the spanwise location at 75% along the blade. The power one propeller requires to generate the required thrust for cruise conditions is equal to $P_{prop} = 1.39$ [kW], and the torque will be equal to $Q_{prop} = 2.96$ [Nm].

7.1.3.2. Take-Off Conditions

The SFD will require more thrust during take-off, the pitch setting will remain the same, therefore, the RPM's are increased during take-off to reach the required thrust. As a drawback, the propeller will be less efficient during take-off, since this mission phase is much shorter than cruise, the additional energy usage is acceptable. The average efficiency of the propeller up to take-off velocity $V_{LOF} = 26.256$ [m/s] can be estimated by using the data points of Figure 7.5, which are taken from $javaProp$, and is equal to $\eta_{TO} = 37.5$ [%]. Consequently, this efficiency could be used to estimate energy usage for take-off, which is important for the battery sizing (see subsection 7.2.1). The take-off requires significantly more thrust than the demonstrator requires during cruise. The runway at NLR Marknesse has a length of $l = 325$ [m]. It was decided that the SFD-2 should be able to take-off in $s = 275$ [m]. To reach the take-off velocity within this distance, a minimum thrust of $T_{LOF} = 188.01$ [N] should be produced, which means every propeller should be able to generate $T_{LOF_{prop}} = 31.335$ [N] of thrust. If this value is compared to the thrust curve at full power in Figure 7.5, it is clear that the propeller can produce sufficient thrust for take-off conditions.

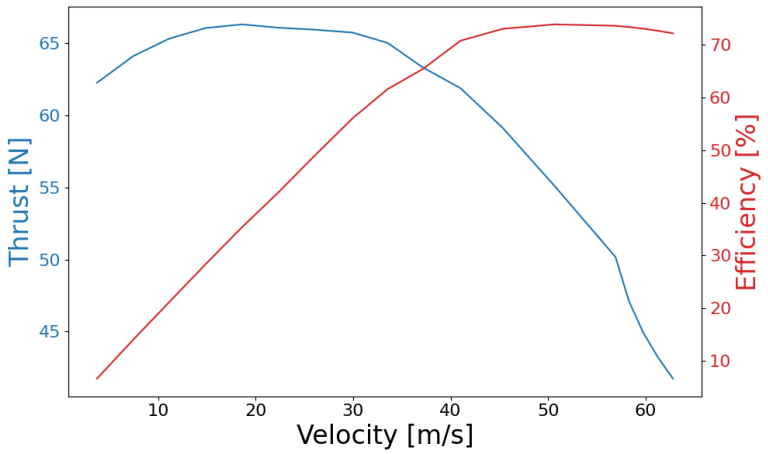

Figure 7.5: Thrust (T) and Efficiency (η) against Velocity (V) of one propeller for full Power ($P = 3.5$ [kW])

7.1.4. Blade Design

As mentioned earlier, the characteristics of the TUD XPROP were taken as the starting point for the propeller design. Consequently, an optimal propeller design was constructed for cruise conditions, which is also favourable for take-off. The blade is made using $javaProp$, a front view of a blade is displayed in Figure 7.6a, and a side view is shown in Figure 7.6b.

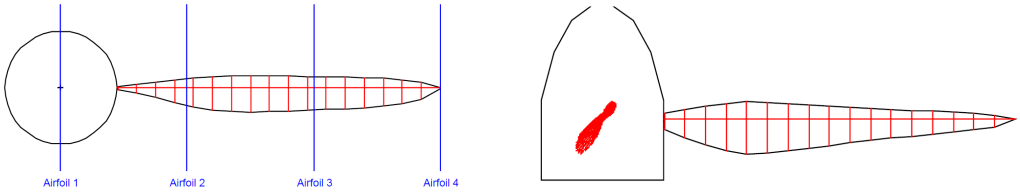

(a) Front View of the blade design made using $javaProp$

(b) Side View of the blade design made using $javaProp$

Figure 7.6: Drawings of the propeller blade design

7.2. Electronics

When designing the electrical systems of the aircraft, there is a multitude of factors to take into account. While having enough energy to complete all mission phases is a very important aspect, there is also the aspect of electrical safety. In this section the important factors are explained before showing the final design.

7.2.1. Energy

In the Midterm Report[20], a trade-off study was also performed to find the type of battery that will be used in the aircraft. Here, the choice was made to opt for a set of LiPo batteries. More specifically, the Tattu Pro Smart battery pack. This battery pack is the same one that was used in the DEP-SFD-D08, which also makes it a proven option in this field of use. At the moment of development, it is still a very competitive option on the market, also equipped with tools like a smart BMS, as well as CAN communication [1], which makes it fit very well into the ecosystem of the aircraft. One battery, however is not enough to supply the full mission energy. Therefore, the amount of batteries should be calculated.

Of course the main design parameter for the electrical system is to make sure enough energy is stored to perform a full mission. To make sure this is fulfilled, a set of calculations can be performed on the energy used in different stages of the mission. This, in turn can be used to size the battery system. These

[1] https://genstattu.com/tattu-pro-22000mah-51-8v-25c-14s-1p-lipo-smart-battery-pack-with-as150u-f-plug/ , accessed on 19/01/2026

calculations have already been touched upon in the Midterm Report [20], but will be summarised again quickly in the following part.

First of all, as energy is defined as $E = P * t$, the power P should be determined. Then, the total time of the different phases should be calculated. To calculate the power per mission phase, the following formulas are used.

$$C_l = \frac{2W}{\rho V^2 S} \quad (7.4) \qquad P * \eta_{motor} * \eta_{prop} = T * V = D * V = \frac{1}{2}\rho V^3 S C_d \quad (7.5)$$

Then, the time per mission phase should be determined. For cruise, this is set to 20 minutes per requirement (here a buffer of 10% is taken to allow for landing). For climb the mission time is calculated to be ~ 100 [s] using Equation 7.6 and Equation 7.7. Here ROC denotes the steady rate of climb, P_a is the available power, determined in subsubsection 7.1.3.2. $D\&V$ denote the drag and velocity respectively, and W_{total} is the total weight of the model. Lastly h_{cruise} displays the chosen cruise altitude, and t is the time taken.

$$ROC = \frac{P_a - D_{climb} * V_{climb}}{W_{total}} \quad (7.6) \qquad t_{climb} = \frac{h_{cruise}}{ROC} \quad (7.7)$$

Then, the energy used by all electronic systems but the propulsion should be estimated. This is done by estimating the total time for these systems to be turned on ($t_{total} = t_{taxi} + t_{climb} + t_{cruise} + t_{ground}$, with t_{ground} denoting the total time for ground operations), which amounts to 35 minutes. The power per component is taken from their datasheets, as can be seen in Table 7.3 (for the control actuators, an average consumption is taken to be 10% of their maximum, as they are never moving at full speed full torque, and most of the time most actuators are not in use) When performing these calculations, for this current stage of the design process, a buffer should be taken to account for possible design alterations, as well as assumptions taken and uncertainties. For this stage, a buffer of 20% was chosen. Performing all these calculations shows a need for energy storage of 5.6 [kWh]. To provide this amount of energy, 5 batteries are needed, that will be placed in parallel to provide this energy without increasing the storage voltage.

Next to the main battery system, a backup system is also in place. This system is comprised of 3 Gens ace Battery packs in series, supplying 22.2 [V], with a storage space of 8.9 [Wh]. Using the same calculation as before, this is enough to supply all LV components with power for 5 minutes, in case the main battery system fails. This means the pilot can then safely make an emergency landing (e.g. in a nearby field).

Lastly, the batteries need to be charged as well. For this, a set of 2 Tattu Dual-Channel Smart Chargers was chosen. These chargers are recommended by the battery manufacturer and have all the communication that is used to safely charge the batteries. They can charge two batteries at a time, with a maximum output power of 60 [A], making for a turnaround time of less than 1.5 hours. This time can be reduced by adding an extra charger, but this is an option left to the customers discretion (if the operator deems it possible to have a longer time in between flights, they could also opt for the purchase of only one charger).

7.2.2. Safety

For designing the system, it is very important to take electrical safety into account. As was seen with the DEP-SFD-D08, it can have serious consequences if this is not done properly [17]. However, things can also be learned from these previous exercises with regard to what to keep in mind.

One of these things is to use a bit higher voltage, with the goal of reducing current flow through the system, as this can reduce heat production [17]. This project also showed that the proper use of fuses can support the technical safety, so for the design of SFD, double redundancy is guaranteed by the use of fuses in the power delivery. This is done using a fuse per battery, as well as on the supply voltage to the motors.

A choice was made to also include a killswitch/battery isolator on the system. On the ground wire, a mechanical switch is inserted that can be pressed to immediately break connection, removing the possibility for any current to flow. This way it is guaranteed that the operator can always stop the system in case of an emergency.

7.2.3. Electronic Components

All electronic components used in the aircraft, are displayed in Table 7.3. It displays the properties that have been used for the design (e.g. cost for the cost breakdown, and power consumption to determine the battery sizing). A number of components will be directly hooked up to the FCMS, instead of using their own power supply. These have been denoted with *FCMS*. Also, the ESC's and Buck Converters have the power consumption noted as -. This is because they don't consume any power themselves, but rather just convert power for other components to use. Lastly, the weight for the charger can be ignored, as this will not be taken along during flight. [2] [3] [4] [5] [6] [7] [8] [9] [10] [11] [12] [13] [14] [15]

7.2.3.1. FCMS

One of the main goals of the SFD, is to gather data on the in-flight behaviour of the E9X. This means that it is important to adequately collect data on this. This is where the Flight Control & Measurement System (FCMS) comes in. For this system, a couple of requirements were set up (as can also be seen in Table 7.4). Based on these requirements, a trade-off study was performed (for more details, the reader is referred to the Midterm Report [20]), leading to the following combination of components: the Embention Veronte 1X, Hensoldt LCR-100 and Simtec ADP-55. Here, the Embention Veronte is chosen as a flight computer, mainly because its option to use custom software makes it very well integrable into the SFD. This, together with its attractive pricing, led to this design choice. The combination of the LCR-100 and ADP-55 was chosen as the data acquisition system, because of reliability reasons. The combination of devices was found to be the most reliable option considered, which was an important metric, as collecting data is the main goal of the mission. This together with its simplicity (this was the only combination that did not need extra components) led to the final decision.

7.2.3.2. Camera System

An important requirement for the SFD is that it needs to be flown beyond visual line-of-sight (BVLOS). This means that a system should be in place to control the model in such situations. For this, an FPV camera system was chosen. Namely, the Walksnail Avatar Avatar GT. This system, together with the HD Pro camera is marked as the camera system with the highest range, with some sources even suggesting a range of over 50 [km] (albeit in optimal conditions).[16] This is found important, as the aircraft should have a mission time of 20 minutes, and has a cruise speed of 44 [m/s], leading to a possibility of flying 25 [km] before the need arises to return.

7.2.3.3. Motor System

Lastly, a motor system had to be chosen, or more specifically, a motor and ESC. Here, a number of variables had to be considered, ruling out almost every option, except the final choice. Firstly, the system needed to be compatible with the batteries. With the battery system consisting of 14 LiPo cells in series (14S), this rules out a lot of motor systems, as most of them were designed for systems up to 12S. Secondly, the right amount of power and RPM had to be available. Looking at the propeller calculations in section 7.1, these were found at 6000 [RPM] and 4 [kW]. This left the option to opt for the U12 Efficiency KV120, together with the FLAME 100A 14S ESC. This combination of components was

[2] https://droneshop.nl/walksnail-avatar-gt-kit , accessed on 15/01/2026

[3] https://www.embention.com/veronte-ecosystem/autopilots/1x-sensor-redundancy/ , accessed on 15/01/2026

[4] https://www.aeroexpo.online/prod/hensoldt/product-187125-63303.html , accessed on 15/01/2026

[5] https://poynting.tech/nl/antennas/2x-puck-2-v2/ , accessed on 15/01/2026

[6] https://www.swiss-airdata.com/products/air-data-systems/adp-55 , accessed on 15/01/2026

[7] https://store.tmotor.com/product/flame-100a-14s-esc.html , accessed on 15/01/2026

[8] https://store.tmotor.com/product/u12-v2-kv120-u-efficiency.html , accessed on 15/01/2026

[9] https://genstattu.com/tattu-pro-22000mah-51-8v-25c-14s-1p-lipo-smart-battery-pack-with-as150u-f-plug/ , accessed on 15/01/2026

[10] https://genstattu.com/gens-ace-400mah-7-4v-60c-2s1p-lipo-battery-pack-with-jst-xhr-plug/ , accessed on 15/01/2026

[11] https://www.digikey.nl/nl/products/detail/rf-solutions/FLEXI-SMA90-433/2781768 , accessed on 15/01/2026

[12] https://nl.mouser.com/new/taoglas/taoglas-aa-205-151111-antennas/ , accessed on 15/01/2026

[13] https://www.fruugo.nl/48v-dc-dc-converter-48v-naar-24v-20a-step-down-voeding-ducer-buck-regulator-spanning-voor/p-349750981-762694180 , accessed on 15/01/2026

[14] https://wetronic.nl/power-hd-wh-80kg-big-scale-digitale-hv-servo-80kg_nl , accessed on 15/01/2026

[15] https://genstattu.com/tattu-dual-channel-smart-charger-60a-3200w-for-6s-14s-ultra-high-voltage-tattu-smart-battery/ , accessed on 15/01/2026

[16] https://www.youtube.com/watch?v=e9JycBbQ36Y , accessed on 19/01/2026

found to satisfy the required values. They are also designed specifically for UAV's, which makes them a reliable option, as their design is built around a constant high load.

Table 7.3: All electric components and their used properties

Component	Product	Cost Per Piece [$]	Mass Per Piece [g]	Rated Voltage [V]	System Voltage [V]	Max Power [W]	Amount
Camera Transmitter + Camera	Walksnail Avatar GT Kit	219	41.6 + 15.4	6-25	24	15	1
Flight Computer	Embention Veronte 1X	8,100	198	6.5-36	24	15	1
Flight Data Recorder	Hensoldt SferiRec LCR100	15,000	1000	12-32	24	10	1
5G Transmitter	Poynting Puck V2	80	376	FCMS	FCMS	10	1
Data Collection System	SimTec ADP-55	20,000	900	9-32	24	2.5	1
ESC	Flame 100A HV 14S ESC	225	139	51.8	Main	Motor	6
Motor (+cables)	U12 Efficiency Multirotor	370	778	51.8	Main	4560	6
Battery	Tattu Pro 22000mAh 51.8V 25C	1,120	7350	51.8	Main	-	5
Backup Battery	Gens ace 400mAh 60C	17	18	22.2*	24	-	*3 in series
Flight Actuator	Big Scale 1/5	109	186	8.4	8	33	9
RF Antenna	FLEXI-SMA90-433	5	50	FCMS	FCMS	-	1
GNSS Antenna	Taoglas AA.205.151111 MagmaX2	75	160	FCMS	FCMS	-	1
Buck Converter	Unbranded	20	200	48	Main	-	2
Rudder Servo	Big Scale 1/5	109	186	8.4	8	33	1
Ground Equipment							
Battery Charger	Tattu Dual-channel smart charger	750	-	51.8	Main	3200	

7.2.4. Electrical Design

The final design of the electrical systems is laid out in Figure 7.7 (as can be seen, the design of this diagram is strongly influenced by the one made by Döll et al.[17]), containing all components that are part of the electrical system (for more detail about the components, the reader is referred to Table 7.3). The main batteries power a busbar that is used to distribute power to all components. This busbar is located on the wing connection and continues into the wing itself. This is done so that, when the wing is replaced (for modularity), there only needs to be one electrical connection point connected to the aircraft. This creates both simplicity and security, as the risk of breaking wires becomes a lot smaller. The main batteries all connect to the busbar through a set of fuses, as well as individual switches on each battery, to allow for individual isolation.

Connected directly to the busbar, are the ESC's. These, in turn power the three phases of the electric motors, comparable to the infrastructure of the D08 DEP-SFD [17]. The ESC's have internal protections against different motor failures, including, but not limited to, a short. When the current reaches 340 [A] the ESC will shut down. However, to prevent damage to the rest of the system, fuses are also

implemented on each individual motor (These fuses are now put at 110 [A], as this would already be higher than the maximum motor current).

Also connected to the busbar, is the LV system. This consists of a buck converter converting the 48 [V] "High Voltage" to 24 [V] "Low Voltage", and passing it onto a passive distributor. This then distributes the power onto all LV components, including, but not limited to, the flight computer and the data recorder, as well as the control servos (again through a buck converter, converting from 24 [V] to the needed 8 [V]). Also connected to this distributor is a 22.2 [V] backup battery. This battery is of a bit lower voltage than the 24 [V] supplied from the main battery, and is connected using a diode. This way, it is made sure that this backup battery is not used during normal operation, but it will still be powerful enough to power all LV components, as all have their minimum voltage below 20 [V]. The backup battery is enough to supply the LV components with power for 5 minutes, guaranteeing pilot control of the aircraft, even when the main battery fails. In addition, this battery is connected through a fuse, making sure that the discharge current does not exceed the allowed 60 [C].

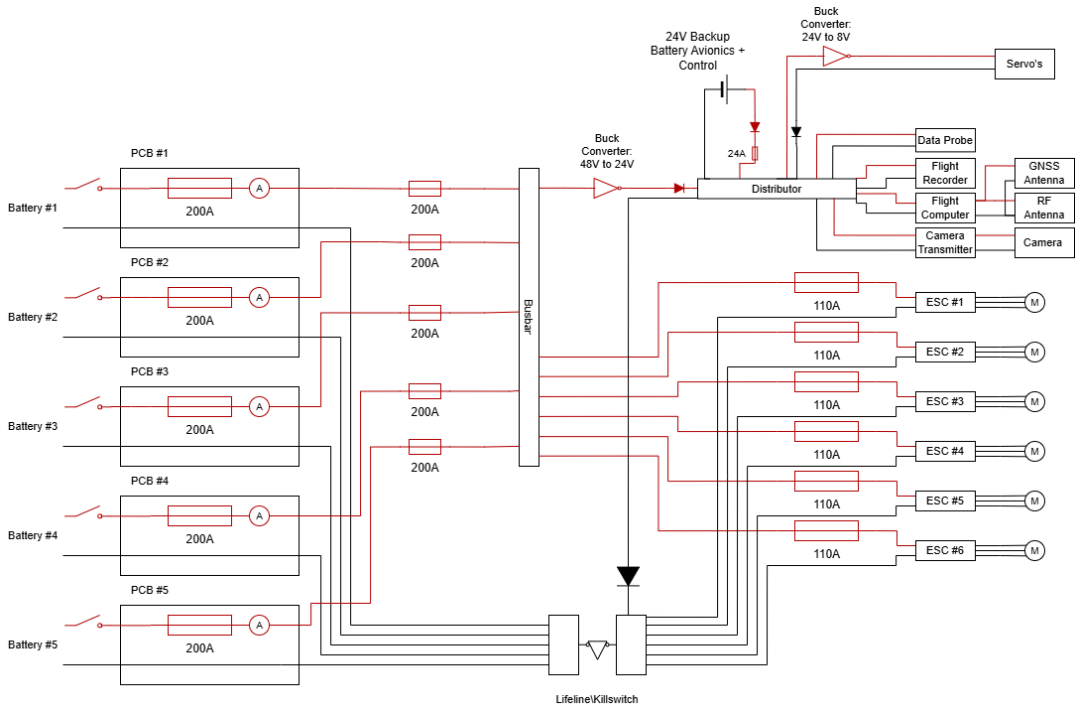

Figure 7.7: Electrical diagram depicting all components and their connections

7.3. Internal Communication

To make sure all components can also interact fully, a communication diagram was made that shows all connections between devices that are not laid out in the electrical diagram. As can be seen in Figure 7.8, there is internal communication using PWM signals, CAN, and RS-458. The control servo's use PWM signals to drive the amount of deflection of the surface. CAN is used by the BMS of the batteries. This way, the flight computer can check the data of the BMS, including, but not limited to, temperatures and voltages. CAN is also used by the flight data recorder. The flight computer has a CAN output, that is used to make sure all relevant attitude data is sent to this flight recorder. Lastly, the data probe uses RS-458 to communicate the recorded data to the flight computer, where it can be used to control the aircraft. It also has an RS-232 connection which is used for the maintenance interface of the probe. For both the CAN and RS protocols, the exact data rates are still to be determined. This, is left to the discretion of the operator, as they can find what works best when using the system. Both protocols have set options for data rates (125, 250, 500 and 1000 [kbps] are recommended for UAVCAN [17], and for the

[17] https://legacy.uavcan.org/Specification/8._Hardware_design_recommendations/, accessed on 15/01/2026

RS protocols 57.6, 115.2, 230.4 and 460.8 [kbps] are the options[18]). Based on the choice made for this, the data rates will also change, creating a different final data stream between the flight computer and its ground station.

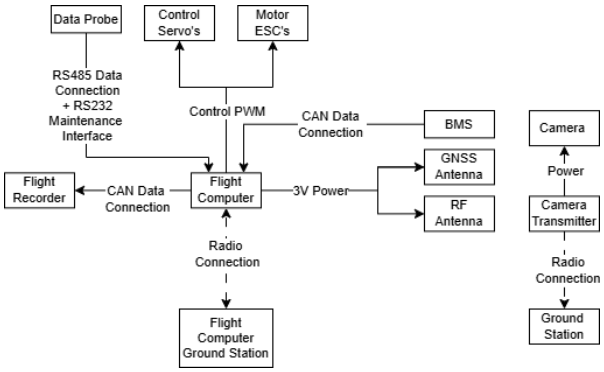

Figure 7.8: Communication Diagram showing how electronic components communicate

7.4. Software

When all the hardware connections have been set up, it is not immediately validated that the system will work. There needs to be some form of software control over all components to make sure they do what they need to do (and do not do what they should not do). One of the reasons for choosing the Embention Veronte flight computer was that it has an option to use a custom software interface. This can be used both to create a control interface where the pilot has all information needed to fly the aircraft, as well as the ability to control all the components.

To visualise the different components such a software system would entail, a software diagram was made. Figure 7.9 shows the different pieces that are part of the network that controls the aircraft in a safe and proper way. It consists of the following parts:

Energy Management System (EMS) This system will take control over the amount of energy that can be used by the different devices. When working with electronic components it is important to take care that they do not go over their maximum rated temperatures, discharge rates or that they go above or below their maximum and minimum SoC. By having a software system that can regulate this, it is ensured that there will not be any electronic hazard throughout the operation of the aircraft.

State of Charge estimator (SoCe)[13] To properly control the batteries using the EMS, it is important to have a reliable measurement for the State of Charge of the batteries. However, this entails more than just measuring the voltage. To properly estimate the amount of energy that is present in the batteries, a State of Charge estimator can be used. By performing the Coulomb counting method (using parameters like cell temperature and measured voltage), the energy in the batteries can be calculated. Apart from the SoC, if deemed necessary, this system can also provide an estimate for the State of Health (SoH) of the batteries.

Diagnostics A system should be in place that will monitor all important sensor data, to create an overview of the state of the aircraft. This system can send a warning to the pilot when values are close to reaching critical values, giving the pilot enough time to respond to them. It can even be used to safely turn off components in case they reach critical values (i.e. when the motor or ESC would reach a temperature outside the safe range). Of course this would have to be implemented with caution, as it should not turn off anything critical for the operations.

Flight Controller Between the pilot giving inputs into the interface, and the control servos outputting a specific angle, there should be a controller that converts the radio signal into the correct PWM signal for the servo to respond to. There is also an option here for operators to create their own

[18]https://www.swiss-airdata.com/products/air-data-systems/adp-55 , accessed on 15/01/2026

flight controllers that can aid the pilot. This way the response of such software can be tested in a more physical way, rather than just using simulations.

FCMS All of the data that is collected from sensors and actuators, should be organised and logged to perform research on. This can be done in multiple ways; first of all, data is send to the flight data recorder. This then logs it onto an SD card, to be used both for research purposes, as well as acting as a black box in case of an accident. Secondly, the data can be sent through the data link of the Embention. This way it can be watched from the ground station during operation already. This in turn also helps the operating crew with their work.

Pilot Interface + Controls To actually fly the aircraft, a pilot should have control over the aircraft through a wireless connection. This is done using the data link of the Embention Veronte, which, apart from sending data, also receives the command inputs of the ground station. To input these controls, the pilot can make use of any controller system that can be connected to a computer (or the computer on its own) of their preference, as the Embention software allows for versatile control options. There is also a separate camera connection in place that allows the pilot to see from the aircraft's POV.

Other devices Apart from these pieces of software that shall be run on the Embention Veronte, there are also a number of other devices that interact with the software, that already have the software pre-made by their respective manufacturer. The motor ESC's and the control actuators have a relatively simple control using just a PWM signal that is an output of the Veronte. However, the Battery Management System (BMS) of the batteries uses a bit more elaborate connection over CAN, to send data to the computer. This, together with a possibility for control.

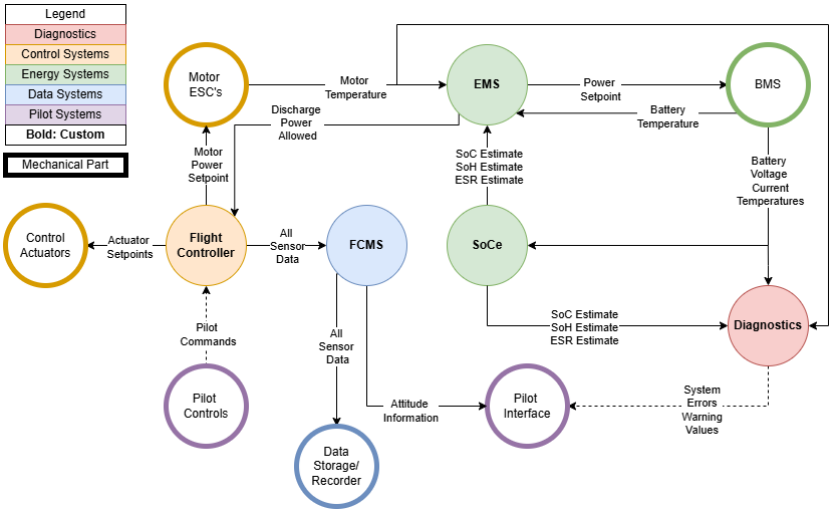

Figure 7.9: Diagram showing main software elements and their relations

7.5. Final Powertrain Design

In Figure 7.10, the full design of the powertrain system of the model can be found. This diagram summarises the different types of connections between different components (i.e. communication or power). It also shows the rough location of each component, although some parts are not exactly in the correct spot, with the goal of making the diagram more readable (for the exact locations, see subsection 6.1.2. One note that should be added is that this diagram is not a full representation of the wiring harness (e.g. each component that is controlled through PWM will have their own connection, and power lines will always exist of more than one cable).

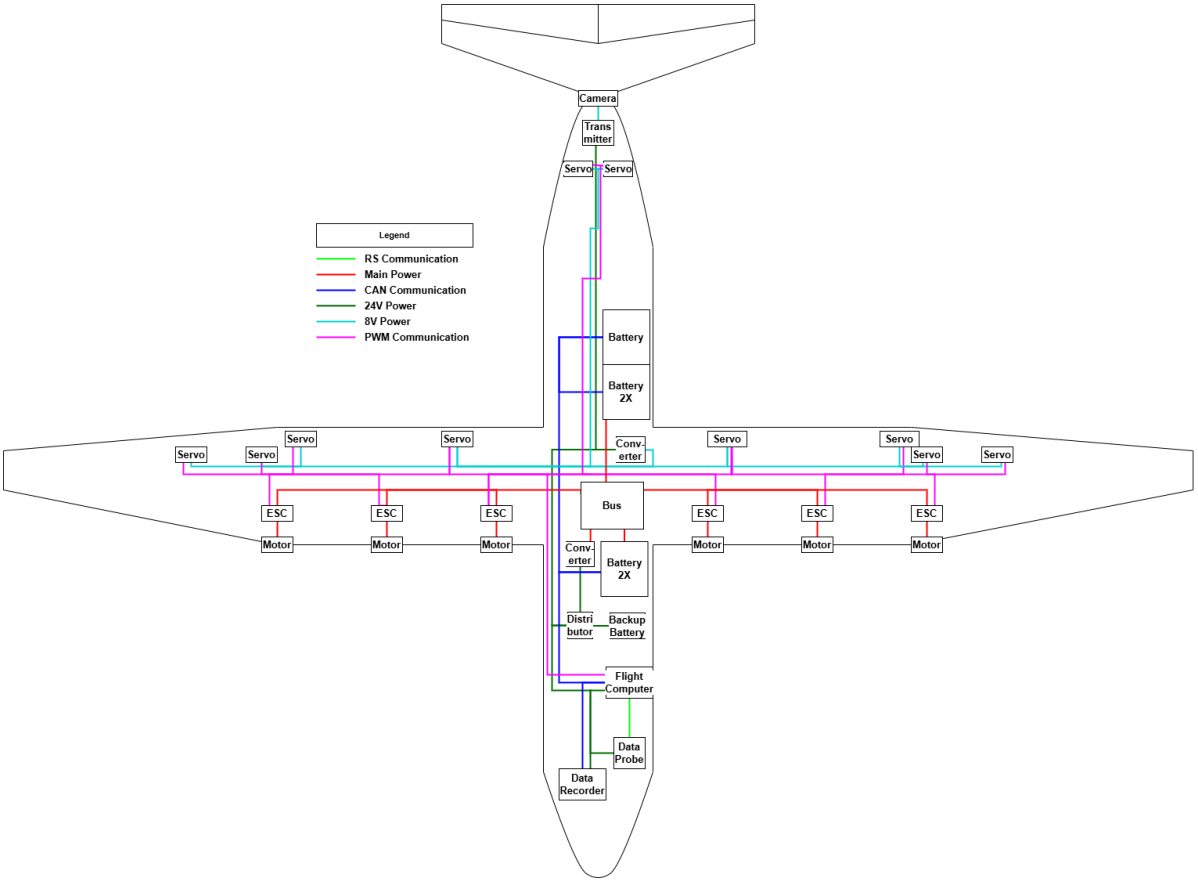

Figure 7.10: Hardware Diagram showing physical connections between electronic components in their location

7.6. Requirement Compliance Verification

Now that the full powertrain system is designed, it should also be check for compliance with the requirements set up in the previous design stages. This is done in Table 7.4.

Table 7.4: Requirement compliance power & propulsion requirements

ID	Requirement Description	Verification Method	Compliance Level
SFD-SYS-PRO-01	The propulsion system shall generate a maximum combined thrust of at least 380 N.	Analysis	The maximum thrust calculated for the model amounts to 390N.
SFD-SYS-PRO-02	The motors shall be positioned on the wings in a configuration geometrically similar to the Elysian E9X.	Inspection	The design of the powertrain was made with the motor location based on the location specified for E9X.
SFD-SYS-PRO-03	The Electronic Speed Controllers (ESCs) shall provide telemetry data (RPM, Voltage, Current, Temp) to the Avionics bus at 10Hz.	Inspection + Demonstration	The ESC type works at 600Hz, which amount to more than enough. Once the software has been written this should be demonstrated as well before taking flight.
SFD-SYS-PRO-04	The motors shall be compliant with COTS availability standards.	Inspection	All components chosen can be bought by commercial vendors.

SFD-SYS-PRO-05	The propulsion system components shall be selected from vendors with existing supply chains to minimize lead time.	Inspection	For all components there is at least one vendor with available stock.
SFD-SYS-PRO-06	The propulsion system with all engines operating shall be able to continuously provide **7000** W of power	Analysis	With all engines operable at lowest efficiency, there is still more than 9000 W Available.
SFD-SYS-PRO-07	The system shall have independently operated Electronic Speed Controllers (ESCs) to support differential thrust and redundancy.	Inspection	Due to the design choices made, each motor has their own ESC, individually controlled by the flight computer.
SFD-SYS-PRO-08	The propulsion system shall retain full functionality between ambient temperatures of 0 K and 35 K.	Test	This functionality shall be verified with iron bird testing.
SFD-SYS-PRO-09	In case of propeller separation, the design shall ensure that remaining engines or structural components are not critically damaged (containment/separation path).	Test	
SFD-SYS-PWR-01	The battery system shall have a total usable capacity of at least 4700 Wh (sufficient for the most power-heavy mission + 1 go-around + ground ops).	Inspection	The battery system has over 5600Wh available.
SFD-SYS-PWR-02	The power distribution system shall provide redundant 24V regulated lines for the Avionics and Control systems.	Inspection	By use of a backup battery, it is made sure that the avionics and control systems have 5 minutes of power after a main battery failure.
SFD-SYS-PWR-03	The battery packs shall be removable and capable of being swapped within 15 minutes to support multi-mission days.	Demonstration	Although the exact time cannot be given at this stage, the design allows for easy access to the batteries, which makes swapping a quick task.
SFD-SYS-PWR-04	The battery system shall be capable of recharging to full capacity within 60 minutes to support mission turnaround.	Analysis	By use of two battery chargers, and using the full 3C charging capacity, all 5 batteries can be charged within an hour.
SFD-SYS-PWR-05	The power system shall allow for full isolation of the main battery in case of failure.	Inspection	Through the use of individual switches, the operator has full control over the batteries in the system.
SFD-SYS-PWR-06	The power distribution system shall include individual overcurrent protection for each component.	Inspection	Each battery is connected to the busbar through two separate fuses, allowing for quick overcurrent protection.
SFD-SYS-PWR-07	The electrical system shall retain full functionality between ambient temperatures of 0 K and 35 K.	Test	This functionality shall be verified with iron bird testing.
SFD-SYS-PWR-08	The power wiring and connectors shall support modular reconfiguration (usable in different aircraft layouts).	Demonstration	The use of a central busbar connected at the connection point for the wing, allows for quick and easy swapping of the wing.
SFD-SYS-PWR-09	The BMS shall possess a diagnostic capability to detect failures within a span of 30 seconds.	Inspection	The BMS of the main batteries has its own diagnostic capability.

SFD-SYS-PWR-10	The BMS shall estimate State of Charge (SoC) with a precision of 99%.	Test	As this will be the task of the software that still has to be written, it shall be tested as part of iron bird testing.
SFD-SYS-PWR-11	The BMS shall estimate State of Health (SoH) with a precision of 99%.	Test	As this will be the task of the software that still has to be written, it shall be tested as part of iron bird testing.
SFD-STK-SUS-03	The equipment and propulsion system shall only use Commercially Off- The-Shelf (COTS) available components	Inspection	All components chosen can be bought by commercial vendors.
SFD-SYS-SOP-02	The system shall comply with all relevant EASA SORA BVLOS standards regarding data logging, radio connection, and required components.	Inspection	Although the rules are described in this report, a full analysis should still be performed when the full model has been built.
SFD-SYS-AVI-01	The FCMS shall log all flight variables (IMU, GPS, Air Data, Control Inputs) at a minimum rate of 100 Hz for post-flight analysis.	Inspection + Demonstration	The ADP-55 can send data at a rate of 100Hz according to the datasheet. The Veronte will use custom software to log this, which should be demonstrated to work before taking flight.
SFD-SYS-AVI-03	The pitot-static system shall be calibrated to provide airspeed accuracy within ±TBD m/s in the flight envelope.	Test	The ADP-55 will be factory calibrated to customer requirements. This calibration shall be tested during ground testing.
SFD-SYS-AVI-04	The FCMS shall log Air Data (Speed, Pressure, Altitude) and Motor Data (RPM, V, I) at 50 Hz.	Inspection + Demonstration	The ADP-55 can send data at a rate of 100Hz according to the datasheet. The Veronte will use custom software to log this, which should be demonstrated to work before taking flight.
SFD-SYS-AVI-05	The FCMS shall log Control Surface positions (commanded and measured) at 50 Hz	Inspection + Demonstration	The servo's for control have a working frequency of 333Hz according to the datasheet. The Veronte will use custom software to log this, which should be demonstrated to work before taking flight.

8
Stability & Control

This chapter provides an overview of the design process of the model's control surfaces and analysis of its static and dynamic stability, together with appropriate assumptions. It starts with approximating the mass moment of inertia of Elysian E9X and scaling it down for similitude in section 8.1, as it is necessary for all further design and analyses of the similitude. Next, the static stability was discussed in section 8.2. After obtaining relevant parameters, the primary control surfaces were sized in section 8.3. An analysis of the dynamic stability of the E9X and SFD was then conducted in section 8.4 and finally, a summary of the verification and validation methods is discussed in section 8.5.

8.1. Mass moment of inertia approximation

The goal of this section is to approximate the mass moment of inertia of Elysian E9X. This is an essential factor for achieving similitude in static and dynamic stability. Since the full-scale aircraft does not exist yet, an approximation based on existent aeroplanes was performed, and the stability was assessed using the approximation. Then, a scaling was performed using methods given in section 5.1 for further investigations of similitude in control and stability.

Jan Roskam provides a method of moment of inertia approximation using aircraft's weight, length, wingspan and historical data with the following equations [52, pp. 17]:

$$I_{xx} = \frac{4mR_X^2}{b^2} \tag{8.1}$$

$$I_{yy} = \frac{4mR_Y^2}{L^2} \tag{8.2}$$

$$I_{zz} = \frac{16mR_Z^2}{(L+b)^2} \tag{8.3}$$

Where R_X, R_Y and R_Z are dimensionless values that are similar for similar historical aeroplanes [52, pp. 197–206]. Given the data of existent propeller aircraft, the following values were chosen:

$$R_X = 0.384; \quad R_Y = 0.320; \quad R_Z = 0.503$$

The value of R_Y was chosen based on an average of all wing-mounted propeller aircraft. The remaining, R_X and R_Z values were assumed to be the highest given values for propeller aircraft due to E9X mass distribution: more than usual number of engines and heavy batteries on a wing, which distribute aircraft's mass further away from the X and Z axes, and therefore increase the mass moment of inertia. Using the given mass, length, wingspan and equations 8.1 - 8.3 the following values of mass moment of inertia were found:

$$I_{xx} = 8,814,921 kg \cdot m^2; \quad I_{yy} = 2,767,598 kg \cdot m^2; \quad I_{zz} = 10,053,881 kg \cdot m^2$$

To obtain the appropriate goal mass moments of inertia of the model, the Froude scaling explained in section 5.1 was used. The final model's goal inertia is presented in table 8.1.

Table 8.1: Goal inertia of the model aircraft for mechanical similitude

	I_{xx} $[kg \cdot m^2]$	I_{yy} $[kg \cdot m^2]$	I_{zz} $[kg \cdot m^2]$	$Mass$ $[kg]$
Lower range	133.22	41.91	159.96	142.00
Higher range	140.62	44.24	168.85	150.00
Average	136.92	43.08	164.41	146.00

8.2. Static stability

The assessment of static stability is a fundamental requirement for the Scaled Flight Demonstrator (SFD), as it ensures the aircraft returns to its initial equilibrium state following a disturbance without pilot intervention. For this project, the stability analysis serves a dual purpose: first, to guarantee the safety and controllability of the demonstrator during flight testing; and second, to achieve aerodynamic similitude with the Elysian E9X full-scale conceptual design. By replicating the flight-mechanical behavior rather than absolute performance, the SFD acts as a validation tool for the complex interactions present in distributed electric propulsion.

8.2.1. Longitudinal Static Stability

The objective of the longitudinal stability calculation is to determine the stick-fixed neutral point of the SFD configuration, including the influence of the distributed propellers, such that the demonstrator

reproduces the full-scale aircraft's flight-mechanical behaviour and can be ballasted within a justified CG envelope for flight testing. At the end of this section, a CG point is estimated based on the data that is available to make an educated estimation on where the CG point is on the full scale; this CG will also be the CG point on the SFD. This aligns with the project requirement to replicate flight mechanical behaviour rather than absolute performance, while explicitly addressing stability and control characteristics such as CG limits and including sensitivity analysis in the design process. The full-scale geometry available was therefore used as the basis for the scaled configuration, as propeller aerodynamic information at full scale is unavailable; the information from the propellers for the SFD is used. To still include propulsion effects on longitudinal stability, the aerodynamic coefficients from an unpowered Flow5 analysis were combined with propeller thrust and normal-force data obtained for the selected demonstrator propellers, thereby yielding a powered total pitching-moment slope and a powered neutral point estimate. The intention of this method is to determine the neutral point and C_{m_α}; from there, the neutral point directly sets the aft CG limit through a chosen static margin, and, based on moment equilibrium, a CG point is chosen.

8.2.1.1. Propeller Normal-force Model

The propeller normal force N_p, force component normal to the propeller axis caused by oblique inflow, is estimated using the USAF DATCOM-based correlation. Report LR-761 is intended for preliminary stability-and-control build-up and assumes small-angle linear behaviour, meaning that the normal force scales linearly with inflow angle[45]. The analysis is evaluated at three angles of attack around the powered trim condition, $\alpha_R = \{0°, 2°, 4°\}$, to obtain $N_p(\alpha_R)$ for the longitudinal force and pitching-moment build-up[45].

First, the flight-condition reference quantities and the thrust coefficient used by LR-761 are defined. For the powered operating point $\rho = 1.1773\ \mathrm{kg\,m^{-3}}$ and $V_\infty = 43.8\ \mathrm{m\,s^{-1}}$ will be used, giving $q_\infty = \frac{1}{2}\rho V_\infty^2$. The propeller disk area is given by $S_p = \pi D^2/4$ with $D = 0.4064$ m from subsection 7.1.3. The thrust coefficient appearing in LR-761 is based on free-stream dynamic pressure and disk area

$$T_c' = \frac{T}{q_\infty S_p} \tag{8.4}$$

where the trim thrust per propeller is taken from subsection 7.1.3, $T = 23.29N$, together with the blade angle at 0.75R, $\beta_{0.75} = 36.5°$). Over the small α_R sweep, $\beta_{0.75}$ and T are held at their trim values (consistent with linearization about trim); in the LR-761 normal-force model, the sensitivity of the normal-force slope to T is weak because T enters only through T_c' inside a slowly varying correction term[45].

The LR-761 correlation requires an effective solidity σ_e, defined as propeller solidity based on an average blade chord[45]. Because LR-761 provides definitions of σ and σ_e rather than a full derivation, σ_e is implemented directly from the definition of solidity as blade element area divided by annulus area at $0.75R$, using an average chord in place of the local chord. From the blade chord distribution $c(r)$ provided by the propeller design output, an average chord over the lifting blade span is computed as

$$\bar{c} = \frac{1}{R - r_h} \int_{r_h}^{R} c(r)\, dr \tag{8.5}$$

where r_h is the spinner cutout radius (taken as the first non-spinner station in the chord table, $r_h/R = 0.15$). The effective solidity is computed from the chord distribution by averaging

$$\sigma_e = \frac{B\,\bar{c}}{2\pi(0.75R)} \tag{8.6}$$

with $B = 6$ blades and $R = D/2$ from subsection 7.1.3. Applying this to the given chord distribution yields $\sigma_e = 0.135$, which is treated as constant in the α_R sweep because it is purely geometric.

The inflow-angle derivative of the propeller normal-force coefficient, $C'_{N\alpha,\mathrm{in}}$ (per rad), is computed from the DATCOM correlation as a function of σ_e, $\beta_{0.75}$, and T_c'[45]. Since the propellers are counter-rotating,

the counter-rotating form is used here; this is

$$C'_{N\alpha,\text{in}} = \left(\frac{3.86\,\sigma_e}{1+\sigma_e}\right)\sin(\beta_{0.75}+14^\circ)\left[1+\frac{3T'_c}{8\sqrt{1+\frac{2}{3}T'_c}}\right] \tag{8.7}$$

where the thrust-dependent bracket includes the square root exactly as in LR-761[45]. Substituting $\sigma_e = 0.135$, $\beta_{0.75} = 36.5^\circ$ (from subsection 7.1.3), and the corresponding T'_c from $T = 23.29$ N yields $C'_{N\alpha,\text{in}} = 0.375\ \text{rad}^{-1}$.

The inflow angle at the propeller disk is then computed using LR-761's inflow-angle relation, which is written in terms of α_R and $\alpha_{CL=0}$[45]. To avoid ambiguity, α_R denotes the aircraft angle of attack used in the sweep, referenced to the same geometric datum as the zero-lift angle, and $\alpha_{CL=0} = -4^\circ$ is the wing zero-lift angle in that same reference, which is approximated using the wing zero-lift angle from Flow5. The aerodynamic angle from zero lift is therefore $(\alpha_R - \alpha_{CL=0})$[45]. The propellers are aligned with the freestream during cruise, so with the installed prop incidence $i_{\text{prop}} = -3.6^\circ$, LR-761 gives

$$\alpha_{\text{prop}} = \left(\frac{d\alpha_{\text{in}}}{d\alpha}\right)(\alpha_R - \alpha_{CL=0}) + \alpha_{CL=0} + i_{\text{prop}} \tag{8.8}$$

The local gradient $\frac{d\alpha_{\text{in}}}{d\alpha}$ is computed from the LR-761 placement model using the measured installation distances that can be found in Figure 8.1: an unswept wing with prop plane at $X = 0.04$ m ahead of the wing leading edge (so $X_{L,0.75} = X_{R,0.75} = X$), $A_w = 15.004$ (the wing aspect ratio), $c_r = 0.469$ m, and fuselage radius $R_{\text{fus}} = 0.16$ m, together with the lateral hub positions from the aircraft layout $y_{\text{hub}} = \{0.446, 0.892, 1.338\}$ m (inner/mid/outer). The blade positions are evaluated at the 0.75R points, $Y_{L,0.75} = |y_{\text{hub}}| - 0.75R$ and $Y_{R,0.75} = |y_{\text{hub}}| + 0.75R$, leading to $\frac{d\alpha_{\text{in}}}{d\alpha} \approx \{3.398, 3.265, 3.247\}$ for the inner, mid, and outer prop groups, respectively. Because all computed $|\alpha_{\text{prop}}|$ remain below 30° for the present sweep, the assumption $K = 1$ is used [45].

Finally, LR-761 also presents an aircraft-level "total coefficient" form that includes the factors $n_p S_p/S_w$ and the degree-to-radian conversion; however, for this calculation, the per-propeller normal force using the disk-based definition $C_N = N/(q_\infty S_p)$ is computed instead, and then summed over the installed propellers in the aircraft build-up.Using $C_N = C'_{N\alpha,\text{in}}\alpha_{\text{prop,rad}}$, the per-propeller normal force is

$$N_p = K\,q_\infty S_p\,C'_{N\alpha,\text{in}}\,\alpha_{\text{prop,rad}} \tag{8.9}$$

With the inputs above, the resulting normal forces are per propeller $N_{p,\text{inner}} = \{7.29, 13.81, 20.33\}$ N, $N_{p,\text{mid}} = \{6.77, 13.04, 19.30\}$ N, and $N_{p,\text{outer}} = \{6.70, 12.93, 19.16\}$ N at $\alpha_R = \{0^\circ, 2^\circ, 4^\circ\}$, respectively.

8.2.1.2. Cma and the stick-fixed neutral point

Longitudinal static stability is assessed through the derivative $C_{m_\alpha} = \partial C_m/\partial\alpha$, where static stability requires $C_{m_\alpha} < 0$ and the stick-fixed neutral point $x_{n,\text{fix}}$ is defined by the CG location for which $C_{m_\alpha} = 0$[40]. In the adopted convention, $C_m > 0$ corresponds to a nose-up pitching moment, consistent with the stability sign convention used for interpreting trim and stability slopes[40]. Flow5 provides $C_L(\alpha)$, $C_D(\alpha)$, and $C_m(\alpha)$ about the user-defined reference point (in this case the Flow5 "CoG" reference values $x_{\text{ref}} = 1.70$ m from the nose and $z_{\text{ref}} = 0$ in the Flow5 coordinate system). Because the neutral point derivation is written in terms of normal and tangential force coefficients rather than lift and drag, the Flow5 outputs were transformed to C_N and C_T using the standard stability-axis relations[40]

$$C_N = C_L\cos\alpha + C_D\sin\alpha, \qquad C_T = C_D\cos\alpha - C_L\sin\alpha \tag{8.10}$$

This transformation is particularly important once propulsion is included, because the tangential component is no longer negligible and C_T is not interchangeable with C_D outside the small-angle, unpowered approximation[40]

The propulsion influence was added as an external force and moment contribution about the same reference point used by Flow5. For each propeller i, thrust $T_i(\alpha)$ and normal force $N_i(\alpha)$ were resolved into a body-axis force pair $(X_{p,i}, Z_{p,i})$ using the installation angle i_p, here $i_p = -2°$, which was selected such that at the cruise condition $\alpha = 2°$ the propeller axis aligns with the freestream direction, minimising steady vertical thrust component at cruise. The normal-force calculation model is treated separately in the preceding section; the resulting $N_i(\alpha)$ curves are taken as inputs here. The propeller centres were located at known coordinates relative to the nose and relative vertical offsets between propeller rows, allowing the pitching moment about the reference point to be computed from a force–arm relation[40]. In coefficient form, the incremental propeller contributions were written as

$$C_{N,p}(\alpha) = \frac{\sum_i Z_{p,i}(\alpha)}{q_\infty S}, \qquad C_{T,p}(\alpha) = \frac{\sum_i X_{p,i}(\alpha)}{q_\infty S} \tag{8.11}$$

$$C_{m,p}(\alpha) = \frac{1}{q_\infty S \bar{c}} \sum_i \left[(x_{\text{ref}} - x_{p,i})\, Z_{p,i}(\alpha) - (z_{\text{ref}} - z_{p,i})\, X_{p,i}(\alpha) \right] \tag{8.12}$$

where $q_\infty = \frac{1}{2}\rho V^2$ is the freestream dynamic pressure, S and $\bar{c}$ are the wing reference area and mean aerodynamic chord used consistently with Flow5, and $(x_{p,i}, z_{p,i})$ are the propeller centre coordinates. The total coefficients, including propulsion, then follow directly as

$$C_N(\alpha) = C_{N,\text{off}}(\alpha) + C_{N,p}(\alpha), \qquad C_T(\alpha) = C_{T,\text{off}}(\alpha) + C_{T,p}(\alpha), \qquad C_m(\alpha) = C_{m,\text{off}}(\alpha) + C_{m,p}(\alpha) \tag{8.13}$$

Since the neutral point is determined by the slope C_{m_α}, only the parts of the propeller forces that vary with α affect the neutral point location; constant thrust offsets primarily affect the trim moment C_{m0} but not the stability derivative in this reports implementation, where prop forces are built up in aircraft axes and thrust is held constant over the small α-range.

The stability derivatives were extracted assuming linear behaviour over the small-angle range by fitting straight lines through the computed points at $\alpha = \{0°, 2°, 4°\}$ with α expressed in radians, yielding C_{N_α} and C_{m_α} (and where needed C_{T_α}). The stick-fixed neutral point relation follows directly from the stick-fixed stability identity[40], which links the pitching-moment slope to the distance between the moment reference point and the stick-fixed neutral point[40]. Using the Flow5 reference location x_{ref} as the point about which C_{m_α} is defined, the neutral point is obtained as

$$C_{m_\alpha} = C_{N_\alpha} \frac{x_{\text{ref}} - x_{n,\text{fix}}}{\bar{c}} \quad \Rightarrow \quad x_{n,\text{fix}} = x_{\text{ref}} - \bar{c}\, \frac{C_{m_\alpha}}{C_{N_\alpha}} \tag{8.14}$$

This formulation is particularly convenient because it does not require the true CG position to be known a priori; it only requires that C_{m_α} and C_{N_α} are evaluated consistently about the same reference point[40]. Once $x_{n,\text{fix}}$ is available, the aft CG limit is defined via the static margin $SM = (x_{n,\text{fix}} - x_{cg})/\bar{c}$[55]. A conservative minimum static margin of $SM_{\min} = 0.05$ was selected to set the aft limit, because conventional aircraft guidance warns against placing the CG within only a few per cent of the neutral point due to reduced robustness of longitudinal dynamics; selecting 5% provides a buffer against modelling uncertainty in propulsion effects and downwash[55]. The resulting aft limit is therefore

$$x_{cg,\text{aft}} = x_{n,\text{fix}} - SM_{\min}\, \bar{c} \tag{8.15}$$

Including propulsion produced a forward shift of the neutral point compared to the power-off case, consistent with a positive propulsion contribution to C_{m_α} (destabilising increment) when the α-dependent propeller forces act with a net nose-up moment arm about the reference point[40]. The final result yields a powered stick-fixed neutral point located at $x_{n,\text{fix}} \approx 1.74$ m from the nose, and, for the cruise-trim CG estimate reported below, a total stability derivative $C_{m_\alpha,\text{total}} \approx -1.06\ \text{rad}^{-1}$, which lies within the typical range reported for conventional aircraft (≈ -0.3 to $-1.5\ \text{rad}^{-1}$) and therefore has a plausible magnitude for a statically stable configuration[55].

After the neutral-point determination and CG envelope definition, a separate cruise-condition estimate of the CG position was obtained by enforcing pitching-moment equilibrium about the nose at $\alpha = 2°$, based

on linearised aerodynamic moments for wing and tail plus the propulsion moments. The aerodynamic pitching moments were written as linear functions of angle of attack, $C_{m,w}(\alpha) = C_{m,w0} + C_{m_{\alpha,w}}\alpha$ and $C_{m,h}(\alpha_h) = C_{m,h0} + C_{m_{\alpha,h}}\alpha_h$, consistent with the standard linear static stability model[40]. The effective tail angle of attack was reduced by downwash, modelled through the derivative factor $d\alpha_h/d\alpha = 1 - d\varepsilon/d\alpha$, so that the tail contribution to the pitching-moment slope includes the downwash correction[40]. In dimensional form, the pitching-moment equilibrium about the nose was written as

$$\sum M_{\text{nose}} = M_{w,0.25}(\alpha) + N_w(\alpha)\, x_{w,0.25} + M_{h,0.25}(\alpha_h) + N_h(\alpha_h)\, x_{h,0.25} + M_p(\alpha) - W\, x_{cg} = 0 \tag{8.16}$$

with the aerodynamic moments expressed through coefficients as $M_{w,0.25} = C_{m,w}(\alpha)\, q_\infty S_w \bar{c}_w$ and $M_{h,0.25} = C_{m,h}(\alpha_h)\, q_\infty S_h \bar{c}_h$, and the normal forces as $N_w = C_{L,w}(\alpha)\, q_\infty S_w$ and $N_h = C_{L,h}(\alpha_h)\, q_\infty S_h$ evaluated at the quarter-chord locations $x_{w,0.25}$ and $x_{h,0.25}$. Solving the above for the unknown x_{cg} yields a cruise-consistent CG estimate of $x_{cg} \approx 1.66$ m from the nose. Using the stick-fixed stability relation[40] $C_{m_\alpha} = C_{N_\alpha}(x_{cg} - x_{n,\text{fix}})/\bar{c}$ then provides the total stability slope at that CG location[40]. This results in $C_{m_\alpha,\text{total}} \approx -1.19\ \text{rad}^{-1}$, confirming a statically stable cruise condition since $C_{m_\alpha} < 0$[55]. This is to show that the demonstrator is guaranteed to fly stable at cruise, just like what would be expected from the full-scale model, and therefore the best estimation that can be made on where the CG point of the full-scale lies.

A sensitivity analysis was performed to identify which inputs most strongly affect the neutral point and the aft CG limit. From the neutral-point expression $x_{n,\text{fix}} = x_{\text{ref}} - \bar{c}(C_{m_\alpha}/C_{N_\alpha})$, the first-order sensitivities are

$$\frac{\partial x_{n,\text{fix}}}{\partial C_{m_\alpha}} = -\frac{\bar{c}}{C_{N_\alpha}}, \qquad \frac{\partial x_{n,\text{fix}}}{\partial C_{N_\alpha}} = \bar{c}\,\frac{C_{m_\alpha}}{C_{N_\alpha}^2} \tag{8.17}$$

These relations show that the neutral point is most sensitive to uncertainty in the fitted slopes C_{m_α} and C_{N_α}, which in turn are driven by the assumed linear range in α and by the α-dependence of the propeller normal force model. The propulsion contribution enters C_{m_α} predominantly through the moment-arm term $\sum(x_{\text{ref}} - x_{p,i})\,\partial Z_{p,i}/\partial\alpha$, so uncertainties in the propeller normal-force slope $\partial N_i/\partial\alpha$, the installation angle i_p (which affects force resolution), and the vertical/longitudinal propeller locations directly translate into uncertainty in $x_{n,\text{fix}}$. The aft CG limit depends linearly on the chosen minimum static margin, $x_{cg,\text{aft}} = x_{n,\text{fix}} - SM_{\text{min}}\bar{c}$, so $\partial x_{cg,\text{aft}}/\partial SM_{\text{min}} = -\bar{c}$, implying that the static-margin choice is a dominant driver for the numerical value of the aft limit independent of the aerodynamic fit. The selection of $SM_{\text{min}} = 0.05$ is therefore not only a stability requirement but also a robustness choice to accommodate modelling uncertainty in distributed propulsion effects while remaining safely away from the neutral point, consistent with conventional guidance on avoiding extremely small static margins[55].

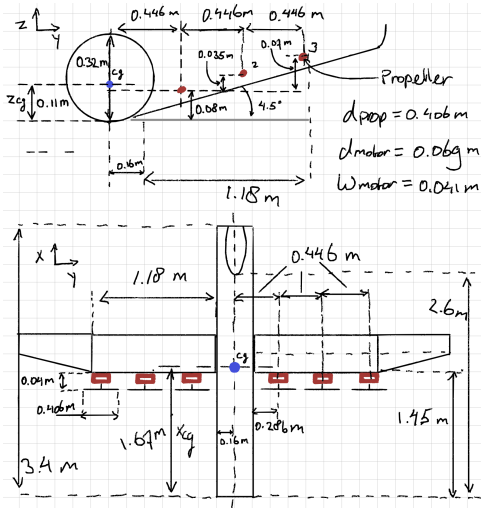

Figure 8.1: Top and front view drawing showing dimensions for the moment arms used in the stability calculations

8.2.2. Lateral stability

As previously mentioned, one of the primary objectives of the SFD is to replicate the flight mechanical behaviour of the Elysian E9X. However, as the E9X is still in the conceptual design phase, estimates must be obtained of the lateral stability derivatives, based on the design parameters currently available. This is primarily done using the methods outlined in [53], including all empirical factors.

8.2.2.1. Sideforce-due-to-sideslip C_{Y_β}

The sideforce-due-to-sideslip derivative is calculated by adding up the various contributions, namely, of the wing, fuselage and vertical tail. The wing contribution is a function of the dihedral, as laid out by Equation 8.18:

$$C_{y_{\beta_w}} = -0.00573 \cdot |\Gamma| \tag{8.18}$$

The fuselage contribution can then be found by Equation 8.19, where K_i is an empirical factor based on the distance from the body centerline to quarter-chord point of exposed wing root chord and maximum body height at wing-body intersection and S_0 the cross-sectional area of the fuselage at the point where the flow ceases to be potential.

$$C_{y_{\beta_f}} = -2 \cdot K_i \cdot \frac{S_0}{S} \tag{8.19}$$

Finally, the contribution of the vertical tail is given by Equation 8.20, where k_v is an empirical factor based on fuselage depth and length, $(1 + \frac{d\sigma}{d\beta}) \cdot \eta_v$ can be found from an empirical relationship based on vertical tail area, quarter-chord sweep, effective aspect ratio of the vertical tail, fuselage depth and the aforementioned distance from body centerline to to quarter-chord point of exposed wing root chord.

$$C_{y_{\beta_v}} = -k_v \cdot (C_{L_{\alpha_v}}) \cdot (1 + \frac{d\sigma}{d\beta}) \cdot \eta_v \cdot \frac{S_v}{S} \tag{8.20}$$

8.2.2.2. Yawing-moment-due-to-sideslip C_{n_β}

The yawing-moment-due-to-sideslip is also made up of various contributions, namely the fuselage and vertical tail, as the wing only contributes at very high angles of attack and is thus not considered at this stage. The contribution of the fuselage is found using Equation 8.21, where K_N is an empirical factor accounting for wing-fuselage interference based on aircraft geometry and K_{R_1} a factor dependent on Reynold's number. The vertical tail contribution Equation 8.22 is a function of $C_{y_{\beta_v}}$, aircraft geometry and angle of attack.

$$C_{n_{\beta_f}} = -57.3 \cdot K_N \cdot K_{R_1} \cdot \frac{S_{B_s} \cdot l_f}{S \cdot b} \tag{8.21}$$

$$C_{n_{\beta_v}} = -(C_{y_{\beta_v}}) \cdot \frac{(l_v \cdot cos\alpha + z_v sin\alpha)}{b} \tag{8.22}$$

8.2.2.3. Rolling-moment-due-to-sideslip C_{l_β}

The rolling-moment-due-to-sideslip, better known as the dihedral effect, is the most difficult derivative to achieve similitude due to compressibility effects, and is also the sum of various contributions. The same equation, Equation 8.23, is used for the wing-fuselage contribution as the horizontal tail-fuselage contribution, using the respective parameters.

$$\begin{aligned} C_{l_{\beta_{wf}}} = 57.3 \Bigg[& C_{L_{wf}} \left\{ (C_{l_\beta}/C_L)_{\Lambda_{C/2}} (K_{M_\Lambda})(K_f) + (C_{l_\beta}/C_L)_A \right\} + \Gamma \left\{ (C_{l_\beta}/\Gamma) K_{M_\Gamma} + \right. \\ & \left. + (\Delta C_{l_\beta}/\Gamma) + (\Delta C_{l_\beta})_{z_w} + (\varepsilon_t \tan \Lambda_{c/4}) \left\{ (\Delta C_{l_\beta})/\varepsilon_t \tan \Lambda_{c/4} \right\} \right] \end{aligned} \tag{8.23}$$

To isolate the contribution of the horizontal tail, as the fuselage contribution is already considered in the wing-fuselage contribution, Equation 8.24 is utilised.

$$C_{l_{\beta_h}} = (C_{l_{\beta_{hf}}}) \cdot \frac{S_h \cdot b_h}{S \cdot b} \tag{8.24}$$

Finally, the vertical tail contribution is, similarly to $C_{n_{\beta_v}}$, computed as a function of $C_{y_{\beta_v}}$, using Equation 8.25:

$$C_{l_{\beta_v}} = C_{y_{\beta_v}} \left\{ \frac{z_v \cos\alpha - l_v \sin\alpha}{b} \right\} \tag{8.25}$$

8.2.2.4. Final results

The final stability derivatives computed are outlined in Table 8.2, and are all of the desirable sign to maintain lateral stability. Nevertheless, there are some discrepancies in the derivatives between the full-scale aircraft and the model.

Due to sideforce-due-to-sideslip derivative being entirely dependent on geometry, there is no difference between the full-scale aircraft and the model. There is a slight difference in the yawing-moment-due-to-sideslip derivatives, as there is a factor dependent on Reynold's number with respect to the fuselage contribution, however, this doesn't have too sizeable of an effect, resulting in only a 3.29% divergence. As previously mentioned, the rolling-moment-due-to-sideslip diverges the most as there are a number of factors that are dependent on compressibility.

As outlined in section 5.1, of the three possible scaling methods for similitude, one had to be chosen at the expense of the other two, which resulted in Froude scaling being utilised over Mach scaling and Reynold's scaling, as to maintain kinematic similitude.

Table 8.2: Lateral stability derivatives

Stability derivative	Elysian E9X (full-scale)	Model	Difference [%]
$C_{y_{\beta_w}}$	-0.0258	-0.0258	-
$C_{y_{\beta_f}}$	-0.357	-0.357	-
$C_{y_{\beta_v}}$	-0.704	-0.704	-
C_{y_β}	-1.09	-1.09	-
$C_{n_{\beta_w}}$	-	0	-
$C_{n_{\beta_f}}$	-0.0301	-0.0249	- 20.9
$C_{n_{\beta_v}}$	0.182	0.182	-
C_{n_β}	0.152	0.157	+ 3.29
$C_{l_{\beta_{wf}}}$	-0.0393	-0.0305	- 28.9
$C_{l_{\beta_h}}$	-0.00158	-0.00143	- 10.5
$C_{l_{\beta_v}}$	-0.0619	-0.0619	-
C_{l_β}	-0.103	-0.0938	- 9.81

8.3. Control surfaces

This section covers the approach to sizing of the model's control surfaces. Firstly, a theory behind a local change of lift is explained in subsection 8.3.1. Then ailerons, elevators and rudder sizing are discussed in subsections 8.3.2, 8.3.3 and 8.3.4 respectively. Then, a sensitivity analysis of the results is performed in subsection 8.3.5.

8.3.1. Control surface theory

The control surfaces allow to steer the aircraft by changing lift force locally, using a large moment arm, to obtain a rotating force moment. The local change of a wing lift force is found in the following way

[55, pp.659]:

$$\Delta C_L = C_{L_\alpha} \tau \delta \tag{8.26}$$

Where δ is the deflection angle (angle of attack) of the control surface and τ is a control surface angle of attack effectiveness parameter dependent on a control surface-to-lifting surface chord ratio. This dependence is shown in figure 8.2.

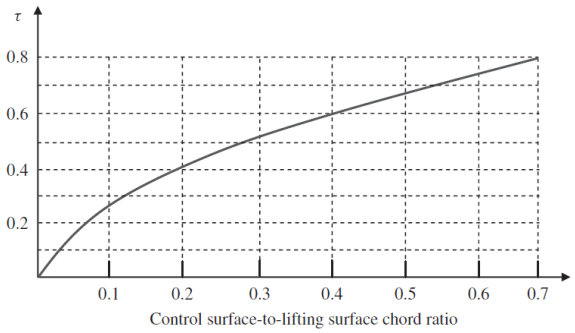

Figure 8.2: Control surface angle of attack effectiveness parameter (τ)

8.3.2. Ailerons

Ailerons allow aircraft control in the roll axis. It is obtained by a pair of control surfaces close to wing tips deflected in opposite directions. The total rolling moment due to ailerons opposed by the drag moment force and wing damping effect results in rotational acceleration in the roll axis. The equation of motion in that axis is presented in equation 8.27.

$$I_{xx} \cdot \dot{p} = L_{aileron} - L_{drag} - L_{damping} \tag{8.27}$$

This simplified equation shows the relation of aircraft's rate of roll change ($\dot{p}$) due to aileron's moment force $L_{aileron}$, which is opposed by drag moment L_{drag}. Both of these components were found using theory found in Sadraey's [55, pp.658–660]. Damping moment $L_{damping}$, although less significant, is included. The damping equation was found in another design approach found by Snorri Gudmundsson [27, pp.993]. Each of the components is expanded below.

$$L_{aileron} = \rho V^2 C_{L_{\alpha_{wing}}} \tau \delta_a \int_{b_1}^{b_2} c(y) y dy = \frac{1}{2} \rho V^2 S b C_{l_{\delta_a}} \tag{8.28}$$

$$L_{drag} = \frac{1}{2} \rho p^2 C_{D_R} (2 \int_{b_{root_{wing}}}^{\frac{b_{wing}}{2}} c_{wing}(y) y^3 dy + 2 \int_{b_{root_{hortail}}}^{\frac{b_{hortail}}{2}} c_{hortail}(y) y^3 dy + \int_{b_{root_{vertail}}}^{b_{vertail}} c_{vertail}(y) y^3 dy) \tag{8.29}$$

$$L_{damping} = \rho V p \frac{(c_{l_\alpha} + c_{d_0})}{b} \int_0^{b/2} y^2 c(y) dy \tag{8.30}$$

Equation 8.28 uses the theory explained in subsection 8.3.1 applied to a wing section with a rate of change of lift coefficient over angle of attack $C_{L_{\alpha_{wing}}}$. In this equation ailerons stretch between two chords of a wing distanced from the aircraft's X axis by b_1 and b_2 respectively and are deflected by the angle δ_a. The local chord length at distance y from the X axis is described as $c(y)$. Equation 8.29 is a summation of drag moments from wing, horizontal tail and vertical tail. The drag coefficient C_{D_R} value is conservatively assumed to be 1.2, as it is the higher range provided by Sadraey [55, pp.658]. Since no approximation for y_D is given in the source, the original formula was adjusted to sum drag force moments of infinitely thin sections by integration. The drag force was calculated based on the airspeed component normal to the wing plane. The integrations are performed from the root chords of each lifting surface to their tip. Equation 8.30 is found by considering a change to angle of attack due to aircraft's rolling [27, pp.993]. As the Elysian E9X aileron sizes and positions are known, these values

and appropriately scaled down values for the SFD are used. By performing a numerical integration of the equation of motion over time, time-to-bank was found. This was done using dimensions and estimated aerodynamic coefficients for both the Elysian E9X and the SFD assuming higher range mass moment of inertia, as it requires more force moment to rotate.

Elysian E9X aileron control analysis

The maximum aileron design deflection angle of Elysian E9X is not known. It was decided that Elysian E9X fits aircraft class III [55, pp.641–643] criteria and that it is a "very comfortable" (level 1) aircraft. Therefore, taking the most conservative values from Sadraey, the aircraft should be able to perform a 30° turn in 2 seconds for the take-off, landing configurations and other demanding circumstances (class B), and in 2.5 seconds for other, less demanding circumstances (class C). Therefore, it was decided to identify possibly most crucial parameters, so conservative assumptions could be made. As while performing numerical simulations it became obvious that the drag and damping forces are significantly lower than the force moments coming from ailerons, only this factor was taken into account. The only parameters not dependent on the aircraft's geometry are the dynamic pressure, mass moment of inertia and the $C_{L_{\alpha_{wing}}}$. The dynamic pressure is constant nevermind the altitude of an airport. It was decided that the influences of payload change are negligible, as Elysian E9X is a battery-powered aircraft with heavy, immovable batteries placed in wings, and therefore have the biggest influence on the weight and mass moment of inertia. That concludes that the take-off dynamic pressure should not change, and so should not the mass moment of inertia. The remaining parameter, $C_{L_{\alpha_{wing}}}$, is dependent on the angle of attack and Reynolds number. For this factor, conservative (α=$\alpha_{stall} - 2°$, stall speed, airport altitude $1000m$) value of $0.0716\frac{1}{°}$ is assumed. With these assumptions, to obtain a bank angle of 30° within 2 seconds, required deflection angle rounded up to the integer of 23° was found. For the less demanding conditions, the time requirement is lower (2,5s). Assuming the conservative lower value of dynamic pressure used in the first calculations (requiring higher lift coefficient) and the same low value of $C_{L_{\alpha_{wing}}}$, it becomes obvious that a lower value of deflection angle is required, and that is 15°. For the typical cruise conditions, to achieve a bank angle of 30° within 2 seconds, a deflection of 6° was found to be sufficient.

For the sub-scale version of the aircraft, the same bank angles as described above can be achieved quicker, almost exactly as according to Froude's scaling (within 31.1% of the original scale). The same conclusion can be drawn by performing the simulation. Therefore, scaled similitude was achieved. Using the Froude's scaling, similitude can be achieved in the way the aeroplane reacts to the control surfaces by scaling the control surface deflections by 0.097. Required deflection values for all mentioned situations are presented in table 8.3. Additionally, a comparison between sample Elysian E9X reaction to aileron deflection and SFD reaction to scaled aileron deflection is shown in figures 8.3 and 8.4. It is important to mention however, that despite matching control reaction speeds, times related to aircraft's passive stability are scaled.

Table 8.3: Aileron response summary

Aircraft	2s to 30°, take-off/landing	2.5s to 30°, take-off/landing	2.5s to 30°, cruise
Elysian E9X	23.0°	15.0°	6.0°
SFD	2.3°	1.5°	0.6°

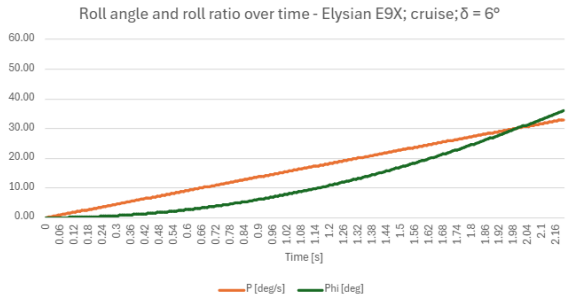

Figure 8.3: Roll angle and roll ratio change over time for Elysian E9X

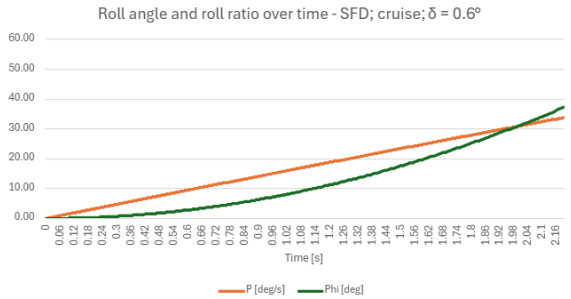

Figure 8.4: Roll angle and roll ratio change over time for the SFD

Control derivative

Using the obtained aileron moment force values, a control derivative of ailerons was found. This derivative is crucial for assessing the aileron's effectiveness, crosswind resistance and calculations of the system's reaction to aileron deflection for dynamic stability. The derivative is defined as presented in equation 8.31

$$C_{l_{\delta_a}} = \frac{L_{aileron}}{\frac{1}{2}\rho V^2 S b \delta_a} \tag{8.31}$$

The values found do not differ much between the SFD and the Elysian E9X. That is due the fact, that after applying scaling the only differing factor is the wing lift slope. The values found are presented in table 8.4

Table 8.4: Aileron control derivative values

	Elysian E9X	SFD
$C_{l_{\delta_a}}$	0.33833	0.33850

Stall characteristics

Ailerons are vulnerable to stall, which could lead to lose of manoeuvrability. To make sure the aircraft is manoeuvrable under the typical mission profile, a maximum deflection angle was found [55, pp.675]. This was done based on the stall angle of attack provided in Table 5.5, aileron to lifting surface chord ratio and a margin of 2° to the stall angle of attack, as it is a limit critical to safety. The obtained possible deflections within specifc angles of attack are presented in table 8.5

Table 8.5: Maximum Angle of Attack for various Aileron Deflections

δ_a [°]	0	5	10	15	20	25	30
α_{max} [°]	14.7	13.6	12.6	11.5	10.5	9.4	8.3

Based on this table, it is seen that the maximum angle of attack to fly on while using the aileron deflection found to be the one used by Elysian E9X is 9.4°. The value can be raised to 13.63° in case of scaling the SFD's aileron deflection down to ressemble the Elysian E9X behaviour.

Crosswind requirement

The crosswind causes aircraft's rolling, which has to be overcome by the ailerons. For these calculations, crosswind value of $6\frac{m}{s}$ is used based on section 12.6. By assumption that the rolling moment due sideslip is equal to the rolling moment due ailerons, the following required deflection formula was found:

$$\delta_a = -\frac{C_{l_\beta}}{C_{l_a}} atan(\frac{V_{crosswind}}{V_{TAS}}) \tag{8.32}$$

For the take-off configuration (the most vulnerable one), a required deflection of 3.74° was found. By combining it with the take-off deflection angle of Elysian E9X for preserving similitude, a required deflection angle of 26.8° was found, which allows for operations under the angle of attack of 8.3° with a reserve of 10,6% of maximum deflection, and therefore it was concluded that the aircraft is capable of operating during crosswind.

8.3.3. Elevator sizing

Take-off

The elevator is a control surface on the trailing edge of the horizontal tail, which can deflect upwards and downwards to change the camber of the horizontal tail and thus the tail lift coefficient C_{L_h}. It is crucial with respect to the longitudinal stability and trim of the aircraft, through changing the tail plane lift and thus the tail plane pitching moment. The elevator sizing method outlined in [55] was employed

Firstly, a number of parameters have to be selected for the sizing, namely the take-off rotation requirement, the elevator to tail span ratio and the maximum elevator deflection. The required take-off pitch angular acceleration for a remote control model aircraft is $(10-15)\,^\circ/s^2$, thus, to be conservative, a value of $15\,^\circ/s^2$ was chosen. Furthermore, a maximum deflection of $-25\,^\circ$ (up) and $+20^\circ$ (down) was chosen and the Elysian E9X has an elevator to tail span ratio of 1.

In order to find the required tail lift at take-off to achieve the selected angular acceleration, the relevant contributing pitch moments at are computed and plugged into Equation 8.33, from which C_{L_h} can subsequently be found using Equation 8.34:

$$L_{\mathrm{h}} = \frac{\left[L_{\mathrm{wf}}\left(x_{\mathrm{mg}} - x_{\mathrm{ac_{wf}}}\right) + M_{\mathrm{ac_{wf}}} + ma\left(z_{\mathrm{cg}} - z_{\mathrm{mg}}\right) + W\left(x_{\mathrm{mg}} - x_{\mathrm{cg}}\right) + D\left(z_D - z_{\mathrm{mg}}\right) + T\left(z_T - z_{\mathrm{mg}}\right) - I_{yy\mathrm{mg}}\ddot{\theta}\right]}{x_{\mathrm{ac_h}} - x_{\mathrm{mg}}} \tag{8.33}$$

$$\therefore\ L_h = -18.96\,N$$

$$C_{L_{\mathrm{h}}} = \frac{2L_{\mathrm{h}}}{\rho_{\mathrm{o}} V_{\mathrm{R}}^2 S_{\mathrm{h}}} = -0.208 \tag{8.34}$$

Considering $\alpha_h = -0.1599\,rad$ and $C_{L_{\alpha h}} = 4.22\ rad^{-1}$, the angle of attack effectiveness of the elevator, τ_E, is then found using Equation 8.35

$$\tau_{\mathrm{e}} = \frac{\alpha_{\mathrm{h}} + \left(C_{L_{\mathrm{h}}}/C_{L_{\alpha\mathrm{h}}}\right)}{\delta_{\mathrm{E_{max}}}} = 0.479 \tag{8.35}$$

According to Figure 8.2, this means that an elevator to tail chord ratio of 0.26 is required.

Longitudinal trim

In order to calculate the elevator deflection required to maintain longitudinal trim, the elevator effectiveness derivatives have to be found using Equation 8.36, Equation 8.37 and Equation 8.38.

$$C_{\mathrm{m}_{\delta\mathrm{E}}} = -C_{L_{\alpha\mathrm{h}}}\eta_{\mathrm{h}} \cdot \overline{V}_{\mathrm{H}} \cdot \frac{b_{\mathrm{E}}}{b_{\mathrm{h}}}\tau_{\mathrm{e}} = -2.037 \tag{8.36}$$

$$C_{L_{\delta\mathrm{E}}} = C_{L_{\alpha\mathrm{h}}}\eta_{\mathrm{h}}\frac{S_{\mathrm{h}}}{S} \cdot \frac{b_{\mathrm{E}}}{b_{\mathrm{h}}}\tau_{\mathrm{e}} = 0.3948 \tag{8.37}$$

$$C_{L_{\mathrm{h}\delta\mathrm{E}}} = C_{L_{\alpha\mathrm{h}}}\tau_{\mathrm{e}} = 2.024 \tag{8.38}$$

Using Equation 8.39, the elevator deflection required for cruise conditions is found to be:

$$\delta_{\mathrm{E}} = -\frac{\left(\frac{T \cdot z_T}{\bar{q} \cdot S \cdot \bar{C}} + C_{\mathrm{m_o}}\right) C_{L_\alpha} + (C_{L_1} - C_{L_\mathrm{o}}) C_{\mathrm{m}_\alpha}}{C_{L_\alpha} C_{\mathrm{m}_{\delta\mathrm{E}}} - C_{\mathrm{m}_\alpha} C_{L_{\delta\mathrm{E}}}} = -7.35\,^\circ \tag{8.39}$$

8.3.3.1. Stall

Finally, a check must be performed to ensure the tail does not stall during take-off. The tail angle of attack at take-off can be found using Equation 8.40, which yields:

$$\alpha_{\mathrm{h_{TO}}} = \alpha_{\mathrm{TO}} \left(1 - \frac{\mathrm{d}\varepsilon}{\mathrm{d}\alpha}\right) + i_{\mathrm{h}} - \varepsilon_{\mathrm{o}} = -4.97\,^\circ \tag{8.40}$$

The stall angle of the horizontal tail when the elevator is deflected can be found using Equation 8.41, where $\alpha_{\mathrm{h_{s;\delta E=0}}}$ is the stall angle when there is no elevator deflection and $\Delta\alpha_{\mathrm{h_E}}$ the reduction in stall angle due to the elevator deflection, which, for an elevator to tail chord ratio of 0.26 and maximum deflection of 25 °, is 4.18 °.

$$\alpha_{\mathrm{h_s}} = \pm\left(\alpha_{\mathrm{h_{s;\delta E=0}}} - \Delta\alpha_{\mathrm{h_E}}\right) = \pm 9.82\,^\circ \tag{8.41}$$

Since the tail angle of attack at the end of rotation is less than half of the stall angle, the horizontal tail does not stall during take-off.

Final elevator design

The final design for the elevator can be seen in Figure 8.5. Despite not requiring a positive (downwards) deflection for this exact configuration due to the relative positions of the aerodynamic centre and the chosen centre of gravity, however, the decision was made to maintain the $+\delta_{E_{max}}$ of +20 °, should Elysian want to test different centre of gravity positions, in which case they most likely will need positive deflections of the elevator.

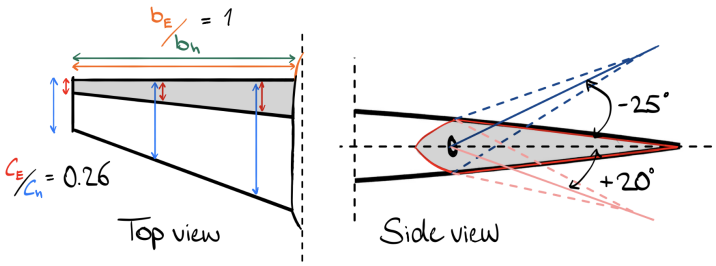

Figure 8.5: Final elevator design

8.3.4. Rudder sizing

To size the rudder, Sadraey's approach from Aircraft Design[55] has been used. It shows the most crucial directional trim authority cases. For this six-propeller demonstrator, that is, a low-speed asymmetric thrust and crabbed cross-wind landing. It then confirms that the needed deflection does not stall the vertical tail. For this calculation, the rudder is treated as a displacement control surface. The trim checks use the standard non-dimensional yawing-moment and side-force models applied by Sadraey for rudder design[55], and the data that is obtained from Flow5.

8.3.4.1. Reference geometry and rudder limits

The wing reference quantities used to non-dimensionalise forces and moments are kept consistent with the lateral-directional derivative dataset

$$S = 1.943\ \mathrm{m}^2, \qquad b = 5.60\ \mathrm{m} \tag{8.42}$$

The vertical tail geometry is taken from the aircraft configuration model

$$S_V = 0.204\ \text{m}^2, \qquad b_V = 0.491\ \text{m}, \qquad l_V = 1.494\ \text{m} \tag{8.43}$$

where l_V is measured from the aircraft CG to the vertical-tail aerodynamic centre, where the CG point is taken from Figure 8.1 and the aerodynamic centre is taken from FLow5. The maximum rudder deflection is limited to

$$\delta_{R,\text{max}} = \pm 25^\circ \tag{8.44}$$

and is consistent with typical preliminary rudder limits[55].

The vertical-tail aspect ratio is computed directly from the tail span and planform area

$$AR_V = \frac{b_V^2}{S_V} \tag{8.45}$$

Using $b_V = 0.491$ m and $S_V = 0.204\ \text{m}^2$, the resulting vertical-tail aspect ratio is

$$AR_V = 1.18. \tag{8.46}$$

This value is reported to document the tail planform slenderness used in the design and analysis.

To remain consistent with the aerodynamic dataset used to build the lateral-directional derivatives, the vertical-tail lift-curve slope is calculated by

$$C_{L\alpha V} = \frac{2\pi AR}{AR + 2} \tag{8.47}$$

With $AR_V = 1.18$, the resulting slope is

$$C_{L\alpha V} = 2.33\ \text{rad}^{-1} \tag{8.48}$$

8.3.4.2. Aerodynamic derivatives used in the trim equations

The rudder yaw control power is the derivative of the yawing-moment coefficient with respect to rudder deflection[55],

$$C_{n_{\delta R}} = \frac{\partial C_n}{\partial \delta_R} \tag{8.49}$$

and is used in the linearised yawing-moment model.

The rudder control derivatives $C_{n_{\delta R}}$ and $C_{y_{\delta R}}$ are taken directly from subsection 8.2.2 rather than being re-estimated using Sadraey's semi-empirical expressions. Because the derivatives are imported from the lateral-stability analysis, the cross-wind trim does not use the auxiliary estimation factors K_{f1}, K_{f2}, or the sidewash gradient $d\sigma/d\beta$ that appear in Sadraey's approximate derivative build-up formulas[55].

The derivative values used in the trim checks (per radian) are:

$$\begin{aligned} C_{n_{\delta R}} &= -0.0775\ \text{rad}^{-1}, & C_{y_{\delta R}} &= 0.291\ \text{rad}^{-1}, \\ C_{n\beta} &= 0.152\ \text{rad}^{-1}, & C_{y\beta} &= -0.734\ \text{rad}^{-1} \end{aligned} \tag{8.50}$$

8.3.4.3. Case 1: Asymmetric thrust directional trim at low speed

In this case, the propellers are turned off on one wing, which creates an asymmetric thrust that the rudder needs to counteract to still fly in a controllable straight line. A low-speed situation will be looked at, which would be the hardest one to control. For minimum-control evaluation, the minimum controllable speed is selected as a fraction of stall speed:

$$V_{MC} = 0.8\, V_s. \tag{8.51}$$

Using $V_s = 22$ m/s, the minimum controllable speed is $V_{MC} = 17.6$ m/s. At sea level ($\rho = 1.225\ \text{kg/m}^3$), the dynamic pressure at V_{MC} is

$$q_{MC} = \frac{1}{2}\rho V_{MC}^2 \tag{8.52}$$

which gives $q_{MC} = 189.7\ \mathrm{N/m^2}$.

The asymmetric yawing moment is computed by summing each operating propeller thrust contribution about the CG.

$$N_{\text{asym}} = \sum \left(T_{\text{p}}\ y_T \right) \tag{8.53}$$

Using $T_{\text{op}} = 23.29$ N and the thrust arm set in Figure 8.1 corresponding to $(0.446 + 2 \cdot 0.446 + 3 \cdot 0.446)$ m, the resulting asymmetric yawing moment is

$$N_{\text{asym}} = 62.32\ \mathrm{N\,m} \tag{8.54}$$

The trim requirement for asymmetric thrust is checked by moment equilibrium between the asymmetric yawing moment and the aerodynamic yawing moment generated by rudder deflection. Using a non-dimensional yawing-moment definition, $N_A = qSbC_n$ and linear dependence on rudder deflection, the required rudder deflection is obtained from[55]

$$\delta_{R,\text{asym}} = \frac{N_{\text{asym}}}{-q_{MC} S b\, C_{n_{\delta R}}} \tag{8.55}$$

With $N_{\text{asym}} = 62.32$ N m, $q_{MC} = 189.7\ \mathrm{N/m^2}$, $S = 1.943\ \mathrm{m^2}$, $b = 5.60$ m, and $C_{n_{\delta R}} = -0.0775\ \mathrm{rad^{-1}}$, the required rudder deflection is

$$\delta_{R,\text{asym}} = 0.389\ \mathrm{rad} = 22.32^\circ \tag{8.56}$$

Since $22.32^\circ < \delta_{R,\max} = 25^\circ$, the asymmetric-thrust trim requirement is satisfied.

8.3.4.4. Case 2: Cross-wind landing trim in a crabbed approach

The next case simulates a cross-wind landing as a crabbed approach, in which the wind induces a side force on the projected side area S_S. The trim unknowns are the rudder deflection δ_R and the crab angle σ. In Figure 8.6, the situation of a cross-wind landing is shown.[55].

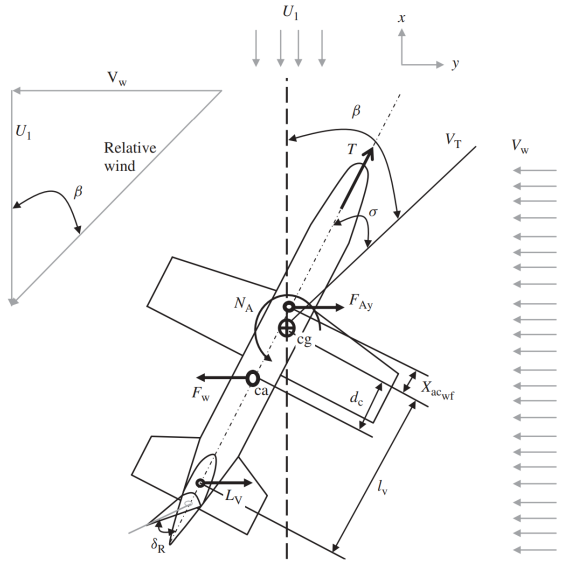

Figure 8.6: Top View of Cross-Wind Crabbed Landing Showing Forces and Angles[55]

The approach speed and cross-wind speed are

$$U_1 = 26.4\ \mathrm{m/s}, \qquad V_W = 6\ \mathrm{m/s} \tag{8.57}$$

The total airspeed and wind-induced sideslip are

$$V_T = \sqrt{U_1^2 + V_W^2}, \qquad \beta = \tan^{-1}\left(\frac{V_W}{U_1}\right) \tag{8.58}$$

Using the above values yields $V_T = 27.07$ m/s and $\beta = 0.2235$ rad $= 12.80°$. The dynamic pressures are defined as $q_T = \frac{1}{2}\rho V_T^2$ and $q_W = \frac{1}{2}\rho V_W^2$, giving $q_T = 448.9$ N/m^2 and $q_W = 22.05$ N/m^2.

The wind side force is modelled as a drag-like force on the projected side area

$$F_w = \frac{1}{2}\rho V_W^2 S_S C_{Dy} \tag{8.59}$$

Using $S_S = 1.324$ m^2, $C_{Dy} = 0.60$, and $\rho = 1.225$ kg/m^3 yields $F_w = 17.52$ N. The side-area centroid arm about the CG is $d_c = 0.21$ m, by taking the side area of the fuselage and the side area of the vertical tail together with their respective centres.

Sadraey's crabbed cross-wind trim uses yaw-moment and side-force equilibrium[55].

$$\begin{aligned} &\frac{1}{2}\rho V_T^2 S b\Big(C_{n0} + C_{n\beta}(\beta - \sigma) + C_{n_{\delta R}}\delta_R\Big) + F_w d_c \cos(\sigma) = 0, \\ &\frac{1}{2}\rho V_W^2 S_S C_{Dy} - \frac{1}{2}\rho V_T^2 S\Big(C_{y0} + C_{y\beta}(\beta - \sigma) + C_{y_{\delta R}}\delta_R\Big) = 0 \end{aligned} \tag{8.60}$$

With $C_{n0} \approx 0$ and $C_{y0} \approx 0$, and with $C_{n\beta}$, $C_{y\beta}$, $C_{n_{\delta R}}$, and $C_{y_{\delta R}}$, solving these coupled equations yields

$$\delta_{R,\mathrm{cw}} = -0.199 \text{ rad} = -11.39°, \qquad \sigma = 0.330 \text{ rad} = 18.88° \tag{8.61}$$

The cross-wind trim requirement is therefore satisfied because $|\delta_{R,\mathrm{cw}}| = 11.39° < 25°$.

8.3.4.5. Resulting rudder geometry

The deflection that will determine the rudder geometry is the largest deflection of the asymmetric-thrust and cross-wind requirements

$$\delta_{R,\mathrm{req}} = \max\big(|\delta_{R,\mathrm{asym}}|,\ |\delta_{R,\mathrm{cw}}|\big) \tag{8.62}$$

Using the results above gives $\delta_{R,\mathrm{req}} = 22.32°$, so the asymmetric-thrust case is limiting.

The rudder planform is then set by the selected preliminary geometry ratios relative to the vertical tail[55]. With $b_R/b_V = 1.0$ and $C_R/C_V = 0.30$, the rudder area is

$$S_R = \left(\frac{b_R}{b_V}\right)\left(\frac{C_R}{C_V}\right) S_V. \tag{8.63}$$

Using $S_V = 0.204$ m^2 yields $S_R = 0.0612$ m^2. The corresponding mean chords and span are obtained from

$$C_V = \frac{S_V}{b_V}, \qquad C_R = \left(\frac{C_R}{C_V}\right) C_V, \qquad b_R = \left(\frac{b_R}{b_V}\right) b_V \tag{8.64}$$

which gives $C_V = 0.415$ m, $C_R = 0.1246$ m, and $b_R = 0.491$ m.

8.3.4.6. Vertical-tail stall margin check

Sadraey recommends checking whether the applied control surface deflection reduces the tail stall angle enough to cause tail stall during the controlling manoeuvre[55].

The allowable vertical-tail stall angle with rudder applied is calculated by

$$\alpha_{vs,\mathrm{allow}} = \alpha_{vs,\delta_R=0} - \Delta\alpha_{vR} \tag{8.65}$$

Using $\alpha_{vs,\delta_R=0} = 14°$ and using $\Delta\alpha_{vR} = 4.2°$ for a chord ratio of $C_R/C_V = 0.30$ at a representative large deflection yields $\alpha_{vs,\mathrm{allow}} = 9.8°$

In the crabbed cross-wind condition, the effective vertical-tail incidence is approximated as the relative flow angle at the tail,

$$\alpha_{v,\mathrm{eff}} \approx (\beta - \sigma) \tag{8.66}$$

which, using a assumed conservative vertical tail stall angle $\beta = 12.80°$ and $\sigma = 18.88°$ both obtained from Sadraey[55], gives $\alpha_{v,\mathrm{eff}} = -6.08°$. The stall margin is therefore

$$\alpha_{vs,\mathrm{allow}} - \left|\alpha_{v,\mathrm{eff}}\right| = 3.72° \tag{8.67}$$

which remains above a conservative 2° buffer that is also defined in Sadraey[55].

After the rudder size passed all the situations, this is the resulting rudder geometry: $S_R = 0.0612$ m^2, $b_R = 0.491$ m, $C_R = 0.1246$ m, with a governing trim requirement of $\delta_{R,\text{req}} = 22.32°$. Both the asymmetric-thrust and cross-wind landing trim checks are satisfied, and the vertical-tail stall margin remains positive under the evaluated conditions. The final geometry is also shown in Figure 8.7.

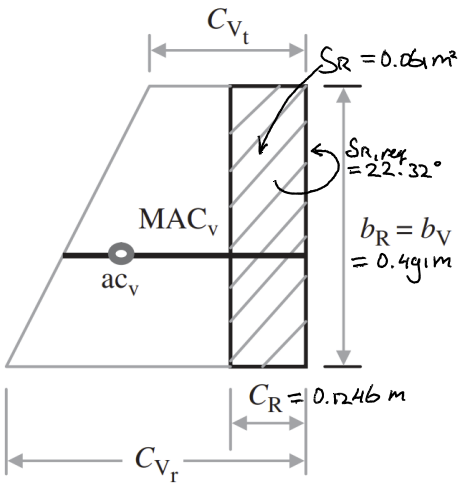

Figure 8.7: Vertical Tail and Rudder Geometry (Side View)

8.3.5. Sensitivity analysis

A dead band width is a metric for servomechanisms that expresses possible servo's position error. For the actuator's choice mentioned in section 7.2.3, it was identified that the dead band width is equal to $3\mu s$, while having a running degree of 270° for the pulse width range of 500-2500μs. This means the servo rotates by 0.135° per each width of $1\mu s$, and therefore the actuator's position is subject to an error of 0.4 °. By performing a numerical integration for this aileron deflection angle and the lower range of model's inertia (for quicker, conservative situation), it was found that it leads to a bank angle of 22° within 2 seconds of no correction applied. A graph representing the reaction is shown in figure 8.8. It is however worth to notice that the range of aileron's deflection angle is significantly lower than 270°. A suggested solution to this problem is creation of a mechanism that lowers the effective running degree, for example by using different gearwheels in the servomechanism.

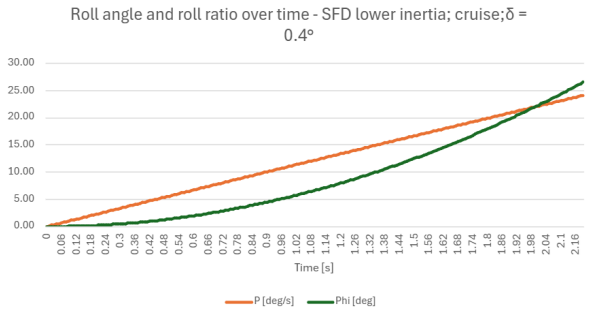

Figure 8.8: Roll reaction to a dead band width error

8.4. Dynamic stability

An analysis of model's dynamic stability has been decided to be performed. The goal of this analysis is to asses the similitude of the SFD to Elysian E9X dynamic stability. For this purpose, the stability derivatives were found first in subsection 8.4.1. Then, equations of motion and the aeroplane's dynamic model was found in 8.4.2. The final similitude and discussion are presented in subsection 8.4.3.

8.4.1. Stability derivatives

The main tool for dynamic stability derivatives was Flow5 described in subsection 5.2.1. This software calculates all of the derivatives using a panel method. Although this method appears to provide results close to reality[1], it was found it was not capable of calculating second order derivatives $C_{Z_{\dot{\alpha}}}$, $C_{m_{\dot{\alpha}}}$ and assumes their values to be 0[2]. Additionally, Flow5 does not account for the propulsion influence, which is going to be approximated.

Second derivative approximations

Etkin and Reid provide the following approximations for $C_{Z_{\dot{\alpha}}}$ and $C_{m_{\dot{\alpha}}}$ [23, pp.155]:

$$C_{Z_{\dot{\alpha}}} = -2C_{L_{\alpha_{hortail}}} V_h \frac{\delta\epsilon}{\delta\alpha} \tag{8.68}$$

$$C_{m_{\dot{\alpha}}} = -2C_{L_{\alpha_{hortail}}} \frac{l_h}{c_{MAC}} V_h \frac{\delta\epsilon}{\delta\alpha} = -2C_{L_{\alpha_{hortail}}} \frac{S_w}{S_h} V_h^2 \frac{\delta\epsilon}{\delta\alpha} \tag{8.69}$$

The equation 8.69 was transformed using the tail volume equation. Majority of the variables were able to be taken from Flow5, although the downwash effect $\frac{\delta\epsilon}{\delta\alpha}$ was not easily obtainable. In literature the following equation was found [55, pp.310]:

$$\frac{\delta\epsilon}{\delta\alpha} = \frac{2C_{L_{\alpha_{wing}}}}{\pi AR} \tag{8.70}$$

Using aircraft's geometry and values known from Flow5, the following approximations were found and presented in table 8.8

Table 8.6: Aerodynamic stability second derivatives comparison between the full-scale and subscale.

Aircraft Type	$\frac{\delta\epsilon}{\delta\alpha}$	$C_{Z_{\dot{\alpha}}}$	$C_{m_{\dot{\alpha}}}$
Elysian E9X	0.25567	−1.60922	−7.00296
SFD	0.25564	−1.60900	−7.01219

Comparison of stability derivatives between aeroplanes

An approximation of dynamic stability coefficients was performed by performing VLM2 simulations using Flow5. The values were found for both Elysian E9X and the model during cruise conditions. The values are presented in table 8.7

Table 8.7: Comparison of Aerodynamic Stability Derivatives (VLM2 + second derivative approximations)

Derivative	Elysian E9X	SFD	Diff. (%)
C_{X_u}	−0.03433	−0.03433	0.00000
C_{Z_u}	−0.05628	−0.02500	−55.58584
C_{m_u}	−0.17716	−0.17716	−0.00056
C_{X_α}	0.43741	0.43741	0.00000
C_{Z_α}	−5.01550	−5.01550	0.00000
C_{m_α}	−1.51498	−1.51498	0.00000
C_{X_q}	−1.25556	−1.25554	−0.00159
C_{Z_q}	−8.62472	−8.62466	−0.00070
C_{m_q}	−27.59030	−27.59020	−0.00036

Derivative	Elysian E9X	SFD	Diff. (%)
C_{Y_β}	−0.29603	−0.29603	0.00000
C_{l_β}	−0.12451	−0.12451	0.00000
C_{n_β}	0.04006	0.04006	0.00025
C_{Y_p}	−0.23133	−0.23133	−0.00086
C_{l_p}	−0.57975	−0.57975	−0.00017
C_{n_p}	−0.00494	−0.00494	0.00020
C_{Y_r}	0.10671	0.10672	0.00469
C_{l_r}	0.00056	0.00056	0.00755
C_{n_r}	−0.02894	−0.02894	0.00069
$C_{Z_{\dot{\alpha}}}$	−1.60922	−1.60900	−0.01369
$C_{m_{\dot{\alpha}}}$	−7.00296	−7.01219	0.13180

It is seen that all derivatives are close to each other except for C_{Z_u}. This could be explained by compressibility effects. Etkin provides approximations of the influence of the mach number [23, pp.155].

[1] https://www.Flow5.tech/docs/Flow5_Mode_Measurements.pdf, accessed on 20/01/2026
[2] https://github.com/techwinder/flow5/blob/main/fl5-lib/api/stabderivatives.h/#L59, acessed on 20/01/2026

The compressibility effects are seen to affect all speed derivatives: C_{X_u}, C_{Z_u}, and C_{m_u}. In this case, however, only C_{Z_u} seems to be influenced. According to the mentioned approximations, C_{Z_u} is heavily dependent on C_L, which is scaled by highly speed-dependent Prandtl-Glauert correction [3, pp.754], and therefore C_{Z_u} differs significantly. C_{X_u} however, is a parameter heavily dependent on drag. Since the aircraft is not reaching the drag divergence mach number, the difference of drag in this case is not significant [3, pp.766]. The value of C_{m_u} is heavily dependent on the moment coefficient C_m, on which the Prandtl-Glauert correction is applied as well. However, since aeroplanes are built in a way that lowers down the value of C_m and such that the tail force moment shall equalizes the main wing force moment, the effect of compressibility is not seen for the entire aircraft. The influence of this difference is going to be assessed in the further subsections.

Influence of propulsion

Based on literature, thrust-based corrections were found [23, pp.155]. They are presented in the equations below.

$$C_{x_u} = C_{x_u,0} + \Delta C_{x_u} = C_{x_u,0} + \frac{\delta C_T}{\delta u}(1 - \frac{\delta C_D}{\delta C_T}) \tag{8.71}$$

$$C_{Z_u} = C_{Z_u,0} + \Delta C_{Z_u} = C_{Z_u,0} - \frac{\delta C_T}{\delta u}\frac{\delta C_L}{\delta C_T} \tag{8.72}$$

$$Cm_u = C_{m_u,0} + \Delta Cm_u = C_{m_u,0} + \frac{\delta C_T}{\delta u}\frac{\delta C_m}{\delta C_T} \tag{8.73}$$

Various propulsion-related derivatives are present in the equation. The influence of thrust on lift and drag was already discussed in subsection 5.2.4. The $\frac{\delta C_L}{\delta C_T}$ and $\frac{\delta C_D}{\delta C_T}$ derivatives are computed using numerical differentiation based on a small increment of T_C using the equations presented in that subsection. It is important to note that the definition of the thrust coefficient T_C mentioned in the paper differs from the thrust coefficient C_T mentioned in equations 8.71 - 8.73. Therefore, the derivatives obtained in this calculation were multiplied by $\frac{S}{2D_p^2}$. The $\frac{\delta C_T}{\delta u}$ value was found by performing a numerical differentiation of data provided by JavaProp around speed of $43.8\frac{m}{s}$, which was discussed in section 7.1. The differentiation was done on the thrust coefficient T_C, which has the same definition as in the paper mentioned above. Therefore, the obtained result was also multiplied, by an inverse of the factor above (as C_T is not denominator, but numerator). The $\frac{\delta C_m}{\delta C_T}$ derivative was found by assuming the moment change is caused solely by the additional moment force a higher thrust produces. By derivation, it was found that it was equal to a negative ratio between an average of z-positions of motors relative to the centre of gravity divided by the mean aerodynamic chord. The minus sign in the front comes from the fact that if the average motor position is in the positive Z direction (see figure 8.1), the thrust generates a pitching down moment. A summary of all values found is shown below.

Table 8.8: Thrust derivatives values

$\frac{\delta C_T}{\delta u}$	$\frac{\delta C_L}{\delta C_T}$	$\frac{\delta C_D}{\delta C_T}$	$\frac{\delta C_m}{\delta C_T}$	ΔC_{x_u}	ΔC_{z_u}	ΔC_{m_u}
−0.00294	0.00000	−0.02446	0.01190	−0.00302	0.00000	0.00004

Using these approximations, the final values for the speed derivatives were found. The values and value changes are presented in table 8.9. The only visible change is made to C_{X_u}. Therefore, the propulsion is not expected to have a big influence on the aircraft's dynamic performance.

Table 8.9: Propulsion altered derivatives

Derivative	Value	Change
C_{X_u}	−0.03735	8.79%
C_{Z_u}	−0.02500	0.00%
C_{m_u}	−0.17720	0.02%

8.4.2. Stability model

The linearized equations of motion for an aircraft are derived by applying a small-perturbation analysis to the general rigid-body equations of motion. According to the methodology established by Etkin [23, pp.112–113], these equations are organized into a state-space format where the rate of change of the state vector is defined by the system matrix and the current states.

The motion is decoupled into two independent groups: the longitudinal and lateral-directional modes. The longitudinal state-space model is defined by the state vector $\mathbf{x}_{lon} = [u, w, q, \theta]^T$, representing forward speed increment, vertical speed increment, pitch rate, and pitch angle. The equations of motion are expressed in equation 8.74. The lateral-directional model governs asymmetric motion with the state vector $\mathbf{x}_{lat} = [v, p, r, \phi]^T$, representing lateral velocity (sideslip), roll rate, yaw rate, and roll angle. The corresponding state-space equations are presented in equation 8.75.

$$\begin{bmatrix} \dot{u} \\ \dot{w} \\ \dot{q} \\ \dot{\theta} \end{bmatrix} = \begin{bmatrix} X_u & X_w & 0 & -g\cos\theta_0 \\ Z_u & Z_w & u_0 & -g\sin\theta_0 \\ M_u + M_{\dot{w}}Z_u & M_w + M_{\dot{w}}Z_w & M_q + M_{\dot{w}}u_0 & 0 \\ 0 & 0 & 1 & 0 \end{bmatrix} \begin{bmatrix} u \\ w \\ q \\ \theta \end{bmatrix} \tag{8.74}$$

$$\begin{bmatrix} \dot{v} \\ \dot{p} \\ \dot{r} \\ \dot{\phi} \end{bmatrix} = \begin{bmatrix} Y_v & Y_p & Y_r - u_0 & g\cos\theta_0 \\ L_v & L_p & L_r & 0 \\ N_v & N_p & N_r & 0 \\ 0 & 1 & \tan\theta_0 & 0 \end{bmatrix} \begin{bmatrix} v \\ p \\ r \\ \phi \end{bmatrix} \tag{8.75}$$

In this matrix, the terms X, Z, and M are dimensional derivatives calculated from the non-dimensional coefficients derived from aerodynamic analysis in subsection 8.4.1. The physical forces and moments are in most cases reconstructed using the reference parameters of the aircraft:

- Forces (X, Y, Z) are typically scaled by $\frac{1}{m}\rho u_0 S$, where S is the wing area.
- Moments (L, M, N) are scaled by the inverse of the moment of inertia and the product $\rho u_0 S\bar{c}$, where $\bar{c}$ is the mean aerodynamic chord.

This mathematical structure allows the non-dimensional coefficients derived from subscale models or numerical methods to predict the dynamic stability modes, including the short-period and phugoid longitudinal modes, as well as the Dutch roll, spiral, and other rolling modes. The general response of the aircraft to impulses can be found by calculating eigenvalues of matrices.

8.4.3. Results

By calculating eigenvalues of the state-space equations it is possible to analyse the aircraft's stability. These were initially calculated using Flow5, and therefore excluding the propeller effect and the second derivative values. The values are presented are in table 8.4.3.

Table 8.10: Comparison of Dynamic Stability Eigenvalues (λ): Subscale vs. Full Scale

Mode Group	Subscale (SFD)		Full Scale (Elysian E9X)	
	Oscillatory / Fast	Slow / Non-Osc.	Oscillatory / Fast	Slow / Non-Osc.
Longitudinal	$-2.232 \pm 5.568i$	$-0.0010 \pm 0.2265i$	$-0.7121 \pm 1.754i$	$-0.0004 \pm 0.0713i$
Lateral	$0.0275 \pm 1.7921i$	$-2.824, -0.0258$	$0.0086 \pm 0.5610i$	$-0.8987, -0.0081$

Note: Longitudinal modes typically represent the Short Period and Phugoid modes; Lateral modes represent Dutch Roll, Roll Subsidence, and Spiral modes.

It is seen that despite the high difference in C_{Z_u}, all subscale eigenvalues differ from the full scale by the factor of $\frac{1}{\sqrt{0.097}}$. Therefore, the damped period and time to half amplitude values follow the Froude scaling, and therefore the similitude is preserved. It is however important to notice that the Dutch roll mode is unstable for both aircraft, and therefore it would be recommended to perform a deeper

investigation in this field.

Further calculations were performed to obtain a closer approximation of the eigenvalues, after applying the second derivatives and the effects of propulsion. The results are presented in table 8.11.

Table 8.11: Comparison of eigenvalues for different derivatives configurations

Configuration	Modes	Eigenvalues (λ)			
		λ_1	λ_2	λ_3	λ_4
Subscale	Longitudinal	$-2.232 - 5.568i$	$-2.232 + 5.568i$	$-0.001028 - 0.2265i$	$-0.001028 + 0.2265i$
	Lateral	-2.8516	-0.0259	$0.0275 + 1.7921i$	$0.0275 - 1.7921i$
Subscale - 2nd deriv.	Longitudinal	$-2.5760 + 5.4090i$	$-2.5760 - 5.4090i$	$-0.0020 + 0.2265i$	$-0.0020 - 0.2265i$
	Lateral	-2.8516	-0.0259	$0.0275 + 1.7921i$	$0.0275 - 1.7921i$
Subscale - 2nd deriv. + propulsion	Longitudinal	$-2.5760 + 5.4090i$	$-2.5760 - 5.4090i$	$-0.0020 + 0.2265i$	$-0.0020 - 0.2265i$
	Lateral	-2.8516	-0.0259	$0.0275 + 1.7921i$	$0.0275 - 1.7921i$

It is seen that applying the second derivative resulted in higher stability in the longitudinal modes. The propulsion does not have any significant influence on stability, and therefore the distributed propulsion is not an issue for dynamic stability. Moreover, a potential variable thrust distribution could aid in the Dutch roll stability maintaining by correcting the attitude.

8.4.4. Sensitivity analysis

Since the stability derivatives calculation is subject to error by various factors, such as uncertainty of Flow5 VLM2 method, imperfect surfaces or additional drag, a sensitivity analysis of the stability has to be performed. In order to have an overview of how the aircraft reacts to changes in each stability derivatives, a localized perturbation method was made.

A "One-at-a-Time" (OAT) perturbation is applied to each derivative. Let p be a baseline stability derivative and $\zeta(p)$ be the damping ratio of a specific mode. The derivative is perturbed by a factor $\Delta p = 0.01p$. The local damping sensitivity Index (S_D) is then calculated as the elasticity of the damping ratio:

$$S_D = \frac{\zeta(p + \Delta p) - \zeta(p)}{\zeta(p)} \cdot \frac{p}{\Delta p} \tag{8.76}$$

The resulting matrix $S \in \mathbb{R}^{m \times n}$ (where m is the number of derivatives and n the number of modes) provides a normalized heatmap. A magnitude $|S| > 1$ indicates that the mode stability is very sensitive to that specific aerodynamic parameter, highlighting vulnerable areas. A similar metric was defined for relative changes of the eigenvalues:

$$S_\lambda = -\frac{\lambda(p + \Delta p) - \lambda(p)}{|\lambda(p)|} \cdot \frac{p}{\Delta p} \tag{8.77}$$

It differs from equation 8.76 by the minus sign, as more negative values are desirable for increasing stability. The denominator is an absolute value of the eigenvalue, as eigenvalues can be both positive and negative. A summary of the most influential derivatives with respect to phugoid and Dutch roll is shown in table 8.12.

Table 8.12: Sensitivity of individual control derivatives

Stability mode	Dutch roll	Phugoid
Damping sensitivity	C_{Y_β} : 1.70; C_{l_β} : −4.09; C_{n_β} : 1.71; C_{l_p} : 5.40; C_{n_r} : 1.52	C_{X_u} : 3.11; C_{X_α} : 5.00; C_{X_α} : 1.76
Eigenfrequency sensitivity	C_{Y_β} : 1.69; C_{l_β} : −4.18; C_{n_β} : 1.33; C_{l_p} : 5.43; C_{n_r} : 1.52	C_{X_u} : 3.11; C_{X_α} : 5.00; C_{X_α} : 1.30

It was found that the drag related derivatives are the most influential for the phugoid mode. Since the Flow5 VLM2 does not account for extra drag, skin friction and underestimates the viscous effects, it is believed that values of these derivatives are higher in reality [3], and therefore lead to higher stability in the phugoid mode.

8.5. Verification and validation summary

This section covers the verification and validation approach and methods used through stability and control design and analysis. To ensure the reliability of calculations, verification and validation methods were applied to calculation tools. The requirements mentioned in table 8.13 were seen as the goals during the design process and verified through the process.

8.5.1. Verification and validation of calculation tools

For this chapter, various tools were created and used. The calculation tools included hand calculators, Python code, Excel sheets and Flow5 simulations. To ensure reliability, verification and validation methods were applied.

Verification

Each analysis and design step requires in-depth and complicated calculations, which are difficult to track. To ensure that the calculations are easily verifiable, they were divided into small blocks. As an example, instead of calculating the lift force in one equation, separate values such as the the dynamic pressure were calculated first. That ensures easy traceability and ease of performing unit tests. Thanks to that, each calculation could be easily verified for units compliance and whether results match values presented in worked out solutions in the literature.

Validation

To answer whether the tool created is the right tool, it was checked whether each of them meets the desired purpose, and therefore provide necessary values. As an example, Python flight dynamics simulation code was written and compared with results of Flow5, to make sure that for the sensitivity analysis the right tool calculating change of eigenfrequencies and damping ratios is used. Moreover, the created calculators were used to compute specific values for existent and well-documented aircraft. These values were compared to the ones provided in literature.

8.5.2. Compliance matrix verification

Table 8.13: Requirement compliance stability & control

ID	Requirement Description	Verification Method	Compliance Level
SFD-SYS-CNF-01	The aircraft shall encompass a Static Margin (SM) that matches the full-scale Elysian E9X target value within a tolerance of ±2% of the Mean Aerodynamic Chord (MAC).	Analysis	Based on literature study for conventional propeller aircraft with a T-tail, a SM of 0.05 is chosen.
SFD-SYS-CNF-02	The aircraft mass distribution shall provide non-dimensional radii of gyration (k_{xx}, k_{yy}, k_{zz}) that match the Elysian E9X values within ±5% to ensure dynamic similarity.	Analysis & Inspection	The model modularity capabilities allow for achieving a range of mass moments of inertia, including scaled approximated E9X data.
SFD-SYS-CNF-03	Control surface sizing and deflection limits shall be scaled to provide control authority coefficients equivalent to the Elysian E9X.	Analysis	The model is able to reach the same and scaled time-to-bank values as E9X.

[3] https://www.xflr5.tech/docs/Results_vs_Prediction.pdf, accessed on 21.01.2026

SFD-SYS-STA-01	The aircraft shall exhibit positive longitudinal static stability (Static Margin between 5% and 15% MAC) for all allowed CG positions and thrust settings.	Analysis	Based on literature study for conventional propeller aircraft with a T-tail, a SM of 0.05 is chosen.
SFD-SYS-STA-02	The aircraft shall exhibit positive directional stability and positive dihedral effect (sideslip creates restoring yaw/roll moments) throughout the envelope.	Analysis	Compliant as stability derivative for directional stability is positive, and for dihedral effect is negative,
SFD-SYS-STA-03	Primary dynamic modes (Short Period, Phugoid, Dutch Roll, Aperiodic Roll) shall be naturally damped	Analysis	All dynamic modes are damped including possible errors, except for Dutch roll
SFD-SYS-SOP-06	The aircraft shall be capable of maintaining stable level flight with 50% of engines inoperative (OEI condition).	Analysis	The rudder can handle the moment caused by all three propellers on one side of the wing that are turned on and on the other side of the wing turned off.
SFD-SYS-CTR-01	The control laws shall artificially augment the Dutch Roll damping (ζ_{DR}) to match the scaled E9X target value if passive stability is insufficient.	Inspection	Available FCMS allows for control loops.
SFD-SYS-CTR-03	The elevator shall be sized to trim the aircraft from $1.2V_S$ to V_{max} without exceeding 75% of available deflection.	Analysis	The maximum deflection required is 74 %
SFD-SYS-CTR-04	The ailerons/differential thrust shall achieve a roll rate $\geq 30°/s$ and counteract crosswind using $\leq$ 90% authority.	Analysis	The ailerons allow for roll control during take-off conditions with 6m/s crosswind and 90% of authority without stalling in this configuration.
SFD-SYS-CTR-05	The rudder shall be sized to maintain heading ($\pm 10°$) and sideslip ($\lvert\beta\rvert \leq 5°$) during a critical single-motor failure using $\leq$ 90% deflection.	Test	The rudder can handle the moment caused by all three propellers on one side of the wing that are turned on and on the other side of the wing turned off and fly stable. The exact heading and sideslip shall be tested during flight testing
SFD-SYS-STR-EMP-01	The empennage control surfaces (Elevator/Rudder) shall provide sufficient control authority to trim the aircraft at $C_{L_{max}}$.	Analysis	At $C_{L_{max}}$, the elevator is capable of trimming the aircraft.

9 Performance

A considerable number of performance characteristics have been calculated and presented in the previous chapters as they were relevant for the design processes outlined in them. Therefore, this chapter provides an overview of the performance characteristics not yet addressed or presented, as well as the mission profile, addressed in section 9.1. The take-off and landing performance and requirements are outlined in section 9.2, the climb and glide characteristics are addressed in section 9.3 and the compliance matrix for the performance requirements in section 9.4.

9.1. Mission

The ultimate purpose of the DEP-SFD-02, as signified by requirement SFD-STK-PER-01, is to provide a means for testing flight mechanical behaviour accurately, without the need for expensive, full-scale testing. Furthermore, according to requirements SFD-STK-SOP-02/03, it must be able to do this across 20 flight missions, with a minimum time-per-mission of 20 minutes. A general mission profile diagram is presented in 9.1.1 and a general description of the types of missions that must be conducted are set out in 9.1.2.

9.1.1. Mission Profile

As the DEP-SFD-02 will be used for testing, and not every test is the same, a general mission profile diagram has been constructed..

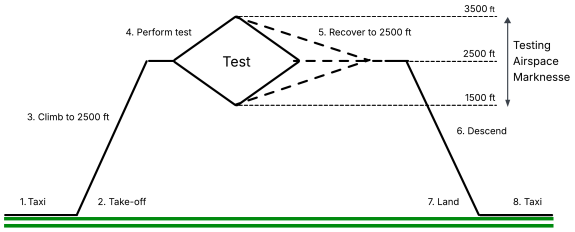

Figure 9.1: General mission profile diagram

9.1.2. Mission Description

In order to deduce the flight mechanical behaviour of the DEP-SFD-02 and the equations of motion, several tests must be carried out.

9.1.2.1. Test 1: Aerodynamic properties

In order to find the basic aerodynamic properties of the DEP-SFD-02, a very simple set of measurements must be taken. The DEP-SFD-02 must be tested at different angles of attack in constant increments in the wind tunnel and in flight testing. From the data measured by the FCMS, the drag polar, lift curve, drag curve, zero lift drag coefficient and the Oswald factor can then be obtained. Having these properties for the DEP-SFD-02 then enables the further analysis of the stability. [40]

9.1.2.2. Test 2: Longitudinal stability

When flying in equilibrium, shift the centre of gravity by moving ballast a known distance, or by dropping ballast from the DEP-SFD-02. This generates a moment which can then be overcome using the elevator to return to equilibrium. Using the data recorded by the FCMS, the elevator effectiveness can be found and from that the longitudinal stability can be found. [40]

9.1.2.3. Test 3: Dynamic stability

The dynamic flight behaviour can be explored by exciting the natural dynamic motion of the aircraft. Considering this is a prototype, preliminary estimates of the aircraft dynamic modes will have to be found before more complex tests can be performed. This can be done by performing piloted multistep inputs to excite the natural frequencies of the various modes. Later in development, more complex automated excitations/tests can be performed using the flight controller. [57]

9.2. Take-off & Landing performance

9.2.1. Take-off

The model must be capable of taking off at Marknesse drone-center, which has a runway of 325m. Requirement SFD-SYS-PER-06 states that the model must be capable of clearing a screen height of 15m within 230m. However, it was decided that compliance to the FAR-25 requirement would be sufficient, which states that by the end of the take-off field length a screen height of 12.27m must have been cleared, as this allows for adequate stopping distance in case of an engine failure. The method outlined in [54]

will be used to calculate whether that requirement has been met, utilising Equation 9.1.

$$s_{TO} = f_{TO} h_{TO} \left((\frac{1}{\gamma_{LOF}}) + \frac{(\frac{V_3}{V_{s_{TO}}})^2 (\frac{W}{S})_{TO} [((\frac{\overline{T}}{W})_{TO} - \mu')^{-1} + 1.414]}{(h_{TO} \rho g C_{L_{max_{TO}}})(1 + 1.414\gamma_{LOF})} \right) = 227.18\, m \tag{9.1}$$

As the take-off field length is 325m, this requirement has been met.

9.2.2. Landing

As for the landing requirement, FAR-25 was also considered sufficient, which entails that the aircraft, from a screen height of 15.24 m, must be able to land and stop within 60% of the total field length. The landing distance is found using Equation 9.2.

$$s_L = s_{air} + s_{LG} = (\frac{1}{\overline{\gamma}})[(V_A^2 - V_{TD}^2)/2g + h_L)] + \frac{V_{TD}^2}{2\overline{a}} = 146.75\, m \tag{9.2}$$

Therefore the minimum required field length is $s_{FL} = \frac{s_L}{0.6} = 244.58\, m$, considering the landing field length at Marknesse is 325 m, this requirement has also been met.

9.3. Climb & Glide performance

9.3.1. Climb

The rate of climb of the model was calculated for the battery sizing in subsection 7.2.1. Assuming a velocity of 30 m/s and maximum thrust, the rate of climb was found to be $ROC = 5.95\, m/s$.

9.3.2. Glide

The model needs to be capable of unpowered (gliding) flight. For a glide, the equations of motion reduce to Equation 9.3 and Equation 9.4

$$C_D \overline{q} S + W sin\gamma = 0 \tag{9.3}$$

$$C_L \overline{q} S - W sin\gamma = 0 \tag{9.4}$$

Therefore the flight path angle follows from $tan\gamma = -(\frac{C_D}{C_L})$ and the rate of descent from Equation 9.5.

$$RD = \left((W/S)(2/\rho)(C_D^2/C_L^3)(cos\gamma)^3 \right)^{1/2} = 2.58\, m/s \tag{9.5}$$

Assuming glide starts at cruise conditions and continues at a constant lift-to-drag ratio, the glide range would be roughly 12 km with a glide time of roughly 290 seconds. As outlined in subsection 7.2.1, there is a back up battery system capable of supplying 5 minutes of power to all LV components. In case of a propulsion malfunction, this would be significantly longer. Thus, even in the event of a loss of power and propulsion malfunction, the FCMS would be sufficiently powered to complete the glide.

9.4. Compliance matrix

Table 9.1: Compliance matrix performance requirements

ID	Requirement Description	Verification Method	Compliance Level
SFD-SYS-PER-01	The aircraft shall accommodate a payload consisting of the Flight Control and Measurement System (FCMS) with a mass of no more than 5 kg and volume no more than 0.1 m^3.	Inspection	The total mass of the FCMS is 2.098 kg and the volume approximately 0.00125 m^3.

SFD-SYS-PER-02	The aircraft shall be capable of steady-state flight at a range of airspeeds sufficient to capture aerodynamic derivatives in the linear lift region.	Analysis	Further analysis is required to establish the exact range of airspeeds, however, it is at least 25 m/s, which is sufficient.
SFD-SYS-PER-03	The aircraft Maximum Takeoff Mass (MTOM) shall not exceed 150 kg.	Inspection	The MTOM is 150 kg.
SFD-SYS-PER-05	The aircraft shall operate in an envelope that supports powered, partially powered, and unpowered (gliding) flight modes.	Inspection	Compliant
SFD-SYS-PER-06	At MaximumTake-Off Mass(MTOM), ISA+20°C, zero wind, dry level runway, the distance from brake release to passing 15m screen height shall be ≤ 230 m.	Analysis	Not compliant, however, the requirement was deemed unnecessarily stringent, as there is no operational or regulatory reason, and instead FAR-25 was chosen, to which it is compliant
SFD-SYS-PER-07	At Maximum Landing Mass, ISA+20°C, zero wind, dry level runway, flying approach at $1.3V_s$, the distance from 15m screen height to full stop shall be ≤ 230 m.	Analysis	Not compliant, however, the requirement was deemed unnecessarily stringent, as there is no operational or regulatory reason, and instead FAR-25 was chosen, to which it is compliant
SFD-SYS-PER-08	At MTOM, ISA+20°C, all motors operating, climb config, the minimum rate of climb at best-rate-of-climb speed shall be ≥ 2 m/s.	Analysis	The steady rate of climb = 5.95 m/s
SFD-SYS-PER-09	Under conditions of SYS-PER-08, the initial climb gradient from lift-off to 50m AGL shall be ≥ 4%.	Analysis	It is approximately 9.25 %
SFD-SYS-PER-10	The SFD shall have a minimum still-air range of 20 km while landing with ≥ 20% usable battery energy remaining.	Analysis	Compliant
SFD-SYS-PER-11	At MTOM,landing configuration, power-off 1g flight, the stall speed $V_{S_{LDG}}$ shall not exceed 18 m/s.	Analysis	Not compliant, however, 18 m/s is considered unnecessarily stringent, as there is no operational or regulatory reason, and $V_{S_{LDG}}$ = $23.29m/s$ is sufficient for the relevant landing regulations.

10 Design summary

The engineering processes elaborated on in previous chapters 4.5 to 7.6, result in a preliminary design of the scaled demonstrator based on the Elysian E9X. In this chapter, the basis geometry and weight of the design are given and explained. Using CAD, a 3d model is constructed of the SKRIBBL, visualising the model itself and its modular capabilities. Lastly, a compliance matrix validates the fulfilment of the project objectives.

10.1. Model design

As stated before, the model design is mainly guided by the Elysian E9X's design and layout to simulate the flight characteristics as accurately as possible. Led by scaled aerodynamics, mass moment of inertia,

and stability coefficients, the model is scaled with a factor of 9.7% with respect to the full-scale Elysian E9X. The base geometry of the SKRIBBL is given in table 10.1 below. More elaborate wing details and geometry is shown in table 10.2.
The total model weight and mass moments has a large influence on the flight mechanical similitude to the full-scale Elysian E9X. As explained in section 5.1, the total weight is estimated to be required for an accurate similitude, resulting in approximately 150$[kg]$. The component masses and total mass of the model are given in table 10.3 below. The weights of each component include all the electronics mounted inside, such as the batteries counting towards the fuselage, and the ESC's to the wings. The propulsion section is the summed mass of 6 times the engine nacelle, propeller, and electric motor.

Figure 10.1 below shows the 3-view drawing of the latest developments of the Elysian E9X, directly shaping the design of the SKRIBBL.

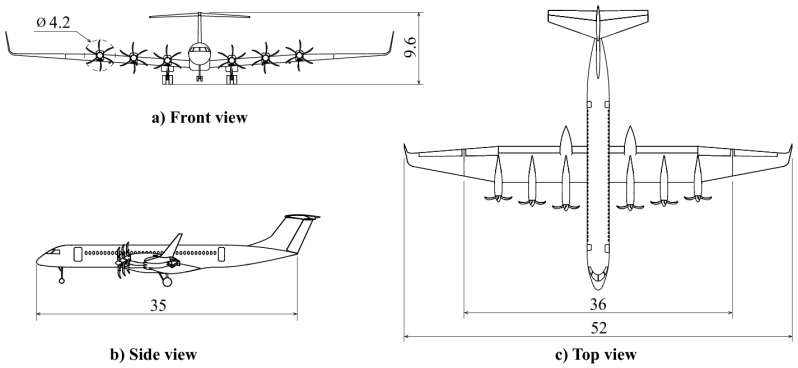

Figure 10.1: 3-view drawing of the Elysian E9X by Elysian [71]

An isometric view of the resulting SKRIBBL base design, modelled in CAD software, is shown below in figure 10.2.

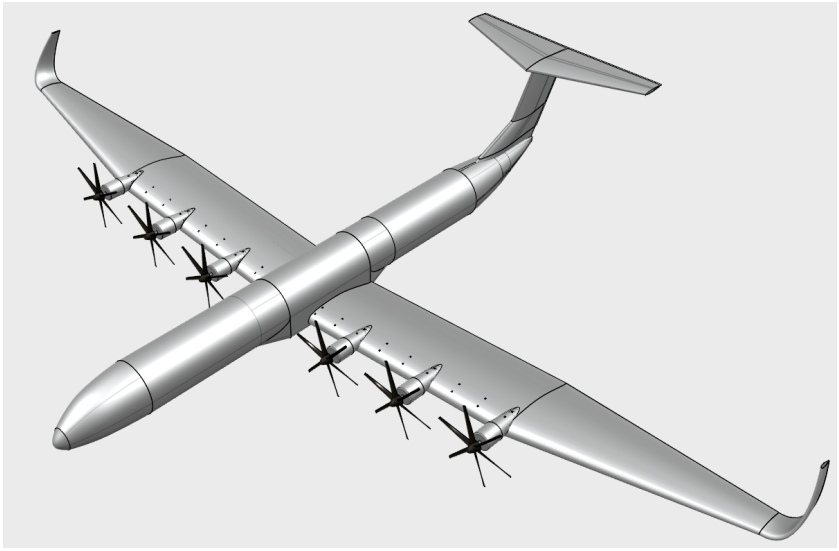

Figure 10.2: Isometric view of the SKRIBBL

A 3-view representation of the model is shown below in figures 10.3, 10.4a, and 10.4b.

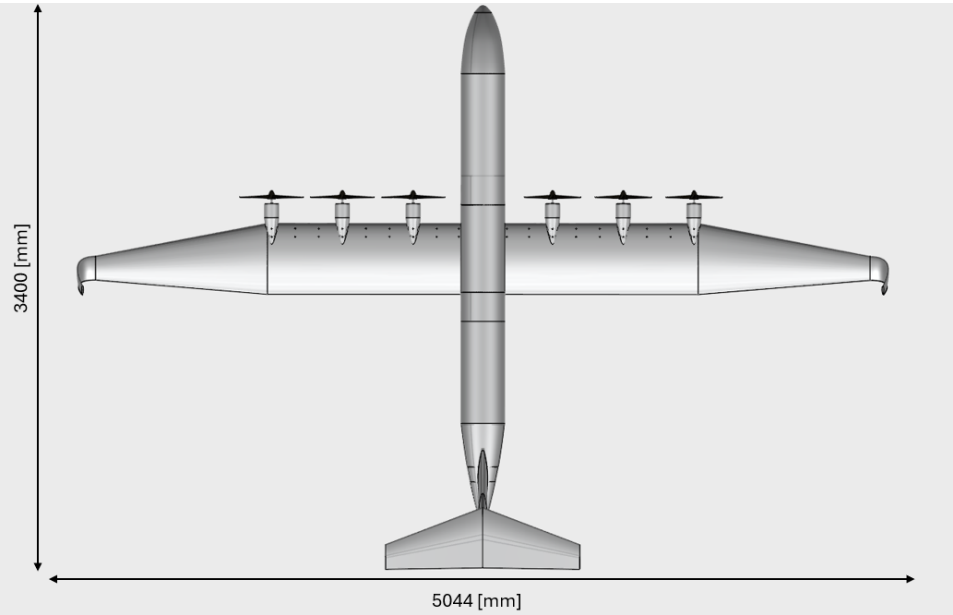

Figure 10.3: Top view of the SKRIBBL, with length and wingspan noted in millimetres

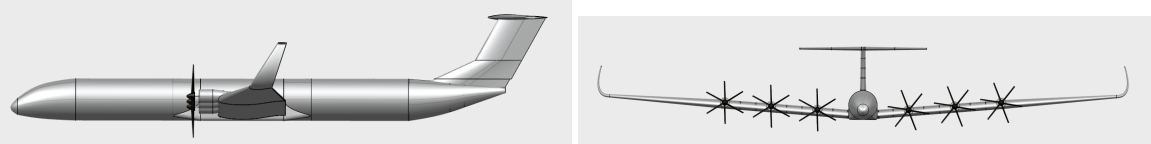

(a) SKRIBBL side view

(b) SKRIBBL front view

Figure 10.4

As seen from the figures above, the shape of the model is accurately representing the Elysian E9X and features the same configurations. Fitted with a T-tail, 6 electrically driven propellers on the leading edge of the wing, and equal proportions between wing and fuselage. Furthermore, the wing is split into two sections: a straight part, on which the engines are mounted, and a tapered part. Added to the tips are winglets. General dimensions of the model are given in the table below:

Table 10.1: General dimensions

Parameter		
Length	[m]	3.4
Wingspan	[m]	5.044
Height from ground	[m]	1.208
Fuselage diameter	[m]	0.3
Nose cone length	[m]	0.45
Tail cone length	[m]	0.70
Fuselage skin thickness	[mm]	1.75
Tail height	[m]	0.45
Tail area	[m^2]	0.161
Horizontal stabilizer span	[m]	1.335
Horizontal stabilizer area	[m^2]	0.388
Motor count	[-]	6
Propeller diameter	[m]	0.4064
Propeller blade count	[-]	6
Landing gear height	[m]	0.45

As explained before, the wing consists of 2 surface sections and winglets. All the motors are mounted on the straight section, which also includes the electronics to operate the motors. Both sections will feature control surfaces, which are not drawn in the 3D model. Similar to the Elysian E9X, trailing-edge flaps are installed on the first wing section; more details can be found in section 5.3 of this report. Ailerons are fitted on the tapered section of the wing. Details of the wing geometry can be found in table 10.2 below.

Table 10.2: Wing geometry

Parameter		Total wing	Section 1	Section 2
Span	[m]	3.044	1.21	1.08
Area	[m^2]	2.02	0.64	0.37
Aspect ratio	[-]	13	2.3	3.2
Sweep	[deg]	1.6	0	3.4
Root chord	[m]	0.486	0.486	0.486
Tip chord	[m]	0.162	0.486	0.162
Taper ratio	[-]	0.33	1	0.33
Dihedral	[deg]	5	5.1	4.9
Skin thickness	[mm]	1.75		
Profile thickness	[%]	20		
Winglet height	[m]	0.32		

To accurately resemble the flight characteristics of the full-scale Elysian E9X, the model is weighted to scale with Froud's scaling method. The details and procedures of this method are explained later in section 5.1. For high accuracy, the total mass must be close to 150[kg]. The mass contribution of each principal component is given in table 10.3 below. These are the operating weights of the components, meaning the fuselage holds and includes the weight of the batteries, wings the ESCs and control servos, and propulsion includes the propellers, electric motors, and nacelles. In short, these are the weights of all the separable components, which are visualised in figure 10.5.

Table 10.3: Operating weights

Component	Mass [kg]
Fuselage	52.1
Wing	75.1
Empennage	5.7
Propulsion	6.1
Landing gear	11
Total	**150**

10.2. Modularity

The project objective to have a modular scaled flight demonstrator, which can be flown in different configurations to the operator's demand, is taken into account during all design phases. The modular aspects that the model features and their motivations are elaborated on in section 16.3. The results incorporating these ideas are visualised in the exploded view below, showing all the components that can be removed or replaced.

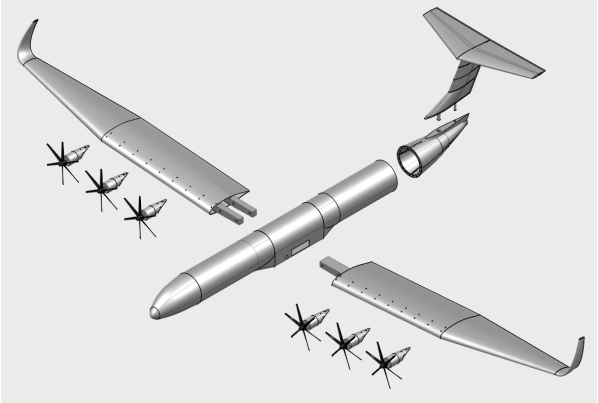

Figure 10.5: Exploded view of all separable parts of the model

As an example of its capabilities, several concepts that can be realised with the model are demonstrated below. Figure 10.6 shows two possibilities for attaching different wings and propulsion systems. Subfigure 10.6a displays slender, high aspect ratio wings with distributed electric propulsion along the entire leading edge. Subfigure 10.6b shows a different, more complex wing planform. Furthermore, an alternative propulsion system is attached. These Electric Ducted Fans, or EDFs, simulate high-bypass ratio jet engines. Although requiring major fuselage and fuel system modifications, combustion jet engines can also be installed. However, the project is focused on electric flight, which makes the previous outside the scope of this report and is not thoroughly considered. Lastly, different wings can also be used to test various control systems. Sketched in this example is a full-span flaperon. Other complex flap systems can also be integrated with adequate modifications.
The fuselage in its standard configuration only allows for a low-wing configuration. However, the wing connection design in the fuselage does make it possible to attach a wing the other way around. By flipping the fuselage 180 degrees, a high-wing configuration can be realised. This, however, requires minor modifications of the placement and construction of the electronics inside the fuselage. A mid-wing configuration is not feasible with the current fuselage design.

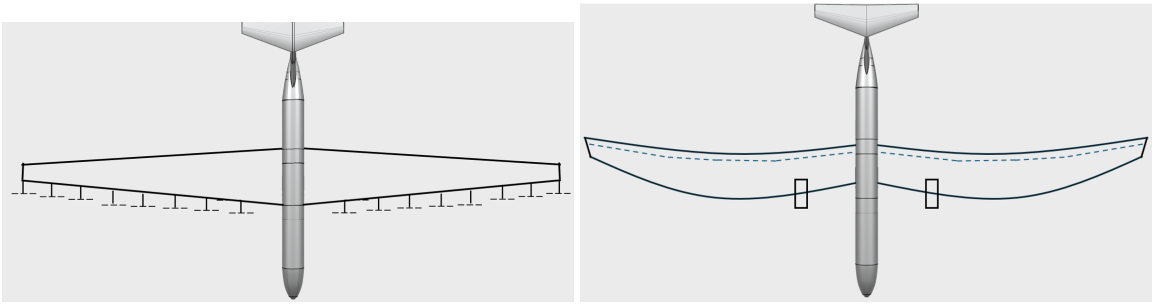

(a) Concept with slender wings and 16 electric motors **(b)** Concept with curved wings, EDFs, and full span flaperons

Figure 10.6: Possible wing, control, and propulsion configurations

With the separability of the tail cone, different empennage configurations can be tested. A few examples of ideas are shown in figure 10.7. The left subfigure, 10.7a, shows a conventional tail layout as found on almost every commercial, general aviation, or military aircraft flying today. This configuration, therefore, makes an interesting and relevant modular option.
Secondly, in figure 10.7b, a V-tail is drawn. This configuration is found only on a few aircraft and makes use of a mixed rudder and elevator, named ruddervator. This imposes different control and stability characteristics, which can be the subject of research.
In the last figure 10.7c, an exotic idea is sketched, showcasing the utility for evaluating new concepts.

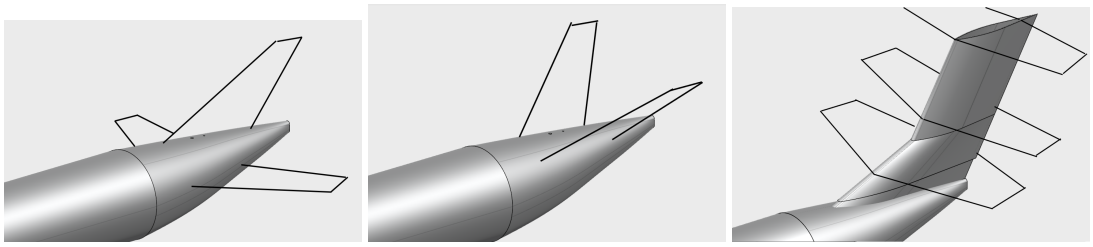

(a) Conventional tail configuration **(b)** Tail concept with V-tail configuration **(c)** Concept with 3 stacked stabilisers

Figure 10.7: Feasible empennage configuration concepts

At last, dummy weights can be installed at various places in the model. This can adjust the centre of gravity and mass moment of inertia around all axes, providing full flexibility in modifying stability and control characteristics.

10.3. Compliance matrix

Table 10.4 shows that the above-described design complies with the original stakeholder requirements, and therefore adheres to the project objectives. Per stakeholder requirement, a verification method and a brief argumentation for compliance are given.

Table 10.4: Compliance matrix stakeholder requirements

ID	Requirement Description	Verification Method	Compliance Level
Performance Requirements			
SFD-STK-PER-01	The flight vehicle (further referenced as: 'the model') shall be able to perform tests on flight mechanical behaviour to a level that supports an OEM to check the validity of the proposed aircraft layout in the conceptual design phase.	Analysis and demonstration	The model is designed to concept statements from the client and includes all hardware components required for data measurements and collection. Test flights shall be performed to verify the operation of the model and the validity of the collected data.
SFD-STK-PER-02	The size and mass shall be selected such that the aircraft can carry a flight control and measurement system (FCMS) that allows analysis of the vehicle flight characteristics in powered, partly powered, and unpowered conditions.	Inspection	Aerodynamic analysis yield a 9.7% scale, with a mass of 150$[kg]$. A COTS FCMS is found which fits inside the fuselage scaled to 9.7%. The electronics are powered by main batteries. A back-up battery powers the electronics in case of main battery failure.
SFD-STK-PER-03	The model shall meet initial specifications of maximum 150 kg mass.	Demonstration	For accurate scaling the model is set to be 150$[kg]$, which is reached by implementing dummy weights.
SFD-STK-PER-04	A trade-off study shall be performed on scale factors 5%, 8% and 10% to determine the optimal choice.	Analysis	This is performed in section 5.1.
SFD-STK-PER-05	The model shall meet initial specifications of a maximum 7.5 m wingspan.	Inspection	With a scaling of 9.7% the model has a wingspan of 5.044$[m]$.

11 Production

The production plan outlines the manufacturing, integration and assembly strategy for the SFD, based on the finalized structural design and the validated sizing of all major components. The SFD comprises of COTS, outsourced and in-house developed components. The scope of this production plan is focussed to the latter category and therefore focuses on the manufacturing of the primary structural components including the wing, fuselage, and empennage as well as the integration of the outsourced components.

For each of the to be manufactured components, the principal design drivers, such as buckling resistance, load transfer, modularity, and integration of the major structural elements, have been identified and addressed during the detailed design phase, as documented in section 6.2. This section will describe the production approach for each individual component in section 11.1. Subsequently, the integration and assembly of the complete system are adressed in section 11.2.

Throughout the production plan, emphasis is placed on manufacturing commonality and process simplification. Although the SFD is not intended for mass production, its modular architecture may appeal to a broader range of users if supported by an efficient and repeatable manufacturing approach. Consequently, wherever feasible, identical or closely related production methods are selected across components to reduce complexity.

11.1. Component Production

This section describes how each component will be manufactured prior to integration and assembly. This section will not focus on the COTS and outsourced components but solely on the components that will have to be manufactured by the manufacturer of the SFD. Three types of components are documented, CFRP structural parts, the Aluminium 7075-T7451 mounting part, and Polyamide brackets.

11.1.1. CFRP parts

For the production of CFRP parts a moulding process called vacuum-bag-only (VBO) procedure will be used using out-of-autoclave (OaA) pregpreg materials was chosen. This process achieves low porosity and tight dimensional tolerances [10], while having flexible tooling flexibility. The process follows the following steps:

1. **Mould Preparation:** A female mould is manufactured to meed the required geometric accuracy and surface-quality standards of the component. Special attention will have to be given to regions with tight radii, such as the wingbox nose or complex curvatures such as the airfoil. The mould is sealed and treated with an appropriate release agent, which prevents the cured product from adhering to the mould and ensures the component can be removed without damaging it or the mould.
2. **Material Conditioning:** The prepreg material is stored under controlled temperature conditions and allowed to reach a suitable layup temperature before use. This step avoids moisture condensation and ensures stable handling properties. The prepreg plies are then placed into the mould following the laminate schedule, which defines the fibre orientations and stacking sequences. Care must be taken here to ensure that the plies fully follow the mould surface, especially in areas with complex geometry.
3. **Vacuum Bagging:** After the layup is completed, the laminate is covered with supporting materials. These include a peel ply, which creates a bondable surface after curing, a release film, and a breather layer which allows air to flow towards the vacuum outlet. Then, the entire assembly will be sealed inside a flexible vacuum bag, when this vacuum is applied, the laminate is compacted and trapped air will be removed.
4. **Oven Cure:** The still vacuum-bagged assembly is placed in an oven and will be cured using a temperature cycle specified by the manufacturer of the prepreg. This cycle often consists of a

heating phase, a constant temperature phase at the most efficient curing temperature and finally a controlled cooling phase.

5. **De-moulding:** Once the cure cycle is completed and the component has cooled to a safe handling temperature, the vacuum bag and supporting materials are removed. The cured component is carefully separated from the mould. After de-moulding, the part will be trimmed to its final dimensions and undergo inspection. This inspection will focus on surface quality, dimensional accuracy, and the presence of manufacturing errors such as voids, wrinkles or resin-rich areas.
6. **Post-processing:** Depending on the component, additional steps follow the de-moulding process. These processes will be elaborated on for each component separately in its assigned section. These post-processing steps are necessary before integration of each component.

11.1.1.1. Wing

The wing is composed of six distinct parts: the left and right wing skins, the wingbox and three different rib sizes. Each of these elements requires a separate mould to produce the part. Owing to geometric asymmetry, separate mould are required for the left and right wing skin, in contrast, the wingbox exhibits symmetry when rotated about the x-axis, thereby only requiring one mould. This simplifies the production process and contributes to lower tooling cost.

The rib manufacturing process similarly benefits from this mould reusability in an even higher degree. The primary rib design, of which the SFD has 18 in the standard wing configuration, can be produced using one mould. In addition, one mould is required for the rib in each tapered section of the wing and a final mould for the wing-tip ribs.

Finally, to incorporate the different engine location possibilities on the SFD, multiple small holes must be drilled at each of the 8 attachment points per wing, which requires high precision machining and care.

11.1.1.2. Fuselage

The fuselage consists of four distinct parts: The nose cone, the load-bearing lower fuselage, the upper fairing, and the tail section. While the nose cone and upper fairing can be manufactured using the process documented at the start of subsection 11.1.1, the lower fuselage and tail section require additional manufacturing considerations due to integration requirements.

11.1.1.2.1 Lower Fuselage The lower fuselage requires three cut-outs to enable integration of the wing structure and nose landing gear. These openings are introduced after curing and are made using conventional composite drilling and milling processes. As identified in the previous report [20], machining of composite materials must be carried out with extreme caution, as well as employing appropriate tools, preferably polycrystalline diamond tools, which help to prevent delamination, fibre pull-out and surface damage.

In the absence of high-end composite machining capabilities, an alternative approach could be used to create the lower fuselage. By introducing an additional mould, the need for post-processing cut-outs could be eliminated. This solution would however, require the manufacturing of an additional mould. For the baseline configuration of the SFD, post-machining was selected as the preferred approach. This decision was primarily motivated by sustainability considerations, as manufacturing an additional mould for the largest structural component of the SFD was deemed as unnecessary material usage.

11.1.1.2.2 Tail Section The mould design for the tail section requires special consideration due to the presence of an opening needed for the wind-tunnel attachment. Rather than introducing this opening with post-processing operations, the decision was made to create it directly with the mould. While this approach results in a more complex mould design, it avoids the need for drilling operations on cured CFRP, which as stated before, requires a high degree of precision and pose a greater risk of introducing structural defects.

11.1.1.3. Empennage

The manufacturing process of the empennage closely follows that of the fuselage tail section. The empennage consists of three primary elements: the main structural body, the elevator and the rudder. Of these components, the main structure presents the greatest manufacturing complexity, as it requires

multiple cut-outs to enable the integration of the control surfaces as well as an additional cut-out to place the forward-facing camera. For the same reasons outlined in paragraph 11.1.1.2.2, these cut-outs are made directly into the mould design rather than being created by post-processing operations.

11.1.2. Aluminium Parts

The SFD has a single component manufactured from the aluminium alloy 7075-T7451, namely the payload mounting sheet. This sheet is placed in the lower section of the fuselage and serves as a structural interface for the installation of the payload components, including the flight computer and batteries.

As the payload sheet is not subject to tight dimensional tolerances, complex geometries or great loads, it can be manufactured using a variety of conventional processes. Milling, cutting, and punching are all technically feasible options. However, cutting was identified as the most suitable manufacturing method for this application, as it is widely available, does not require dedicated tooling, and unlike milling, does not generate significant metal scrap.

After the fabrication of the sheet, a set of pre-drilled holes are made to allow for the bolted attachment of payload components. To ensure secure fastening, a nut of the appropiate dimensions is tack-welded to the underside of the sheet at each pre-drilled hole. This is necessary since the relatively small thickness of the sheet (1.5 mm) does not provide sufficient thread engagement to ensure that the fasteners remain tight during flight.

11.1.3. Polyamide Parts

As will be detailed in section 11.2, a number of polyamide (PA) brackets are required to support the final integration and assembly of the SFD. These brackets serve as secondary structures, enabling attachment of avionics, batteries and other equipment to the airframe without permanent modifications to the composite structure. The use of these brackets, therefore, improves the sustainable design philosophy of the SFD by allowing easy replacement of small parts.

The manufacturing of PA brackets is a mature and widely established process, with numerous commercial suppliers offering these services for engineering-grade polyamides. This additive manufacturing process allows for complex tailored geometries, while maintaining low tooling costs.

Polyamide was selected over more conventional plastics due to its superior mechanical properties, including higher strength and improved toughness. These characteristics make PA a suitable material for aerospace applications like the SFD.

11.2. Component Integration

The integration of components is already partially addressed, as several aspects of the SFD assembly are inherently linked to its modular design philosophy. As a result, this section is limited to the integration of the wing structure and the installation of COTS components within the SFD. For the assembly of the large structures please reference back to section 6.4.

11.2.0.0.1 Wing To preserve the structural integrity of the wing assembly that has been used in the buckling analysis presented in section 6.3, the individual wing elements are bonded together to form a single, rigid structure. This co-moulding and bonding process can only be performed after the electrical wiring for the engines and landing gear has been routed, which is designed to fit within the limited space between the wingbox and wing skin.

The integration of the wing skin, ribs and wingbox is achieved using a high-performance structural adhesive suitable for both composite-to-composite as composite-to-metal bonding. The adhesive chosen for this process is Araldite 2031, which provides high shear and peel strength, meanwhile ensuring reliable load transfer between the wing components [30]. The engines are subsequently mounted at the designated attachment points on the wing structure followed by their fairings. Finally, the landing gear is mounted on the wing using the same adhesive and a 3D-printed polyamide (PA) mount, followed by its respective fairing, completing the wing assembly.

11.2.0.0.2 Fuselage The majority of the fuselage components are connected using the modular interfaces described in section 6.4. Therefore, only the integration of the aluminium payload mounting plate and the nose landing gear remain to be addressed. Both components can simply be bonded using the same adhesive used in the wing. Although the mounting plate could be mounted with a slightly less strong adhesive, to keep the simplicity of the design, it was chosen to use the same adhesive. The nose landing gear, similarly to the main landing gear, will make use of a polyamide bracket which will be glued to the fuselage after which the nose gear is attached.

11.2.0.0.3 Avionics Following the integration of all the primary structural components, the avionics and aerodynamic control surfaces are installed. Given the large number and variety of components, their integration follows a set of general conventions rather than being described on a component-by-component basis.

All components housed within the fuselage are bolted to the aluminium mounting sheet at predefined locations, as indicated in Figure 7.10. Components that are intended to be attached to this sheet but do not feature dedicated mounting brackets, such as the batteries, are first bonded to a custom designed PA bracket, after which this bracket is bolted to the aluminium sheet, ensuring that the component remains easily replaceable while limiting waste to a low-cost, easily manufactured PA part.

Similarly, components that must be mounted directly to the CFRP shell of the SFD, including the camera integrated in the empennage and multiple actuators, are installed using dedicated PA brackets. This approach once again facilitates straightforward replacement and maintenance of small components without impacting the primary composite structure.

12
Operations & Logistics

This chapter describes the operational concept for the SFD (Scaled Flight-Demonstrator), covering the period from the moment the SFD is system integration-ready until the completion of the flight-test campaign. The concept includes the use of operational locations, logistics and transport between the locations, ground support and maintenance, and flight-test day organisation, including contingency procedures. The operational concept is written as an engineering workflow, basically a repeatable procedure of preparing, moving, testing and recovering while maintaining the quality of the data obtained.

The project requires planning for both research and operational test environments across all locations. There is chosen for a build-verify-test structure that will reduce uncertainty before the SFD will be exposed to free-flight variables such as gusts, runway effects, and BVLOS operational constraints. Where relevant, the concept follows test phases for distributed electric propulsion demonstrator, including extensive wind-tunnel characterisation, static mission-profile ground tests, taxi testing, and iron-bird qualification of the electric architecture [18].

12.1. Operational concept overview

The SFD operates under a workflow that has safety gates. The campaign begins with integration and verification in an environment where controlled assembly is possible, enabling configuration control and the safe handling of batteries and avionics. The propulsion and electrical systems will be validated for thermal margins safety before the airframe is exposed to wind-tunnel or flight-test environments. This is the stationary qualification. Subsequently, the aerodynamic performance and propulsion interaction effects are characterised in a large low-speed wind tunnel to reduce uncertainty in stability, control, and thrust modulation effects. Only after these steps does the campaign transition into outdoor ground runs, taxi tests, and BVLOS flight tests in a controlled operational volume.

This approach combines safety and test validation. By constraining the early testing to controlled conditions and breaking it down into more steps, the team can discover failure modes while reducing

consequences. This allows the team to write manuals based on both measured derivatives and simulations.

12.2. Operational environments and facilities

Operations are divided across three environments: a central integration and support facility, a wind-tunnel facility, and the BVLOS flight-test site.

12.2.1. Central integration and support facility

Since this SFD is for the customer and there are no requirements stating a specific location for the central integration and support facility, this environment is defined by function rather than by location. Although the manufacturing of the SFD can be outsourced, it must provide controlled storage for batteries and sensitive avionics, and include a dedicated charging area sized for the campaign's electrical load and equipped with appropriate fire-safety provisions. If it is also integrated there, it must support airframe assembly and system integration. The facility must also provide tooling and space for structural repairs, harness rework, and configuration changes. This functional definition makes the operational environments and support facility variable: it remains valid whether the facility is hosted by a university partner, an OEM workshop, or a contracted prototype facility, as long as the required capabilities are available and the same configuration-control standards are there.

12.2.2. Wind-tunnel environment: DNW-LLF (Marknesse)

Aerodynamic and propulsion-interaction testing is conducted at DNW-LLF, a large low-speed wind tunnel located in Marknesse. This facility is used to validate aerodynamic performance trends, stability and control behaviour, and propulsion interaction effects under controlled flow conditions. The DNW-LLF provides enough space for the demonstrator to fit in (9.5mx9.5m) and has windspeeds up to $62 m/s$ in this configuration, which is enough to simulate our cruise speed of $43.8 m/s$[16]. It is also close to the outdoor flight-test hub, reducing transport complexity and accelerating iteration between tunnel findings and free-flight validation.

12.2.3. BVLOS flight-test environment: NLR Drone Centre (Marknesse, EHR66)

BVLOS flight testing will be done at the NLR Drone Centre in Marknesse. The existing drone-port has infrastructure and a paved runway and is located within the controlled airspace volume EHR66. The runway length provides a practical margin relative to the demonstrator's take-off and landing distance, as the runway is 325 m long. EHR66 provides a controlled operational volume and a ground-risk buffer that supports containment planning, observer placement, and emergency response logistics. To make BVLOS flight testing restrictions easier to handle, airspace activation, altitude constraints, and operational coordination are essential for flight operations, as BVLOS operations depend not only on the vehicle state but also on the external airspace state. EHR66 can provide all of this, making the testing campaign much easier.

12.3. Logistics, transport, and maintenance

12.3.1. Transport Concept

To minimise handling risk and support quick recovery from minor failures, the transport must be a straightforward process. Due to the SFD's modularity, transport can be done in a road trailer by simply disassembling the SFD. All the components of the SFD are supported on wheeled racks that allow movement between the trailer and the different environments. This reduces manual lifting and limits the risk of damage during the movement of the SFD. Chargers, ground control station hardware, tools, and inspection equipment are transported in standardised cases so that when arriving at the test site the ground systems are ready to use and free from damage.

12.3.2. Maintenance

Maintenance is structured into two levels to make sure there is a balance between on-site quick repairs and the repair quality. Line maintenance is performed at the test site and covers tasks that are likely to occur between flights, and that can be accomplished safely with field tools and spares, such as propeller replacement, battery changes, or minor wiring repairs. With the tools used for line maintenance,

inspections can also be performed on-site. Depot maintenance is performed at the central facility and covers structural repairs, major harness rerouting, power-distribution changes, and any corrective action that affects safety-critical behaviour or requires re-qualification prior to return to flight. The boundary between these two levels is chosen conservatively: if troubleshooting indicates any change that could alter safe-state behaviour, the SFD will be repaired on depot maintenance level to preserve configuration control and to avoid unverified field modifications.

To ensure that many maintenance situations can be solved on-site, a selection of spares is chosen that includes the most likely quick-turn failures. The field support kit is therefore equipped with components such as propellers, landing-gear consumables, servo components, and electrical consumables that enable safe and documented replacement. This idea is consistent with prior DEP-SFD operational experience, where the support kit was identified as essential following a major incident and extensive integration testing on an iron-bird bench was used to reduce the probability of recurring electrical faults[18]. In Figure 12.1, the flow of maintenance and transport between the operation locations is shown.

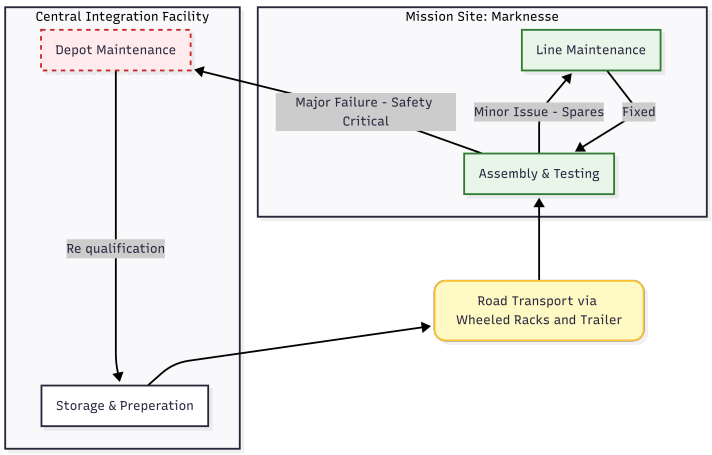

Figure 12.1: Diagram Showing the Maintenance and Transport Connections Between Locations

12.4. Staged verification and test campaign

The test campaign can be seen as an energy ladder that starts from constrained and low-energy tests to free flight testing. This progression in the different stages reduces the operational risks and uncertainties. In this ladder, it is also clear what the safe state is and when that point in time occurs. When a critical failure occurs, it is easy to identify which stage was the defined safe state before.

Figure 12.2 summarises the energy ladder stages and the intent of each gate. The gate concept is not meant to be bureaucratic: each gate exists because it removes a class of unknowns before exposing the demonstrator to a higher-consequence environment.

Figure 12.2: Staged verification and test progression, energy ladder, from integration readiness to BVLOS flight testing.

12.4.1. Stationary powertrain validation and iron-bird testing

To reduce uncertainties, the propulsion system and electrical architecture are validated under stationary conditions. The conditions replicate the environment it is expected to be in during the wind-tunnel and flight tests. Here, the goal is to validate the entire system, including the mechanical mounting and cable routing, so it is not just a validation plan for individual components. An iron-bird bench can be used to reproduce the way the system will be placed in the SFD, eventually installing the electrical motors with representative mounts and integrating the safety devices in their intended place [18].

Validation of the systems on the Iron Bird is performed using power profiles that will also be used during testing. The systems must be monitored carefully during the tests; temperatures, currents, and voltages can all show different behaviour than expected and give new insights. Introducing fault cases during testing will help to verify all the fail-safe responses, for example, to confirm that the main battery can be isolated during a failure while the backup power ensures a safe landing can be made. In the end, these tests result in operational limits that are later described in the manual and flight cards, because they define the acceptable current levels and thermal states.

12.4.2. Wind-tunnel campaign at DNW-LLF

Wind-tunnel testing at DNW-LLF is used to validate aerodynamic performance, stability and control trends, and the interaction effects of distributed propulsion under controlled conditions. This is basically a variant on the stationary iron bird testing; the tests are again done in a controlled environment. The goal of the wind tunnel test is to reduce uncertainty before the first BVLOS flights. Also here, based on measured trends and verified control authority margins, the manual and flight cards can be adjusted. For the SFD, this stage is also critical for throttle-matrix testing, because yaw and roll moments can be generated via thrust modulation, and these effects must be quantified to define safe margins for crosswind and failure of the propulsion system cases. The test results are used to identify boundaries, to validate the aerodynamic model used, and to reduce uncertainty in derivatives that affect take-off, landing, and those that affect any way off recovery.

12.4.3. Marknesse ground runs, taxi testing, and BVLOS flight testing

After wind-tunnel characterisation, the campaign proceeds to Marknesse for ground and flight testing in EHR66. But before the SFD is going to fly, there is still one step to go: static ground runs with the SFD. By testing representative power sequences (such as those for the missions), it can be confirmed that the integrated propulsion system behaves as expected in the outdoor environment. The power tests will also show that take-off and landing procedures are reproducible. The goal is to make sure that any behaviour that could affect the take-off or controllability is observed before the SFD is released for taxi or flight

Taxi testing is then used as a second step in the energy ladder. It validates runway steering, braking, and controllability as power settings are increased. Even taxi testing provides a controlled environment. What can be seen: the controlled environment is a little less controlled each time, but still more controllable than the next test. This controlled environment is to rehearse abort logic and to confirm that runway procedures remain valid with the actual propulsion response and acceleration capability. Taxi testing is an operational gate to flight on the energy ladder because it validates that the vehicle remains controllable on the ground and that a mission abort can be performed safely within the runway margins.

Now the flying can start! Flight testing is done per mission by expanding the envelope. It depends per mission what is tested, but eventually every system should have been tested in the air. A three-dimensional geofence is defined to keep operations within EHR66, and a boundary buffer triggers safety actions as the SFD approaches the limit. All the missions are performed inside this geofenced operational volume. A Flight Termination System (FTS), independent from the primary flight-control system, provides the final containment layer and can be triggered manually by the pilot or automatically if defined conditions occur, such as a critical failure or a geofence violation. This way, it can be assured that the missions are performed outside populated areas, and even if the SFD is uncontrolled, it will not reach any populated area. The height of the EHR66 volume is (when activated) 3500 ft[35], which can be entirely deactivated for all other air traffic and therefore, indeed, a controlled environment is created. This covers a significant part of the BVLOS regulations, and the area is shown in Figure 12.3. The operational concept further assumes that the SFD retains sufficient control authority to maintain stable flight and complete a safe recovery landing after significant propulsion degradations, including cases where up to 50% of engines are inoperative. This assumption is treated as a verification objective and is progressively demonstrated in flight within a conservative envelope.

Figure 12.3: Map of EHR66 and TGB NLR Testcentrum High[35]

12.5. Flight-test day execution and team organisation

12.5.1. Daily Routine

The daily routine assumes that everything needed has already been transported to Marknesse. Also, safety procedures at NLR or any other site should be prioritised over the daily routine when necessary. A flight-test day begins with the physical setup and system preparation. The wheeled racks are used to move all the components from storage to the hangar for assembly. Using a short checklist, the SFD is assembled, and the batteries and avionics are prepared (if the site has specific preparation requirements, follow them). Next, a readiness review is done, looking at the weather and relevant operational notices and checking them against the environmental limits. The airspace activation for EHR66 should be confirmed, and the corresponding activated altitudes should be checked. The Chief of Operations will then brief the team on the planned mission of that day, potential hazards and relevant information for the engineers to know for that day

Each mission begins with a combined visual and functional pre-flight inspection. The pre-flight checks include verification that the geofence parameters, Return-to-Home (RTH) behaviour, and the flight-termination logic are loaded correctly in the ground station and match the day's operational volume. Control surfaces are checked for correct direction and freedom of movement, and propulsion arming and safety interlocks are confirmed. After landing, the SFD is recovered from the runway, batteries are isolated as required, and the SFD is prepared for turnaround through inspection, data download, and line-maintenance actions. Throughout the day, configuration discipline is maintained by tying each flight to a recorded configuration state that includes the relevant propulsion settings, battery set identification, and any changes applied since the previous sortie. This ensures that anomalies can be traced to configuration changes and that post-flight analysis remains interpretable.

Each mission begins with a visual and functional pre-flight inspection. Control surfaces are checked for correct direction and freedom of movement, and propulsion systems are enabled, and safety mechanisms are verified. It also needs to be verified that the geofence parameters and the flight-termination system are correctly loaded in the ground station and match the day's operational volume. After landing, the SFD is recovered from the runway, and batteries are removed from the SFD as required. The SFD is being inspected, the data is downloaded, and line-maintenance actions are done if required. To maintain consistency, a log for every flight is created. This log records the exact setup used, including propulsion settings, which batteries were installed, and any recent changes. This practice ensures that if an issue occurs, it can be easily linked to a specific change, and it gives the context needed to understand the flight data later.

12.5.2. Roles, responsibilities, and authority

BVLOS operations are safety-critical and time-limited (because of the activated airspace). The team is structured so that everyone has a specific authority. The operations lead is responsible for go/no-go authority for the day, confirms that airspace and environmental requirements are satisfied, and ensures that briefing and emergency procedures are performed correctly. The remote pilot holds authority over flight execution, including the authority to trigger the FTS if containment or control is at risk. Observers and the safety officer continuously monitor operational volume and the ground-risk buffer, providing real-time calls that support timely abort decisions and boundary avoidance. Propulsion and avionics technicians manage configuration control, conduct pre-flight functional checks, and perform safe electrical isolation and line maintenance activities. This structure ensures that every safety-critical function has an owner, while keeping the workflow compatible with a small test team.

12.6. Environmental limits and daily go/no-go criteria

The SFD is intended for Day-VMC missions; however, to ensure safety, there are additional internal weather limits. At all times when the SFD is airborne, visual monitoring of the operational volume from the ground must be feasible; this means there must be a minimum visibility and a minimum cloud base relative to the planned operational volume. The runway must be dry and free of standing water to support braking predictability (as water degrades the braking) and to limit electrical hazards. Wind limits are there for both safety and test validity. The crosswind component for take-off and landing is limited to 6 m/s to reduce the risk of runway excursion due to lateral drift and to preserve propeller ground clearance margins that may be reduced by bank angles during crosswind landing. There are also temperature limits for battery performance and mission objectives, determined before flight operations.

12.7. Contingency procedures and emergency response

12.7.1. Safe state and containment concept

Failures can occur at any stage; it is important to define for every situation a safe state to transfer to and to ensure safety. On the ground, the safe state is achieved by removing the batteries or isolating the battery system from all other systems with the isolation mechanisms. In flight, the safe state is reached by terminating the test that was being performed and setting up for a controlled landing within the operational volume. Only if containment cannot be maintained can the flight be terminated. Containment is applied in layers in the system, from normal navigation within the operational volume to safety actions when there is a link loss or approach to the geofence limit, and finally to manual termination by the pilot when required.

12.7.2. Propulsion and power-system

The propulsion failures are treated conservatively, as this would mean that the SFD is potentially harder to control. Any motor failure will result in termination of the test that was being performed, and a controlled landing will be performed when possible. The SFD is designed in a way that, with up to half of the engines inoperative, the SFD can still maintain stable flight and land safely. Being conservative prevents the mission from being performed in abnormal conditions, simply to complete the mission. If battery or power-distribution issues occur, the operational response prioritises a controlled landing and electrical isolation after landing. Main-battery isolation is available, and a backup power source supports essential functions, enabling a controlled recovery even if the main power system degrades significantly. After any abnormal power event, the SFD is landed safely on the ground before further handling, and the fault is investigated before starting a new mission.

12.7.3. Major incidents, emergency response, and return-to-flight gating

In the event of a crash or forced landing outside the intended runway, operations are suspended, and the area is secured to prevent secondary hazards, particularly battery fire or re-energisation of damaged wiring. The site is secured first, then hardware is recovered only when it is safe, and event data required for investigation is preserved, so this is all treated as a controlled operation. After a major incident, the SFD returns to depot maintenance for repair, and the campaign resumes only after corrective actions and re-qualification checks have been completed, including a stationary powertrain verification when applicable.

12.8. Verification and validation summary

12.8.1. Compliance matrix verification

Table 12.1: Requirement compliance operations

ID	Requirement Description	Verification Method	Compliance Level
SFD-STK-SOP-01	The system's design and operation shall satisfy all Dutch and International regulations regarding BVLOS flight.	Analysis + Inspection	The SYS-OPS and SYS-SOP requirements are derived from EASA SORA BVLOS constraints and the operational concept assumes BVLOS testing at NLR Drone Centre inside controlled airspace EHR66 to ensure regulatory compliance.
SFD-STK-SOP-02	The system shall be able to finish a minimum of 20 flight missions.	Analysis + Test	The staged campaign, maintenance concept, and configuration-controlled flight logging support and verify completion of at least 20 flight missions without exceeding defined operational limits.
SFD-STK-SOP-03	The system shall be able to finish a minimum time-per-mission of 20 minutes.	Analysis + Test	The energy budget and battery sizing are based on a 20-minute mission requirement, and mission endurance is confirmed during flight testing.
SFD-SYS-OPS-01	The flight control system shall implement a 3D geofence restricted to the EHR66 airspace.	Inspection + Demonstration	A three-dimensional geofence is defined for EHR66 operations, and its parameters are verified during pre-flight checks in the ground station before each mission.
SFD-SYS-OPS-02	The geofencing system shall automatically trigger a safety action when approaching the boundary buffer.	Demonstration + Test	A boundary buffer is implemented to trigger predefined safety actions as the SFD approaches the geofence limit, validated during ground checks and progressive flight testing.
SFD-SYS-OPS-03	The probability of leaving the operational volume due to failure shall be $< 1\times10^{-4}$ per flight hour.	Analysis	The containment safety case relies on layered mitigations (geofence, boundary-buffer action, RTH behaviour, and an independent FTS) and conservative operational procedures to meet the required containment probability.
SFD-SYS-OPS-04	The system shall define a 'Safe State' and automatically transition to it upon critical failure.	Analysis + Demonstration	Safe state is defined for both ground and flight, and transitions are implemented through flight-control logic and procedures.
SFD-SYS-OPS-05	The control laws shall implement envelope protection.	Inspection + Test	Envelope limits are implemented via flight-control configuration and validated during simulation/ground checks and envelope-expansion testing.
SFD-SYS-OPS-06	The system shall enforce a maximum operating speed V_{MAX} consistent with ground-risk kinetic energy assumptions.	Analysis + Demonstration	V_{MAX} is treated as a safety-critical operational limit and is enforced via flight-control configuration and operational procedures to remain consistent with the assumed ground-risk kinetic energy constraints.

SFD-SYS-OPS-07	The SFD design shall be compatible with Day-VMC operations (no requirement for night lighting or anti-icing systems).	Inspection	The campaign is defined as Day-VMC, avoiding night operations and conditions that would require anti-icing.
SFD-SYS-OPS-08	The flight control system shall enforce a vertical altitude limit (lower of 3500ft AMSL or Authorised Altitude) independent of the lateral geofence.	Inspection + Demonstration	The operational altitude ceiling is implemented as an independent flight-control limit and is verified during daily readiness review and pre-flight ground-station configuration checks.
SFD-SYS-SOP-01	The system shall include a Flight Termination System (FTS) independent of the primary flight control computer, compliant with EASA SORA BVLOS standards.	Inspection + Demonstration	An independent FTS is included as the final containment layer and can be triggered manually by the remote pilot or automatically under defined conditions.
SFD-SYS-SOP-02	The system shall comply with all relevant EASA SORA BVLOS standards regarding data logging, radio connection, and required components.	Analysis + Inspection	Compliance is ensured through traceable requirements, avionics/component selection, and operational procedures.
SFD-SYS-SOP-03	The Command, Control, Telemetry, and Video links shall maintain continuous connectivity at a range of 25 [km] to support BVLOS operations.	Analysis + Test	The C2/telemetry link architecture and the video link (FPV camera system) are selected for BVLOS use; link performance is confirmed by link-budget assessment and ground/range testing at the BVLOS site to demonstrate continuous connectivity for the required range once baselined.
SFD-SYS-SOP-04	The SFD shall demonstrate a Mean Time Between Critical Failures (MTBCF) greater than 10 flight hours.	Test	The target MTBCF is demonstrated by accumulating flight hours under configuration control and tracking critical failures; staged verification is used to reduce the probability of critical failures before BVLOS flights.
SFD-SYS-SOP-05	The energy storage system shall provide sufficient capacity for a take-off procedure and 20 minutes of flight at cruise power.	Analysis + Test	Battery sizing and the energy budget support take-off and a 20-minute cruise mission (with reserve margins), and endurance is validated during flight testing.
SFD-SYS-SOP-06	The SFD shall be capable of maintaining stable level flight with 50% of engines inoperative (OEI condition).	Analysis + Demonstration	The rudder is sized in a way that it can withstand the moment caused by the operative engines.
SFD-SYS-SOP-07	The system shall be able to land safely with 50% inoperative engines (critical engine failure scenario).	Analysis + Demonstration	The rudder is sized in a way that it can withstand the moment caused by the operative engines.
SFD-SYS-SOP-08	The power architecture shall provide at least one layer of backup power to all control actuators and the flight camera to ensure safe emergency landing capability.	Inspection + Test	A dedicated backup power source supports essential LV loads to enable controlled recovery if the main battery system fails, and is verified through integration and iron-bird fault-injection testing.

13 Finances & market analysis

In this chapter the financial state of the project is evaluated. First the previously estimated cost breakdown is re-visited and finalised. This in combination with the research & development costs and the operational costs will determine the total cost of the project. After which, the market analysis will be revisited and the SFD's market potential will be investigated.

13.1. Cost breakdown

In order to project the potential return on investment, the development costs of the SFD need to be quantified. In the preliminary cost breakdown, only the expected allocation of the budget was given. Now, a distinction between research & design costs, component & manufacturing costs and operational costs is made. Costs will be estimated based on comparative projects and on current (similar) off-the-shelf products.

13.1.1. Research and design costs

Research and design is one of, if not the most crucial phases in any design project. Here, the fundamentals of the design are established and the viability is constantly being assessed. Design teams are responsible for a great amount of work, ranging from conceptual design to making sure the design abides by the control laws. In table 13.1, the main design elements can be found, along with the amount of hours worked on it. The costs are based on a professional engineer's hourly rate of €150, as presented in DSE briefing [64]. For the purpose of obtaining a full overview, the design phase over the past 10 weeks is considered the full research and design phase. However, for completeness sake, hours for testing have been incorporated.

Table 13.1: Cost breakdown structure of the research and design phase

Research and Design Costs [FY26]			
Description	**Amount**	**Total costs (€)**	**Reference**
Conceptual design	500 hours	75000	[15]
System architecture design	100 hours	15000	[15]
Aerodynamics	700 hours	105000	[15]
Structural analysis	700 hours	105000	[15]
Propulsion analysis	500 hours	75000	[15]
Control law development	100 hours	15000	[15]
Software development & Powertrain	600 hours	90000	[15]
Simulation and modelling	500 hours	75000	[15]
Integration and debugging	300 hours	45000	[15]
Design testing	300 hours	45000	[15]
Documentation, reporting & presenting	200 hours	30000	[15]
Total research and design costs	4500 hours	**675,000**	

As can be seen, a total of 4500 will be spent on the research and design of the SFD, which equates to €675.000. In section 13.1.4 there will be a brief explanation of the margins, while section 13.1.5 goes into how this total falls within the requirements.

13.1.2. Component & manufacturing costs

The component and manufacturing costs are costs which purely pertain to the physical usability of the design. This, in combination with the research & design cost, is also know as the ready-to-fly manufacturing costs, which are of importance for design requirement *SFD-STK-COS-02*. The component costs and their origin can be found in section 7.2.3, and are as mentioned commercial-of-the-shell

components. For other parts, like the structure, the origins are also referenced. Table 13.2 shows these component and manufacturing costs.

Table 13.2: Cost breakdown structure of components and manufacturing

Component and Manufacturing Costs [FY26]				
Component	**Cost per piece (€)**	**Amount**	**Total costs (€)**	**Reference**
Camera transmitter + camera	219	1	219	subsection 7.2.3
Flight computer	8,100	1	8,100	subsection 7.2.3
Flight data recorder	20,000	1	20,000	subsection 7.2.3
5G transmitter	80	1	80	subsection 7.2.3
Data collection system	20,000	1	20,000	subsection 7.2.3
Electronic speed controller (ESC)	225	6	1,350	subsection 7.2.3
Motor (+ cables)	370	6	2,220	subsection 7.2.3
Main battery	1,120	5	5,600	subsection 7.2.3
Backup battery	17	3	51	subsection 7.2.3
Flight actuator	109	9	981	subsection 7.2.3
Rudder servo	109	1	109	subsection 7.2.3
RF antenna	5	1	5	subsection 7.2.3
GNSS antenna	30	1	30	subsection 7.2.3
Buck converter	20	2	40	subsection 7.2.3
Battery charger (ground station)	750	2	1,500	subsection 7.2.3
Ground station RF antenna	5	1	5	subsection 7.2.3
Ground station GNSS antenna	30	1	30	subsection 7.2.3
Fuselage half (CFRP)	5,000	1	5,000	[29] [60]
Component floor fuselage (Aluminium)	200	1	200	[29] [60]
Nosecone (CFRP)	2,500	1	2,500	[29] [60]
Tail (CFRP)	3,000	1	3,000	[29] [60]
Empennage incl. control surfaces (CFRP)	8,000	1	8,000	[29] [60]
Wingbox (CFRP)	3,500	2	7,000	[29] [60]
Wing skin right (CFRP)	3,500	1	3,500	[29] [60]
Wing skin left (CFRP)	3,500	1	3,500	[29] [60]
Wing tip right (CFRP)	1,500	1	1,500	[29] [60]
Wing tip left (CFRP)	1,500	1	1,500	[29] [60]
Front landing gear (outsourced)	N/A	1	7000	[29] [60]
Main landing gear right (outsourced)	N/A	1	5000	[29] [60]
Main landing gear left (outsourced)	N/A	1	5000	[29] [60]
Landing gear fairing (CFRP)	1,375	2	2,750	[29] [60]
Engine fairing (CFRP)	666.67	6	4,000	[29] [60]
Total component and manufacturing costs			**121,770**	

The total component and manufacturing costs amount to €121,770. Again, similar to the research and design cost, the margin of these costs and how it complies to the system requirements will be discussed in section 13.1.4 and 13.1.5.

13.1.3. Operational costs

The operational costs for the SFD stem from the operational requirements. *SFD-STK-SOP-02* states the system shall be able to finish a minimum of 20 flights while *SFD-STK-SOP-03* sets the minimum required mission time. Therefore, the total operational costs will accumulate until those mission requirements are fulfilled. Since there is little to no information about comparable SFDs, the values will be estimated. For the electricity consumption, a single mission uses 5.7 kWh (section 7.2.3), for 20 minutes amounts to 114kWh. Regarding flight testing, it is assumed 2 engineers are necessary to operate, with the cost of €150 an hour. For a 20 minute flight, a 4 hour testing duration is taken. This amounts to 80 hours. To account for any risk, or broken part, 10% of the total manufacturing cost is expected for maintenance and repairs. For the insurance, a similar SFD from clean aviation was insured for €2,000,000, where

their entire project cost was around €100,000,000 [8]. Therefore, 2% of the total project cost is taken as insurance cost. The logistics are assumed to account for the transport from the TU Delft Laboratory to the test facility at Marknesse. With the necessary safety equipment this would amount to roughly €300 per 2-hour trip from or to Marknesse. [1]

Table 13.3: Cost breakdown structure of operational costs

Operational Costs [FY26]			
Description	**Amount**	**Total costs (€)**	**Reference**
Electricity consumption (battery charging)	114 kWh	28	7.2.3
Flight testing	80 hours	12,000	subsection 13.1.3
Maintenance and repairs	N/A	12,177	subsection 13.1.3
Insurance and permits	1	16,000	subsection 13.1.3
Logistics and transport	40	12,000	subsection 13.1.3
Total operational costs		**40,505**	

Having concluded the operational cost, the final cost budget of the entire project can be seen in table 13.4

Table 13.4: Overall project cost summary

Cost category	**Subtotal (€)**
Research and design costs	675,000
Component and manufacturing costs	121,770
Operational costs	40,505
Total project cost	**837,275**

13.1.4. Cost margin

As in every preliminary design, budgeting is a rather complicated task as the design still has many dependencies and uncertainties. As proposed in [15], at the initial design phase, a margin of 50% should be applied to all budgets to account for these uncertainties. As a design project progresses, these uncertainties reduce and so does the margin. At the current stage of the design, a 20% margin should be applied to the budgets. Regarding the cost budget, as explained in section 13.1, the research phase is considered fulfilled, therefore the margin will not be applied to this phase. The final project cost summary can now be found in table 13.5

Table 13.5: Overall project cost summary

Cost category	**Subtotal (€)**
Research and design costs	675,000
Component and manufacturing costs	146,124
Operational costs	48,606
Total project cost	**869,730**

13.1.5. Requirement Compliance Verification

With the cost budget fully mapped out, it is now possible to review the requirements concerning the cost. The requirements, description and their compliance can be found in table 13.6

Table 13.6: Requirement compliance cost budget

ID	**Requirement Description**	**Verification Method**	**Compliance Level**

[1] https://www.transportscanner.eu/kennisbank/transport-en-vervoer/speciaal-en-zwaartransport/ accessed on 20-01-2026

SFD-STK-COS-01	The system shall have a total research and design cost not exceeding 800,000 euros	Analysis	As seen in section 13.1.3, the design costs amount to 675,000 euros and the system therefore fully complies
SFD-STK-COS-02	The system shall have a total ready-to-fly manufacturing cost not exceeding 1 million euros	Analysis	As seen in section 13.1.3, the ready-to-fly manufacturing costs amount to 821,124 euros and the system therefore fully complies.

13.2. Market analysis

As the design stages develop, and potential market entry becomes imminent, it is important that design still satisfies the market needs as initially intended. In order to fully verify if this is the case, the fundamentals of the earlier performed market analysis will be repeated. Then, in combination with the cost breakdown, a final conclusion on the viability can be made.

As stated before, a design of any technological advancement is not driven solely by technical or sustainability requirements but also on its designated market. Simply designing for the satisfaction of current user and customer requirements is not economically viable. It means that, regardless of how well a product might function, it should focus on market gaps in order to successfully break into the market.

Currently, there is an ever-increasing need for technological advancements within the aviation sector, mainly driven by sustainability concerns. Where the International Civil Aviation Organization's (ICAO) current CORSIA guidelines determine that every airline must offset any increase in carbon emission growth compared to 2020, their new goal (in line with the Paris agreement) requires net-zero emissions by international aviation in 2050. [31] This new requirement means that drastic changes must be made to current aviation standards. In order to achieve this, various systems like the propulsion-system will undergo significant changes and will need extensive testing, which is very time- and cost-consuming. Consequently, the demand for cost-effective testing methods - such as the use of scaled flight demonstrators - is also increasing.

13.2.1. Market definition

In order to define the market, it has to be clear what exactly is being developed. A Scaled Flight Demonstrator (SFD) is a downsized, unmanned version of a full-scale aeroplane, made to replicate its flight mechanics and dynamics. It is meant to replicate dynamic characteristics such as aerodynamic properties, aeroelastic behaviour and stability and control. This is specifically valuable to companies and organisations who perform extensive testing in order to introduce ground-breaking innovations, such as Elysian. The SFD market is actually not a market of it's own, but rather an ever-increasing part of the total flight demonstrator market. This rapidly growing market is expected to nearly triple in the next 6 years, with SFDs projected to fuel a majority of this growth.[11]

13.2.1.1. Total Addressable Market

As the market is being defined, a list of potential customers needs to be defined, which is done by looking at the Total Addressable Market (TAM). The TAM is the maximum revenue opportunity a business could generate if they captured 100% of the target market. In order to define this target market, an extensive list of potential customers is given here. All organisations that develop, validate or certify new aircraft configurations which require physical flight testing are included in the TAM:

Commercial aircraft manufacturers & Original Equipment Manufacturers (OEM): Aircraft manufacturers such as Airbus, Boeing and Lockheed make up the biggest part of the flight demonstrator market as they are the biggest producers of aircraft. As commercial aircraft manufacturers are constantly confronted with new environmental requirements, they are in continuous research and development. Currently, most aircraft manufacturers and OEMs (like Northrop Grumman) produce their own flight demonstrators, nevertheless, they are in need of more efficient (scaled) options as the increasing volume of testing is more cost-intensive on a full-scale level. [37]

Electric & Hybrid aviation start-ups: Electric aviation start-ups, much like Elysian and Heart Aerospace, are becoming a centerpiece in the scaled flight demonstrator market. As the rapid shift towards sustainable aviation desperately calls for innovative ideas and start-ups, SFDs provide an accurate, accessible and affordable way to test new technological advancements.

Research institutions: Research institutions, like NLR and DLR, are also key players within the flight demonstrator field. Similarly to electric aviation start-ups, these institutions perform a lot of extensive testing to find novel sustainable aircraft configurations. Research institutions, however, remain more focused on the social and sustainable implications of these advancements, while the start-ups are more commercially oriented. [44]

Organizations & Projects: As sustainability matters become more urgent, the number of initiatives, projects and organisations grow. The Clean Aviation Joint Undertaking, co-funded by the European Union, is a prime example of a public-private collaboration dedicated to accelerating innovation for the benefit of society. This heavily funded initiative, along with other joint undertakings of the Horizon Europe scheme, contribute to the demand for scaled flight demonstrators. [8]

Universities: Universities, with their great resources in terms of researchers, are often drivers of innovation by means of testing various concepts. Usually, they collaborate with other institutions (like NLR), or more commercial companies which might have more resources to offer, since they often have limited funds for specific research. This sets a need for a low-cost flight demonstrator to accommodate for the various tests.

Defense contractors: Defense is becoming a more common theme as of late which means the, already large, demand for testing flight models is increasing. National armies and defense contractors use a wide range of aerial vehicles; from classic aeroplanes to Vertical Take-off and Landing (VTOL) aircraft and UAV's. This also means that their demand for testing models is not limited to a certain type of aircraft, but rather prompts the need for modular flight demonstrators which can be used for various research missions.

Government agencies & regulatory bodies: Regulatory bodies make up for a significantly smaller portion of the market. Some regulatory bodies do have flight models for the sole purpose for legislation. The bigger contribution of government agencies, however, is through their funding of R&D projects. Through this way projects like horizon Europe get funded. [24]

13.2.1.2. TAM Calculation

In order to get a realistic estimation of the TAM, the market of flight demonstrators will be used in combination with the projected demand for scaled flight demonstrators. This is done to get a more accurate analysis as the Scaled Flight Demonstrator demand is expected to triple over the course of 7 years. [11]

In 2023, the flight model market was estimated to be 12.8 billion dollars. A compounded annual rate of growth of 8.2 % was deducted which means that the expected market size in the future can be estimated. Estimating a market entry in 2030, the total market size would be 22.22 billion dollars. Based on an estimate [1] that the current SFD sub-market makes up for 8-10% of the total market, and the significant increase in interest in SFDs, the projected market share of SFD in 2030 is 20-25%. Then the final total addressable market during entry would be roughly 5.0 billion dollars.

13.2.2. Market segmentation, target market & competitors

As seen in the mid-term report [20], this total addressable market can be split up into various segmentations. The main ones are:

- Application based segmentation
- Research segmentation
- Budget segmentation
- Regional segmentation

With each of those consisting of various categories. After analysing all these segmentations, an initial target market can be deduced. Based on the technological advancements currently made in certain

areas, and the volume of certain consumers, it seems that the initial focus should be on European and North American based OEM's and start-ups in order to maximize the addressable market.

Currently, the main players in the market are major commercial aircraft manufacturers like Airbus and Boeing. They make up for the highest demand of flight demonstrators but, as of yet, still manufacture their own. Airbus is currently increasing spending on scaled flight demonstrators as they are determined to design a distributed electric propulsion aircraft. [9] Other major companies are Northrop Grumman and Lockheed Martin who, as OEMs, also benefit from more cost-effective flight models.

Regarding the competitors, the biggest ones appeared to be:

- Commercial Aircraft OEM's
- Defense & developed aerospace firms
- Research institutions
- Specialist engineering companies.

The competitor analysis in the mid-term report [20] showed the competitive landscape is highly fragmented. No standardized commercial SFD product exists, making modularity and cost-effectiveness strong competitive differentiators for a strong market entry.

13.2.3. Stakeholder analysis

Having established and identified various consumers, competitors and the market needs, an analysis can be made of the stakeholders. In this analysis, every group which is influenced by, or has influence on the design, will be categorized. Within these categories, a distinction is made between their level of interest in the design, their level of influence on the design, their needs and their concerns. This preliminary influence-interest matrix can be seen in figure 13.7.

Table 13.7: Stakeholder power-interest matrix

Stakeholder Group	Influence	Interest	Needs	Concerns
Commercial aircraft OEMs	High	High	safe & predictable flight behaviour, easily changeable configurations	Safety risks, delays during testing, high operational costs
Electric / Hybrid aviation start-ups	High	High	Low-cost demonstrator, easy modification for new concepts	Budget overruns, delays jeopardizing investments, dependency on external testing facilities
National research institutes	High	High	Consistent and repeatable, compatible with existing research infrastructure	low modularity
Universities / Educational institutes	Low	High	Low-cost	Limited infrastructure to fly , safety constraints
Regulatory bodies	High	Low	Compliance with UAV rules	Airspace safety, public safety
Funding programmes	Medium	Medium	Clear environmental benefit, achievable project milestones	misuse of funding, insufficient innovation
Defense contractors / Military organisations	Low	Medium	Robust test platform, suitable for mission-type research	Security restrictions
Local authorities / General public	Low	Low	Safe operation near populated areas, minimal disturbance	privacy concerns

With the use of this table, it becomes clear to what extent certain parties are detrimental to a successful design of the SFD, and which party's requirements might be more driving. From this preliminary table we can determine the more commonly used metric: The stakeholder power-interest matrix. This simple table gives an overview of what parties have to be satisfied to what extent, it can be seen in figure 13.1

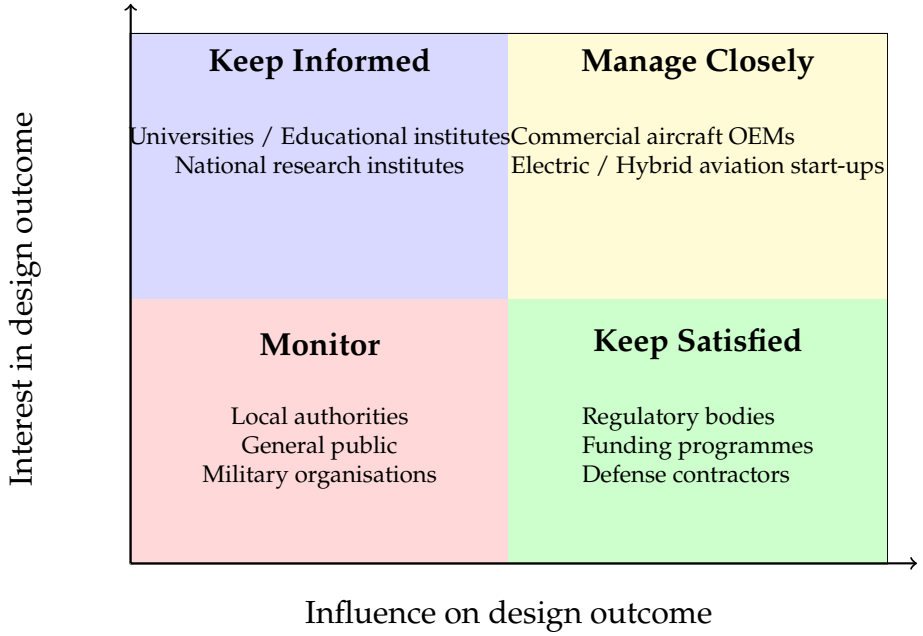

Figure 13.1: Stakeholder power-interest matrix for the SFD project.

13.2.4. SWOT analysis

To evaluate the position of the SFD within the current flight demonstrator landscape, a SWOT analysis is conducted. This analysis identifies the internal strengths and weaknesses of the concept, as well as the external opportunities and threats coming from market developments, regulatory trends, and competitor capabilities. Similar to the method used in the Baseline Report, the SWOT provides a concise overview of the key factors that influence the feasibility, competitiveness, and strategic value of the SFD concept during market entry

Table 13.8: SWOT analysis of the Scaled Flight Demonstrator

Strengths	**Weaknesses**
- Lower cost and lower operational risk than full-scale testing - Modular platform suitable for multiple test campaigns - Short development cycles enable rapid iteration - Applicable across a wide range of research domains (aeroelastic, aerodynamic, propulsion)	- Scaling limitations reduce aerodynamic and aeroelastic fidelity - Limited payload volume for instrumentation - Requires specialised flight test ranges - Not suitable for certification-level data without full-scale validation
Opportunities	**Threats**
- Strong growth in demand for sustainable aviation research -Increasing interest in distributed propulsion and novel aircraft configurations - EU funding initiatives for demonstrator-based validation - Lack of standardised commercial SFD platforms creates a market gap	- OEMs may rely on in-house demonstrator development - Strict UAV regulations limiting flight operations - Competition from specialist engineering firms - Reputational risk if flight tests fail or data proves to be unreliable

From this SWOT analysis it can be seen that most opportunities lie in accommodating for sustainable aviation. Since there is significant sustainability-driven funds going into the flight demonstrator market,

and a there is an increasing number of start-ups, it can be derived that designing for a low-cost, standardised (modular) design is the most viable design for market entry.

13.3. Estimated revenue and return on investment

Having re-visited the market analysis, a very rigorous estimation of the potential revenue can be performed. Although the following estimation is based on many assumptions and will not be accurate, it is necessary to create a preliminary return on investment.

Referring back to the total addressable market, it can be seen that upon market entry, the SFD addressable market is roughly 5 billion dollars. As the consumer and competitor landscape are overlapping, due to the in-house development SFD's, it is difficult to estimate potential revenue. However, in order to achieve a conservative estimate, a few assumptions can be made to simplify the process. First of all, it will be assumed that due to big commercial OEMs not being eager to share SFD designs (necessary for building an appropriate SFD), only 10% of the market is available for the sale of (modular) SFD's. As there is currently no company with its core business being the sale of specialised SFDs, this competitive advantage is assumed to gain 10% of the attainable market. This would yield a revenue of:

$$5,000,000,000 * 0.1 * 0.1 = 50,000,000 \tag{13.1}$$

Taking comparable profit margins for UAV/drone manufacturer profit margins [2], the profit margin is expected to be 10%. Thus net profits yielding €5,000,000.

As return on investment is defined as:

$$ROI = \frac{Netprofit}{Investmentcost} \tag{13.2}$$

And the investment cost was estimated to be €869,730, that would yield a return on investment of:

$$ROI = \frac{7,500,000}{860,730} = 5.81 \tag{13.3}$$

So a 5.81 multiple on the investment is expected based on the current market.

13.4. Conclusion

Now, as the financial feasibility and market viability of the SFD have been evaluated, a few conclusions can be derived. First of all, the total project cost, including the margin, of €869,730 is well within the set requirement and therefore a good indication of the feasibility of the design within the acceptable budgetary limits.

From a market perspective, the SFD operates within the rapidly expanding flight demonstrator market, driven by increasingly constraining environmental regulations and the need for new aircraft configurations. The analysis confirms that scaled flight demonstrators are becoming an essential tool for reducing development risk and cost, especially in the context of sustainable aviation. Europe and North America seem to be the most attractive initial regions for market entry, due to high research activity, increased regulations, and a high concentration of relevant stakeholders.

The stakeholder and SWOT analyses highlight that the primary strengths of the SFD lie in its modularity, lower operational risk, and suitability for fast iteration for a wide range of research. While there are limitations in terms of scaling and regulatory constraints, these do not outweigh the opportunities created by growing investment in sustainable aviation research and demonstrator-based validation.

Overall, the analysis demonstrates that the SFD is both financially viable and well-positioned within the current and projected market. With the increasing environmental pressure, the SFD poses a credible and competitive solution for future experimental flight testing applications.

[2] https://financialmodelexcel.com/blogs/owner-makes/drone-manufacturing-solutions - accessed 20-1-2026

14 RAMS Characteristics

Before a good overview of the technical risks can be made, it is important to know the situations that can occur related to possible failures. A good tool for this is the usage of a RAMS analysis. In this chapter all four of the RAMS categories will be analysed, with the goal of understanding more about the cost- and operational effectiveness of the aircraft.

14.1. Reliability

The first metric of the RAMS analysis is Reliability. This quantifies the probability of a failure happening, compared to number of flights. Although quantifying this into a number is a task far exceeding the scope of this report, a proper estimate can still be made of important factors influencing this characteristic.

First of all, the testing environment is of big importance. The goal of the model is to perform a specific number of flight tests to collect data. This means that the model will likely only be used for a small amount of flights. This already heavily reduces the possibility of accidents happening during flight. It also means that checks will be performed relatively often. After each flight of no longer than 20-30 minutes, a full list of checks will be performed, that allow the operator to fully make sure every component is in a safe state to fly with. Apart from this, the flights will also only performed in nearly optimal conditions. This means the aircraft will not often come into contact with harsh weather conditions, meaning that normal wear and tear of components will go even slower.
Secondly, the design also makes for a number of reliability options. The motors that are chosen for the model are made for VTOL drones. [1] This means that they have been designed for long durations of heavy loading conditions. However, in the SFD model, they will only be loaded at their maximum condition for short amounts of time (only during take-off). This means that they will not wear as much. And in case a motor does fail, the impact will also be of smaller scale. As the aircraft makes use of distributed propulsion, the moment caused by an OEI scenario is less than it would be in an aircraft with only one engine per wing.
There are, however, also a few downsides. Firstly, due to the smaller scale of the design, only one layer of redundancy could be added. This means that, in case there is a failure, there is only one backup system. In turn, the model should be brought to safety as swiftly as possible on backup power in case there turns out to be something wrong in the main system.
Next to that, the modularity aspect of the model also acts as an increase of failure modes. There are multiple connection points on the aircraft that were made to be taken apart. Although these should be designed for structural integrity during flight, it does add an extra point of failure that would not be there on an average aircraft. Also, as the model will be taken apart relatively often, this leads to the possibility of something not being put back together properly. This is especially risky if there is pressure on operators to deliver a quick turn-around time. This risk can, however, be counteracted by performing a standardized checklist everytime before takeoff.

14.2. Availability

Availability measures the effect of downtime due to possible failures. Here, a check is performed on what happens in such cases, and how quickly the model can be operational again.

For this model, there are a few things to consider in this aspect. Firstly, the fact that most components are commercially available. This is not only a very important factor to keep the production cost down, but in this case it also helps the operator get things back on track quickly. When a failure occurs in any of the electronic components, there are multiple supply chains that can provide new parts on a relatively short term. It also means that the price of these components is relatively low, making for a smaller financial blow.
However, there is also a disadvantage to the model. Due to the fact that only one aircraft (or at least

[1] https://store.tmotor.com/product/u12-v2-kv120-u-efficiency.html , accessed on 20/01/2026

a very small number of them) is built, it does not make sense to have a very elaborate set of backup components in store. This would only provide a lot of leftovers after the intended tests are done. It also means that there is no backup aircraft to use while waiting for the current one to be repaired. This could cause downtime in testing procedures.

14.3. Maintainability

The third factor is the maintainability. This shows how easily repairs can be performed. Here a number of aspects beneficial in this design.

Firstly, the design is very "maintenance-friendly". Due to the fact that multiple components can be taken off for modularity's sake. Together with the fact that the fuselage has a big hatch at the top, to allow for easy removal of the batteries for charging, this makes that any maintenance engineer can very quickly access most points in the aircraft. Not only the fuselage, but also the electronics have all been designed for this, which makes fixes faster, and in turn, reduces downtime due to maintenance. Lastly, the scale also simplifies things for any engineer working on maintenance. Since the model is relatively small, everything can be reached without having to make use of any external tools like hydraulic platforms.
Another benefit, is the fact that the tests are very concentrated around a central location. The flights do not last any longer than $20 - 30$ minutes, and the aircraft is always returned to the same base. This means that, if any flaws are found, a quick response can be made by the operators in the ground station.
Lastly, the use of the Embention Veronte as the main flight computer, allows the operator to use custom software made with C++. As this is a very accessible language, that is well-known by most software engineers, any mistakes in the original design of the software can more quickly be found and repaired.
A disadvantage of this system could be that there are a lot of electronics involved. This can make troubleshooting a bit more elaborate process compared to traditional fully mechanical designs. However, this disadvantage is mitigated partly with the fact that it is a relatively small system, hence using only a small amount of connections.

14.4. Safety

The last metric of this analysis is safety. Both technical safety, as well as operational safety should be taken into account here (although here described in this section as one). It comprises of determining possible risks that could impact the operators or environment in an unsafe way.

Here, the testing area comes in beneficial again: Due to the fact that a special area is used for these tests, the risk of interfering with other parties in the airspace is very low. The same goes, in case of flying from Marknesse, for the ground level surroundings. In case there is a crash, it is relatively unlikely to hit anything, as the tests are performed on a comparatively remote area of the Netherlands.
For technical safety, a lot of lessons were learned from the DEP-SFD-D08. As there was an accident in the initial tests of this program, they hit a couple of setbacks that cost a lot of time and budget[17]. However, the improved model includes more safety measures on the electronics that are also applicable to this aircraft. From the use of redundant fusing, as well as using a mechanical emergency switch to allow operators to make sure the system is fully turned off when needed. A final thing that was new, however, is the use of a backup power system. This battery is capable of powering all LV system, granting the pilot the opportunity to make an emergency landing using all control actuators, as well as make use of the full functionality of the FCMS in case of a main battery failure.
There are also a number of risks involved with the model. Firstly, the use of Lithium batteries, gives a possibility of thermal runaway [12]. This could cause irreparable damage to the model, but it also have a very big impact on any person involved if proper safety precautions are not taken. This means that any engineer working on the aircraft should have clearance from the main test operator before they start their work. This way it can be prevented that anyone is working while the system is in unsafe state. This also has to do with the fact that a lot of electronic systems are used. Working with voltages of around $50V$ can be dangerous if not using proper procedures. It can cause different results from muscle spasms, up to cardiac arrests in the worst cases [2].

[2] https://www.hse.gov.uk/electricity/injuries.htm , accessed on 20/01/2026

15 Technical Risk Assessment

In this section, the technical risks of the project are summarized. All identified risks are listed in the risk assessment section 15.1 and likelihood and consequence of individual risks are displayed in the risk map. Mitigation strategies for the most severe risks are presented in section 15.2 and the result can be seen in the new risk map. Further action to be taken if the new risk were still to occur, despite attempted mitigation, is presented in the contingency plan section 15.3.

15.1. Risk Assessment

All the risks identified throughout the project are listed below and the most severe risks with a risk rate equal to or above 10 are elaborated in Table 15.2. The full descriptions and analysis of the risks not listed in this table can be found in the baseline and midterm report. Each risk has a unique ID number which corresponds to the type of risk it is. The risks involved in meeting the technical performance requirements during the design and development phase have an ID number beginning with P. The risks during the operation of the model after it's construction have an ID number beginning with O. The risks involved in bringing this scaled flight demonstrator to market as a product have an ID number beginning with M. The likelihood and consequence score is elaborated in Table 15.1 and the risk rate is defined as the product of these scores. For every risk, a person has been chosen who is responsible for monitoring that risk and implementing the mitigation and contingency plans where applicable. An initial risk assessment was presented in the baseline report and as the design progressed new risks were identified in the midterm report. As the design configuration has remained the same from the baseline no risk was able to be removed. [19][20]

Initial risks identified in the Baseline report:

- P-RSK-1: Similitude
- P-RSK-2: FCMS
- P-RSK-3: Failure
- P-RSK-4: Endurance
- P-RSK-5: COTS
- P-RSK-6: Windtunnel
- P-RSK-7: Stability
- P-RSK-8: Controllability
- P-RSK-9: Batteries budget
- P-RSK-10: OEW
- P-RSK-11: Link budget
- P-RSK-12: Modularity
- P-RSK-13: Assumptions
- P-RSK-14: Calculation errors
- P-RSK-15: Exceeding Load factor
- O-RSK-1: Regulations
- O-RSK-2: Engine failure
- O-RSK-3: Battery failure
- O-RSK-4: Propeller separation
- O-RSK-5: Stopping distance
- O-RSK-6: Landing gear
- O-RSK-7: Pilot error
- O-RSK-8: Range
- O-RSK-9: Bird strike
- O-RSK-10: Go around
- O-RSK-11: Water ingress
- O-RSK-12: Dust contamination
- O-RSK-13: Cyber Security
- O-RSK-14: Test area
- M-RSK-1: Cost
- M-RSK-2: Uncompetitive price
- M-RSK-3: Total addressable market
- M-RSK-4: Supply chain

Additional risks identified in the Midterm report:

- P-RSK-16: Geometric scale
- P-RSK-17: Attachable parts
- P-RSK-18: Mass ratio
- P-RSK-19: Moment of inertia ratio
- O-RSK-15: Poor Visibility
- O-RSK-16: Icing
- O-RSK-17: Wind gusts

Table 15.1: Likelihood & Consequence Explanation

Score	Likelihood Explanation	Consequence Explanation
1	p≤1% Minimal liklihood that this event will occur	Negligible impact on the ability to achieve the mission objective
2	1%≤p<25% Low likelihood that this event will occur	Small impact on the ability to achieve the mission objective
3	25%≤p<50% It is likely that this event will occurr	Moderate impact on the ability to achieve the mission objective, possible partial mission failure
4	50%≤p<75% Highly likely that this event will occur	Large impact on the ability to achieve the mission objective, probable partial mission failure
5	p≥75% Almost a certainty that this event will occur	Severe enough impact to cause mission failure

Table 15.2: Pre-Mitigation Risk Assessment

Risk ID	Risk Description	L	C	Risk Rate	Responsible
P-RSK-1	**Similitude:** The model fails to replicate the flight mechanical behaviour of the full scale DEP system to a sufficient degree of similitude.	2	5	10	Aerodynamics Engineer
P-RSK-3	**Failure:** Critical structural failure of the SFD before it can complete a minimum of 20 flight missions.	3	4	12	Structural Design Engineer
P-RSK-14	**Calculation Errors:** Calculations errors are made during the design process	5	2	10	Systems Engineer
P-RSK-18	**Mass ratio:** Final model mass differs from the design mass such that it is not consistent for scaled similitude	4	3	12	Structural Design Engineer
P-RSK-19	**Moment of inertia ratio:** The mass moment of inertia of the model differs from the valued required for scaled similitude	5	3	15	Structural Design Engineer
O-RSK-01	**Regulations:** The model fails to comply with BVLOS flight regulations.	2	5	10	Chief Operations
O-RSK-02	**Engine failure:** Multiple engines fail during flight and are unable to provide thrust.	3	4	12	Propulsion Engineer
O-RSK-03	**Battery failure:** The main battery fails during flight and can no longer provide power to the engines and other systems.	3	4	12	Electronic Engineer
O-RSK-07	**Pilot error:** An error made by the pilot causes the destruction or damage to the SFD by collision or by operation outside of the designed flight envelope.	4	4	16	Chief Operations
O-RSK-10	**Go-around:** Due to runway misalignment or adverse condition the SFD pilot is forced to abort an attempted landing and must perform a go-around manoeuvre.	5	2	10	Electronic Engineer
O-RSK-13	**Cybersecurity:** Unauthorised access, jamming or spoofing disrupting the control and data link to the SFD.	2	5	10	Data Handling Engineer
O-RSK-14	**Test area:** The SFD goes outside of the EHR66 controlled airspace during flight testing.	4	3	12	Control Engineer
O-RSK-17	**Wind gusts:** will put high levels of stress on the structure and control systems	3	4	12	Chief Operations
M-RSK-01	**Cost:** The total ready-to-fly manufacturing cost of the model is greater than 1 million Euros.	4	3	12	Business Manager

15.2. Risk Mitigation Plan

For each risk with a risk rate equal to or above 10 identified in section 15.1, a mitigation plan was developed to either reduce the likelihood of the risk occurring, reduce the consequence if the risk were to occur or both. If a design requirement is derived from a risk it is included in the mitigation plan. A comparison between the risk map before and after mitigation is shown in Figure 15.1.

Table 15.3: Risk Mitigation Plan and Post-Mitigation Assessment

Risk ID	Mitigation Plan	L	C	Risk Rate
P-RSK-01	**Similitude:** During the design phase specific focus will be paid to design the SFD such that it replicates the flight mechanical behaviour of a DEP as required by SFD-PRF-7. This will reduce the likelihood that this will occur.	1	5	5
P-RSK-03	**Failure:** The structural department will use an appropriate safety margin with all structural calculations. This will reduce the likelihood that failure occurs and that the SFD-SUS-2 requirement is met.	1	3	3
P-RSK-14	**Calculations:** The systems engineer will ensure all departments conduct comprehensive verification and validation of all calculations to reduce the likelihood that errors occurs and when the do are caught early on in the design process.	3	2	6
P-RSK-18	**Mass ratio:** The model will be design such that it's weight is less than what is required for scaling and additional ballast mass can be added to get to the correct ratio	2	2	4
P-RSK-19	**Moment of inertia ratio:** The model will include ballast weight that can be moved to approximate the moment of inertia of the full-scale	2	2	4
O-RSK-1	**Regulations:** All the requirements in SYS-LEG are derived to ensure compliance with all the relevant BVLOS regulations. The chief operations will monitor these requirement to ensure that the design meets with all of them.	1	5	5
O-RSK-2	**Engine failure:** Given the high number of smaller engines on a DEP compared to a conventional aircraft design, engine failure requirement SFD-THR-4 was derived to accommodate a 50% engine inoperative condition. The SFD will be designed to be able to safely land at this condition and pre flight engine inspections will reduce the probability of occurrence	2	2	4
O-RSK-3	**Battery failure:** The SFD will be designed to provide access to the batteries to allow for pre and post flight inspection as stipulated in SFD-OPR-1.2. This will reduce the likelihood of failure of the batteries. Furthermore in accordance with SFD-SYS-PWR-05 the main batteries will be isolated from the rest of the power system in case of failure.	1	2	2
O-RSK-7	**Pilot Error:** A test pilot with suitable certification as specified in SFD-OPR-4.3 will reduce the probability of pilot error occurring.	2	4	8
O-RSK-10	**Go-around:** The batteries system will be designed, according to SFD-SYS-PWR-01, with additional margin above the 20 minutes flight time to allow for a go-around manoeuvre. This will reduce the consequence of being forced to abandon a landing.	4	1	4
O-RSK-13	**Cybersecurity:**The Data Handling engineer will ensure that the comms architecture has a sufficient level of protection against cybersecurity risks as specified by SFD-SFR-6.4.	1	5	5
O-RSK-14	**Test area:** A 3D geofence will be programmed into the flight control system as required by SFD-SYS-OPS-01. This will reduce the likelihood that the SFD leaves the test area.	1	3	3
O-RSK-17	**Wind gusts:** The model will only be operated when surface wind gusts are below 20 kt	3	1	3
M-RSK-1	**Cost:** A detailed analysis of each system will be made by the business manager from which the cost budget of the project will be derived, minimizing the probability of overrun. This first budget will have a large margin however further analyses will be conducted throughout the project with an increasingly refined margin.	2	3	6

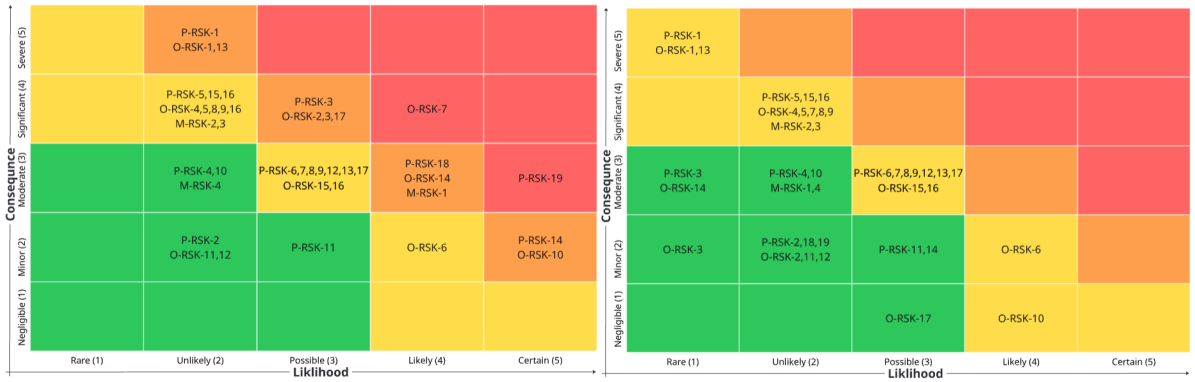

(a) Pre-Mitigation Risk Map

(b) Post-Mitigation Risk Map

Figure 15.1: Comparison of Pre- and Post-Mitigation Risk Maps

15.3. Contingency Plan

A contingency plan for each risk is given in Table 15.4 in case the risk still occurs despite mitigation. Each plan is based on the assumption that the risk mitigation plan, as described in section 15.2, has been implemented.

Table 15.4: Contingency Plan

Risk ID	Contingency Plan
P-RSK-1	**Similitude:** Due to the modularity of the design further adjustments can be made to the design after initial testing to improve the degree of similitude.
P-RSK-3	**Failure:** After each flight the SFD will be inspected and any broken parts or parts with too much ware will be repaired or replaced. The modularity of the design will also allow for easier replacement of larger components and systems.
P-RSK-14	**Calculations:** Any calculations that are identified to be in error must be redone. The design team will use or make design tools that allow for rapid recalculations.
P-RSK-18	**Mass ratio:** The model can fly at a different altitude and height to compensate for the incorrect model mass
P-RSK-19	**Moment of inertia ratio:** The model can fly at a different altitude and height to compensate for the incorrect model inertia
O-RSK-1	**Regulations:** If the SFD is not able to be certified for free flight operations, wind tunnel testing will be prioritised while the necessary design changes are work on. Afterwards, these changes will be implemented and the team will re seek certification.
O-RSK-2	**Engine Failure:** After any engine failure during flight operations the test mission will immediately terminate. The SFD will return to the runway immediately.
O-RSK-3	**Battery Failure:** An independent back up power system will be implemented to allow for a controlled unpowered landing in the event of a failure of the main batteries.
O-RSK-7	**Pilot Error:** The chief of operations must insure that the team and the pilot possesses suitable liability insured. Additionally during flight testing suitable protections for ground crew will be implemented to reduce the chance of injuries and damage caused by any accidents.
O-RSK-10	**Go-around:** The go-around procedure will be developed and communicated with the pilot. Limits to the conditions that the SFD can operate in will also reduce the need of go-arounds.
O-RSK-13	**Cybersecurity:** The SFD will be design with a control system that will enter have a return to home function if the control link from the ground is lost, as required by SFD-SYS-SW-01. This will prevent the SFD from being lost while the link is re-established.
O-RSK-14	**Test area:** If the SFD violates the geofence the flight termination system will be activated by the pilot or automatically.
O-RSK-17	**Wind gusts:** The structure will be design such that it can sustain gust winds up to 15.24 m/s
M-RSK-1	**Cost:** If the cost requirement is determined to be unfeasible further discussion will be made with the stakeholders. The result of this will either be a increase in the requirement or a reduction in scale of the SFD and possibly the scope of the project.

16 Sustainability

With the growing demand of aviation, so does the demand of a sustainable approach to this grow. To have a clear understanding of the term sustainability, it is broken down into three pillars. *Environmental sustainability* focuses on the impact on natural resources, ecosystems, pollution and emissions. *Social sustainability* addresses the impact on people and society, including labour conditions, human health and social equity throughout the supply chain. *Economic sustainability* considers the ability of a product or system to remain financially viable over its life cycle, considering costs, resource efficiency, manufacturability, and long-term scalability. This chapter mainly addresses the environmental sustainability of the SFD through a Life Cycle Assessment (LCA). Subsequently, section 16.2 provides a complementary analysis of the social and economic impacts of the design, and section 16.3 investigates the sustainability impacts of adopting a modular approach for the SFD.

16.1. Life Cycle Assessment

As mentioned in the baseline report [19], the LCA consists of four steps. Step one is the *Goal and scope*; here, the reason for conducting the study is specified, system boundaries, like Cradle to Gate or Cradle to Grave, are defined, and the study's limitations and the functional unit are set. Step two is the *Inventory analysis*; in this step, data on resource consumption, pollution, and emissions are collected and verified. Step three is the *Impact assessment*; this step converts the collected data into environmental impact categories. Finally, step four is the *Interpretation*; here, conclusions are drawn.

16.1.1. Goal and Scope

The goal of this LCA is to evaluate the environmental impact a scaled flight demonstrator has. The study assumes that the SFD will enter production at a scale of at least one thousand units. This enables the assessment of a measurable impact. The system boundary is set to be cradle-to-grave. Thus, the SFD will be assessed on all life-cycle stages, starting with the extraction of raw materials, up to maintenance, and finally its end-of-life treatment and disposal. This enables the study to get a complete overview of the influence of the utilisation of an SFD during the design process of an aircraft. The data used in this study is based on literature. This study is limited to the preliminary stage of the design; therefore, not all data is yet available. Additionally, supply-chain complexities still pose challenges in accurately tracking energy consumption, monitoring waste regulation in manufacturing processes, and tracing the origin of materials. Finally, this LCA is limited to the assessment of only the battery and the composite structural components of the SFD. This limitation is due to the lack of available data for all system components, and the batteries and structure are expected to contribute the most to the environmental impact the SFD has.

16.1.2. Inventory analysis and Impact assessment

This section contains the data on resource consumption, pollution, and emissions during all life-cycle stages. Afterwards, using impact categories, the raw data is translated into potential impact on human health and the environment. As mentioned before, this step is divided into two parts: the battery and the composite structure.

16.1.2.1. Battery

The final design will host five LiPo batteries from Tattu [1]. The mass of one battery is $m = 7.20$ [kg], resulting in a total mass of the batteries $m_{bat} = 36.0$ [kg]. The production, recycling, and disposal of these batteries will require a significant amount of resources in terms of materials and labour. Producing these batteries will require a significant amount of resources in terms of materials and labour, which will be elaborated on below.

[1] https://www.grepow.com/uav-battery/25c-22000-14s-lipo-tattu-pro-smart-battery.html

Inventory analysis
Since Vandepaer et al. [66] already performed an LCA of a LiPo battery, this will be used as a basis for this study. Therefore, the inventory analysis shall focus on an explanation of how the impact assessment came to be and what life-cycle stages of the SFD influence the overall sustainability rather than providing a complete inventory.

Material extraction
LiPo batteries use a combination of materials like Graphite, Lithium metal oxides such as lithium cobalt oxide or lithium manganese oxide, and a polymer electrolyte. In terms of the environmental aspects of the extraction of the materials used, LiPo batteries have a significant impact. Lithium can be extracted in two ways, from salt lake brines or brine deposits through evaporation, or hard-rock mining (e.g., spodumene) [36].

Brine extraction has the upper hand in global lithium supply. It requires large bodies of water and can significantly lower groundwater levels. This depletion of water resources can negatively affect local ecosystems. Additionally, the use of acids and solvents during the process requires careful management and thus often causes environmental contamination [68].

Hard-rock lithium mining, though very different from brine extraction, poses its own environmental risks. This extraction method often utilises open-pit mining, which can result in habitat disruption, landscape alteration, and changes to local waterways, thus affecting local ecosystems [36]. Furthermore, waste materials generated during ore processing and tailings disposal require strict management to prevent environmental contamination. The mining and processing operations are, in addition to the previous challenges, energy-intensive and thus a significant contribution to greenhouse gas emissions.

Manufacturing process
According to Vandepaer et al. [66], the manufacturing phase is the largest contributor to environmental impacts with LiPo batteries. The production of battery cells, which includes electrode fabrication, drying, and cell assembly, is an energy-intensive operation. In addition, the manufacturing process uses toxic chemical agents, which, when unregulated, can lead to significant local toxicity impacts and water pollution.

Battery performance and maintenance
The selected LiPo battery reports to have a cycle life of 600+ charge-discharge cycles [62]. As the 20-minute test flights will drain the battery pack considerably, it will require a recharge. Therefore, the battery supports about 600 flights before its performance degrades and needs replacement. This relatively high cycle life allows the battery packs to be reused across multiple different types of SFDs, as the testing shall be done collaboratively between the user and the manufacturer.

Recyclability and disposal
Lithium batteries present a growing end-of-life challenge due to the rapidly increasing usage of sustainable systems and thus batteries. Currently, materials like cobalt, nickel manganese, copper and aluminium can be recovered from batteries [48], but other recycling rates remain relatively low because existing facilities are optimised for older chemistries and only high-value components. As a result, many materials such as lithium, electrolytes and mixed materials are not recycled [75]. Consequently, these materials often end up in residual waste streams where they are then landfilled or incinerated.

Impact assessment
The study Vanderpaer et al. [66] used the impact assessment method IMPACT 2002+. This method converts up to 1500 different environmental flows into 14 categories. From this, the impacts the entire life of the SFD has in the different categories are listed in Table 16.1 and will be discussed in subsection 16.1.3.

Impact category	Unit	LiPo battery
Carcinogens	kg C2H3Cl eq	9.27E-2
Non-carcinogens	kg C3H3Cl eq	9.73E-2
Respiratory inorganics	2.5 eq	3.28E-3
Ionizing radiation	Bq C-14 eq	3.06E+1
Ozone layer depletion	CFC-11 eq	1.89E-7
Respiratory organics	kg C3H4 eq	8.59E-4
Aquatic ecotoxicity	kg TEG water	7.29E+2
Terrestrial ecotoxicity	kg TEG soil	1.20E+2
Terrestrial acid/nutri	kg SO2 eq	5.30E-2
Land occupation	m2org.arable	6.67E-2
Aquatic acidification	kg SO2 eq	1.73E-2
Aquatic eutrophication	kg PO4 p-lim	9.80E-3
Global warming	kg CO2 eq	1.95E+0
Non-renewable energy	MJ primary	2.87E+1
Mineral extraction	MJ surplus	8.97E-1

Table 16.1: Life cycle assessment of a LiPo battery [66].

16.1.2.2. Composite structure

Carbon Fibre Reinforced Polymer (CFRP) will be used almost exclusively for the structure of the demonstrator. While this material enables significant weight savings during operation, its production and end-of-life stages are known to have a significant impact on environmental sustainability. The amount of CFRP that will be used in the demonstrator is m = 46.3 kg. The production process of CFRP parts is thoroughly explained in subsection 11.1.1.

Inventory analysis

Since ATescan et al. [5] already performed an LCA of CFRP, this will be used as a basis of this study. Therefore, the inventory analysis shall focus on how the impact assessment came to be and what life-cycle stages of the SFD influence the overall sustainability rather than providing a complete inventory.

Material extraction and Manufacturing process

CFRP is a composite that consists of carbon fibre and an epoxy resin. About 90% of carbon fibre starts as Polyacrylonitrile (PAN). PAN is produced from acrylonitrile, which is a polymer that is a by-product of fossil fuel refining [65]. Therefore, the production of PAN is associated with non-renewable resource depletion and greenhouse gas emissions. Afterwards, to turn PAN into carbon fibre, the PAN polymer is first spun into continuous fibres. Afterwards, the fibres are first heated to 200-300°C, then they are heated a second time to about 1500°C in an inert atmosphere, removing all atoms except carbon. This part of the manufacturing process requires high levels of energy, contributing again largely to greenhouse gas emissions.

In the second phase of the manufacturing carbon fibre is layered by hand in the mould, whereafter the resin is transferred into the mould by a generated vacuum. Under this vacuum, the resin is then cured, which is referred to as autoclave-curing. As Chizoba J. et al. said, "autoclave curing is one of the most energy-consuming processes in manufacturing carbon fibre reinforced polymers."[46]. This is due to the long cure cycles and high temperatures, thus requiring high levels of energy [46].

Additionally, machining and trimming of the cured composite parts add significantly to waste generation in the form of dust and cutouts or cutoffs.

Recyclability and disposal

Due to the fact that, unlike metals, thermoset-based composites cannot be remelted, CFRP is less sustainable. Current recycling options generally result in downcycled filler materials with limited structural integrity. While thermal processes such as pyrolysis can recover fibres, this does require high energy input and often degrades fibre properties [7]. What cannot be recycled is commonly landfilled or incinerated. Landfilling composite waste contributes to long-term environmental burdens because polymer matrices are non-biodegradable and can contribute to soil contamination due to the slow release of additives or because of degradation. Incineration reduces waste volume, but in turn contributes to

greenhouse gas emissions and resin-incineration releases hazardous and toxic pollutants. Though the incineration of carbon fibre poses negative impacts, new progress is being made with incineration with energy recovery as an end-of-life route for CFRP [41].

Inventory assessment The reviewed studies indicate that the dominant impact categories for composite structures include global warming potential, non-renewable resource use, and human toxicity. The contributions are largely caused by fibre production, curing energy demand, and poor recycling and disposal options. The scores of different CFRP types and aluminium are displayed in Figure 16.1[5]and will be discussed in subsection 16.1.3.

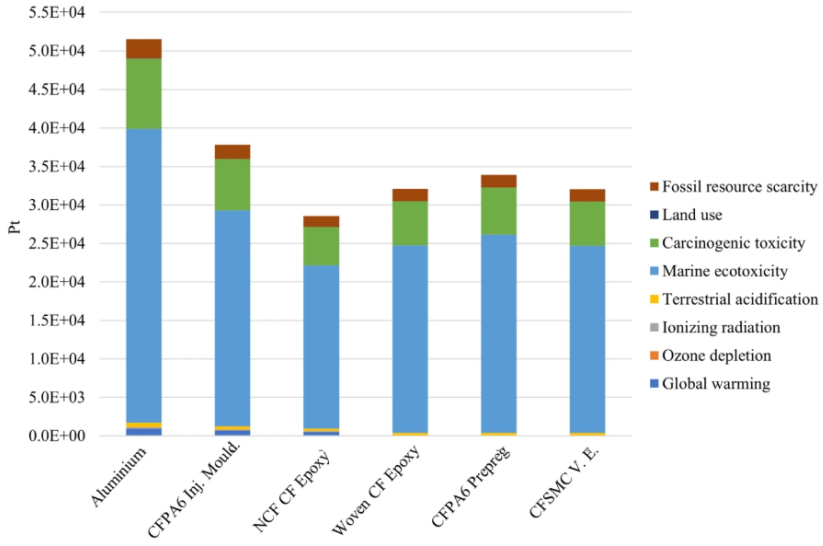

Figure 16.1: Impact results for manufacturing and disposal aluminium and five different composite skin panels [5].

16.1.3. Interpretation

The interpretation phase of this LCA aims to analyse and contextualise the results obtained from the impact assessment, identify the main contributors and evaluate the implications of material and design choices within the defined goal and scope. Given the cradle-to-grave system boundary and the limitation of the assessment to the battery system and composite structure, the interpretation focuses on these two components and their relative contribution to different impact categories.

16.1.3.1. Battery

The results presented in Table 16.1 show that the LiPo battery system contributes notably to several environmental impact categories. The dominant impacts are aquatic ecotoxicity (7.29E+2 kg TEG water), terrestrial ecotoxicity (1.20E+2 kg TEG soil), non-renewable energy use (2.87E+1 MJ primary), and global warming potential (1.95 kg CO_2 eq). These results are caused by the life-cycle stages of brine-based lithium extraction, which are associated with significant water depletion, ecosystem disturbance, chemical pollution and soil occupation. In addition, the energy-intensive manufacturing of battery cells likely contributes largely to the global warming potential. According to VanderPaer et al., the manufacturing step contributes between 87% and 50% to all impacts.

Though the selected batteries can be used across multiple SFDs due to their 600+ cycles, they still degrade over time and need to be replaced at some point. The end-of-life treatment of batteries remains challenging due to the limited recycling efficiencies and therefore the resources such as lithium and electrolyte remain to be disposed of in landfills or be incinerated. Both largely contribute to environmental impact categories, particularly in toxicity-related categories.

16.1.3.2. Composite structure

The impact assessment results for the composite structure show that the largest impact is the marine ecotoxicity, followed by carcinogenic toxicity. The high contribution of CFRP to global warming potential and fossil resource depletion can be traced back to the production of carbon fibres from

polyacrylonitrile (PAN) and the energy-intensive autoclave-curing. Impact on marine ecotoxicity can largely be acknowledged to the poor disposal option that releases high rates of toxic emissions and chemical releases like heavy metals and volatile organic compounds.

16.1.3.3. End-of-Life strategies

As described in the above sections, the End-of-Life (EoL) treatment contributes largely to the overall environmental impact of the scaled flight demonstrator due to the limited recyclability of both the LiPo batteries and the CFRP structures.

For the battery system, reuse and lifetime extension represent the most effective EoL strategies. Batteries that no longer meet the flight performance requirements can be repurposed in secondary applications. When the batteries have degraded so much that they are no longer functional, recycling is preferred over disposal. However, recycling processes remain energy-intensive and are unable to recover all materials within the batteries.

CFRP components are hard to recycle because thermoset composites cannot be remelted. Current recycling options are down-cycling, or energy-intensive thermal methods such as pyrolysis that recover fibres, though they do reduce their properties. New developments are also arising that can recover energy from the carbon fibres, though this does require incineration and thus releases toxic emissions.

16.1.3.4. Implications for design decisions

The results of both the batteries and the composite structure impose a key trade-off inherent to aerospace design. While CFRP normally enables significant mass reduction and thus fuel/energy saving in aerospace applications. Since this is a demonstrator, and thus needs to match the behaviour of a full-scale aircraft, the weight that is saved with the CFRP will be added back on the SFD to get to the mass and mass moment of inertia needed to match the characteristics of the full-scale aircraft. The CFRP production and disposal inflict a considerable environmental impact. Therefore, it could be valuable to look into other material options that perform equally but are more sustainable.

Similarly, the battery system emerges as a big contributor to toxicity-related impact categories, emphasising the importance of reuse across demonstrators and design-for-disassembly principles.

16.1.3.5. Limitations of results

The LCA relies on data from literature sources, and represents a preliminary design stage, and limited system coverage. Though the literature studies have been properly checked, some data about the batteries is relatively old with respect to battery innovation advancements. And, as the sources are from other studies, the results are less reliable as they are not focussed on the specific materials and batteries that this design uses.

16.2. Complementary sustainability analysis

The Life Cycle Assessment (LCA) only investigates the environmental impact of the SFD; this is not the only sustainability pillar that the SFD has an impact on. Therefore, this section will elaborate on its social and economic impact.

16.2.1. Social sustainability

The SFD has a large impact on social sustainability due to the batteries used for propulsion. The batteries chosen use a large amount of conflict minerals, such as lithium, cobalt and copper. The mining of minerals also often sparks conflicts due to the high demand. According to UNEP, 40% of conflicts over the last 60 years were mining-related [38]. Though completely abstaining from using the conflict minerals is not possible, with new programs, like the conflict-free sourcing program (CFSP), and Conflict Free Smelter (CFS) program, companies have proven it is possible to get these minerals sustainably [73] [74].

16.2.2. Economic sustainability

CFRP production is currently considerable more expensive than the production of their aluminium counterparts [61]. The CFRP-parts are often only produced on a small-scale, and are characterised by complex geometric properties. Moreover, the lead times are high because the material has to be

cured, and all fibres are hand-laid in the mould. To achieve growth in the usage of CFRP, a reduction in production cost and material cost is necessary [33]. The production process for composite parts is a lot more complicated than aluminium parts. To compose a CFRP-part carbon fibres, epoxy resins and a mould are needed. Whereas for an aluminium part, one just needs aluminium. The processes in the life cycle of these parts have been displayed in Figure 16.2. Therefore, for a larger amount of SFDs produced, alluminium would be advised.

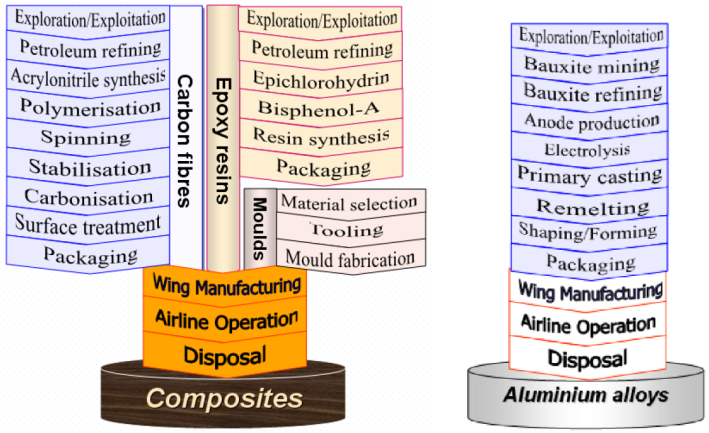

Figure 16.2: Typical processes in the life cycle of materials applied in aerospace engineering (a) Carbon Fibre Composite, and (b) Aluminium Alloys [61]

16.3. Modularity

Finally, a large part of the project has been dedicated to designing the SFD in a modular way. The main advantage of a modular SFD is that it can be used by other aircraft manufacturers to validate their designs. Moreover, Elysian could also reuse the SFD with, in example a swapped out wing, if their proposed design changes over time, provided it stays within the boundaries dictated by the previous design. A thorough analysis of the modularity options the design hosts is given in section 6.4.

16.3.1. Environmental Sustainability

Once a certain design has been tested by an SFD, and design choices are reconsidered, the same model can be used rather than rebuilding a new model each time the design changes. By doing so, this reduces the material usage, reduces negative environmental impact due to the reduction in extensive manufacturing processes needed and disposal of materials. Furthermore, with a more general design than the Elysian E9x, with the modularity, model can also be used multiple times for different types of research purposes, not needing a new design every time, or full scale tests.

Another way in which the environment is spared is that there is no need to produce the same parts again. The current design is based on the Elysian E9X; it will thus mimic the flight mechanical behaviour of their conceptual design. Nevertheless, with the modularity, it could be tailored to fit the requirements of other conceptual aircraft. Thus reducing not only the resources used for manufacturing, maintaining, recycling, and disposing the SFD, but also the hours made to come to a feasible design from scratch.

16.3.2. Economic Sustainability

The modularity aspect of our design allows a diversification of possible use cases. One of the reasons the modularity is chosen as a key design factor is to make the SFD attractive for multiple customers. If the SFD is only designed to fit Elysian's needs, the customer base will be limited to one. To ensure resources utilised for designing the SFD are regained, whereafter a possible profit could be made, having multiple customers is a major advantage.

16.4. Requirement Compliance

With the sustainability aspect of the SFD analysed, the compliance of the sustainability requirements can be assessed, and are found in Table 16.2. All requirements are met, with an exception to requirement SFD-SYS-SUS-03. Two complications were found with this requirement, the first being the fact that no data is available on a realistic emission rate of SFDs or similar designs. The second complication is the fact due to the preliminary nature of the design, no complete LCA could be executed. Though, a preliminary one has been conducted, this will not be an accurate representation.

Table 16.2: Requirement compliance sustainability requirements

ID	Requirement Description	Verification Method	Compliance Level
SFD-SYS-SUS-01	The propulsion system shall be purely electric, utilizing rechargeable battery energy storage.	Inspection	The SFD has engines that require an electric energy source and sufficient batteries installed.
SFD-SYS-SUS-02	~~The propulsion, actuation, and avionics subsystems shall consist exclusively of Commercial Off-The-Shelf (COTS) components.~~		All components named are Commercial Off-The-Shelf except for the propellers.
SFD-SYS-SUS-03	~~Total emission from manufacturing to end of life shall not exceed **<TBD>** kg of CO2-equivalent.~~		A full Life Cycle Analysis still needs to be performed.
SFD-SYS-SUS-04	Ten parts of the model shall be able to be reused in ten alternative layouts.	Demonstration	The six modularity options. Therefore, more than ten alternative layouts are achieved.
SFD-SYS-SUS-05	The manufacturing process shall comply with the energy-efficiency requirements of ISO 50001.	Analysis	An analysis will be performed in the supply chain of the SFD.
SFD-SYS-SUS-06	A risk analysis shall be conducted.	Inspection	A risk analysis has been performed
SFD-SYS-SUS-07	Parts on and in the model shall be replaceable without having to build a new model.	Demonstration	The SFD has a fuselage with a removable top fairing, allowing access to internal components. In addition, components are either fastened with screws, or bonded in separate housings that are then fastened with screws, enabling replacement.

17
Development plan

The goal of this chapter is to present the Project Design & Development Strategy after submitting the final report and presenting the project to the public during symposium. This chapter presents an updated approach to the development plan, aslaws of the previous development plan[20] have were identified and removed.

During the design process and analysis, further advantages of the modularity aspect of the aircraft were found. Furthermore, an initial interest of Elysian representatives and NLR was proclaimed.

Therefore, the group has grown in even higher motivation for the further development of the project and eventually leading to bringing the design to the market. To address that interest, an official visit to the Royal Netherlands Aerospace Centre in Marknesse and meeting with representatives is currently planned for the first weeks proceeding the symposium on 29th January 2026. During the meeting, it is planned to get to know with the local research and test facilities. Moreover, it is planned to discuss further cooperation possibilities.

Following the end of DSE, team is planning to finalize the current design by iterating further and applying both own conclusions, as well as feedback of tutors and the industry specialists. It is also hoped that a cooperation with NLR could be established to the level that could support the further design process. As an optimal design is reached, a detailed design of each component begins. Having detailed designs allows for production of prototypes, verifying them and validating them by component, subsystem and system testing. As an initial model is produced and assembled, it can be tested in a wind tunnel to validate the aerodynamic characteristics, as well as dynamic stability behaviour. Knowing the aerodynamic behaviour of the scaled aircraft, initial conclusions could be drawn for the final design of Elysian E9X aircraft, or the next iterations of the SFD. Having confirmed that the aeroplane behaves as intended, further on-ground, and eventually in-flight tests could be performed. The SFD is set to be mission ready in May 2027, however, there should be taken into account some margin because of setbacks and/or delays. The entire process is presented graphically using a Gantt chart in Figure 17.1. It was prepared as a tool to keep track of progress for the post-DSE activities.

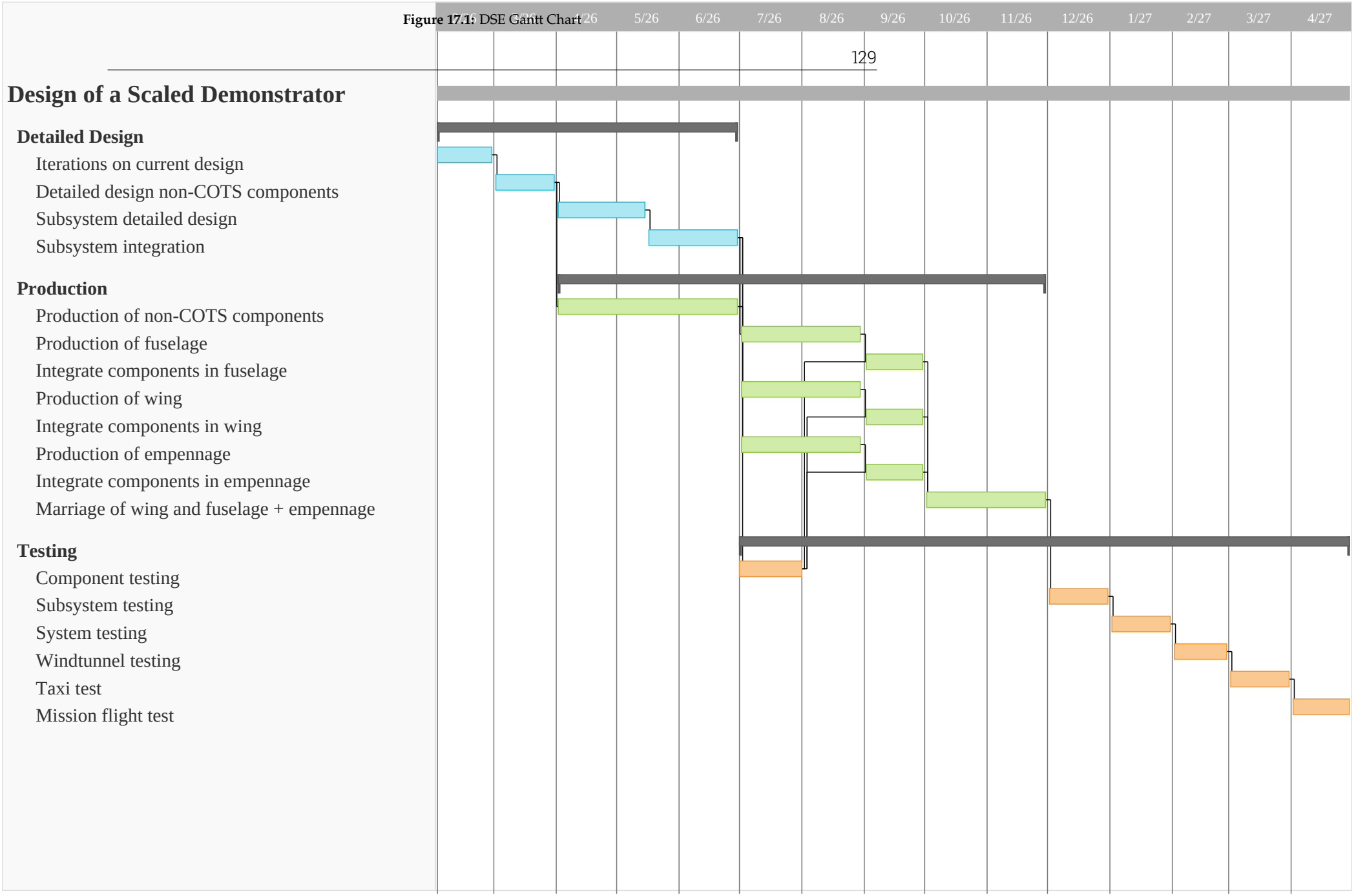

Figure 17.1: DSE Gantt Chart

18
Conclusion and Recommendations

18.1. Conclusion

The aim of this project was to develop an SFD (Scaled Flight Demonstrator) based on the Elysian E9X, with an option to generate more modularity. The goal of having a modular design was to make the SFD attractive to other customers by enabling them to fit the SFD to their design. To accomplish this, the task was given to a group of ten students performing their DSE (Design Synthesis Exercise) under the supervision of the Faculty of Aerospace Engineering at TU Delft.

The stakeholder requirements on performance are summarised as: the flight-model shall be able to perform tests on flight mechanical behaviour of the proposed aircraft, size and mass shall be chosen such that the demonstrator can carry an FCMS (Flight Control and Measurement System), the mass shall not exceed 150 [kg], a trade-off shall be made for 5%, 8%, 10% scale, and finally the SFD shall not have a wingspan larger than 7.5 [m]. The proposed design will be able to perform tests on the flight mechanical behaviour of the Elysian E9X, the design is tailored to fit their latest design choices. The FCMS is incorporated into the design; size and mass were chosen accordingly. The total mass of the SFD is 107.58 [kg] (without dummy weights); therefore, the mass does not exceed 150 [kg]. After thorough analysis using Froude scaling, 10% scaling was chosen; for technical analysis, 9.7% was used. The wingspan of the SFD is equal to 5.044 [m], which means the 7.5 [m] limit is met.

Regarding safety and operational mandates, the following requirements were set: the system's design shall satisfy all Dutch and International regulations regarding BVLOS flight, the system shall be able to perform 20 missions, and every mission shall have a minimum flight time of 20 minutes. The main aspect that had to be tackled regarding regulations is safety; the SFD is not allowed to crash into people or homes. Therefore, it was decided to fly at Marknesse drone-port, an empty enclosed airspace. In addition, the SFD is equipped with a termination system. The structure of the demonstrator is designed to retain sufficient load-carrying capability to sustain at least 20 missions. The fatigue, creep, and fracture properties have also been examined, and it was concluded that these will not endanger the structural integrity of the SFD for the first 20 missions. The powertrain has been designed to have enough power to sustain a mission phase of at least 20 minutes. This segment is allocated 80% of the battery capacity; the remainder is reserved for take-off, landing, and reserve-capacity.

Sustainability is a key design factor for the SFD, as dictated by the following requirements: the system shall be able to complete proof-of-concept flight-testing using battery-electric motors, the demonstrator shall be set up to allow key parts to be used in different configurations, and the equipment and powertrain shall only use COTS (Commercially Off-The-Shelf) available components. The propulsion system consists of 6 battery electric motors combined with propellers; the required energy is supplied by 5 drone-specific LiPo (Lithium-ion Polymer) batteries. The design of the SFD is modular; interchangeable wings allow for various propulsion systems and layouts, a changeable tailcone allows for different empennage configurations, and the possibility to attach dummy weights. The wing can be equipped with various slat or flap configurations, and the dummy weights can be used to adjust the cg (centre of gravity) location or the mass moment of inertia of the system. The equipment chosen is all on COTS availability, for the propulsion system, COTS components have been selected, except for the propeller blades. The TUD-XPROP was selected, but a different blade design was chosen for our demonstrator; therefore, these blades will have to be manufactured custom.

Regarding the cost of the demonstrator certain limitations were set: the total research & design cost may not exceed 800k euros, and the system shall have a total ready-to-fly manufacturing cost not exceeding 1 million euros. The total amount for research & design was estimated as 675k euros, thus meeting the requirement of 800k euros. The system's ready-to-fly manufacturing cost comes down to 821,124 euros, comfortably below the 1 million euros ceiling.

In conclusion, an SFD has been created that is fitting to the needs of Elysian and also hosts modular features, is safe and can perform 20 missions of 20 minutes, is fully battery-electric, and managed to stay within budget. A render of the proposed design with the modularity options separated from the fuselage is shown in Figure 18.1.

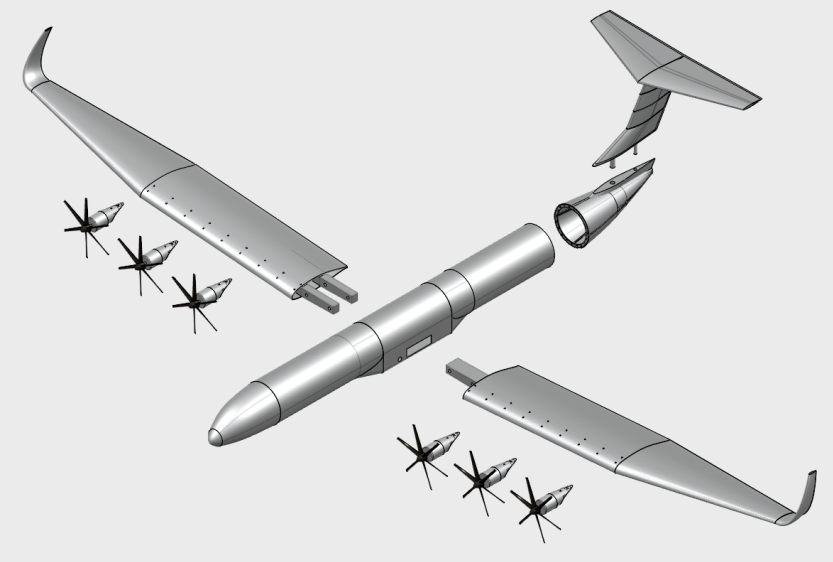

Figure 18.1: Exploded view of the S.K.R.I.B.B.L. with modularity options

18.2. Recommendations

This report demonstrates that an overall design has been established. However, it has not been developed into detail yet. Therefore, this section presents a number of recommendations for future studies

18.2.1. General

During the initial design phase, the decision was made to use pixel counting as a sizing method for the full-scale model of the Elysian E9X. This decision was made as no accurate data was available besides the technical drawings provided by de Vries et al.[71]. The consequence is that the measurements used in the calculations throughout this report could be off and affect the accuracy of the results. Therefore, it is recommended that a closer collaboration with Elysian be established, enabling access to more accurate data.

Furthermore, this report focussed on creating a design that will imitate the properties of the Elysian E9X as closely as possible. While this aligns with the intended objective, in terms of market attractiveness, it could be interesting to pursue a more general design. This could mean that the same SFD design would be able to meet the requirements of multiple other customers. Though this carries the risk of losing Elysian as a potential customer.

Finally, the estimations made for the revenue and return on investment were not based on accurate data. It is recommended that a reliable database be consulted in future analyses.

18.2.2. Modularity

While this report had a significant focus on modularity, the design focused initially on the SFD itself, with modularity considered afterwards. In some cases, this approach limited the potential of modular design. Therefore, it is recommended that modularity is assessed earlier in the design process. From that, the SFD can be developed upon those modular decisions.

18.2.3. Technical departments

Aerodynamics

The N-factor is a measure of free-flow turbulence, the disturbance of the flow. The e^N method predicts

the transition point of the disturbance. This factor has a significant influence on the aerodynamic similitude of the SFD, as it directly affects the flow conditions encountered by the model, which must closely replicate those of the full-scale aircraft. For this report, the estimation of N that best simulates the full-scale behaviour was found through multiple iterations in Flow 5 with a fixed Reynolds number. To build upon this, in a wind tunnel where N can be varied, tests can be performed to find the value that would provide the most similitude to the full scale at given altitudes.

In addition, a significant amount of simulations in this report were performed using Flow5. While this is an acceptable method in this preliminary stage, more accurate estimation methods are required as the design is developed in to further detail. This can be achieved with other tools such as Computational Fluid Dynamics (CFD) simulation. For the estimation of the propeller effects, the airfoil is assumed to be symmetrical, though this is not the case. For a future study, it is advised to research what the value of α_p is through experimental or numerical data, to more accurately account for the effect of the non-symmetric airfoil.

Furthermore, the propulsion system affects the Oswald efficiency factor. However, this was not accounted for during the estimation of the factor. In future studies, it is recommended through wind-tunnel tests or CFD calculations.

Structures
During the material selection, CFRP composite was chosen for its high strength-to-density ratios, while aluminium scored better in cost, manufacturability, and sustainability categories. The design also showed that, regarding weight, aluminium is feasible, though the design would be less modular. In future studies, it could be beneficial to reassess the material selection to determine the most suitable material.

Second, during the initial design phase, a wingbox configuration was selected. As the design has been developed into further detail, it has become apparent that a full wingbox could be redundant. It is suggested that the feasibility of a wing structure design of solely the wing-foil and two spars be investigated.

Power and Propulsion
As the propeller was a custom design, its characteristics could only be estimated. For more accurate determination of performance parameters and properties, it is recommended to conduct experimental testing.

Furthermore, the propeller, motor, and ECS were selected as separate components, without assessing their interactions. It would be beneficial to investigate the coupled behaviour of these components in future work.

Finally, cooling performance was not taken into account during the design process. It is encouraged for future work to investigate this, as inadequate motor cooling could mean cooling ducts need to be added, which can affect the aerodynamic properties.

Stability and Control
While other lateral dynamic stability modes were found to be stable, the Dutch roll was found to be an issue. It could be resolved by applying a controller such as PID, or by changing the design by increasing the vertical tail size or lowering down the horizontal tail or wing's dihedral.

Since the phugoid mode is close to instability, it is recommended that measures are taken to improve its stability. This could be achieved by moving the CG forward, or by adjusting the angle of incidence of the horizontal tail.

Currently, the actuator's dead band width and running angle lead to the aircraft rapid responses to actuator position error. This could be lowered by adjusting the positions of the gearwheels to improve control stability.

References

[1] P. Schmollgruber et. al. "RESULTS OF THE SCALED FLIGHT DEMONSTRATOR FLIGHT TESTS". In: *ICAS 2024* (2024), pp. 1–15.

[2] Ali Alamry. "Fatigue damage and analysis of laminated composites: A state-of-the-art". In: *Journal of Engineering Research* 13.3 (2025), pp. 2066–2076. ISSN: 2307-1877. DOI: https://doi.org/10.1016/j.jer.2024.09.006. URL: https://www.sciencedirect.com/science/article/pii/S230718772400244X.

[3] John Anderson. *Fundamentals of Aerodynamics*. Mcgrawhill, 2016. ISBN: 9780070016798.

[4] Nando van Arnhem et al. "Engineering method to estimate the blade loading of propellers in nonuniform flow". English. In: *AIAA Journal* 58.12 (2020), pp. 5332–5346. ISSN: 0001-1452. DOI: 10.2514/1.J059485.

[5] Yagmur Atescan-Yuksek et al. "Comparative life cycle assessment of aluminium and CFRP composites: the case of aerospace manufacturing". In: *The International Journal of Advanced Manufacturing Technology* 131 (2024), pp. 4345–4357. DOI: 10.1007/s00170-024-13241-3. URL: https://doi.org/10.1007/s00170-024-13241-3.

[6] K. Biber. "Estimating Propeller Slipstream Drag on Airplane Performance". In: *Journal of Aircraf* 48.1 (2011). URL: https://doi.org/10.2514/1.C031458.

[7] José Antonio Butenegro et al. "Recent Progress in Carbon Fiber Reinforced Polymers Recycling: A Review of Recycling Methods and Reuse of Carbon Fibers". In: *Materials* 14.21 (2021), p. 6401. DOI: 10.3390/ma14216401. URL: https://www.mdpi.com/1996-1944/14/21/6401.

[8] CA. *Clean sky 2*. 2025. URL: https://www.clean-aviation.eu/research-and-innovation/clean-sky-2 (visited on 11/18/2025).

[9] CA. *Clean sky 2*. 2025. URL: https://www.clean-aviation.eu/research-and-innovation/clean-sky-2/clean-sky-2-achievement-report/clean-sky-2s-key-achievements/novel-aircraft-scaled-flight-test-demonstration (visited on 11/19/2025).

[10] T. Centea, L. K. Grunenfelder, and S. R. Nutt. "A review of out-of-autoclave prepregs – Material properties, process phenomena, and manufacturing considerations". In: *Composites Part A: Applied Science and Manufacturing* 70 (2015), pp. 132–154. DOI: 10.1016/j.compositesa.2014.09.029. URL: https://www.sciencedirect.com/science/article/pii/S1359835X14003108.

[11] CMI. *Global Flight Demonstrator Market 2024–2033*. 2024. URL: https://www.custommarketinsights.com/report/flight-demonstrator-market (visited on 11/18/2025).

[12] Y. Dai and A. Panahi. "Thermal runaway process in lithium-ion batteries: A review". In: *Next Energy* 6 (2025). DOI 10.1016/j.nxener.2024.100186, pp. 123–456.

[13] M. Danko et al. "Overview of batteries State of Charge estimation methods". In: *Transportation Research Procedia* 40 (2019). DOI 10.1016/j.trpro.2019.07.029, pp. 186–192.

[14] TU Delft. *ADSEE lift and drag estimation*. https://brightspace.tudelft.nl/d2l/le/content/782584/viewContent/44408 [Accessed 02-12-2025]. 2025.

[15] TU Delft. *PMSE lecture 1*. https://brightspace.tudelft.nl/d2l/le/content/782584/viewContent/4440833/View. [Accessed 02-12-2025]. 2025.

[16] DNW. *Large Low-Speed Facility (LLF)*. German-Dutch Wind Tunnels. 2025. URL: https://www.dnw.aero/wind-tunnels/llf/ (visited on 12/09/2025).

[17] C. Döll, M.F.M. Hoogreef, and P. Iannelli. "Final Design, Manufacturing and Testing of the Clean Sky 2 Distributed Electric Propulsion Scaled Flight Demonstrator D08 DEP-SFD". In: *Proceedings of the AIAA SCITECH 2024 Forum* (2024). AIAA Paper, doi:10.2514/6.2024-1304.

[18] Carsten Döll et al. "Final Design, Manufacturing and Testing of the Clean Sky 2 Distributed Electric Propulsion Scaled Flight Demonstrator D08 DEP-SFD". In: *AIAA SCITECH 2024 Forum*. Also available at http://arc.aiaa.org. Orlando, FL: American Institute of Aeronautics and Astronautics, Jan. 2024. DOI: 10.2514/6.2024-1304.

[19] DSE Group 2. "Baseline Report". In: *Design of a Scaled Demonstrator Flight Test Model+* 1 (2025), pp. 1–50.

[20] DSE Group 2. "Midterm Report". In: *Design of a Scaled Demonstrator Flight Test Model+* 1 (2025), pp. 1–75.

[21] Larry L. Erickson. "Panel Methods - An Introduction". In: *NASA* 1.5 (1990), p. 49. DOI: 19910009745.
[22] ESDU. *Introduction to installation effects on thrust and drag for propeller-driven aircraft*. 2006. URL: https://www.esdu.com/cgi-bin/ps.pl?sess=unlicensed_1260114081559gck&t=doc&p=esdu_85015b.
[23] B. Etkin and L. D. Reid. *Dynamics of Flight: Stability and Control*. 3rd. John Wiley & Sons, Inc., 1996. ISBN: 0-471-03418-5.
[24] EU. *Horizon Europe*. 2025. URL: https://research-and-innovation.ec.europa.eu/funding/funding-opportunities/funding-programmes-and-open-calls/horizon-europe_en (visited on 11/19/2025).
[25] Touraj Farsadi and Jaber J. Hasbestan. "Calculation of Flutter and Dynamic Behavior of Advanced Composite Swept Wings with Tapered Cross Section in Unsteady Incompressible Flow". In: *Mechanics of Advanced Materials and Structures* 26 (Oct. 2017). DOI: 10.1080/15376494.2017.1387322.
[26] Flow5 Tech. *Flow5, The Jibe2 experiment - revisited*. 2020. URL: https://flow5.tech/docs/flow5_doc/Validation/Jibe2.html%5C#conclusions (visited on 01/14/2026).
[27] Snorri Gudmundsson. *General Aviation Aircraft Design: Applied Methods and Procedures*. 2nd. Oxford, UK: Matthew Deans, 2022. ISBN: 978-0-12-818465-3.
[28] Mark W. Hilburger. *Buckling of Thin-Walled Circular Cylinders*. Special Publication NASA/SP-8007-2020/REV 2. Available from NASA Technical Reports Server (NTRS); Document ID: 20205011530. Hampton, VA, United States: National Aeronautics and Space Administration, Langley Research Center, Dec. 2020. URL: https://ntrs.nasa.gov/api/citations/20205011530/downloads/20205011530%20Rev%202FINALa%201-2023.pdf.
[29] Christian Hueber, Konstantin Horejsi, and Ralf Schledjewski. "Review of cost estimation: methods and models for aerospace composite manufacturing". In: *Advanced Manufacturing: Polymer & Composites Science* 2.1 (2016), pp. 1–13. ISSN: 2055-0340 (Print), 2055-0359 (Online). DOI: 10.1080/20550340.2016.1154642.
[30] Huntsman Advanced Materials. *Araldite 2031 Structural Adhesive: Technical Data Sheet*. Huntsman Advanced Materials. Jan. 2023. URL: https://www.huntsman.com/advanced-materials.
[31] ICAO. *Title of the Website*. 2024. URL: https://www.icao.int/news/aviation-sector-advances-towards-net-zero-carbon-emissions-goal-icao-stocktaking-event (visited on 11/17/2025).
[32] J. van Ingen. "The eN Method for Transition Prediction. Historical Review of Work at TU Delft". In: *AIAA* 1.5 (2012), p. 49. DOI: https://doi.org/10.2514/6.2008-3830open_in_new.
[33] M. Kafara et al. "Comparative Life Cycle Assessment of Conventional and Additive Manufacturing in Mold Core Making for CFRP Production". In: *Procedia Manufacturing* 8 (2017). 14th Global Conference on Sustainable Manufacturing, GCSM 3-5 October 2016, Stellenbosch, South Africa, pp. 223–230. ISSN: 2351-9789. DOI: https://doi.org/10.1016/j.promfg.2017.02.028. URL: https://www.sciencedirect.com/science/article/pii/S2351978917300343.
[34] Sportine Aviacija ir Ko. *Mainenance manual for the LAK-17B FES sailplane*. Sportine Aviacija ir Ko, 2014.
[35] Koninklijk Nederlands Lucht- en Ruimtevaartcentrum. *Safety leaflet: Waarschuwing Gebruik Luchtruim – EHR66 & TGB NLR Testcentrum High*. Safety Leaflet. Contact: nrtc@nlr.nl. NLR (Royal Netherlands Aerospace Centre), n.d. URL: https://www.nlr.nl.
[36] Renjith Krishnan and Gokul Gopan. "A comprehensive review of lithium extraction: From historical perspectives to emerging technologies, storage, and environmental considerations". In: *Cleaner Engineering and Technology* 20 (2024), p. 100749. DOI: 10.1016/j.clet.2024.100749. URL: https://doi.org/10.1016/j.clet.2024.100749.
[37] M&M. *Aircraft platforms market by type*. 2025. URL: https://www.marketsandmarkets.com/Market-Reports/aircraft-platforms-market-158064874.html (visited on 11/18/2025).
[38] R. A. Matthew, O. Brown, and D. Jensen. *From conflict to peacebuilding: The role of natural resources and the environment*. 1. UNEP/Earthprint, 2009.
[39] T. H. G. Megson. *Aircraft Structures for Engineering Students*. English. 6th. Elsevier Aerospace Engineering Series. Oxford: Butterworth-Heinemann, an imprint of Oxford, 2017. ISBN: 978-0-08-100914-7.
[40] J. A. Mulder et al. *Flight Dynamics: Lecture Notes*. Faculty of Aerospace Engineering, Course AE3202. Delft University of Technology, Mar. 2013.

[41] S.R. Naqvi et al. "A critical review on recycling of end-of-life carbon fibre/glass fibre reinforced composites waste using pyrolysis towards a circular economy". In: *Resources, Conservation & Recycling* 136 (2018), pp. 118–129. DOI: 10.1016/j.resconrec.2018.04.013. URL: https://doi.org/10.1016/j.resconrec.2018.04.013.

[42] Nederlands Lucht- en Ruimtevaartcentrum. *NLR Drone Centre*. NLR. 2025. URL: https://www.nlr.org/newsroom/facility/nlr-drone-centre/.

[43] J. Nitzsche et al. "Fluid-mode flutter in plane transonic flows". In: *IFASD 2019* (2019).

[44] NLR. *Scaled Flight Demonstrators*. 2025. URL: https://www.nlr.org/newsroom/case/scaled-flight-demonstrator-sfd/ (visited on 11/18/2025).

[45] E. Obert. *A method for the determination of the effect of propeller slipstream on static longitudinal stability and control of multi-engined aircraft*. Report LR-761. Delft, The Netherlands: Delft University of Technology, Faculty of Aerospace Engineering, Dec. 1994.

[46] Chizoba J. Ogugua et al. "Energy analysis of autoclave CFRP manufacturing using thermodynamics-based models". In: *Composites Part A: Applied Science and Manufacturing* 168 (2023), p. 107365. DOI: 10.1016/j.compositesa.2022.107365. URL: https://www.sciencedirect.com/science/article/pii/S1359835X22005462.

[47] Michael D. Patterson. "Conceptual Design of High-Lift Propeller Systems for Small Electric Aircraft". PhD thesis. Georgia Institute of Technology, 2016.

[48] Mark Peplow. "Lithium-ion battery recycling goes large". In: *Chemical & Engineering News* 101.38 (2023). Accessed: 2026-01-XX, pp. 24–32. URL: https://cen.acs.org/environment/recycling/Lithium-ion-battery-recycling-goes/101/i38.

[49] Daniel P. Raymer. *Aircraft Design: A Conceptual Approach*. 2nd ed. 370 L'Enfant Promenade, S.W., Washington, D.C. 20024: American Institute of Aeronautics and Astronautics, 1992.

[50] Jan Roskam. *Airplane Design Part I: Preliminary Sizing of Airplanes*. Lawrence, Kansas: DARcorporation, 2018. ISBN: 978-1-884885-42-6.

[51] Jan Roskam. *Airplane Design Part II: Preliminary Configuration Design and Integration of the Propulsion System*. Lawrence, Kansas: DARcorporation, 2004. ISBN: 1-884885-43-8.

[52] Jan Roskam. *Airplane Design Part V: Component Weight Estimation*. Table of contents available at provided URL; full text from DARcorporation series on airplane design methods including Cessna landing gear estimation (Section 5.5.1.1). Lawrence, Kansas: DARcorporation, 1999. ISBN: 9781884885501. URL: https://shop.darcorp.com/Books/Contents/APD_V.pdf.

[53] Jan Roskam. *Airplane Design Part VI: Preliminary Calculation of Aerodynamic, Thrust and Power Characteristics*. Lawrence, Kansas: DARcorporation, 1987. ISBN: 978-1884885525.

[54] Jan Roskam. *Airplane Design Part VII: Determination of Stability, Control and Performance Characteristics: FAR and Military Requirements*. 2002 Reprint. Lawrence, Kansas: DARcorporation, 2002. ISBN: 978-1-884885-54-9.

[55] Mohammad H. Sadraey. *Aircraft Design: A Systems Engineering Approach*. Aerospace Series. Chichester, UK: John Wiley & Sons, Ltd, 2013. ISBN: 978-1-119-95340-1.

[56] Hermann Schlichting. *BoundaryLayer Theory*. 9th. Ger: Springer, 2022. ISBN: 978-3-662-52917-1.

[57] B. M. Simmons, H. G. Visser, and C. C. de Visser. "Flight Test System Identification Techniques and Applications for Small, Low-Cost, Fixed-Wing Aircraft". In: *Aerospace* 10.5 (2023), p. 427. DOI: 10.3390/aerospace10050427.

[58] Tomas Sinnige. *Propeller Propulsion Aerodynamics*. AE4130 - Aircraft Aerodynamics, Lecture #14, Faculty of Aerospace Engineering, TU Delft. [Accessed 13-01-2026]. 2025.

[59] Thomas W. Strganac. "(NASA-TM-101126) A numerical model of unsteady, subsonic aeroelastic behavior". In: (Aug. 1987).

[60] Marko Szcesny et al. "The advanced ply placement process – an innovative direct 3D placement technology for plies and tapes". In: *Advanced Manufacturing: Polymer & Composites Science* 3.1 (2017), pp. 2–9. ISSN: 2055-0340 (Print), 2055-0359 (Online). DOI: 10.1080/20550340.2017.1291398.

[61] X. Tan et al. "Cost-Efficient Materials in Aerospace: Composite vs Aluminium". In: *Collaborative Product and Service Life Cycle Management for a Sustainable World*. Ed. by Richard Curran, Shuo-Yan Chou, and Amy Trappey. London: Springer London, 2008, pp. 259–266. ISBN: 978-1-84800-972-1.

[62] *Tattu Pro 22000mAh 51.8V 25C 14S1P LiPo Smart Battery Pack with AS150U-F Plug*. https://genstattu.com/tattu-pro-22000mah-51-8v-25c-14s-1p-lipo-smart-battery-pack-with-as150u-f-plug/. Accessed: 20/01/2026. n.d.

[63] Tomas Sinnige. *XFLR5 Analysis of foils and wings operating at low Reynolds numbers*. Online paper. 2009.
[64] TU Delft. "AE3-200 project description". In: *The Title of the Journal* (2000), pp. 1–12.
[65] United States Environmental Protection Agency. *Locating and Estimating Air Emissions from Sources of Acrylonitrile*. EPA Technical Report EPA-450/4-84-007a. Accessed: 2026-01-XX. U.S. Environmental Protection Agency, Office of Air Quality Planning and Standards, 1984. URL: https://www.epa.gov/sites/default/files/2020-11/documents/acrylonitrile.pdf.
[66] Laurent Vandepaer, Julie Cloutier, and Ben Amor. "Environmental impacts of Lithium Metal Polymer and Lithium-ion stationary batteries". In: *Renewable and Sustainable Energy Reviews* 78 (2017), pp. 46–60. DOI: 10.1016/j.rser.2017.04.057. URL: https://www.ourenergypolicy.org/wp-content/uploads/2017/05/1-s2.0-S1364032117305580-main.pdf.
[67] L.L.M. Veldhuis. "Propeller Wing Aerodynamic Interference". PhD thesis. TU Delft, 2005.
[68] María L. Vera et al. "Environmental impact of direct lithium extraction from brines". In: *Nature Reviews Earth & Environment* 4.3 (2023), pp. 149–165. DOI: 10.1038/s43017-022-00387-5. URL: https://doi.org/10.1038/s43017-022-00387-5.
[69] R. de Vries, M. Brown, and R. Vos. "Preliminary Sizing Method for Hybrid-Electric Distributed-Propulsion Aircraft". In: *JOURNAL OF AIRCRAFT* 56.6 (2019).
[70] Reynard de Vries et al. "A New Perspective on Battery-Electric Aviation, Part II: Conceptual Design of a 90-Seater". In: *Proceedings of the AIAA SCITECH 2024 Forum*. American Institute of Aeronautics and Astronautics (AIAA), 2024. DOI: 10.2514/6.2024-1490.
[71] Reynard de Vries et al. "Conceptual Redesign of a 90-Seater Battery-Electric Aircraft". In: *Proceedings of the AIAA Aviation Forum and ASCEND 2025*. American Institute of Aeronautics and Astronautics (AIAA), 2025. DOI: 10.2514/6.2025-3153.
[72] C.H. Wolowicz, J.S. Brown, and W.P. Gilbert. *Similitude requirements and scaling relationships as applied to model testing*. Tech. rep. NASA, 1979. URL: https://ntrs.nasa.gov/citations/19790022005.
[73] S. B. Young. "Responsible sourcing of metals: certification approaches for conflict minerals and conflict-free metals". In: *The International Journal of Life Cycle Assessment* 23.7 (2018), pp. 1429–1447.
[74] S. B. Young and G. Dias. "Conflict-free minerals supply-chain to electronics". In: *2012 Electronics Goes Green 2012+*. IEEE. 2012, pp. 1–5.
[75] Xianlai Zeng, Jinhui Li, and Narendra Singh. "Recycling of Spent Lithium-Ion Battery: A Critical Review". In: *Critical Reviews in Environmental Science and Technology* 44.10 (2014), pp. 1129–1165. DOI: 10.1080/10643389.2013.763578. URL: https://doi.org/10.1080/10643389.2013.763578.